

# **Resonant optical trapping in microfluidic-integrated hollow photonic crystal cavities**

THÈSE N° 5904 (2013)

PRÉSENTÉE LE 13 SEPTEMBRE 2013  
À LA FACULTÉ DES SCIENCES DE BASE  
LABORATOIRE D'OPTOÉLECTRONIQUE QUANTIQUE  
PROGRAMME DOCTORAL EN PHOTONIQUE

ÉCOLE POLYTECHNIQUE FÉDÉRALE DE LAUSANNE

POUR L'OBTENTION DU GRADE DE DOCTEUR ÈS SCIENCES

PAR

**Nicolas DESCHARMES**

acceptée sur proposition du jury:

Prof. C. Moser, président du jury  
Prof. R. Houdré, directeur de thèse  
Prof. H. Benisty, rapporteur  
Prof. J. Faist, rapporteur  
Prof. S. Maerkl, rapporteur



ÉCOLE POLYTECHNIQUE  
FÉDÉRALE DE LAUSANNE

Suisse  
2013



# Abstract

The recent years have highlighted the potential of photonic nanostructures to extend the capabilities of optical tweezers and to perform advanced optical manipulations. In this context, two-dimensional photonic crystal cavities have been regarded as promising candidates owing to their high quality factors and low mode volumes. The work presented in this thesis reports the setting up of a complete experimental platform and the demonstration of optical trapping using the field confined in a planar photonic crystal cavity. In this work, cavities formed by a large circular defect, 700 nm in the diameter, in a triangular lattice are studied. These cavities possess a high quality factor (up to 7000 in air, around 2000 in water) and a central region where the confined field overlaps with the immersion medium. This feature offers a singular advantage for the maximization of the interaction between the cavity field and a particle as compared with standard photonic crystal cavity. An ultra-thin PDMS microfluidic membrane ( $\approx 170 \mu\text{m}$ ) is developed for the reliable immersion of the hollow cavities and the control of the flow of nanoparticles to be trapped. The hollow cavities are then integrated within a microchannel within the membrane. The characterization and excitation of the cavities is then performed on the developed optical bench. Fluorescent imaging of the polystyrene particles is performed along with position tracking. The micro manipulation of the particles in the neighborhood of the cavity is realized through a combination of microfluidic valves and optical tweezers. Based on this experimental platform, the resonant optical trapping of 250 and 500 nm polystyrene particles is demonstrated. Trapping times of the order of several tens of minutes are obtained at sub-milliwatt optical powers. Further investigations are then performed on the perturbation of the cavity mode induced by the presence of a particle. This perturbation is experimentally observed in the form of a resonance wavelength shift of more than two cavity mode linewidth in the case of a 500 nm particle. Finally, the existence of back-action between the trapped particle and the cavity mode is experimentally evidenced. The later allows to observe the presence of two distinct trapping regimes. A qualitative understanding of these regimes is proposed based on a finite element method analysis.

## Keywords

Photonic crystals, hollow cavities, optical trapping, single-particle manipulation, single-particle detection.





# Résumé

Ces dernières années ont mis en avant la capacité des nanostructures photoniques à dépasser les performances actuelles des pinces optiques classiques, ou à permettre l'émergence de nouvelles méthodes. Dans ce contexte, les cavités à cristaux photoniques bidimensionnels sont perçues comme très prometteuses. Elles possèdent notamment de forts facteurs de qualité et des volumes de mode restreints. Le travail documenté dans cette thèse présente la mise en place d'une plateforme expérimentale puis la démonstration du piégeage de nanoparticules dans le champ confiné d'une cavité à cristaux photoniques planaire. Dans ce travail, les cavités étudiées sont constituées d'un défaut circulaire de 700 nm de diamètre dans un réseau triangulaire. Ces cavités possèdent un grand facteur de qualité (jusqu'à 7000 dans l'air, environ 2000 dans l'eau). Elles possèdent également une région centrale où le champ confiné recouvre le milieu d'immersion. Cette particularité leur confère un grand avantage en terme de maximisation de l'interaction entre la particule et le champ confiné, par rapport aux cavités à cristaux photoniques traditionnelles. Une très fine membrane en PDMS ( $\approx 170 \mu\text{m}$ ) est développée dans le but d'effectuer l'immersion des cavités de manière fiable et de permettre le contrôle du flux de particules utilisées pour le piégeage. Les cavités creuses sont ensuite positionnées au cœur d'un microcanal, lui-même situé au sein de la membrane. La caractérisation ainsi que l'excitation des cavités est effectuée sur le banc d'optique développé. L'imagerie en fluorescence des particules injectées y est également obtenue, et permet le suivi de particules individuelles. L'usage conjoint de valves microfluidiques et de pinces optiques permet aussi leur micromanipulation dans le voisinage d'une cavité. Sur la base de cette plateforme expérimentale, le piégeage résonant de particules en polystyrène de 250 et 500 nm est démontré. Des temps de piégeage de l'ordre de plusieurs dizaines de minutes sont obtenus pour des puissances optiques inférieures au milliwatt. La perturbation du mode cavité induite par la présence de la particule est ensuite étudiée. Cette perturbation est mesurée de manière expérimentale. Il se traduit sous la forme d'un décalage de la fréquence de résonance supérieur à deux largeurs de raie du mode de cavité, dans le cas d'une particule de 500 nm. Enfin, l'existence d'une rétroaction entre la particule piégée et le mode de cavité est mise en évidence. Cette dernière se manifeste notamment par l'existence de deux régimes de piégeage distincts. Une explication qualitative de la nature de ces deux régimes est proposée sur la base d'une analyse numérique effectuée par éléments finis.

---

## Mots-clefs

Cristaux photoniques, cavités creuses, piègeage optique, manipulation de particule unique, détection de particule unique.

# Contents

<b>Abstract (English/Français)</b>	<b>iii</b>
<b>Table of contents</b>	<b>ix</b>
<b>List of figures</b>	<b>xiii</b>
<b>List of tables</b>	<b>xv</b>
<b>Glossary</b>	<b>xvii</b>
<b>1 Introduction</b>	<b>1</b>
<b>2 Light confinement in planar photonic crystal cavities</b>	<b>7</b>
2.1 Photonic crystals and photonic bandgaps . . . . .	7
2.1.1 Introduction . . . . .	7
2.1.2 Examples of photonic crystal structures . . . . .	7
2.1.3 Band diagrams and photonic bandgap . . . . .	9
2.1.4 Brief history of photonic crystal materials . . . . .	12
2.2 Silicon photonic crystal membranes . . . . .	13
2.2.1 Properties . . . . .	13
2.2.2 Fabrication process . . . . .	15
2.2.3 Computation methods . . . . .	17
2.2.4 Line defect waveguide in a triangular lattice . . . . .	18
2.3 Two-dimensional photonic crystal cavities . . . . .	20
2.3.1 Physics of the cavities . . . . .	20
2.3.2 Standard photonic crystal cavities . . . . .	21
2.3.3 Hollow cavities . . . . .	23
<b>3 Optomechanical forces and applications</b>	<b>27</b>
3.1 Optical forces on a mechanical object . . . . .	27
3.1.1 Introduction . . . . .	27
3.1.2 The Maxwell Stress Tensor . . . . .	28
3.1.3 Optical forces on a point-like dipole . . . . .	31
3.1.4 Optical forces on a small spherical particle - Rayleigh approximation . . . . .	32
3.1.5 Beyond the Rayleigh approximation . . . . .	34
	vii

## Contents

---

3.2	Optical tweezers . . . . .	35
3.2.1	History . . . . .	35
3.2.2	Principle . . . . .	36
3.2.3	Applications . . . . .	40
3.3	Nanostructures for optical trapping . . . . .	42
3.3.1	Nano-antennas and plasmonic structures . . . . .	42
3.3.2	Dielectric waveguides . . . . .	44
3.3.3	Dielectric microcavities . . . . .	45
<b>4</b>	<b>Experimental set-up</b>	<b>49</b>
4.1	Overview and general considerations . . . . .	50
4.2	Fourier imaging . . . . .	51
4.2.1	k-vector conservation . . . . .	53
4.2.2	Optical arrangement . . . . .	54
4.2.3	Example of characterization of a photonic crystal structure . . . . .	55
4.3	Fluorescence excitation and imaging . . . . .	56
4.3.1	Particles, fluorescent markers and laser excitation . . . . .	58
4.3.2	Optical arrangements . . . . .	60
4.3.3	Detection and choice of camera . . . . .	64
4.4	Auxiliary optical tweezers . . . . .	66
4.4.1	Optical arrangement . . . . .	66
4.4.2	Trapping wavelength . . . . .	67
4.5	Confocal sensing . . . . .	69
4.5.1	Principle . . . . .	70
4.5.2	Optical arrangement . . . . .	72
4.5.3	Performance . . . . .	73
4.5.4	Limitations . . . . .	75
4.6	Possible additions and improvements . . . . .	75
<b>5</b>	<b>The optofluidic chip</b>	<b>77</b>
5.1	Motivation and early experiments . . . . .	77
5.1.1	Local infiltration approach . . . . .	78
5.1.2	Glass reservoir approach . . . . .	79
5.2	Microfluidic circuit and chip design . . . . .	81
5.2.1	Introduction to microfluidics . . . . .	81
5.2.2	Design of the optofluidic chip . . . . .	83
5.3	Fabrication of the optofluidic chip . . . . .	86
5.3.1	Design and etching of the photolithography mask . . . . .	86
5.3.2	Photolithography of the master moulds . . . . .	87
5.3.3	Membranes replica molding . . . . .	89
5.3.4	Chip assembly . . . . .	89
5.3.5	Some important aspects in fabrication . . . . .	91
5.4	Actuation and performance . . . . .	94

5.4.1	Pneumatic control system . . . . .	94
5.4.2	Valving and flow speeds . . . . .	96
5.4.3	Sample lifetime . . . . .	99
5.5	Limitations and alternative approaches . . . . .	101
5.5.1	Optical quality . . . . .	101
5.5.2	Fabrication and reusability . . . . .	106
5.5.3	Smaller sized chips . . . . .	109
<b>6</b>	<b>Resonant optical trapping and back-action effects</b>	<b>113</b>
6.1	Properties of the circular cavities . . . . .	113
6.1.1	Hollow cavity in air . . . . .	114
6.1.2	Hollow cavity in water . . . . .	117
6.2	Resonant optical trapping . . . . .	119
6.2.1	Resonant trapping of 500 nm polystyrene particles . . . . .	119
6.2.2	Particle confinement and suspended nature of the trap . . . . .	121
6.2.3	Exclusivity and trapping volume . . . . .	124
6.2.4	Estimation of the trapping power . . . . .	125
6.2.5	Resonant trapping of 250 nm polystyrene particles . . . . .	127
6.2.6	Application to multiple addressable traps . . . . .	128
6.2.7	Summary . . . . .	130
6.3	Particle-induced eigenfrequency shift . . . . .	131
6.3.1	Mechanism of the perturbation . . . . .	131
6.3.2	Description of the experiment . . . . .	133
6.3.3	Experimental measurement . . . . .	134
6.3.4	Application to single particle detection, tracking and analysis . . . . .	136
6.4	Back-action: mutual interaction between the particle and the cavity mode . . . . .	138
6.4.1	Introduction to back-action . . . . .	139
6.4.2	Escape threshold power experiment . . . . .	140
6.4.3	Trapping regimes . . . . .	141
6.5	Summary . . . . .	144
<b>7</b>	<b>Conclusion and Outlook</b>	<b>147</b>
	<b>Bibliography</b>	<b>167</b>
	<b>Acknowledgements</b>	<b>169</b>
	<b>Curriculum Vitae</b>	<b>171</b>



# List of Figures

2.1	Illustration of the multiple scattering of a electromagnetic wave by a periodically arranged medium . . . . .	8
2.2	Examples of one, two and three dimensional photonic crystal structures. . . . .	9
2.3	Illustration of the creation of a photonic bandgap in a one dimensional lattice .	11
2.4	Scanning electron micrograph of silicon photonic crystal membranes . . . . .	14
2.5	Band diagram of a bulk photonic crystal membrane . . . . .	15
2.6	Schematic of the silicon membrane patterning . . . . .	16
2.7	Schematic of the sacrificial oxide layer removal . . . . .	17
2.8	Band structure of a line defect waveguide. . . . .	19
2.9	Illustration of a defect induced localized state with its energy level inside the photonic bandgap . . . . .	20
2.10	Example of photonic crystal point-defect cavities . . . . .	22
2.11	Examples of line-defect cavities . . . . .	23
2.12	Slotted and circular hollow cavities . . . . .	24
3.1	Schematic of linear momentum exchange between an incident field and a mechanical object . . . . .	28
3.2	Arbitrary surface for the calculation of the Maxwell stress tensor. . . . .	30
3.3	Illustration of a focused Gaussian beam and generated field gradients . . . . .	37
3.4	Experimental demonstration of power dependent trapping potential . . . . .	39
3.5	Commercial optical tweezers and applications . . . . .	40
3.6	Examples of plasmonic nanostructures used for near-field optical trapping. . .	43
3.7	Slotted waveguide for optical trapping . . . . .	45
3.8	Examples of microcavities for optical trapping. . . . .	47
4.1	Schematic of the experimental apparatus . . . . .	50
4.2	Overview of the spectral distribution of light sources and detectors . . . . .	51
4.3	k-vector conservation at a waveguide interface . . . . .	52
4.4	Principle of the Fourier Imaging technique . . . . .	53
4.5	Folding of the k vector using a periodic arrangement . . . . .	54
4.6	Schematic of the Fourier Imaging optical setup . . . . .	55
4.7	SEM micrograph of a coupled-cavity waveguide . . . . .	56
4.8	Experimental recording of the dispersion properties of a CCW . . . . .	57

## List of Figures

---

4.9 Absorption and fluorescence emission mechanism . . . . .	58
4.10 IFR and PYO fluorescent markers . . . . .	59
4.11 Transmission properties of a long-pass dichroic filter used for fluorescence excitation separation . . . . .	60
4.12 Optical arrangement of the fluorescence excitation . . . . .	60
4.13 Optical arrangement of the visible illumination . . . . .	61
4.14 Optical arrangement of the visible imaging . . . . .	62
4.15 Imaging of 500 nm polystyrene particles with and without fluorescence. . . . .	63
4.16 Picture of EMCCD camera Hamamatsu ImagEM 512 . . . . .	65
4.17 High frame rate imaging of fluorescent particles. . . . .	66
4.18 Tracking of a 100 nm fluorescent particle in Brownian motion using the EMCCD camera . . . . .	67
4.19 Optical arrangement of the auxiliary optical tweezers . . . . .	67
4.20 Demonstration of optical trapping and displacement of a 500 nm polystyrene particle . . . . .	68
4.21 Influence of tweezers beam on cavity mode. . . . .	69
4.22 Principle of the confocal sensor. . . . .	71
4.23 Optical arrangement of the confocal sensor. . . . .	72
4.24 Fluorescence confocal imaging of two 500 nm sedimented particles. . . . .	73
4.25 Calibration of the confocal sensor for a 500 nm fluorescent particle. . . . .	74
5.1 Local infiltration method . . . . .	79
5.2 Glass reservoir approach . . . . .	80
5.3 Examples of microfluidic chips . . . . .	82
5.4 Design of the optofluidic chip. . . . .	84
5.5 Design of the two-layers microfluidic membrane. . . . .	85
5.6 Fabrication of the chromium mask. . . . .	86
5.7 Schematic of the photolithography process of the transport layer master . . . . .	87
5.8 Schematic of the photolithography of the control layer master . . . . .	88
5.9 Schematic of the assembly of the PDMS membranes . . . . .	90
5.10 Assembly of the two-layers PDMS membrane . . . . .	91
5.11 Assembled optofluidic chip . . . . .	92
5.12 Valve failure due to PDMS membrane stiction . . . . .	93
5.13 Interconnect induced membrane lifting . . . . .	94
5.14 Description of the injection and pneumatic control system . . . . .	95
5.15 Actuation of the integrated valves . . . . .	97
5.16 Typical flow speed achievable in free injection and slowed injection modes . . . . .	98
5.17 Residual flow in isolated mode . . . . .	99
5.18 Example of contaminations in the microfluidic transport channel . . . . .	100
5.19 Description of the modeled microscope objective . . . . .	103
5.20 Influence of the PDMS layer thickness on the quality of optical imaging . . . . .	104



5.21 Comparison of the calculated ray aberrations for the current PDMS/PDMS and proposed Glass/PDMS approaches . . . . .	105
5.22 Fabrication of the clamped interconnect . . . . .	107
5.23 Photograph of the PDMS/Plexiglass interconnect . . . . .	108
5.24 Design of the flexible microfluidic approach . . . . .	110
5.25 Photograph of the fabricated flexible microfluidic device . . . . .	111
6.1 Structure of the circular cavity and light coupling. . . . .	114
6.2 Experimental characterization of the circular cavity in air . . . . .	115
6.3 Water induced resonant wavelength shift . . . . .	118
6.4 Schematic of resonant optical trapping experiment procedure . . . . .	120
6.5 Resonant optical trapping of 500 nm polystyrene particles . . . . .	120
6.6 Determination of the resolution of the centroid tracking method . . . . .	122
6.7 Particle tracking using the centroid method for different optical powers . . . . .	123
6.8 Experimental demonstration of the exclusivity of the resonant trap . . . . .	124
6.9 Electric field distribution calculated by PWE and 3D FEM . . . . .	125
6.10 Schematic of the end-fire setup used for the estimation of the guided power . . . . .	126
6.11 Resonant optical trapping of 250 nm polystyrene particles . . . . .	127
6.12 Design and fabrication of individually addressable traps on a single photonic crystal structure . . . . .	128
6.13 Experimental demonstration of the addressability of individual resonant traps on a single photonic crystal structure . . . . .	129
6.14 Illustration of the dynamic eigenfrequency shift . . . . .	132
6.15 Schematic of the eigenfrequency shift measurement . . . . .	133
6.16 Experimental demonstration and measurement of the dynamic resonance wavelength shift . . . . .	134
6.17 Computation of the resonance wavelength shift with Finite Element Method . . . . .	135
6.18 Experimental demonstration of single particle detection and tracking . . . . .	137
6.19 Influence of the diameter, refractive index and form factor on the resonance shift. . . . .	138
6.20 Measurement of the escape threshold power . . . . .	141
6.21 Optical forces calculated with Finite Element Method . . . . .	142
6.22 Illustration of the resonant optical trapping regimes . . . . .	143



## List of Tables

2.1	Properties of commonly used silicon photonic crystal cavities . . . . .	22
2.2	Properties of the hollow cavities . . . . .	24
3.1	Example of biological particles in the range for manipulation with optical tweezers	41
4.1	Characteristics of utilized microscope objectives . . . . .	52
4.2	Absorption and emission characteristics of common fluorescent molecules . .	58
4.3	Record of reference tube lens length for most common microscope objective manufacturers. . . . .	64
4.4	Tabulated values of the resolution limit for various numerical aperture objectives	64
5.1	Comparison of manufacturer specifications and computed characteristics for the modeled oil immersion objective . . . . .	102
6.1	Computation of the mode volume of the circular cavity using Finite Element Method . . . . .	116
6.2	Experimental and numerical quality factors and resonance wavelength shifts for a water infiltrated circular cavity . . . . .	117
6.3	List of parameters used in the estimation of the guided power near the cavity .	126
6.4	Experimental and numerical quality factors and resonance wavelength shifts for a water infiltrated circular cavity . . . . .	129



# Glossary

- CCD** Charge-coupled device
- EMCCD** Electron multiplying charge-coupled device
- FEM** Finite element method
- FDTD** Finite-difference time-domain
- GME** Guided mode expansion
- HPhC** Hollow photonic crystal cavity
- HMDS** Hexamethyldisiloxane
- ICP** Inductively coupled plasma
- MST** Maxwell stress tensor
- MTV** Mosaic tobacco virus
- OT** Optical tweezers
- PBG** Photonic bandgap
- PDMS** Polydimethylsiloxane
- PGMEA** Propylene-glycol-monomethyl-ether-acetate
- PhC** Photonic crystals
- PWE** Plane wave expansion
- ROT** Resonant optical trapping
- SIT** Self-induced trapping
- TIR** Total internal reflection
- WGM** Whispering gallery mode



# 1 Introduction

The ability to strongly confine light is critical in the pursuit of enhanced interactions between light and matter. Current research topics in this domain include, for example, the study of the coupling between a single atom and light stored in a cavity [1], the efficient generation of non-linear effects in semiconductors and particularly in silicon [2], or the study of optomechanical forces exerted on nanoscale oscillators [3]. The inherent nature of light renders it hard to confine, which makes progresses in the study of its interaction with matter dependent on the advent of new, innovative, confinement methods. The case of optomechanical forces and, in particular, their application to the optical trapping of nano-objects comes as a very interesting illustration of this trend.

An optical trap, as demonstrated by Ashkin and Dziedzic [4], is generally created by the strong focusing of a laser beam in the front focal plane of a microscope objective. In this configuration, the optical manipulation of a large variety of small objects, ranging from a few nanometers to a few microns in size, has been achieved over the last decades. Commercial versions of this technique referred to as "Optical Tweezers" have also been developed. In an optical trap, the amount of force exerted on the captured object is strongly dependent on the focusing of the trapping field. A typical optical tweezers apparatus makes use of a well-corrected, high numerical aperture, microscope objective. In the case of an immersion oil objective, the amount of focusing approaches the dimension of the wavelength of the incident light, but is intrinsically limited by the diffraction limit, as dictated by Abbe's law. Consequently, the optical forces applying on an object collapse very rapidly as the size of the object is decreased, hence prohibiting its manipulation. This limitation has motivated the development of optical trapping techniques making use of photonic nanostructures where light can be confined beyond the diffraction limit. In this context, semiconductor based planar photonic crystal cavities have been regarded as very promising candidates.

Photonic crystals are structures formed by the periodic arrangement of materials with distinct permittivities. This specificity provides them with the compelling property to prohibit the propagation of light in one, two or three dimensions, and over an extended range of optical frequencies, referred to as "photonic bandgap". This feature has been the subject of a variety

of studies over the last twenty years, mainly for the control of spontaneous emission by a quantum emitter. The field of photonic crystals has also benefitted from the technological maturity of the semiconductor industry to progress towards planar integrated components consisting of waveguides, filters or delay lines. More interestingly, the appropriate introduction and engineering of defects in a photonic crystal lattice allows for the strong confinement of light within high quality factor subwavelength microcavities. The large densities of electromagnetic energy are therefore of the highest interest for light-matter interactions, and specifically for optical trapping.

In this work, a specific type of silicon planar photonic crystal cavity has been studied. The latter not only possesses a large quality factor (several thousands) and a small mode volume, but also features a hollow region where a large fraction of the optical field is free to interact with an external object. This type of cavity is referred to as a "hollow cavity". The integration of arrays of hollow photonic crystal cavities in a specially developed, ultra-thin microfluidic membrane comprising of an immersion microchannel has been performed. The membrane, fabricated in polydimethylsiloxane, has been conceived to simultaneously provide a reliable and repeatable infiltration method for the cavities, while maintaining high numerical aperture imaging from the top of the silicon substrate. A set of pneumatically controlled valves has been integrated inside the thin membrane to permit the accurate control and arrest of the flow inside the infiltration channel.

Moreover, a complete optical setup has been assembled. The setup serves several purposes. It allows for the characterization and the monitoring of the hollow cavities in the near-infrared, enables the low-light fluorescence imaging of small polystyrene particles, offers basic optical manipulation capabilities using a set of optical tweezers and finally permits the tracking of the fluorescent nanoparticles through a confocal-type sensor.

The achieved optofluidic chip and experimental apparatus have been finally used to demonstrate the resonant optical trapping of 250 nm and 500 nm polystyrene particles. The intrinsic properties of the hollow cavities in terms of quality factor, mode volume and field overlap have permitted to achieve unprecendently low trapping powers (120 and 360  $\mu\text{W}$  for 500 and 250 nm particles respectively). Further experiments have been then conducted to investigate the perturbation induced by the presence of the particle on the properties of the cavity mode. This perturbation has been identified as a dynamic resonance wavelength shift of up to 1.8 nm in the case of a 500 nm particle, which corresponding to over twice the linewidth of the water-infiltrated cavity has been measured. Finally, the mutual interaction between the cavity mode and the trapped particle has been studied. An experimental demonstration of this mutual interaction has been reached. More interestingly, the existence of two distinct trapping regimes, inherently particle dependent, has been evidenced. The existence of one of these trapping regimes had been predicted as early as 2006 [5]. The second regime is attributed to the specific geometry of the hollow cavity and possesses the advantage to enable the trapping of a small nanoparticle while exposing it to very little optical energy.



---

The combination of all these features, namely the very low trapping powers, the large sensitivity to the presence of a particle, and the particle dependent trapping properties, makes the hollow cavity a very unique tool for the isolation, detection and manipulation of single particles. It is believed that these properties could be of the highest interest to the physics community but also to biology and medicine communities for the study of single submicron biological entities. The compatibility of the technique with silicon photonics process and microfluidic integration is also believed to strongly benefit the possible development of fully integrated devices.

**In the first chapter,** an introduction to photonic crystals, along with a short chronology of their development is provided. Focus is then made specifically on the properties of silicon photonic crystal membranes, which are one type of quasi two-dimensional photonic crystals investigated at the Laboratory of Quantum Optoelectronics. An overview of the fabrication method and computational tools utilized is provided. Finally, a presentation of planar photonic crystal cavities in silicon membranes is provided and especially hollow cavities.

**In the second chapter,** an introduction to the mechanical forces that light exerts on an object is provided. The calculation of these forces in the general case is based on computation of the Maxwell stress tensor, which is rapidly presented. The analytical derivation of the optical force applying on a point-like dipole, and its extension to a very small spherical object are then provided, introducing the familiar concepts of gradient and scattering forces. The most widely used implementation of optical forces, namely optical tweezers, based on the aforementioned gradient force is then presented. In the last part, the development of the photonic nanostructure aiming at extending the capacities of current optical traps is discussed.

**In the third chapter,** a complete description of the optical set up along this thesis is provided. The first section includes a statement of the experimental requirements, and an overview of the different techniques employed to achieve them. Each of the following sections is then dedicated to the accurate assembly and characteristics of a separate constituent. The main parts described are the near infrared Fourier imaging technique, the fluorescence imaging technique in the visible, the auxiliary optical tweezers and the confocal sensing technique. Some discussions on the possible additions and improvements is then provided.

**In the fourth chapter,** the microfluidic integration technique that has been developed and employed for this set of experiments is presented. The need for a reliable infiltration method of the photonic crystal cavity is first pointed out along with the insufficiencies of other attempted approaches. Following these, the design and fabrication of the thin microfluidic membrane developed is described. The operation of the fully assembled optofluidic chip is then demonstrated and basic characterization is performed. The last part records the limitations of the approach that has been employed and suggests alternative methods.

**Finally, in the fifth chapter,** the experimental results that have been achieved regarding the resonant optical trapping of dielectric nanoparticles in planar hollow photonic crystal cavities are presented. The properties of the circular cavity used for the experiments is presented

before and after infiltration in water. In a first set of experiments, the resonant optical trapping of 500 nm and 250 nm particles is demonstrated. A second type of experiment is performed to reveal the perturbation that a particle induces on the cavity mode when being trapped. An application to single particle tracking and counting is proposed. Finally, the existence of a mutual interaction between a trapped particle and the cavity mode, referred to as "back-action" is demonstrated. In a third experiment the existence of two distinct trapping regimes is evidenced. While one of these regimes had been theoretically predicted, the second one which is a consequence of the geometry of our cavity, was not described. A tentative explanation on the nature of these regimes is provided and the properties of the newly demonstrated resonant trap are discussed.

This work has received the financial support from the Swiss National Centre of Competence in Research Quantum Photonics (NCCR - QP) and the Swiss National Science Foundation (SNF) project 200021-134541. The conception and fabrication of the thin microfluidic membrane has benefitted from the kind guidance of Prof. Sebastian Maerkl and his group.

---

## Essential reading

The creation of the appropriate set of experimental conditions necessary to achieve a convincing demonstration of resonant optical trapping has required the development of independent optical and microfluidic tools and techniques. A significant part of this thesis is dedicated to the technical descriptions of each of these elements. In order to give a more convenient access to the main results presented in this thesis, a suggestion of essential readings is provided. Based on these highlights, the reader might find easier to identify, and later redirect towards subsections of specific interest.

**Section 4.1** provides an overview of the experimental optical setup.

**Section 5.2.2** illustrates the design and requirements established for the optofluidic chip

**Section 6.1** presents the experimental characterization of the planar photonic crystal cavities used during this experimental work.

**Section 6.2** presents the demonstration of resonant optical trapping of 250 nm and 500 nm polystyrene particles in the hollow cavity.

**Section 6.3** discusses the perturbation of the photonic crystal cavity mode induced by the particle and provides experimental measurements of this phenomenon.

**Section 6.4** provides the experimental evidence of particle cavity back-action and of the existence of two distinct trapping regimes.



## **2 Light confinement in planar photonic crystal cavities**

This chapter is divided into three sections. In the first section, a general introduction to photonic crystals and photonic bandgaps is provided. In the second section, focus is made on the specific case of photonic crystal membranes in silicon, which are fabricated and studied at the Laboratory of Quantum Optoelectronics (LOEQ / EPFL). The goal of this section is to provide a description of their main properties and also to introduce the fabrication method and computation tools relevant to this work. An example of photonic crystal waveguide based on two-dimensional photonic crystal for the in-plane confinement is presented. Finally, in the third section, the creation of optical microcavities in silicon membranes is presented. The basic properties and the various types of 2D photonic crystal cavities are discussed.

### **2.1 Photonic crystals and photonic bandgaps**

#### **2.1.1 Introduction**

Photonic crystals are periodically structured materials. They are made out of a succession of layers or sub-elements with distinct optical properties, which, in analogy with atomic or molecular crystals, repeats over extended distances forming a lattice. An electromagnetic (EM) radiation impinging on a small object is usually partially or totally scattered. In the same manner an EM wave entering a photonic crystal structure undergoes partial scattering at each layer or sub-element. The resulting multiple scattering phenomenon, along with the vectorial nature of EM waves, gives rise to unique optical properties. One of the most striking feature is the existence of a photonic bandgap (PBG) which corresponds to a range of optical frequencies for which light propagation is prohibited in one or several directions.

#### **2.1.2 Examples of photonic crystal structures**

A variety of materials with periodic arrangement can be found in nature. Some are the reason of the iridescence of opals, the intense colors of peacocks feathers and the wings of some species of butterflies. Nevertheless, the vast majority of the photonic crystal structures investigated

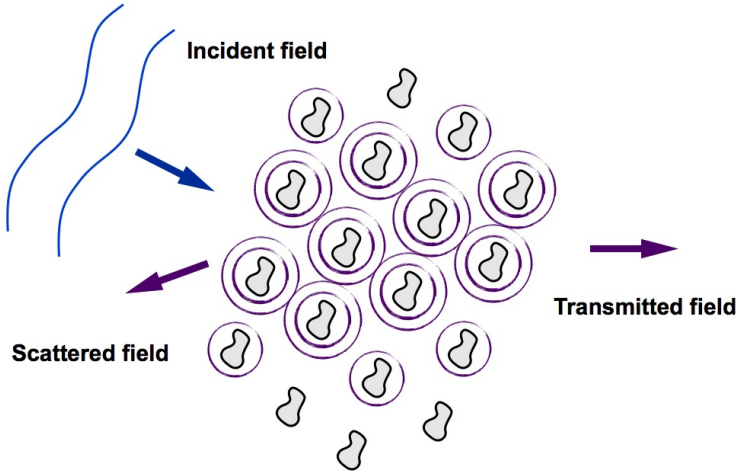


**Figure 2.1:** Illustration of the multiple scattering of an electromagnetic wave by a periodically arranged medium. An incident wave (blue) is impinging on a periodic lattice of individual scatterers. The vectorial summation of the contribution of each scatterer gives rise to a net scattered and transmitted field (purple). Their characteristics are strongly dependent on the properties of the individual scatterers and the geometry of the arrangement.

today are artificially engineered structures. Their classification is usually made according to the number of dimensions (1, 2 or 3D) for which there exists a periodic pattern. Figure 2.2 shows scanning electron micrographs of three examples of engineered periodic structures illustrating each of these cases.

A typical one-dimensional periodic arrangement can be observed in Figure 2.2.a. It corresponds to a stack of AlInN (darker regions) and GaN (brighter) layers forming a distributed Bragg reflector. The successive piling of such layers prohibits the propagation of any waves (perpendicular to the stack) for which a unit layer induces a  $\frac{\lambda}{4}$  dephasing. Thus, an incident wave verifying this condition is reflected off the structure. The coefficient of reflection for this type of assembly can reach values well above 99%.

The case of two-dimensional photonic crystals is well illustrated by the structures obtained in macro porous silicon [7]. Figure 2.2.b shows the scanning electron micrograph of a square lattice of hole obtained through the electrochemical etching of silicon. The pores that are demonstrated on this picture are approximately  $6\ \mu\text{m}$  wide and almost  $350\ \mu\text{m}$  deep. The lattice that is formed by the array of holes induces the existence of separate bandgaps for the transverse-electric and transverse magnetic polarizations in the far-infrared region (around  $30\ \mu\text{m}$  wavelength).

The most common three dimensional photonic crystals are synthetic opals. They consist of stacks of microspheres, typically made out of silicon or silicon oxide. Figure 2.2.b shows one example of a stack of silicon beads obtained through the sedimentation of a colloidal solution. Inverse opals can also be achieved after the stack is covered in a medium, filling the interstitial space and the beads are selectively dissolved. Other three dimensional lattices include the

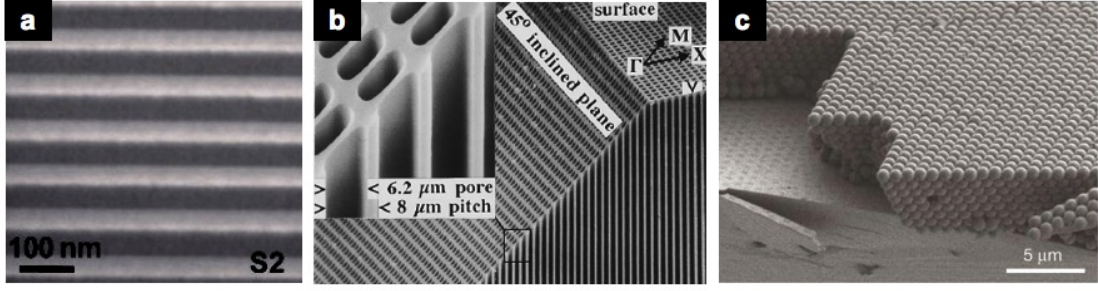


**Figure 2.2:** Examples of one, two and three dimensional photonic crystal structures. *a.* Scanning electron micrograph of a distributed Bragg reflector made of a stack of successive AlInN (darker regions) and GaN (brighter regions). Reprinted from ref. [6]. *b.* Scanning electron micrograph of a macroporous silicon lattice with bandgap in the far-infrared. Reprinted from ref. [7]. *c.* Scanning electron micrograph of a synthetic opal made of silicon microspheres. Reprinted from ref. [8]

woodpile structures [9] and the "Yablonovite" type structures [10].

### 2.1.3 Band diagrams and photonic bandgap

The properties of photonic crystal structures with respect to light propagation are represented in the form of a band diagram or band structure. This is in strong analogy with the propagation of electrons and holes in the periodic potential of a crystal and the propagation of light in a periodic structure.

Part of this analogy can be understood by considering a harmonic wave in a medium with periodic modulation of the dielectric permittivity  $\epsilon(\vec{r})$  such that  $\epsilon(\vec{r} + \vec{T}) = \epsilon(\vec{r})$ . The electric  $\vec{E}(\vec{r}, t)$  and magnetic fields  $\vec{H}(\vec{r}, t)$ , taken in the sense of distributions, can be written as:

$$\vec{E}(\vec{r}, t) = \vec{E}(\vec{r})e^{i\omega t} \quad (2.1)$$

$$\vec{H}(\vec{r}, t) = \vec{H}(\vec{r})e^{i\omega t} \quad (2.2)$$

These field distributions can then be input into Maxwells equation and it is possible to write: (see for example Lourtioz *et al.* [11] or Joannopoulos *et al.* [12])

$$\vec{\nabla} \times \left( \frac{1}{\epsilon(\vec{r})} \vec{\nabla} \times \vec{H}_\omega(\vec{r}) \right) = \left( \frac{\omega}{c} \right)^2 \vec{H}_\omega(\vec{r}) \quad (2.3)$$

Equation 2.3 is the master equation and carries the information on a distribution  $\vec{H}(\vec{r})$  supported by the medium at the frequency  $\omega$ . Note that a similar master equation could be written for  $\vec{E}(\vec{r})$ . Interestingly the master equation can be rewritten in the form of an eigenvalue prob-

lem with  $\left(\frac{\omega}{c}\right)^2$  as the eigenvalue.

$$\hat{\Theta} \tilde{H}_\omega(\vec{r}) = \left(\frac{\omega}{c}\right)^2 \tilde{H}_\omega(\vec{r}) \quad (2.4)$$

where  $\hat{\Theta} = \vec{\nabla} \times \left(\frac{1}{\epsilon(\vec{r})}\right) \vec{\nabla} \times$  is a hermitian operator. This is of particular interest because this property enables the usage of the mathematical tools developed for quantum mechanics over the last century. A noticeable difference between the propagation of light in photonic crystals and electrons in crystals can be found in the absence of fundamental scale limitation in the case of light. This compelling property implies that the propagation through a periodic structure is determined by the ratio of the wavelength of the radiation over the lattice constant, and hence justifies the use of reduced units. A detailed discussion on the hermiticity of the operator  $\hat{\Theta}$  and the scaling laws can be found here [12].

Making abstraction of this difference, the solution for the distribution of magnetic field in a medium of periodic dielectric permittivity, just like electrons in a periodic potentials, can be found using the Floquet-Bloch theorem:

$$\vec{H}_k(r) = \vec{u}_k(\vec{r}) e^{i\vec{k} \cdot \vec{r}} \quad (2.5)$$

where  $u_k(r)$  is a distribution with the same periodicity as  $\epsilon(\vec{r})$ . The  $\vec{H}_k(r)$  distributions are referred to as Bloch states. Getting back to Equation 2.3, it can be seen that there is a unique relation between  $\omega$  and  $k$  for a Bloch mode. This relation is called the dispersion relation. A periodic medium supports a set of Bloch modes, usually labelled from 1 to  $n$ , each of which follows a dispersion curve  $\omega_n(k)$ . The set of dispersion curves for the Bloch modes is called the band structure of the medium. It is commonly represented in  $\tilde{k}$  and  $u$  coordinates where  $\tilde{k} = \frac{ka}{2\pi}$  is the norm of the reduced wavevector and  $u = \frac{\omega a}{2\pi c}$  is the reduced frequency. In analogy to solid-state physics, the band-structure of a multidimensional lattice is represented on a 2D plot although the wavevector is made to follow each characteristic point ( $\Gamma, K, \dots$ ) of the irreducible reciprocal lattice (which is also multidimensional).

Calculations of the band structure of a photonic crystal lattice are performed numerically based on Equations 2.4 and 2.5. There exists a variety of methods that can be employed. A typical and historical example can be found in the work of Ho *et al.* [13] showing the band diagrams of dielectric spheres in a dielectric medium organized in a face-centered cubic-type and in a diamond-type packing. Accurate descriptions of the various methods can be found in Lourtioz *et al.* [11]. Rapid descriptions of three of these methods will be provided in Section 2.2.3 for the computation of quasi two-dimensional structures.

The work presented in Ref. [13] is of critical importance. It illustrates how, for certain types of periodic arrangements and for appropriate permittivity contrasts between the alternating materials, a certain range of frequencies can be depleted of any Bloch state, thus effectively



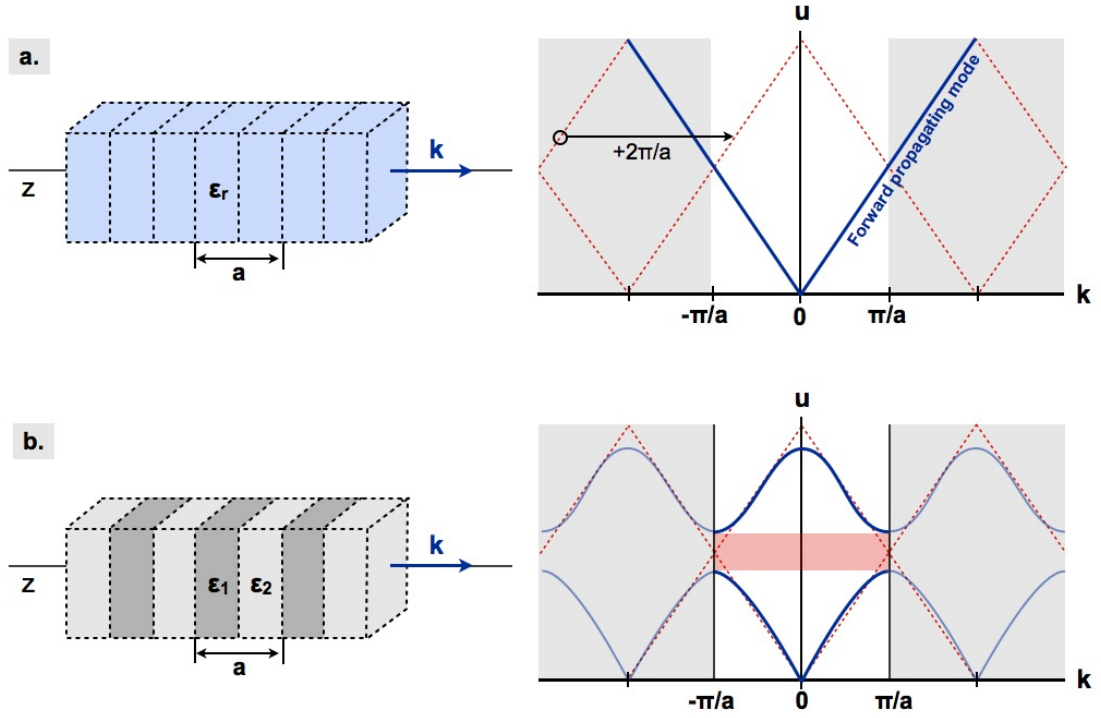


**Figure 2.3:** Illustration of the creation of a photonic bandgap in a one dimensional lattice. *a.* An artificial periodicity (period  $a$ ) is introduced in a homogeneous, infinitely extended, dielectric medium. For an electromagnetic wave propagating along  $z$ , the dispersion curve is a straight line (blue line) with a positive slope for the forward propagating mode and a negative slope for the counter propagating mode. The artificial periodicity allows to limit the study over the first Brillouin zone of the lattice extending from  $k = -\frac{\pi}{a}$  to  $k = +\frac{\pi}{a}$ . A similar construction can be reproduced for the neighboring Brillouin zones (dashed red lines). *b.* Following the construction described in *a.*, a dielectric permittivity contrast is introduced between the two layers constituting one period of the lattice. The light scattering occurring at each interface of the lattice makes the forward and counter propagating modes coupled. This can be seen to induce an hybridization of the two states at  $k = -\frac{\pi}{a}$  and  $k = +\frac{\pi}{a}$ . The consequence is the appearance of a range of frequencies (red shaded) where no propagating state exists and this is referred to as the photonic bandgap.

prohibiting the propagation of light in any of the directions considered. Such a band of frequency is referred to as "photonic bandgap" in analogy with the electronic bandgap of semiconductor materials.

As mentioned earlier, the calculation of the band structure of a photonic crystal lattice is a complex task and therefore the description of the formation of a PBG in several dimensions is not at all straightforward. Nevertheless, an intuitive understanding can be obtained in the case of a one-dimensional structure.

The case of an infinitely extended, homogeneous and isotropic, dielectric material is first considered. An harmonic wave propagates with a wavevector  $\vec{k}$ , along  $z$ . Far away from any

material absorption line, the relationship between  $k = |\vec{k}|$  and  $\omega$  reads:

$$\omega = \frac{c}{n}k = \frac{c}{\sqrt{\epsilon_0\epsilon_r}}k \quad (2.6)$$

The dispersion relation can therefore be represented as a straight line in  $(k, \omega)$  or  $(\vec{k}, \omega)$  coordinates, with a  $+\frac{c}{n}$  slope for the forward propagating mode and a  $-\frac{c}{n}$  for the counter propagating one (Figure 2.3.a). It is now possible to imagine the medium previously considered as made out of successive layers of equal thickness  $(\frac{a}{2})$ , orthogonal to  $z$  and infinitely extended. The artificial lattice of period  $a$  has a first Brillouin zone which is a portion of a line extending from  $0$  to  $\frac{\pi}{a}$  (non-shaded region). The translation invariance of the system allows to reproduce the dispersion diagram obtained over the first Brillouin zone to the neighboring zones. As a consequence, the dispersion curve of the forward propagating mode of one Brillouin zone intersects the dispersion curve of the backward propagating mode of the next Brillouin zone at  $k = -\frac{\pi}{a}$  and  $k = +\frac{\pi}{a}$  (see Figure 2.3.a). This artificial construction has no physical consequences in the case of an infinitely extended homogeneous medium.

This is not true when the medium is constituted of successive layers of thickness  $(\frac{a}{2})$  with different permittivities. In this case the forward and backward propagating modes are coupled through the reflection occurring at the interfaces. This leads to an anticrossing of the modes at the edges of the Brillouin zone, which causes the appearance of a photonic bandgap (see Figure 2.3.b). The width of the bandgap gets larger as the contrast in permittivity increases. The propagating modes on the lower side of the PBG correspond to a state where the electric field is mainly located in the higher refractive index layers, while the modes on the upper side of the PBG correspond to a state where the electric field is mainly located in the lower refractive index layers. As a consequence, the region located below the PBG is commonly referred to as "dielectric band" while the region located above the PBG is referred to as the "air band". Further explanation regarding this localization of the field in one or the other of the medium can be found here [12].

### 2.1.4 Brief history of photonic crystal materials

Although the optical properties of "ordered" media have been the subject of investigations as early as the end of the 19th century with Lord Rayleigh, the fields of photonic crystals and photonic bandgap materials were effectively born in the 1980s. In a series of seminal papers, proposals for theoretical structures displaying a photonic bandgap [14], [13], along with suggestions of fabrication-compatible structures [10], [9] were published. This was followed by the results on structure fabrication [15], [16] and experimental demonstration of the photonic bandgap in the near-infrared [17] in the later years. One of the original motivation behind the development of this rapidly growing field was the control of spontaneous emission through Purcell effect [18], [14]. Demonstrations of this effect was finally achieved in the years 2005/2006 [19], [20]. In the meantime, applications of photonic crystals to lasers [21] [22], [23],

on-chip light bending [24] and slow light for optical memories and delay lines [25] has been proposed and demonstrated.

## 2.2 Silicon photonic crystal membranes

Current research on photonic crystal materials are strongly driven by the fast growing field of integrated photonics. The demonstrated capabilities of photonic crystals to guide and bend light at subwavelength scales, slow down or store light pulses, and enhance light-matter interactions make them ideally suited candidates to realize all optical circuits and operations. In this context, a wide variety of PhC structures compatible with standard semiconductor processes while offering a possibility for on-chip integration have been developed and investigated. This is the case of 2D photonic crystal membranes which are presented in this thesis. A short summary of their properties will be presented in section 2.2.1 and a description of the fabrication process developed at the Laboratory of Quantum Optoelectronics (LOEQ) will be provided in section 2.2.2. Section 2.2.3 summarizes the principle computational tools employed in the design and theoretical understanding of the structures fabricated. Finally, section 2.2.4 shows an example of a light guiding structure based on in-plane photonic bandgap confinement, namely a PhC W1 waveguide.

### 2.2.1 Properties

Photonic crystal membranes are quasi one or two dimensional photonic crystals. This distinction between a perfect and a quasi 1D or 2D device arises from the finite length of the structure in one or two of the dimensions without periodic arrangement, which slightly modifies their band structure with respect to a perfect, infinite, lattice. An example of these modifications can be found in the thesis of Jana Jágerská on page 13. In a semiconductor PhC membrane, the lattice is formed with a thin layer of high refractive index material which can be silicon, GaAs or GaN and surrounded by materials with lower refractive indices. This allows for the in-plane guiding of the incoming light through total internal reflection. The thickness of the layer is chosen depending on the material and operation wavelength such that only a single mode of the planar waveguide that is formed is supported (see for example [26]). The layer is generally a few hundreds of nanometers thick for PhC device operating in the near-infrared. In the specific case of a 1D membrane [27], the lateral dimension is also reduced to sub-micron dimensions. This configuration is often referred to as "nanobeam".

For this thesis, focus has been made specifically on 2D silicon membranes with a triangular lattice of holes. The choice of the triangular lattice of holes over other configurations (for example, a square lattice of holes) comes from its higher degree of symmetry, which allows for a complete omnidirectional bandgap (in silicon) for the Transverse-Electric (TE) polarization, even for lower filling factors [11]. The PhC lattices are design to operate around  $1.5\ \mu\text{m}$ , including the traditional S, C and L bands for optical telecommunications (see Chapter 4 for details on the optical setup). The silicon slab is chosen to be 220 nm thick and is made freestanding.

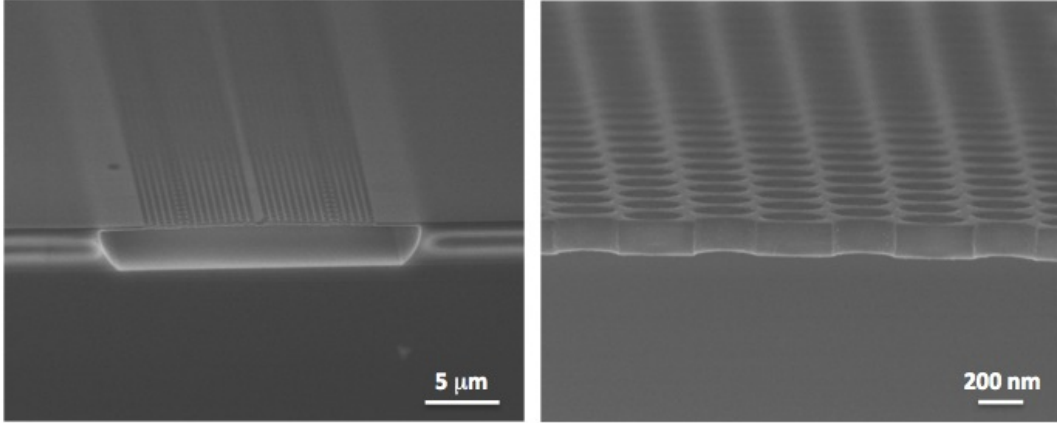


**Figure 2.4:** Scanning electron micrograph of silicon photonic crystal membranes. **Left.** Lower magnification image illustrating the extended triangular lattice of holes and the  $2\ \mu\text{m}$  high air gap resulting from the local removal of the silicon oxide layer. **Right.** Higher magnification image showing the  $220\ \text{nm}$  freestanding membrane and the lattice of air holes.

In this configuration, the full PhC lattice is immersed in air, which maximizes the refractive index contrast and therefore the light confinement. Scanning electron micrographs of silicon PhC membranes can be seen on Fig. 2.4. The left panel shows a lower magnification image of a 2D PhC device. The hollow region can be observed underneath the thin membrane. A close-up on the freestanding silicon membrane can be seen on the right panel, also displaying the triangular lattice of holes. The detailed fabrication procedure is presented in the coming section.

A schematic of a triangular lattice of holes is depicted on Figure 2.5.a. The separation between the holes (lattice constant) is  $a$  and the radius of the holes is  $R$ . Figure 2.5.b shows the calculated band structure for a silicon membrane patterned with such a triangular lattice of holes where  $a = 440\ \text{nm}$  and  $R = 125\ \text{nm}$ . This corresponds to a filling factor  $f = \frac{2\pi R^2}{\sqrt{3}a^2}$  of almost 30 %. The horizontal axis indicates the reduced wavevector. The  $\Gamma$ , M and K points refer to the three characteristic points of the irreducible Brillouin zone, as illustrated on Figure 2.5.c. It can be seen that this configuration possesses a complete photonic bandgap (red shaded region) for the TE polarization centered around 0.3 reduced frequency unit. In other words, any incident light (guided through the slab) with a reduced frequency in the range of the PBG would be entirely reflected off the PhC interface, independent of its angle of incidence. On the contrary, any guided mode with a frequency outside of the PBG range could couple to one or several Bloch modes supported by the lattice and can be transmitted through the membrane.

The quasi-2D nature of the PhC membranes is revealed through two main features. First of all the position of the bandgap in reduced frequency is slightly higher than that of the equivalent 2D structure. This is due to the extra in-plane confinement. Secondly, there exists a region of the band structure for which the condition for total internal reflection does not exist anymore. Any light injected in the silicon slab verifying is hence free to couple to the continuum of

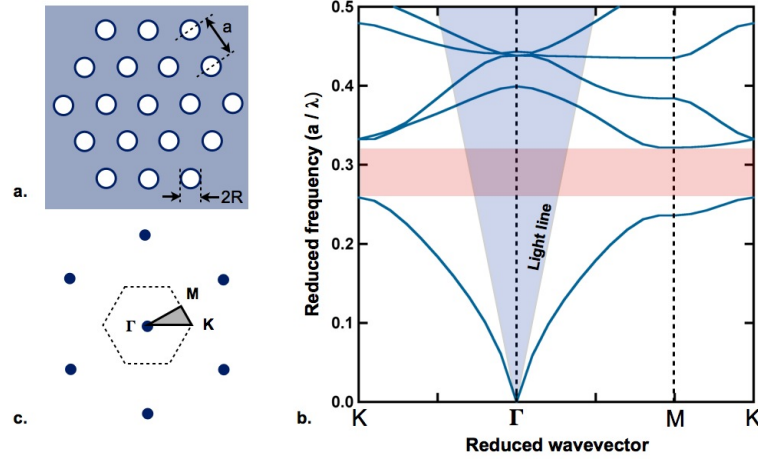


**Figure 2.5:** Band diagram of a bulk photonic crystal membrane. *a.* Schematic of a triangular lattice of with lattice constant  $a$ . *b* Band structure of the photonic crystal membrane as calculated using guided mode expansion. The red shaded area indicates the photonic bandgap. The blue shaded area corresponds to the projected light cone. *c.* Schematic of the reciprocal lattice. The black dashed hexagon indicates the first Brillouin zone while the gray shaded area corresponds to the irreducible Brillouin zone.

freespace modes. This region which is actually three-dimensional and is referred to as the light cone. When projected on the 2D plot of Figure 2.5.b, the light cone forms a triangle (blue shaded region) and the light forming the boundary is referred to as the "light line". Its slope is  $\frac{c}{n}$  where  $n$  is the refractive index of air.

### 2.2.2 Fabrication process

The fabrication of the photonic crystal structures in the visible and near-infrared range requires the ability to reproduce with high fidelity features that are much smaller than the wavelength of operation of the device. The maturity and high performance offered by the semiconductor industry have offered the means to achieve this goal. This has provided, as mentioned earlier, a strong push for the development of planar photonic crystal devices. Owing to its strong inheritance from transistor technology, PhC fabrication is mainly performed by lithographic techniques: either UV lithography as implemented for example at IMEC (Belgium) or electron beam (e-beam) lithography as performed here at the Center of Micro-nanotechnology (CMi) of EPFL. The fabrication process has been developed by H. Zhang (see EPFL Thesis [28]) and further refined by Z. Diao (EPFL Thesis [29]). All the photonic crystal samples used during the work presented here have been fabricated by Z. Diao.

The PhC structures are fabricated on a 8 inches Silicon-On-Insulator (SOI) wafers from SOITEC. Each wafer consists of a three-layer assembly. First is a  $220 \text{ nm} \pm 2 \text{ nm}$  silicon layer, in which PhCs will be etched. The silicon layer is located on top of a  $2 \mu\text{m}$  silica layer ( $\text{SiO}_2$ ) and a  $750 \mu\text{m}$  silicon substrate respectively. There are two main steps to the fabrication of our photonic crystal membranes: the first one is the patterning of the thin silicon layer (Figure 2.6),

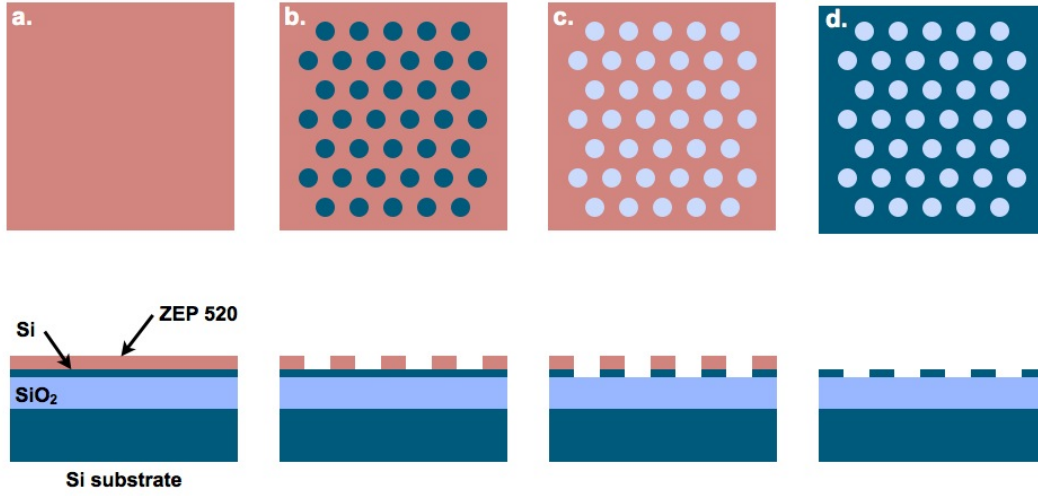


**Figure 2.6:** Schematic of the silicon membrane patterning. *a.* Deposition of the photoresist layer. *b.* Electron-beam patterning and development. *c.* Dry etching of the silicon membrane. *d.* Sample cleaning.

the second one is the removal of the buried silicon oxide layer (Figure 2.7).

A 30 mm x 50 mm piece is first diced off a SOI wafer and is mechanically thinned. The piece is then cleaned and rinsed before it is spin coated with a thin layer (200 nm) of ZEP 520A (positive) photoresist (Fig 2.6.a). The photoresist is then baked and exposed in the electron beam lithography system (Vistec EBPG5000). This system allows for a 2.5 nm e-beam spot size. Development in n-amyl-acetate and rinsing in methyl-isobutyl-ketone are then performed successively. At this stage, the designed photonic crystal pattern is written onto the photoresist layer (Fig 2.6.b). In the following step, the PhC pattern is further transferred onto the silicon layer by dry etching of the unprotected areas (Fig 2.6.c). This step is performed using an AMS200 inductively coupled plasma (ICP) etcher and a gas mixture of  $SF_6$  and  $C_4F_8$ . Finally, the remain ZEP 520A is cleaned off (Fig 2.6.d).

At that point, the photonic crystal structures that are fabricated are usually functional. Nevertheless, the presence of the silicon oxide layer underneath partially decreases the light confinement in the structures and creates an imbalance in the symmetry of the device.

The PhC sample is spin coated first with an adhesion promoter (HMDS) and then with a second positive photoresist (AZ5214) (Fig 2.7.a). The obtained layer is then baked and exposed to UV light in a Microtech MJB3 mask aligner through a chromium mask. The latter comprises rectangular areas of the size of the PhC structures where the chromium layer has been removed (see also Chapter 5, Section 5.3.1 for more details). After careful alignment and exposure the photoresist is developed in MF319 and rinsed. This operation leaves the sample completely protected by the photoresist except for the PhC structures which are left exposed (Fig 2.7.b). The sample is then immersed in a Buffered Hydrofluoric Acid solution (BHF). This wet etching step removes the sacrificial  $SiO_2$  layer, leaving the photonic crystal membrane fully suspended

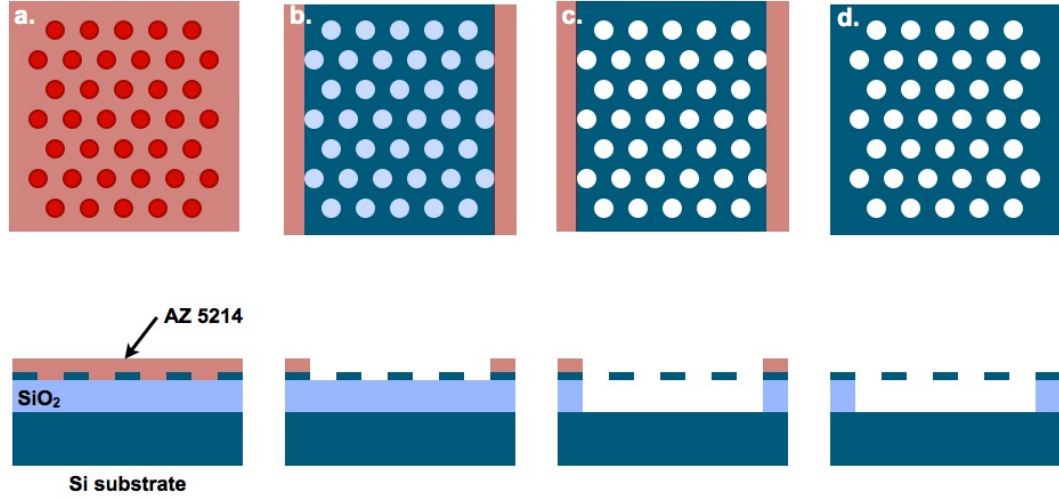


**Figure 2.7:** Schematic of the sacrificial oxide layer removal. *a.* Deposition of the photoresist layer. *b.* UV lithography and development. *c.* Wet etching of the silica layer. *d.* Sample cleaning.

(Fig 2.7.c). Finally the sample is cleaned from the AZ5214 photoresist and carefully dried following a supercritical drying technique. Note that the wet etching step is usually responsible for a small enlargement of the lattice holes (typically 40 nm for a 200 nm diameter hole). An accurate design should therefore anticipate this enlargement.

The very final step of the PhC sample fabrication consists of the deposition of an antireflection coating on the facets. A  $\approx 170$  nm titanium dioxide ( $TiO_2$ ) film is deposited using an electron beam evaporator. Using this technique, the measured reflectivity of the facet is reduced from about 20 % to  $\approx 3$  % at  $1.55 \mu\text{m}$ . The goal of this film is two-fold. First, it increases the amount of light coupled into the devices for a given input power. Second, it decrease the amount of Fabry-Perot type oscillations formed between the input and output facets that can be observed when measuring the spectral properties of the device.

### 2.2.3 Computation methods

A variety of numerical methods have been developed in order to theoretically investigate the properties of photonic crystals. A detailed summary of the existing methods allowing for the calculation of the band structure in the case of both an infinite or a finite crystal can be found in the book of Lourtioz *et al* [11]. Among these, three main methods have been used to design and compute the properties of our planar PhCs along this work. The plane wave expansion (PWE) and guided mode expansion (GME) methods have been used to obtain the band structures and field profiles of the various designs envisaged. The 3D Finite Element Method (3D FEM) has been employed to investigate the perturbation of the optical modes in the presence of a dielectric object as well as the optical forces exerted on the object. Most of these computations, including the entire 3D FEM modeling, have been performed by U.



Dharanipathy.

The plane wave expansion method is a tool developed for the computation of the band structure of infinite photonic crystals. The principle, proposed by Ho *et al* [13] and Plihal *et al* [30], consists in the decomposition of the both the periodic dielectric map and the Bloch modes (solution of the master equation 2.3) into series of plane waves (thus effectively realizing a spatial Fourier transform). The infinite series are then truncated to a finite number of components, which sets simultaneously, the accuracy of the calculation and the requirement for computation resources. Equation 2.4 then reduces to a matrix eigenvalue equation. A detailed development of the calculations can be found here [11] on page 32, as well as considerations on the choice of solving the master equation for the H field or E field. The routine that has been used during this work has been developed internally by D. Leuenberger (EPFL thesis [31]) and V. Zabelin (EPFL thesis [32]).

The guided mode expansion corresponds to an extension of the PWE method for the case of finite photonic crystals. The main difference between GME and PWE comes from the difference in the basis used for the decomposition of the Bloch modes. In the case of GME, the basis corresponds to the set of modes guided in a planar waveguide. This method is therefore highly relevant to the case of planar photonic crystals as studied in the group and produces highly accurate results as experimentally demonstrated by J. Jágerská [33]. The major drawback of this method comes from the superior complexity of the matrix element computation and the larger computing times involved. Here again, the routine used for calculations was internally developed by V. Zabelin [32].

Finally, the last numerical tool employed in this work was 3D finite element method. The principle of this technique relies on the discretization of the three-dimensional system that is modeled. The model therefore consists of a network of small elements or "mesh" whose density has to be carefully adjusted in order to obtain a good balance between the accuracy of the calculations and the computation time. Maxwells equations are then solved in a discrete manner at each of the meshing elements and give access to the eigenmodes of the modeled system. This method is highly adapted to compute the field distributions, energy densities and the Maxwell Stress Tensor. It is also very adapted to the computation of quality factors of cavity modes (Section 2.3). On the contrary, it is not at all convenient for the computation of band structures. The major drawbacks of this method is the enormous requirement in computation resources it requires and the complexity of the boundary conditions involved. A commercial package (COMSOL Multiphysics) and a computational cluster platform have been used to perform the 3D FEM calculations related to this work.

### 2.2.4 Line defect waveguide in a triangular lattice

Beyond the property to inhibit the propagation of an incident radiation, one major interest of photonic bandgap materials is the capacity to strongly confine light within the PhC structure. This can be achieved by introducing defects in the lattice that can be either localized (thus



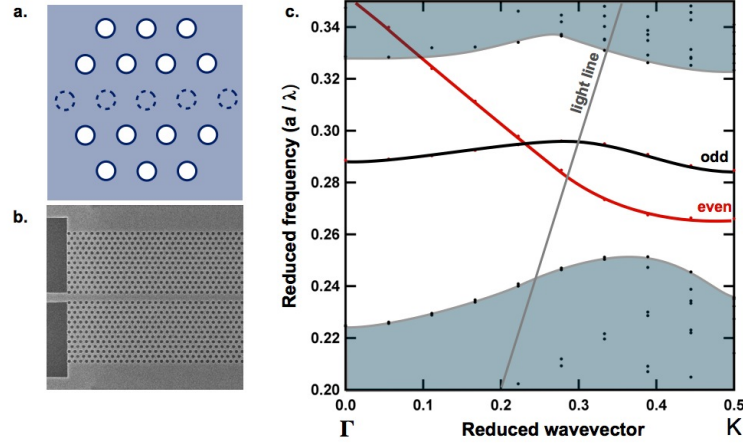


**Figure 2.8:** Band structure of a line defect waveguide. *a.* Schematic of a line defect waveguide. *b.* Scanning electron micrograph of a silicon W1 waveguide after removal of the sacrificial silica layer. *c.* Band structure calculated with guided mode expansion for a line defect waveguide. The red line indicates the even W1 mode. The black line indicates the odd W1 mode. The grey shaded areas correspond to the projected dielectric and air bands.

forming a cavity) or extended, with some degree of invariance through translation, hence forming a waveguide.

A typical example of a photonic crystal waveguide can be obtained by removing a row of holes from a triangular lattice along the  $\Gamma$ -K direction (see Figure 2.8.a and b.). This type of waveguide is commonly referred to as a W1 waveguide. The presence of the line defect leads to the "pulling" of two Bloch modes (TE polarized) of opposite parity from the air band inside the bandgap. Figure 2.8.c shows the calculated band structure of a line defect waveguide, as calculated using guided mode expansion. The even (red) and odd (black) W1 modes are shown in solid lines. The top and bottom shaded areas show the dielectric and air band projected on the  $\Gamma$ -K axis.

Considering only the case of the even mode, it can be understood that there exists a range of frequencies for which an incident wave can be coupled and propagated throughout the defect. For wavevectors above the light line, the associated mode is only weakly guided and the light radiates out of the silicon slab. On the contrary, for wavevectors below the light cone, the mode is truly guided and the light remains confined through the simultaneous total internal reflection (out-of-plane) and photonic bandgap (in-plane) effects. Propagation losses as low as 3 dB/cm have been reported for silicon W1 waveguides operating below light cone [34]. This is comparable with propagation losses in standard ridge/nanowire waveguides.

It is also interesting to note that the even mode of the W1 waveguide possesses two distinct regions, characterized by the distinct slopes of the dispersion curve. The small wavevector region (below 0.3) has a steep slope which corresponds to a high group index velocity  $v_g = \frac{\partial \omega}{\partial k}$ . The longer wavevector region (between 0.3 and 0.5) displays a small group velocity commonly associated with the concept of "slow light". This region is the subject of various investigations

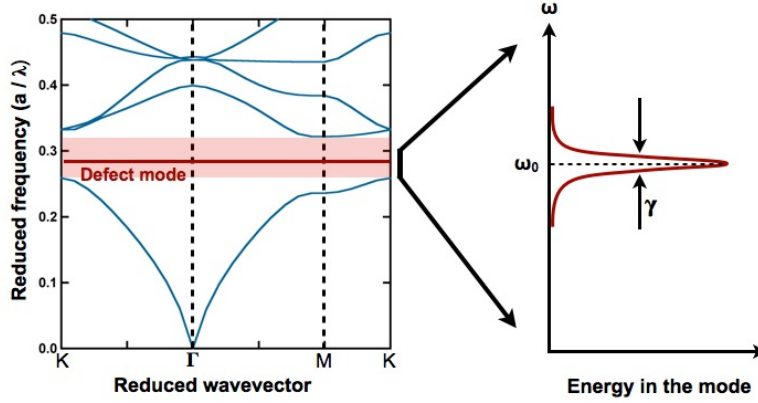


**Figure 2.9:** Illustration of a defect induced localized state with its energy level inside the photonic bandgap. **Left.** Band structure of a bulk triangular lattice in a silicon photonic crystal membrane. The presence of a defect in the lattice introduces a discrete energy level within the bandgap (red line). **Right.** Illustration of the Lorentzian lineshape of a photonic crystal cavity mode with a linewidth  $\gamma$ .

related to optical delay lines and enhanced light-matter interactions.

## 2.3 Two-dimensional photonic crystal cavities

### 2.3.1 Physics of the cavities

The presence of an isolated defect in a bulk photonic crystal lattice leads to the existence of spacially localized modes. These localized modes lead to the presence of one or multiple discrete energy levels within the bandgap, as illustrated in figure 2.9.a. The strong in-plane PBG confinement along with the out-of-plane TIR confinement results in the confinement of electromagnetic energy in the cavity for a finite period of time. A localized defect mode therefore acts like an optical microcavity, that is characterized by a Lorentzian lineshape owing to the exponential decay of the energy coupled to the mode. Hence, a quality factor  $Q$  can be attributed to the mode, that links to the cavity photon lifetime  $\tau$  through:

$$Q = \omega_0 \tau = \frac{2\omega_0}{\gamma} \quad (2.7)$$

Here  $\omega_0$  is the cavity mode frequency and  $\gamma$  corresponds to the linewidth of the mode as shown in Fig. 2.9.b.

The experimental quality factor of the cavity is inversely proportional to the rate at which light escapes from the cavity. There are a variety of mechanism through which the energy is likely to decay. The first one is related to the inherent field distribution of the mode and the coupling of the field components to the continuum of radiating modes (light cone) [35], [36]. This radiative decay is therefore intrinsic to the geometry of the defect and can be engineered in order to increase the cavity photon lifetime. A second decay mechanism can be attributed

to the light coupling channel used to populate the eigenmode. In a similar manner as light is transported from the coupling channel to the cavity mode, light from the cavity mode can couple back to the coupling channel thus resulting in a leakage. Finally, other mechanisms can decrease the lifetime such as losses in the material or scattering from structure roughness and lattice disorder. It is common to express the experimentally measured quality factor ( $Q_{measured}$ ) as:

$$\frac{1}{Q_{measured}} = \frac{1}{Q_{intrinsic}} + \frac{1}{Q_{coupling}} + \frac{1}{Q_{extrinsic}} \quad (2.8)$$

where  $Q_{extrinsic}$  includes both material losses and scattering due to imperfections. A variety of numerical methods can give access to the theoretical (intrinsic)  $Q$  of a cavity, among which finite element method (FEM) analysis or finite-difference time-domain (FDTD). This is of particular interest as it is possible to monitor the evolution of the field distribution and quality factor of a cavity when modifying some of its structural parameters. Nevertheless, there is no existing method allowing to automatically optimize the quality factor of a cavity to this day, and most reported improvements have been obtained through parametric optimization.

### 2.3.2 Standard photonic crystal cavities

The historical motivation behind the development of PhCs in the 1990s is the control of spontaneous emission through Purcell effect. In order to benefit from this effect, the optical microcavities must feature a large  $\frac{Q}{V}$  ratio, which involves having simultaneously, a large quality factor and a small mode volume. Beyond the Purcell effect, very high- $Q$  PhC cavities also offer the possibility to "store" light for short amounts of time, typically of the order of a nanosecond [37]. This can be used for the realization of optical memories. On a different note, the large local densities of energy achievable with simultaneous high  $Q$ , low  $V$  cavities also offer numerous prospects for the maximization of light-matter interactions. The latter is of particular interest in optical sensing but also for the generation of non-linear effects like second harmonic generation. The latest years of research on planar photonic crystals have therefore given birth to a large variety of PhC cavity configurations, each of which featuring mainly either a large quality factors or a small mode volumes.

There exists two main types of photonic crystal cavities: the point-defect type cavities and the extended, line-defect type cavities. In a point defect cavity, a local modification of the lattice is introduced. The modification can consist of one or several missing holes. This is the case for the standard H1 (1 hole missing) or L3 cavities (3 holes missing along  $\Gamma - K$ ), as can be seen in Figure 2.10.a. The defect can also be created by offsetting a certain number of holes from their nominal position, which is the case of the H0 cavity where the interstice between two adjacent holes is increased (see Figure 2.10.b). Finally, a cavity can also be formed by modifying the diameter of one or several holes [39]. Complex cavity designs where a combination of methods are used have also been published [23].

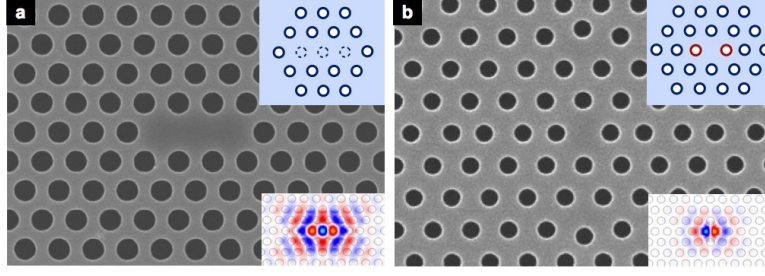


**Figure 2.10:** Example of photonic crystal point-defect cavities. *a.* Scanning electron micrograph of a L3 cavity consisting of 3 missing holes along the  $\Gamma - K$  direction (Picture from Z. Diao, EPFL). The top-right inset illustrates the three missing lattice holes. The bottom right inset shows the norm of the theoretical E-field distribution as calculated with FDTD (reprinted from [38]). *b.* Scanning electron micrograph of a H0 cavity consisting of 2 lattice holes being offset in opposite directions along the  $\Gamma - K$  direction (Picture from M. Tonin, EPFL). The top-right inset illustrates the two displaced holes. The bottom-right inset shows the theoretical E-field (norm) distribution calculated using FDTD (reprinted from [38])

Cavity design	Type	Q	Mode vol. $(\frac{\lambda}{n})^3$	Ref.
H0	Point defect	2500	0.23	[38], [43]
L3	Point defect	4500	0.74	[36], [38]
Modified L3	Point defect	45 000	0.78	[44]
Stretched W1	Line defect	900 000	1.6	[40]
Heterostructure	Line defect	2 500 000	1.4	[42]

**Table 2.1:** Properties of commonly used silicon photonic crystal cavities. The table records the reported experimental quality factors and theoretical mode volumes (FDTD) for a few point-defect and line-defect designs in silicon.

Line defect-type cavities are formed starting from a line-defect waveguide. Further modifications of the side holes along the waveguide are then introduced. One example of line-defect cavity can be found in the paper of Kuramochi *et al.* [40] where the side holes of a W1 waveguide are offset from their nominal position over an area of 2, 4 or 6 lattice periods. (see Figure 2.11.a). In this work, the experimental quality factors measured reached values as high as 900 000. The case of the "photonic heterostructure" cavities as presented by Asano *et al.* [41] and Takahashi *et al.* [42] constitutes another interesting example of line-defect cavities. In analogy to the electronic heterostructure in semiconductors, a cavity is formed by stacking lattices of distinct lattice constants (and thus distinct band structure) along the waveguide axis (see Figure 2.11.b). The experimental quality factors reported using this type of architecture can reach as high as 2.5 million, corresponding to a cavity photon lifetime of 2 ns.

A record of published experimental quality factors and computed mode volumes is presented in Table 2.1 for a few types of cavities in silicon. It is interesting to note how line-defects can present very large quality factors but possess relatively large mode volumes. On the contrary, point defect cavities are limited to lower Q values but can have very small mode volumes. The

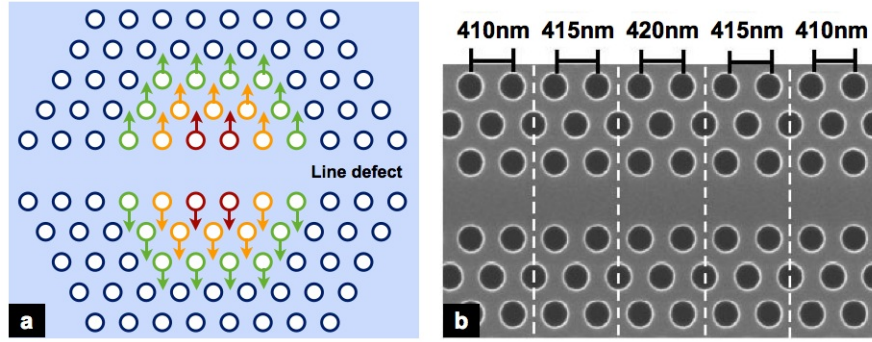


**Figure 2.11:** Examples of line-defect cavities. Illustration of a modulated waveguide cavity as reported by Kuramochi et al. (adapted from [40]) The colored holes are offset from their nominal positions in the  $\Gamma - M$  direction by different amounts, corresponding to the color code. Scanning electron micrograph of a photonic heterostructure cavity as reported by Asano et al. The separation between the side holes is modulated in the  $\Gamma - K$  direction. (reprinted from [41])

"Modified L3" example is particularly interesting as it shows how sensitive the quality factor of a cavity mode can be with respect to small modifications of the dielectric map.

### 2.3.3 Hollow cavities

As mentioned earlier in this section, the large quality factors and small mode volumes achievable with PhC cavities hold great promises for the enhancement of light-matter interactions in integrated devices. Nevertheless, one main hurdle remains to be cleared. It concerns the overlap of the electromagnetic field with the investigated object. The nature of light results in the fact that the EM energy inherently confines itself in the higher refractive index medium rather than the lower one. This is very advantageous when the object that is expected to interact with the resonant field is either a set of monolithically grown quantum wells or nucleated quantum dots. On the contrary, this becomes a very limiting factor in the case of cavities aimed at interacting with external agents like gases, liquids, biomolecules or nanoparticles.

The quality factor of a cavity gives a figure of merit of the statistical time that light in the cavity mode can interact with matter in its vicinity. Similarly, the mode volume of a cavity mode constitutes some figure of merit of the local energy density and therefore of the strength of the interaction. When the resonant field of a cavity is used to interact with an external element, it is then important to consider a third figure of merit, which is the overlap of the field with the low refractive index material. The spaces above and below the PhC membrane and the lattice holes are indeed the only places where interaction with the analyte can occur in the case of standard cavity designs as shown in section 2.3.2. Note that some interaction can also occur due to the adsorption of atoms and molecules on the surface of the silicon membrane, but this corresponds to rather small modifications of the dielectric landscape. Hence, it is interesting to investigate and develop PhC cavities featuring a large overlap with the low refractive index medium.

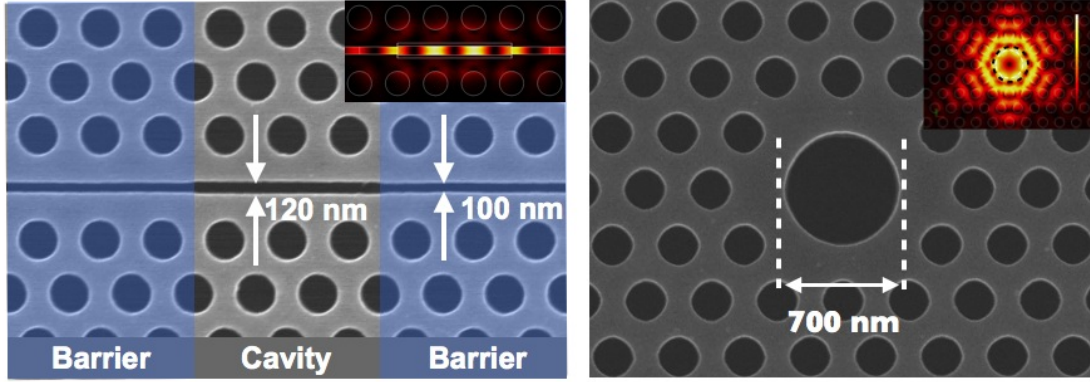


**Figure 2.12:** Slotted and circular hollow cavities. **Left.** Scanning electron micrograph of a slotted cavity. The cavity consists of a 120 nm air slot separated by two barriers which are formed by narrowing making the slot locally narrower (100 nm). The inset shows the electric field distribution (norm) as calculated with finite element method. **Right.** Scanning electron micrograph of a large circular cavity. The cavity is formed by making one hole larger (700 nm) than the other lattice holes (250 nm). The inset shows the norm of electric field calculate with FEM. (Images by Z. Diao, computations by U. Dharanipathy)

Cavity design	Q (air)	Mode vol. $(\frac{\lambda}{n})^3$	Overlap hollow reg. / total(%)	Ref.
Slotted cavity	26 000	0.56	$\approx 40 / 80$	[45]
Circular cavity	7 000	2.3	15 / 40	[46]

**Table 2.2:** Properties of the hollow cavities. This table records the experimental quality factors of the two hollow cavities as measured in air. The computed mode volumes expressed in  $(\frac{\lambda}{n})^3$  units are also presented. Finally, the overlap of the cavity fields with the low refractive index regions are calculated (i) inside the central hollow region (ii) over the total cavity volume. Computations have been performed using 3D FEM by U. Dharanipathy.

There exists a small number of PhC cavity designs displaying large overlaps. In a more exclusive manner, there are only two types of cavities where the majority of the overlap is concentrated in a very restricted region of the low refractive index material. These cavities are usually referred to as "hollow cavities" and can be classified in the similar way as standard cavities. Figure 2.12 shows the two examples of hollow cavities currently existing. The left panel shows a PhC based slotted cavity while the right panel shows a point-defect circular cavity.

The slotted cavity is formed starting from a W1 waveguide. A thin air slot is etched in the center of the line defect which supports a propagating mode. The slot is typically 80 to 120 nm wide in the near-infrared. The continuity of the normal displacement field component at the inner silicon/air interface imposes a large enhancement of the electric field [47]. A large fraction of the electric field of the propagating mode is thus effectively located within the intermediate air slot. This is not a property that is inherent to photonic crystal cavity and similar architectures have been readily demonstrated in ridge waveguides [48], [49]. It is then possible to form a line-defect cavity mode by creating barriers at two positions of the slotted waveguide. A common architecture relies on the modulation of the side holes lattice constant



as in the case of heterostructure cavities [50], [51]. A second approach consist of making the air slot narrower over a few lattice constant units (Fig. 2.12.left). The dispersion curves of the slot modes of different widths are slightly offset in energy. A narrower slot (here 100 nm) has a propagating mode that lies closer to the dielectric band than a wider slot (here 120 nm). As a consequence there exists a narrow range of frequency for which a larger slot supports optical propagation while a narrower slot does not. A local shrinking of a slotted waveguide can therefore constitute a barrier and an appropriate combination of two barriers can be used to form a cavity mode. This phenomenon is further detailed in the thesis of J. Jágerská [33]. Slotted cavity have been reported to feature quality factor in excess of 30 000 in air and field overlap above 80 %. These values are summarized in Table 2.2. Slotted PhC cavities has been successfully used as chemical sensors for glucose [51] and gas [45]. In the later case, the impact of the large overlap manifests in dramatic increase in sensitivity from 8 nm/RIU (refractive index unit) with a standard heterostructure cavity [52] to 500 nm/RIU for the slotted cavity [45].

The circular cavity is based on a point-defect where one of the holes has a different radius than the lattice holes. The experimental demonstration of circular cavities with both a smaller hole [53] or larger hole [54] [55] have been carried out. In the case presented in Figure 2.12 (right panel) case, the central hole is 700 nm in the diameter, as compared to 250 nm for the lattice holes. A finite element method analysis of this system indicates that such a large circular cavity supports a variety of optical modes. For the mode of interest, it can be calculated that the total overlap of the field with air is as high as 40 % and that over 15 % of the total field is located in the vertical cylinder passing through the large hole. The quality factor of this cavity is also lesser than that of slot type cavities in air (see Table 2.2). Nevertheless, the large dimension (700 nm) of the central hole makes it ideally suited to interact with larger nanoparticles of the size of a large virus or a small bacterium, as opposed to the slotted cavity which is more adapted to liquid and gas sensing.





## 3 Optomechanical forces and applications

This chapter summarizes some important concepts on the mechanical actions that light exerts on matter and how it is possible to manipulate nano and micro scale objects with light. The first section introduces the main physical concepts used in the description of the optical forces on a mechanical object. The second section is dedicated to laser based optical traps commonly referred to as "optical tweezers". The last section constitutes a state-of-the-art of the optical nanostructures that have been used or developed to trap particles in their near field.

### 3.1 Optical forces on a mechanical object

#### 3.1.1 Introduction

An electromagnetic (EM) field carries energy, linear momentum and angular momentum. An object placed in such a field perturbs the original distribution. A part of the field is scattered out and the remaining part is either transmitted through or absorbed by the object (Figure 3.1). From this point of view, it can be intuitively understood that the radiation might not only transfer part of its energy to the body, but the difference in momenta between the impinging wave on one hand and the scattered and internal waves on the other hand should also result in a transfer of momentum to the object. This can be associated, following Newton's second law of motion, to the existence of a net opto-mechanical force acting on the body. The latter is commonly referred to as "radiation pressure".

Historically, the possibility that light can exert a mechanical effect on matter has been hypothesized as early as in 1609 by Johannes Kepler. This was envisaged as an explanation for the observation that comets and their tails always pointed towards the Sun, independent of their trajectories. Later on, in 1873, the advent of Maxwell's theory of electromagnetism allowed for the description of energy and momentum transfer from light to an object in the form of "radiation pressure". The first experimental confirmation of light pressure following predictions based on Maxwell's theory was reported in 1901 by Lebedev [56], while the first

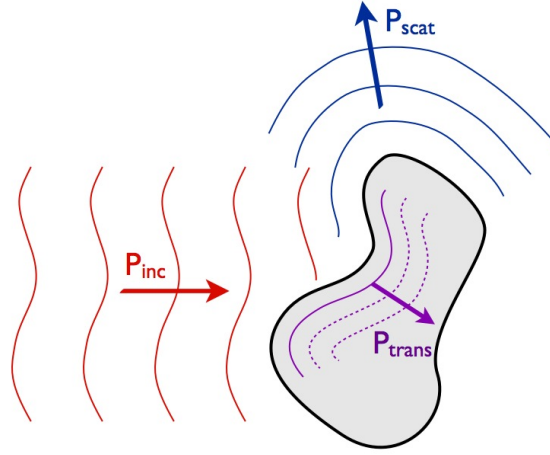


**Figure 3.1:** Schematic of linear momentum exchange between an incident field and a mechanical object. The incoming electromagnetic field (red) carries momentum. A mechanical object scatters back a fraction of the incident field (blue) and transmits/absorbs the remaining part (purple). The change in momentum between the incident and scattered field lead to a transfer of mechanical momentum to the object.

experimental demonstration of angular momentum transfer was only achieved in 1936 by Beth. In the meantime, similarly to the way light transfers energy to matter in quantized units (as hypothesized by Einstein in 1905), the quantized nature of momentum transfer from light to matter was demonstrated by A. Compton in 1925.

The calculation of optical forces on an arbitrary object is usually very complex. It requires solving Maxwell's equations in at least two media separated by an interface. The vast majority of these calculations cannot be performed analytically and therefore rely on numerical methods. One very important tool in that aspect is the Maxwell Stress Tensor (MST) [57]. It allows for the determination of the total mechanical force acting on an object in the presence of the  $\vec{E}$  and  $\vec{H}$  fields on an arbitrary closed surface surrounding the object. The Maxwell stress tensor (see Section 3.1.2) can be computed using Finite Element Method for example which is used to solve Maxwell equations on a discretized (meshed) 2D or 3D system. This type of computations were performed by one of my colleagues in parallel to the experimental investigations presented in this thesis. Some of the numerical results are presented in Chapter 6.

#### 3.1.2 The Maxwell Stress Tensor

The starting point for the derivation of the Maxwell stress tensor (MST) is the Lorentz force. An electromagnetic field exerts a mechanical force  $\vec{F}$  on a charge  $q$  moving with a velocity  $\vec{v}$ .

$$\vec{F} = q[\vec{E} + \vec{v} \times \vec{B}] \quad (3.1)$$

Here  $\vec{E}$  is the electric field and  $\vec{B}$  is the magnetic induction field. For a distribution of charges comprised in a volume  $V$ , a total force can be obtained by integrating the above expression

over the ensemble of charges.

$$\vec{F} = \int_V [\rho \vec{E} + \vec{j} \times \vec{B}] dV \quad (3.2)$$

In this expression,  $\rho$  is the charge density,  $\vec{j}$  the density of current. All of these quantities are functions of spatial coordinates  $\vec{r}$  and time  $t$  which have been omitted for conciseness of the equations. Equation 3.2 can be reformulated using Newton's second law of motion and introducing the total mechanical momentum on the object  $\vec{P}_{mech}$ .

$$\frac{d}{dt} \vec{P}_{mech} = \int_V [\rho \vec{E} + \vec{j} \times \vec{B}] dV \quad (3.3)$$

Although it is rather simple to expand this expression in the case of one or few point-like charges, the treatment of this expression in the case of a large, continuous body can become rapidly complex. A set of derivations on the Maxwell equations (see Chapter 2) permits the construction of the following quantity  $\vec{T}$  referred to as "Maxwell Stress Tensor" where  $\otimes$  refers to the tensorial/outer product and  $\vec{I}$  is the identity tensor.

$$\vec{T} = \left[ \epsilon_0 \vec{E} \otimes \vec{E} - \mu_0 \vec{H} \otimes \vec{H} - \frac{1}{2} (\epsilon_0 E^2 + \mu_0 H^2) \vec{I} \right] \quad (3.4)$$

A detailed version of the aforementioned derivations can be found in the textbook of Jackson [57]. Note that Equation 3.4 stands for the expression of the Maxwell stress tensor for an electromagnetic wave in vacuum. This definition can be extended to the case of a wave in an arbitrary medium [58] by including the specific dielectric permittivity  $\epsilon$  and magnetic permeability  $\mu$  of the corresponding medium as in Equation 3.5.

$$\vec{T} = \left[ \epsilon_0 \epsilon \vec{E} \otimes \vec{E} - \mu_0 \mu \vec{H} \otimes \vec{H} - \frac{1}{2} (\epsilon_0 \epsilon E^2 + \mu_0 \mu H^2) \vec{I} \right] \quad (3.5)$$

From the operations performed on Maxwell equations, it can be shown that the MST verifies the following property:

$$\nabla \cdot \vec{T} = \frac{d}{dt} \frac{1}{c^2} [\vec{E} \times \vec{H}] + \rho \vec{E} + \vec{j} \times \vec{B} \quad (3.6)$$

It is now possible to integrate these quantities over an arbitrary volume  $\Upsilon$  that comprises all the sources of  $\rho$  and  $\vec{j}$ . In this case the new expression reads:

$$\int_{\Upsilon} \nabla \cdot \vec{T} d\Upsilon = \frac{d}{dt} \left( \frac{1}{c^2} \int_{\Upsilon} [\vec{E} \times \vec{H}] dV \right) + \int_{\Upsilon} [\rho \vec{E} + \vec{j} \times \vec{B}] d\Upsilon \quad (3.7)$$

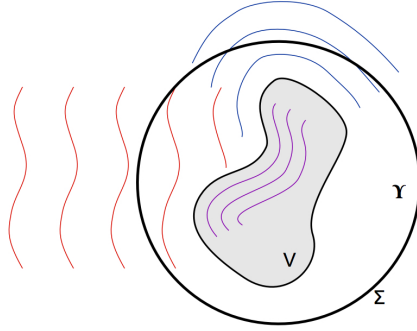


**Figure 3.2:** Schematic of an arbitrary enclosing surface  $\Sigma$  used for the calculation of the Maxwell stress tensor on the scattering object.

The two terms on the right hand-side can be identified to two momenta, and Equation 3.7 can be rewritten as:

$$\int_Y \nabla \cdot \vec{T} dY = \frac{d}{dt} [\vec{P}_{field} + \vec{P}_{mech}] \quad (3.8)$$

Here  $\vec{P}_{field}$  corresponds to the field momentum and arises from the time-varying  $\vec{E}$  and  $\vec{H}$ . This momentum is zero when averaged over the time of a full period of the EM wave.  $\vec{P}_{mech}$  corresponds to the mechanical momentum of the EM field carried through the volume  $Y$  as introduced earlier (Equation 3.3).

$$\vec{P}_{field} = \frac{1}{c^2} \int_Y [\vec{E} \times \vec{H}] dY = \int_Y \vec{g}_{field} dY \quad (3.9)$$

The above also allows for the introduction of  $\vec{g}_{field}$  which is the density of field momentum and is related to the Poynting vector  $\vec{S}$  of the radiation through the following expression:

$$\vec{g}_{field} = \frac{1}{c^2} [\vec{E} \times \vec{H}] = \frac{\vec{S}}{c^2} \quad (3.10)$$

The Gauss law of integration finally allows for the replacement of the volume integration in Equation 3.8 over  $Y$  on the left-hand side with a surface integration over  $\Sigma$ .

$$\oint_{\Sigma} \vec{T} \cdot \vec{n} d\Sigma = \frac{d}{dt} [\vec{P}_{field} + \vec{P}_{mech}] \quad (3.11)$$

Equation 3.11 gives a little more insight on the physical meaning of the Maxwell stress tensor. From this expression it can be inferred that the MST has the dimension of a surface density of

momentum. Finally, using the property that the net field momentum is zero when average over time-period of the radiation,  $\langle \frac{d}{dt} \vec{P}_{field} \rangle = 0$ , it can be recognized using Equations 3.2 and 3.11 that:

$$\langle \vec{F} \rangle = \oint_{\Sigma} \langle \vec{T} \rangle \cdot \vec{n} d\Sigma \quad (3.12)$$

This result is particularly interesting because it allows for the computation of the total optical force on a object with the sole knowledge of the  $\vec{E}$  and  $\vec{H}$  fields at the surface of the chosen volume  $Y$ . Nevertheless, it has to be noticed that the above mentioned fields are the self-consistent fields, meaning the superposition of the incident and scattered field.

On a separate aspect, similar derivations of the Maxwell stress tensor can also be used to express the angular momentum of an electromagnetic radiation and its transfer to a mechanical object. A detailed treatment of this effect can be found in the work of S. Barnett. [59]

#### 3.1.3 Optical forces on a point-like dipole

In very few cases, an analytical expression for the optomechanical force exerted on an object with simpler geometry shapes can be derived. For example, it is possible to derive an analytical expression for the force exerted by an electromagnetic field on a point-like electric dipole. This approach is the basis of a wide range of works that aim at estimating the forces acting on small neutral bodies like stellar dust grains [60], colloids [61] and individual particles in optical tweezers (Section 3.2)

The system considered consists of two equivalent charges, opposed in sign and separated by an infinitesimal distance. It is supposed that the constituted dipole has a polarizability  $\alpha$ , possesses no static dipole moment and responds linearly to an external electric field  $\vec{E}$ . The dipole moment  $\vec{\mu}$  can then be written:

$$\vec{\mu} = \alpha \vec{E} \quad (3.13)$$

The dipole is placed in a non-homogeneous and time-varying electromagnetic field and perceives a Lorentz force:

$$\vec{F}_{dipole} = (\vec{\mu} \cdot \vec{\nabla}) \vec{E} + \frac{1}{c} \frac{d\vec{\mu}}{dt} \times \vec{B} \quad (3.14)$$

The above expression can be rewritten, introducing Equation 3.13:

$$\vec{F}_{dipole} = \alpha \left( (\vec{E} \cdot \vec{\nabla}) \vec{E} + \frac{1}{c} \frac{\partial \vec{E}}{\partial t} \times \vec{B} \right) \quad (3.15)$$

### Chapter 3. Optomechanical forces and applications

---

It is then possible to reformulate Equation 3.14 in the following form, as described in the work of Gordon [62]:

$$\vec{F}_{dipole} = \alpha \left( \vec{\nabla} \left( \frac{1}{2} E^2 \right) + \frac{1}{c} \frac{\partial}{\partial t} (\vec{E} \times \vec{B}) \right) \quad (3.16)$$

Equation 3.16 is the main result of this section. It describes the instantaneous electromagnetic or optical force acting on a point-like dipole of polarizability  $\alpha$ . It is very interesting to notice that this force decomposes into two components. The first one relates to the inhomogeneity of the electric field as is commonly referred to as "gradient force". The second component is related to the variation in time of the  $\vec{E} \times \vec{B}$  quantity, linked to the density of field momentum (3.1.2, Equation 3.10) and is generally referred to as "scattering force".

The physical nature of this term can be seen as an action of the rapidly varying  $\vec{E}$  and  $\vec{B}$  field acting on the charges of the dipole [58], keeping in mind that oscillations of the dipole will lead in turn to the emission of radiations, and therefore a modification of the electromagnetic environment around the dipole. It can also be seen as a transfer of field momentum as discussed by Gordon [62] and later on by Rohrbach and Stelzer [63], which also implies the existence of a scattered field. In any case, this observation points out one of the limitations of the dipolar model. Indeed the optical force is calculated from the knowledge of the incident field, without taking into account the perturbation of the dipole on the local field [58] [64].

#### 3.1.4 Optical forces on a small spherical particle - Rayleigh approximation

The model of an electric dipole described in the previous section is well-adapted for a system composed of an atom or a molecule in an electromagnetic field. In this case the polarizability  $\alpha$  relates to the projection of the dipole moment of the particle on the axis of the electric field. It is possible in some cases to extend some of the results obtained for a point-like dipole to larger bodies like spherical particles. Nevertheless, the accuracy of the calculations becomes strongly dependent on size of the object as compared to the wavelength of incident radiation.

One common method to further Equation 3.14 to an extended particle is to introduce two new parameters. First, a complex value is attributed to polarizability  $\alpha$  in order to account for the "reactive radiation" of the dipole moving in the excitation field and thus effectively modifying the electromagnetic landscape [65], [64], [66]. The second parameter corresponds to the fact that the particle is assumed to move slowly in comparison with the oscillation period of the  $\vec{E}$  and  $\vec{H}$  fields. As a consequence, it is enough to evaluate the optical force applying on the sphere averaged over one oscillation cycle  $\langle \vec{F} \rangle$ . In this case, the fast varying terms occurring in the developments can be canceled out and the force on the particle in a monochromatic field of angular frequency  $\omega$  reads [58]:

$$\langle \vec{F} \rangle = \frac{1}{2} Re(\alpha) \vec{\nabla} \langle |\vec{E}|^2 \rangle + \omega Im(\alpha) \langle \vec{E} \times \vec{B} \rangle \quad (3.17)$$

The above equation can also be rewritten using Maxwell equations for an arbitrary wave of the type  $\vec{E}(\vec{r}, t) = \text{Re}[E_0(\vec{r}) e^{i\vec{k}\cdot\vec{r}} e^{i\omega t}]$ :

$$\langle \vec{F} \rangle = \frac{1}{4} \text{Re}(\alpha) \vec{\nabla} E_0^2 + \frac{1}{2} \text{Im}(\alpha) E_0^2 \vec{k} \quad (3.18)$$

It can be noticed from Equations 3.17 and 3.18 that the real part of the polarizability which illustrates the capacity of the particle to build up an inner electric field in response to the outer excitation contributes to the gradient component of the force. In contrast, the imaginary part of the polarizability which is mainly attributed to absorption and dampening of the electric field contributes to the scattering part of the force.

A well-established expression for the electrodynamic correction was proposed by Draine [60] for a particle in a plane wave, characterized by a wave vector  $\vec{k}$ .

$$\alpha = \frac{\alpha_0}{1 - \frac{2}{3} i k^3 \alpha_0} \quad (3.19)$$

Here  $\alpha_0$  corresponds to the intrinsic polarizability of the particle, which can also be complex-valued in the case of a metallic body for example.  $\alpha_0$  is also generally a function of  $\omega$ .

In the specific case of a spherical dielectric particle in an homogeneous electric field, the polarizability  $\alpha_0$  has a well-known expression which is given by the Clausius-Mossotti relation [57].

$$\alpha_0 = 4\pi\epsilon_m a^3 \frac{\frac{\epsilon_p}{\epsilon_m} - 1}{\frac{\epsilon_p}{\epsilon_m} + 2} \quad (3.20)$$

The parameters in relation 3.20 include the radius of the particle  $a$ , the dielectric permittivity of the particle  $\epsilon_p$ , supposed homogeneous and the dielectric permittivity of the surrounding medium  $\epsilon_m$  which is equal to  $\epsilon_m = 1$  in the case of vacuum. The condition of homogeneity of the electric field around the particle sets a important restriction on the maximum size of particle for which the formulae presented in this Section can be used. Indeed, for a particle in an EM radiation, the electric field can be considered homogeneous only if the particle is much smaller than the wavelength  $\lambda$ . A typical criterion for the validity of this extended dipolar approximation is that the radius  $a$  of the particle should be  $a \leq \frac{\lambda}{20}$ , often referred to as Rayleigh approximation.

In the specific case of a dielectric particle  $\text{Im}(\alpha_0) = 0$ . In the Rayleigh approximation, the "gradient" and "scattering" components of the force can finally be written as:

$$\langle |\vec{F}_{grad}| \rangle = \frac{1}{4} \text{Re}(\alpha) \nabla E_0^2 \quad (3.21)$$

$$\langle |\vec{F}_{scat}| \rangle = \frac{1}{3} k^4 \alpha_0^2 E_0^2 \quad (3.22)$$

where  $\alpha$  is taken from Equation 3.19 and  $\alpha_0$  from Equation 3.20. Variations of Equations 3.21 and 3.22 are extensively used in works related to the optical trapping of small particles using optical tweezers. [67], [68]

Complete developments of the radiations forces on dielectric spheres in the Rayleigh approximation have been performed for a variety of field distributions. The case of Gaussian beams was explored by Harada and Asakura [69] and Zemánek *et al* [70]. The case of a Rayleigh dielectric particle in an arbitrary wave is extensively described in the work of Rohrbach and Stelzer [63].

### 3.1.5 Beyond the Rayleigh approximation

In reality, the vast majority of optical trapping experiments occur outside of the hypotheses made in the previous section (to the noticeable exception of atomic and molecular traps [71] [72]). Especially, the assumption of the particle acting like a single dipole is usually invalidated by the difficulty, so far, to confine light in volumes that are much smaller than a wavelength and thus the small magnitude of optical forces of very small objects.

In the range of size where  $a \approx \lambda$ , the manner with which the particle polarizes under the influence of the trapping EM field is non trivial. Discrete optical modes can be supported by the particle which dictate simultaneously the inner polarization field of the particle, the characteristics of the scattered field, and thus the optical forces applied. An experimental observation of these modes can be found here [73].

As the size of the particle is increased and gets close to the trapping wavelength, the treatment of the inner and scattered field becomes rapidly complex. The scattering of a plane monochromatic EM wave by a homogeneous isotropic sphere, referred to as "Mie theory" after Gustav Mie who developed it, has been the object of extensive studies (see for example Born and Wolf [74]). It consists of a general method to calculate the electric field within a spherical object, where an incoming plane wave is decomposed on a set of spherical modes. Although, the Mie theory applies independently on the size of the particle, trapping experiments where the size of the particle is of the order of the trapping wavelength are said to occur "in the Mie regime".

Several methods have been developed to compute the forces on the particles for this range of sizes. A large number of these are based on the theory of Mie. One such development was performed for dielectric and absorbing sphere by Irvine [75]. Nevertheless, calculations based on Mie theory require cumbersome developments and long computation time. A second method that has been developed proposes to decompose the object into a set of discrete individual dipoles and to investigate the optical force acting on each of these dipoles [76] [77]. The latter is referred to as "Discrete dipole approximation" and also allows the treatment of non-spherical bodies. A third method is the direct computation of the Maxwell stress



tensor using 3D Finite Element Method. The major disadvantage of this method is the heavy computation power that it involves.

It is also possible to trap particles that are much larger than the wavelength of the optical field. Nevertheless, as the size of the object becomes bigger, the optical forces become smaller compared to the weight of the object. The largest particles that can be trapped are usually of the order of a few tens of microns [78] [79]. In this range of sizes (typically  $a \geq \frac{\lambda}{20}$ ), accurate estimation of the trapping forces in the specific case of optical tweezers can be made using geometric considerations on the deflection of the incoming light beams [80], [68]. This regime is usually referred to as "Ray-Optics" regime.

Note that the existence of discrete resonance modes within large particles (of the whispering gallery type) can lead to very interesting phenomena. In particular, the use of a monochromatic trapping field with a frequency that is close to the resonance of the particle can strongly enhance the optical force perceived by the latter. This feature can be used, for example, to propel nanoparticles at very high speed using a surface wave [81], [82]. It could also be implemented to selectively trap particles depending on their size or permittivity.

## 3.2 Optical tweezers

### 3.2.1 History

Optical tweezers are instruments that allow for the all-optical manipulation of small objects ranging from a few nanometers in the case of metallic colloids to a few microns for dielectric particles. The mechanism is based on the radiation pressure and the typical forces generated are of the order of 1 to 100 pN. Their principle was first demonstrated by Arthur Ashkin in a series of papers published between 1970 and 1987.

In his original work [83], Ashkin performed the first implementation of an optical trap by separating the continuous-wave emission of an Argon laser (514 nm) into two counter propagating beams. The two beams were then loosely focused inside a chamber containing latex beads ranging from 0.5 to almost 3  $\mu\text{m}$  in the diameter. The experiment showed that freely suspended particles entering one of the beams were attracted towards the inner region of the beam and then accelerated up to a stable region located between the two laser waists. The disruption of one of the two beams caused the particle to be accelerated again in the direction of the light propagation.

The second major discovery was reported only 16 years later, in 1986, with the observation that a similar optical trap could be created with the help of a single laser beam, tightly focused through a microscope objective [4]. In this case the position of the stable region is located near the waist of the laser beam. The mechanism responsible for the three dimensional confinement of the particle was identified as the gradient force, in contrast with the first experiment where the trapping mechanism was essentially the scattering force.

### Chapter 3. Optomechanical forces and applications

---

The application of optical tweezers to the micro manipulation of biological entities like viruses and bacteria was demonstrated in 1987 [84]. Individual Mosaic Tobacco viruses and *Escherichia Coli* bacteria were isolated and trapped using the single beam configuration without being damaged. This constituted a decisive step which led to the fast development of optical tweezers based techniques in the fields of biology and medicine.

Other significant developments have been demonstrated in later years, for example to demonstrate the applicability of the technique to small metallic particles [68]. A large range of investigations on optical tweezers have also focused on the generation and the use of the trapping beam with complex phase distributions. These investigations lead to the demonstration of orbital angular momentum transfer to a particle in the form of a torque. This is performed with the use of a beam with a helical phase, like a  $TEM_{01}$  [85] or a Laguerre-Gaussian beam [86], [87]. Note that the transfer of optical "orbital angular momentum" to absorbing particles is to be separated from the optical "spin angular momentum" transfer from a circularly polarized beam to a birefringent material [88].

Finally, accurate and real-time control of the phase of single trapping beams have led to the demonstration of the parallel manipulation of multiple particles [89]. This technique is now referred to as "holographic optical tweezers". Detailed description on holographic tweezers and optical vortices (or spanners) can be found in the reviews of Grier [90] and Dholakia [91].

#### 3.2.2 Principle

In their most common implementation, optical tweezers make use of a visible/NIR Gaussian beam focused through a high numerical aperture (NA) objective. Detailed considerations regarding the assembly of the optical setup, including the choice of the microscope objective, laser, but also the detection and calibration methods can be found in two separate reviews from Neuman and Block [67] and Svoboda and Block [68].

The aim of this section is to introduce the basic principle of the instrument, which can be understood by considering the simplest case of a Rayleigh particle (Section 3.1.4) in a focused Gaussian beam. A complete description of this configuration can be found in the work of Harada and Asakura [69]. A rotationally symmetric beam is focused through a perfect lens. A good approximation for the power density  $I(r, z)$  of the laser in the vicinity of the focal plane can be written in cylindrical coordinates:

$$I(r, z) = \frac{2P}{\pi w_0^2} \frac{1}{1 + (2\tilde{z})^2} e^{-\frac{2\tilde{r}^2}{1 + (2\tilde{z})^2}} \quad (3.23)$$

where  $P$  is the total beam power,  $w_0$  the beam waist at the focus. The new coordinates  $\tilde{r}$  and  $\tilde{z}$  are reduced beam coordinates such that:  $\tilde{r} = \frac{r}{w_0}$  and  $\tilde{z} = \frac{z}{kw_0^2}$  with  $k$  the wave vector of the radiation. Figure 3.3.a shows a distribution of intensity as generated using Equation 3.23. The horizontal and vertical axes indicate the spatial coordinates in arbitrary units while the

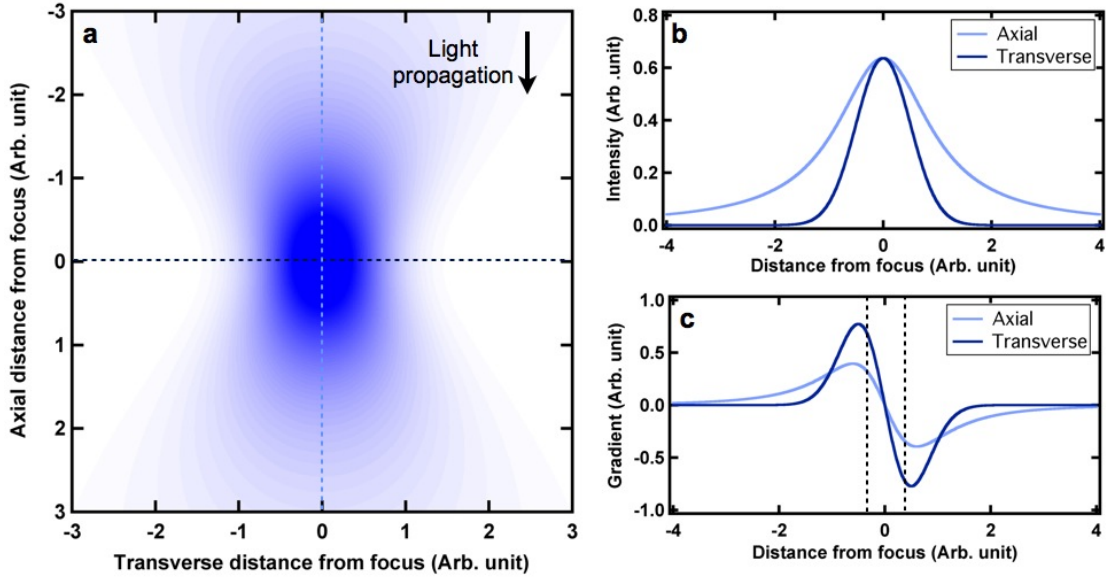


**Figure 3.3:** Illustration of a focused Gaussian beam and generated field gradients. a) Calculated intensity distribution for a focused Gaussian beam. b) Intensity distribution along the optical axis (light blue) and across the beam waist (dark blue). c) Calculation of the intensity gradient for the two distributions shown in b).

colorscale coded from white to blue indicates the light intensity. Figure 3.3.b shows the cross-sections of the intensity along the  $r$  and  $z$ -axis, and passing through  $(0,0)$ .

In the case of a Rayleigh particle in a single beam optical trap, the gradient component of the radiation pressure can be several orders of magnitude stronger than the scattering force component [69]. The effect of the scattering component of radiation pressure will therefore be omitted for the sake of simplicity in this short review. From Equation 3.21 it is known that:

$$\vec{F}_{grad} \propto \vec{\nabla} |\vec{E}|^2 \propto \vec{\nabla} I(r, z) \quad (3.24)$$

The gradient force can be separated into two orthogonal components: the axial component, along  $z$ , in the direction of light propagation and the radial/transverse component, along  $r$ . Using Equation 3.23 the partial derivatives with respect to  $r$  and  $z$  of  $I(r, z)$  can be calculated and written:

$$\frac{\partial}{\partial r} I(r, z) = -\frac{4\tilde{r}}{1 + (2\tilde{z})^2} I(r, z) \quad (3.25)$$

$$\frac{\partial}{\partial z} I(r, z) = -\frac{8\tilde{z}}{1 + (2\tilde{z})^2} \left[ 1 - \frac{2\tilde{r}^2}{1 + (2\tilde{z})^2} \right] I(r, z) \quad (3.26)$$

It is interesting to note that both these quantities are equal to zero when  $r = 0$  and  $z = 0$  respectively. This indicates the existence of an equilibrium position in the center of the focus

point. This is well illustrated by plotting the evolution of these two quantities as a function of their respective spatial coordinates (see Figure 3.3.c). The stability of this equilibrium is given by the negative slope of the two curves indicating that a deviation of the particle from (0,0) along either the axial or transverse axis will give rise to a restoring force that will bring the object back to its original position. The existence of this stable equilibrium in three dimensions is the essential mechanism behind single beam optical trapping and optical tweezers. In reality, one noticeable effect of the scattering force in this case is that the equilibrium position is not actually located in (0,0) but in a slightly offset position along the propagation direction (see Harada [69]).

It is also very interesting to notice that, for small deviations of  $r$  and  $z$  around 0, both the axial and transverse components of the gradient force behave linearly. This region is indicated by dotted lines on Figure 3.3.c. Note that the fact that the extent of the "linear" regions along  $r$  and  $z$  are matching is purely an artifact of the simulated intensity distribution. From this linear behavior, it has been commonly admitted that the restoring gradient force can be associated to a spring constant or "stiffness" in the sense of Hooke's law. The latter can be written for example in the case of the transverse component:

$$\vec{F}_r = -k_r \cdot r \cdot \vec{e}_r \quad (3.27)$$

where  $k_r$  corresponds to the radial stiffness of the optical trap. In the simple case described earlier, it can be understood from Equations 3.25 and 3.26 that the trapping stiffness is proportional to the incident power (for a given, fixed, spatial distribution). From the above expression, it is also possible to define a potential  $U_r$  such that  $\vec{F}_r = -\vec{\nabla} U_r$  and which is harmonic.

$$U_r = \frac{1}{2} k_r r^2 \quad (3.28)$$

This analogy is highly interesting because it allows to relate the physics of the optomechanical system composed of the particle and the optical trap to the physics of an harmonic oscillator. Sub-micron particles immersed in a fluid exhibit random momentum fluctuations due to random thermal energy exchanges with the surrounding medium. This manifests as a characteristic random displacement or "random walk" of the particle in the absence of any other forces and is referred to as Brownian motion. The motion of the particle then follows Langevin equation (Equation 3.29) where  $\vec{F}_{ext}$  is the sum of all external forces,  $\vec{F}_{fr}$  accounts for the friction force of the medium and  $\vec{F}_{th}$  arises from the thermal fluctuations and is a stochastic process.

$$m \frac{d^2}{dt^2} \vec{r} = \vec{F}_{ext} + \vec{F}_{fr} + \vec{F}_{th} \quad (3.29)$$

When a particle is confined in an optical trap, Brownian motion still occurs, but it in a constrained manner. The net displacement of the object over a long period of time is zero for a

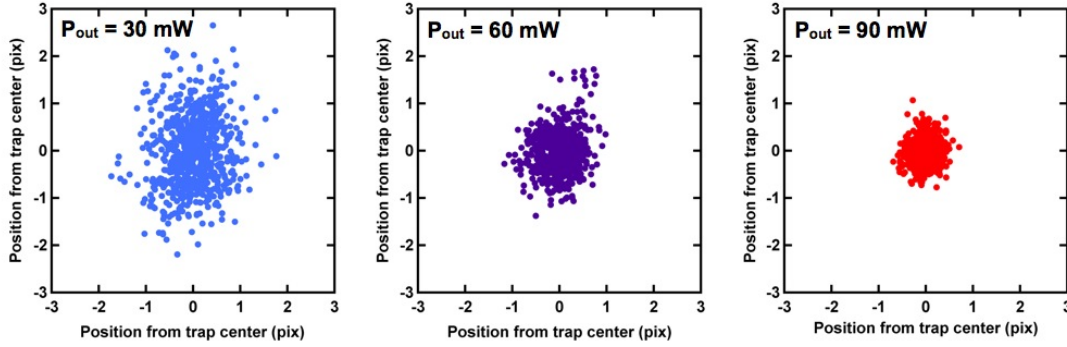


**Figure 3.4:** Experimental demonstration of power dependent trapping potential. The position of an optically trapped particle is tracked for 35 seconds at 30 frames per second for three different laser output powers. Each recorded position is plotted in camera pixel coordinates. The experiment shows a consistent shrinkage of the excursions of the particle from the center of the trap, associated with a narrowing of the trapping potential.

steady trap. The instantaneous excursions of the particle with respect to (0,0) are a function of the thermal energy of the particle and the profile of the trapping potential, as dictated by the Equipartition theorem [67]. This can be used for example in order to define a criterion for the stability of an optical trap. A typical figure of merit states that the height of a trap should be greater than  $10.k_B.T$  to be stable, where  $k_B$  is the Boltzmann constant and  $T$  the temperature of the system.

The motion of a particle in Brownian motion has been the object of a variety of theoretical and experimental works [92], [93]. The knowledge of this motion, in time and space, can be used to retrieve important characteristics from the trap. For example, the statistical distribution of positions of the particle over a long period of time can be used to retrieve the width of the potential and therefore the trapping stiffness defined in Eq 3.27. An example of such analysis can be observed on Figure 3.4. In this case, the distribution of over 1000 positions of a trapped particle was recorded in time, for three different trapping powers. The dependence of the trapping potential profile with power mentioned earlier can clearly be observed on this figure in the form of a shrinking of the "trapping volume" allowed for the particle. Another technique to retrieve the trapping stiffness relies on the analysis of the timescales at which the particle in the trap changes momentum. This method is referred to as "power spectrum analysis" [94]. The principle of this methods uses the Einstein-Ornstein-Uhlenbeck theory of Brownian motion, which predicts a Lorentzian profile for the power spectrum of displacement of a particle in Brownian within a harmonic potential. For such a profile, a cut-off frequency can be determined which is characteristic of the stiffness of the trap and the viscous drag of the particle. The viscous drag of a particle can be calculated using Faxens law, including corrections for the proximity of a surface if required. A direct relationship can then be established between the experimentally measured cut-off frequency of the displacement power spectrum and the optical forces in the trap.

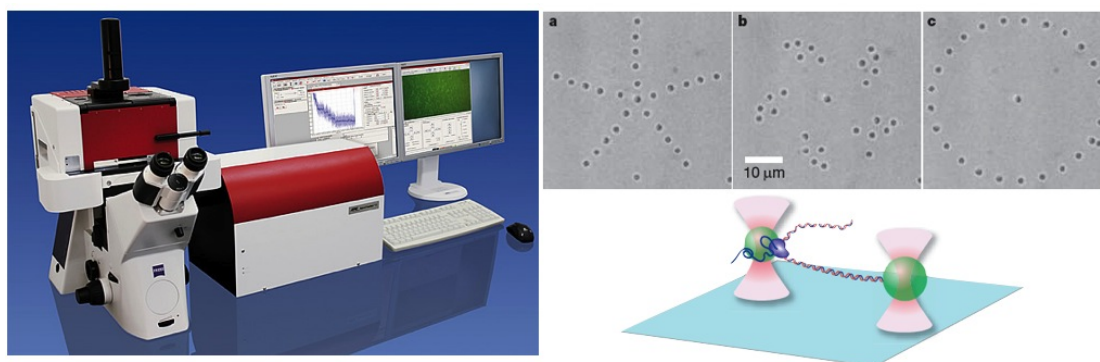


**Figure 3.5:** Commercial optical tweezers and applications. a) A commercial optical tweezers system as produced by JPK ([www.jpk.com](http://www.jpk.com)). b) Example of the complex micro manipulation of several particles in parallel [90]. c) Illustration of a force measurement experiment on a single biomolecule using two optical traps. [95]

### 3.2.3 Applications

Since their beginning in the 1980s, optical tweezers have become a widespread instrument having found applications from physics departments inside universities to medical analysis laboratories. As an illustration of this development, it is now possible to find complete commercial systems, generally based on an inverted microscope architecture allowing for single or holographic multiple beams manipulation. One example of these systems, commercialized by JPK (Germany) can be seen on Figure 3.5, left panel. The parallel control of multiple particles is a complex operation that involves holographic tweezers as illustrated in Figure 3.5 on the top right panel [90].

The applications of optical tweezers cover two main categories:

- the micro manipulation of micron-scale and submicron-scale objects
- the measurement of forces in the range of piconewtons.

The strongest asset of optical tweezers in terms of micro manipulation, on top of intrinsically being a non-contact method, comes from the wide range of particles that can be manipulated. It covers for example inorganic dielectric particles like polymeric probes (microspheres made of polystyrene, PMMA, ...), nano crystals [PEDACI 2011], carbon nanotubes [96], silicon nano wires [97], and quantum dots [98]. It allows for the manipulation of biological organisms like spores, cells, viruses, but also intracellular organelles [99],[100]. A few examples of biological particles falling within the range of manipulation with optical tweezers can be seen in Table 3.1. The approximate dimensions, shape and refractive indices have been mentioned where available. The range of particles that can be manipulated also includes colloidal metallic particles [68].

On top of the fundamental isolation and displacement functions that can be performed, OT

### 3.2. Optical tweezers

Type	Object	Size ( $\mu\text{m}$ )	Shape	Ref. index	Ref.
Bacterium	Escherichia Coli	1 x 3	Rod	1.4	[104]
Bacterium	Mycoplasma Genitalium	0.6 x 0.3	Disk	-	[105]
Bacterium	Staphylococcus Aureus	0.8	Spherical	1.38	[106]
Bacterium	Pseudomonas Aeruginosa	0.6 x 1.5	-	1.38	[106]
Cell organelle	Centriole	0.2	-	-	-
Cell organelle	Lysosome	0.2 - 0.5	Spherical	1.6	[107] [108]
Cell organelle	Mythochondrion	0.5 x 1	Rod	1.4	[109], [108]
Cell organelle	Peroxisome	0.2 - 0.5	-	-	-
Virus	HIV-1	0.1 - 0.2	Spherical	-	[110]
Virus	Influenza	0.1	Spherical	-	[111] [112]
Virus	Mimivirus	0.4	Spherical	-	[113]
Virus	Mosaic Tobacco V.	0.02 x 0.2	Rod	1.57	[84]
Virus	Phage	0.07 - 0.2	-	-	-

**Table 3.1:** Example of biological particles in the range for manipulation with optical tweezers

systems have been used to perform complex operations like the all-optical assembly and manipulation of 3D structures [101]. They are also the basis for advanced biological studies like the investigation of bacterial motility [102]. Finally they have also been used for more fundamental research like hydrodynamic memory effects on the Brownian motion of particles [103]. Further illustrations of the manipulation capabilities of optical tweezers can be found in the review article of Grier [90]. Similarly, a thorough review on the biological application of OT is available in the work of Svoboda and Block [68].

Force measurements based on optical tweezers have been performed according to two methods. In the first method, a polymeric probe is captured in a well-characterized and stabilized trap. As it has been described in the previous section, the statistical properties of the Brownian motion of the trapped particle are related to the local forces perceived by the probe. The monitoring of these statistical properties, for example, the average equilibrium position, the variance of the excursions and power spectrum allows for the detection of any change in the local forces applied to the probe. This principle is often referred to as "photonic force microscopy" [114], [115]. It can be implemented by keeping the probe in a constant position and monitoring changes over time as the environment is modified. The particle can also be scanned using a set of piezo actuators in the same manner as an atomic force microscope. Demonstrated applications cover the measurement of shear flows, local changes in viscosity [116], imaging of polymeric networks [117]. It can also be applied to the measurement of surface roughness [114].

Finally, the second type of measurement makes use of the optical trap to exert a well-defined mechanical force on a specimen while monitoring the response of the latter. This approach has been successfully used in what is now commonly referred to as single molecule spectroscopy

(see Neuman [95] and Mehta [118]). A long biomolecule, for example a DNA or an RNA strand is coupled to a functionalized probe (typically a polystyrene bead) on one end and to a functionalized surface on the other end. The probe is then captured in the optical trap and a well-defined amount of force can be exerted on the biomolecule. The accurate monitoring of the probe position compared to the trap allows to quantify the force involved in the reversible unfolding of single RNA molecule [119]. It also gives access to the measurement of the rupture forces of a DNA strand [120]. A more sensitive and gentle configuration can be obtained by attaching both ends of a single biomolecule to a distinct functionalized probe and using two separate optical traps (see illustration on Figure 3.5, bottom right panel). This led to the observation of the stepping of RNA polymerase along a DNA branch in units of a single base-pair [121].

### 3.3 Nanostructures for optical trapping

The previous sections have revealed the necessity to strongly confine light in order to generate large field gradients and thus large trapping forces. Nevertheless, in the case of "classical" optical tweezers, their reliance on a microscope objective make them intrinsically diffraction-limited. For a dielectric Rayleigh particle, the gradient force components scale down with the cubic power of the diameter (Equations 3.20 and 3.21) while the viscous drag of the immersion liquid against the Brownian motion decrease with the surface (i.e the square power of the diameter) [103]. Consequently, the trapping of very small particles becomes rapidly complex and reaches an intrinsic limitation since the gradient force components only scale up only with the first power of the beam intensity.

On a different aspect, optical manipulation requires large and complex optical systems, which include lasers, well-corrected lenses and positioners. This limits their use to large institutions and universities while the single particle manipulation ability could be very useful in the near-future for on-site diagnostic and analysis methods. As a matter of fact, single particle manipulation and isolation constitute an entire subfield of highly active research domains, namely micro-total-analysis systems ( $\mu$ TAS) and Lab-on-chip systems (LOC).

From these considerations, the impact of a technology that would enable trapping small particles down to the size of a biomolecule with a reduced footprint (and therefore possibly a reduced cost) can be easily anticipated. A large variety of schemes have been proposed in order to progress in these directions. Amongst them, plasmonic nanostructures, dielectric waveguides and optical micro cavities.

#### 3.3.1 Nano-antennas and plasmonic structures

Metallic nanostructures (for example gold or silver colloids) exhibit localized plasmon resonances also referred to as "localized plasmon polaritons (LPPs)" which correspond to collective excitations of their plasma of electrons. This can give rise to a large electric field enhancements



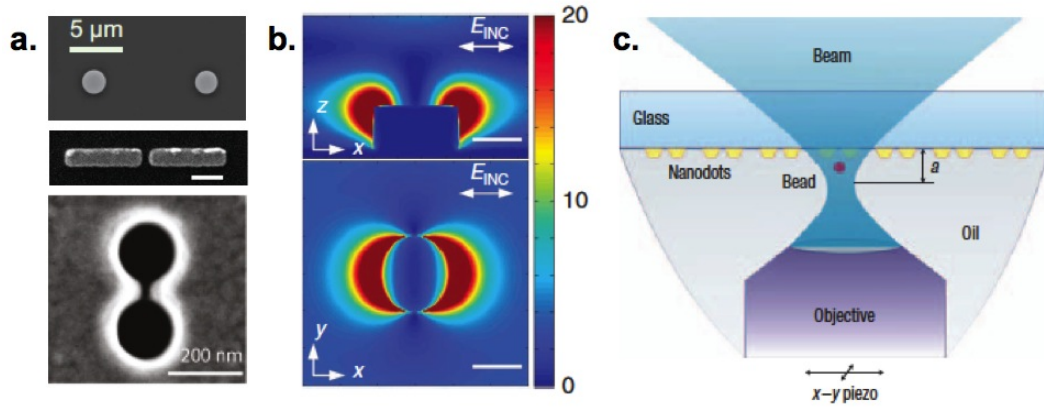


**Figure 3.6:** Examples of plasmonic nanostructures used for near-field optical trapping. *a.* Scanning electron micrograph of gold nanopillars [124], double nano holes [125] and a nano-antenna [28]. *b.* Illustration of the local field enhancement calculated with FDTD for a nanopillar illuminated by a linearly polarized plane wave at normal incidence. Reprint from [126]. *c.* Schematic of the laser excitation of a pair of gold nanopillars in immersion oil. Reprint from [127]

in the vicinity of the nanostructure. It has been suggested as early as 1997 by Novotny [122] that the large field gradients generated in the evanescent near-field of a metallic tip could be used to trap small particles.

The first experimental demonstration of plasmonic trapping was realized only ten years later by Righini *et al* [123] who showed optical trapping of a few micron wide polystyrene particles on a glass substrate patterned with gold nanopillars of the same size. In this work, the surface plasmon resonances were excited by the evanescent field created by the total internal reflection (TIR) of a laser beam passing through a prism which is placed underneath the structures (often referred to as Kretschmann configuration).

The verification of the benefits of near-field trapping with plasmonic nanostructures was shown in the following year by Grigorenko *et al* [127]. Here, a pair of gold nanopillars separated by a small gap exhibited a large field enhancement in the intermediate region when excited with a tightly focused laser beam. In the reported experiment, a 200 nm polystyrene particle was trapped in an optical tweezers beam at 1064 nm and displayed excursions of up to 500 nm from the center of the trap. When the same experiment was repeated in the vicinity of a pair of nanopillars, the equilibrium position of the particle displaced above the small gap, while the residual Brownian motion was quenched to an extent of lesser than  $\approx 50$  nm (Figure 3.6).

Similar approaches were developed as a continuation to this work, by decreasing the size and flattening the shape of the gold nanostructure, towards what is commonly referred to as "nano-antennae" (Figure 3.6). Optical trapping of biological particles (E.Coli) [128] and later, 10 nm gold colloids [28] were demonstrated using this approach. In the mean time, the compatibility of plasmonic trapping with microfluidic integration was demonstrated by Huang *et al* [124]. The latter constituted the first step towards a self-contained, portable, single

particle trapping device.

Finally, the demonstration of optical trapping of dielectric Rayleigh particles was achieved using the plasmon resonance existing in a sub-wavelength hole drilled in a metallic sheet [129]. In the work of Juan *et al* [130], a 310 nm aperture in a 100 nm thick gold layer was used. Trapping times of the order of a few seconds were achieved with sub-milliwatt input powers for 100 nm polystyrene particles. Trapping of 50 nm polystyrene particles was also achieved with lesser than 2 mW excitation power. Another significant step was obtained by Pang and Gordon [125] with the experimental demonstration of the optical trapping of a single protein of bovine serum albumin which is smaller than 4 nm. The structure used here consisted of two contiguous nanoholes forming a 15 nm slot in the intermediate region (see Figure 3.6).

### 3.3.2 Dielectric waveguides

Optical waveguides can exhibit large evanescent fields and therefore can generate strong field gradients in their vicinity. These well understood structures offer another approach to on-chip optical trapping.

The first experimental demonstration of optically trapped particles on the surface of a waveguide was reported by Kawata and Tani [131]. In this work, the authors demonstrated the lateral trapping (half-plane perpendicular to the waveguide) of both metallic and dielectric ((Au, Pt and polystyrene) particles and the propulsion of particles along the direction of the propagating wave. The waveguides consisted of glass based ridge waveguides. The particles were sized from 0.5 to 1  $\mu\text{m}$  for the metallic beads and from 1 to 5  $\mu\text{m}$  for the polystyrene ones. A driving speed of almost 15  $\mu\text{m/s}$  was reported in water for an estimated guided power of 80 mW.

In the following years, similar works were reported the propulsion of small (10 nm) gold colloids in  $K^+$  ion-exchanged glass waveguides [132] and large (10  $\mu\text{m}$ ) polystyrene beads in  $Cs^+$  waveguides [133]. In these works, the dependencies of the particle velocity with power and with the particle diameter were established. The reported velocities typically were in the range of a few  $\mu\text{m/s}$  for small particles to a few tens of  $\mu\text{m/s}$  for the largest ones, while trapping powers typically were from 500 mW to almost 1W. A variety of approaches aimed at larger propelling speeds or smaller powers have been later developed. These cover silicon nitride waveguides [134], optical wires [135], SU8 [136] and  $Ta_2O_5$  waveguides [137]. The later work also extended the waveguide trapping approach to the manipulation of large biological specimen, in this case, red blood cells.

The main drawback of the above approaches lies in the limited overlap existing between the propagating field and the particles on the surface. The consequences are two-fold: the trapping powers required are very large and the range of particles that can be captured is the same as that of standard optical tweezers. To address this issue, Yang *et al* [49] based their approach on a hollow waveguide. The structure can be perceived either as a large ridge

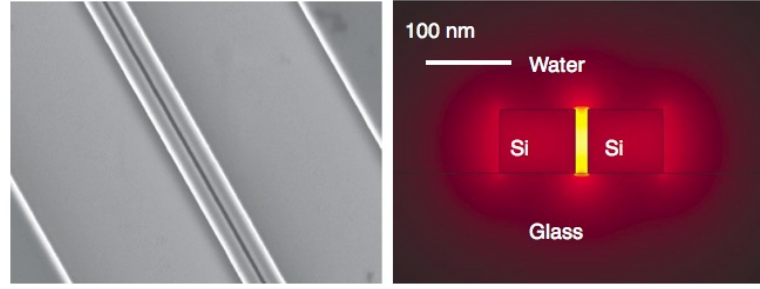


**Figure 3.7:** Slotted waveguide for optical trapping (reprints from [49] ). **Left.** Scanning electron micrograph of a slotted waveguide. The inclined darker line in the center of the image corresponds to the etched slot and corresponds to the largest electric field region. **Right.** Distribution of the electric field (norm) calculated with Finite Elements Method illustrating the field enhancement in the slot.

waveguide with a thin trench etched in the middle (typ. 50 to 100 nm in Si) , or as two sub-wavelength waveguides separated by a small gap and therefore mutually coupled [47]. A scanning electron micrograph of such a slotted waveguide can be seen on Figure 3.7 (left panel). It can be found that this type of structure possesses a propagating mode where a large fraction of the field is located in the interstitial space (Figure 3.7, right panel). This property is inherited from the continuity of the normal component of the displacement field  $\vec{D}$  at the interfaces within the gap. This type of structured permitted the optical trapping and propulsion of 75 nm polystyrene microspheres and DNA strands. The optical powers involved are of the order of a few hundreds of milliwatt.

#### 3.3.3 Dielectric microcavities

The third optical trapping approach based on photonic nanostructures relies on the resonant field confined in a microcavity. The work presented in this thesis forms a part of this framework.

Optical microcavities allow for the confinement of light in volumes that can be comparable to, or smaller than, the wavelength of their excitation field. They can also feature large quality factors associated to long cavity photon lifetimes which implies the storage of energy in the cavity eigenmode. These two combined properties lead to large local field enhancements in their near field which can possibly be used to trap and manipulate particles. The use of microcavity could be perceived as another alternative method to reproduce the performance already achieved using plasmonic nano-antennae or field-enhancing slot waveguides. Nevertheless, microcavities possess an additional interesting feature that is not intrinsic to the other approaches, which is a narrow resonance linewidth. Typical quality factors achievable in silicon microcavities can reach from few hundreds to several millions. This corresponds to linewidths ranging from 1 pm to 1 nm at  $1\mu\text{m}$ . The properties of such sharp linewidths dielectric cavities make them extremely sensitive to the local environment and the variations in permittivity. A particle trapped in the near field of a cavity mode is therefore likely to retroac-

tively impact the optical near-field it is being captured by. This constitutes a major difference with physics of laser beam optical tweezers where the particle does not have an impact on the source of the trapping field [64]. This impact is predicted to become especially noticeable when the "optical volume" of a particle becomes comparable with the mode volume of the cavity. A variety of new effects are thus expected to arise opening the doors for example to simultaneous trapping and sensing of particles, or to particle specific trapping.

Current integrated optical microcavities can be divided into two main families [138]. The first family covers the microring, micro disks and microtoroid-type resonators which confine light through total internal reflection. The nature of the optical modes they support is usually similar to "whispering gallery mode". The second family covers the Bragg resonators and more generally, the photonic crystal cavities (Chapter 2).

Starting with the first family of microcavities, whispering gallery mode (WGM) resonators have received a lot of attention from the optical sensing community. Their geometry, where the eigenmode is located near the outer surface of the nanostructure and possesses an evanescent tail, along with the large quality factors that they display (typ. one million) allowed recently to demonstrate their sensitivity to single viruses and proteins [139] [140]. The demonstration of optical trapping in a whispering gallery mode was achieved in the following year by the same group [141]. The structure consisted of a 100  $\mu\text{m}$  diameter glass microsphere evanescently coupled to a tapered optical fiber. Polystyrene particle down to 300 nm in diameter diluted in  $D_2O_2$  were propelled around an equatorial plane of the sphere for several minutes, with guided power as low as 50  $\mu\text{W}$ . Although this type of structure cannot be considered as an integrated device per say, this pioneering work already justified the hopes placed on resonant optical trapping by achieving trapping at powers two to three orders of magnitude lesser than optical tweezers or waveguides. The authors also performed the first demonstration of simultaneous trapping and sensing by measuring the resonance wavelength shift induced by the trapped particle on the WGM (typically 0.4 nm for a 500 nm polystyrene particle). Following this work, other groups demonstrated technological evolutions of the WGM trap towards integrated CMOS compatible devices. Lin *et al.* achieved resonant trapping of 500 nm polystyrene particles in silicon planar resonators (see Figure 3.8.a) at 5 mW powers [142]. During the same period, two groups independently presented microfluidic-integrated WGM traps in SU8 [143] and silicon nitride [144]. Both these works also demonstrated routing of the particles (1 - 3  $\mu\text{m}$ ) from a conveying ridge waveguide to the ring resonator by adjusting the excitation wavelength.

Concerning the second family of cavities, though theoretically predicted as early as 2006 [148], [5], optical trapping in photonic crystal cavities has received much less attention than the other photonic nanostructure approaches. Planar PhC cavities have been reported to have quality factors comparable with that of WGM resonators, but have the ability to confine light in much smaller volumes. This makes them natural candidates for the low power optical trapping of small particles, but also to evidence particle induced changes on the resonant trapping field. A variety of 2D photonic crystal cavity designs have been proposed and theoretically

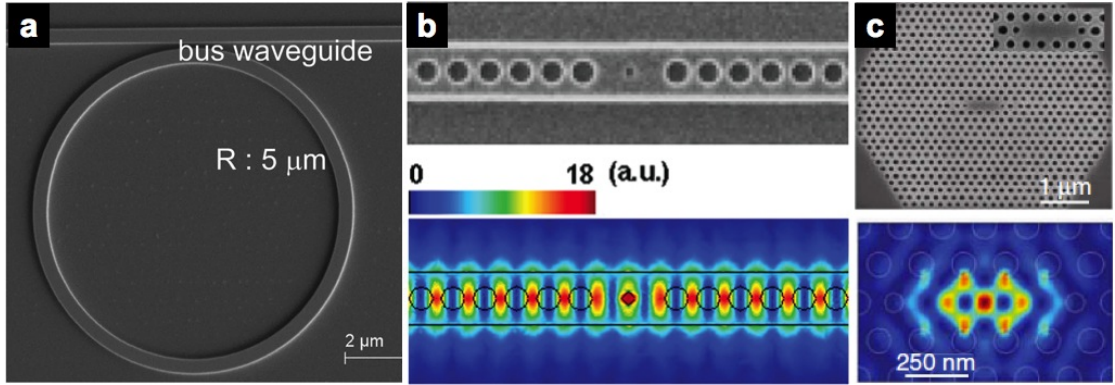


**Figure 3.8:** Examples of microcavities for optical trapping. *a.* A planar ring resonator in silicon as published by Lin et al. [145]. *b.* A 1D "nanobeam" photonic crystal cavity and associated Finite Element Method electric field distribution (reprints from [146]). A modified L3 cavity and associated Finite Element Method electric field distribution as proposed by Van der Sar et al. (reprints from [147])

investigated to attain these goals [148], [5], [145], [147]. The first remarkable demonstration of optical trapping in a periodic structure was achieved in 2010 [149]. In this work, by Mandal and his collaborators demonstrated trapping of Rayleigh polystyrene particles (48 and 62 nm) using a silicon "nanobeam" cavity, which consisted of a one-dimensional Bragg resonator. Further development was demonstrated by the same group with the achievement of optical trapping of 22 nm polystyrene particles and Wilson-disease proteins using a silicon nitride nanobeam [146]. The optical powers coupled to the nanobeam cavities range between 10 and a few tens of milliwatts. More recently, Renaut and collaborators studied the assembly of 1  $\mu\text{m}$  microsphere clusters trapped on a silicon nanobeam cavity in microfluidic environment [150].

It is interesting to note that although originally predicted for 2D structures, experimental demonstration of optical trapping have been only achieved for 1D photonic crystal cavities. Moreover, the observation of particle-induced perturbations of the resonant trapping field is yet to be demonstrated. A theoretical work dedicated to the influence of the trapped particle on the cavity field was recently presented by Hu and collaborators [151]. In this work, the authors use a one dimensional photonic crystal cavity model. On this basis, a perturbative approach allows them to predict the shift in eigenfrequency induced by the presence of a particle within the cavity. One result of their investigation indicates a dependency of the energy coupled to the resonant mode with the position of the trapped particle. As a result of this renormalization, the trapping forces acting on the particle are themselves a function of the position of the particle and the excitation wavelength.



## 4 Experimental set-up

In order to demonstrate the resonant optical trapping of subwavelength particles unambiguously, it is necessary to fulfill a set of complex requirements. It demands the ability of smoothly transporting sub-micrometer sized objects into a 700 nm cavity in a highly fragile silicon membrane. This should be achieved without physical contact while monitoring displacements of the particle that are several times smaller than the highest resolution limit achievable at optical wavelengths. Significant anticipation was necessary in the early stages of this work regarding the main functionalities of the future experimental apparatus. The uncertainty in the trapping powers and trapping times possible in our cavities demands the ability to generate a large number of trapping events. This means ensuring stable and identical working conditions over long periods of time (up to several weeks). Four important functionalities of the experimental set-up were identified during these discussions.

- To optimally and steadily allow excitation and monitoring of the PhC devices under investigation.
- To be able to bring small colloidal dielectric particles in close contact with the photonic devices in a non-invasive manner (Chapter 5).
- To provide high numerical aperture and high contrast imaging of both the devices and the particles.
- To be able to control and accurately monitor nanometre-scale displacements of the particles.

This chapter is organized as follows: In the first section, a general description of the complete apparatus is given. The main architecture is presented along with the motivations and impediments justifying these choices. This overview can be used as a map to guide the reader towards specific parts of the setup which are described in detail. The second section is dedicated to the description of the Fourier imaging set-up which is used in the characterization of PhC structures. In the third section, the fluorescence excitation and imaging of the particles are

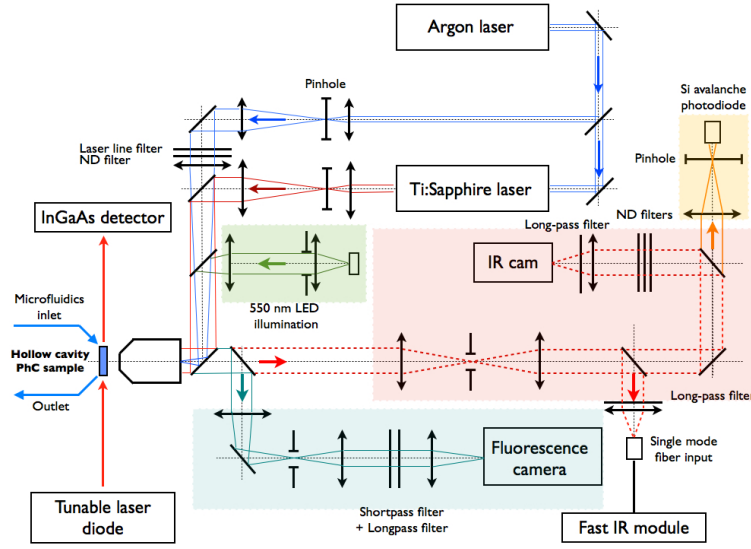


**Figure 4.1:** Schematic of the experimental apparatus illustrating the main functions. The PhC cavities are excited using a tunable laser diode, on the left. Surface scattered light is collected in the Fourier imaging arm (red area). Fluorescence excitation (blue rays) and visible imaging (green area) illuminate the sample which is imaged on the EMCCD camera (blue-green area). Fine displacement of the particle is monitored using the confocal sensor (orange area)

presented. The fourth section is dedicated to the description of the auxiliary optical tweezers that we use in order to generate the trapping events. The monitoring of small displacement of the particles through confocal sensing will be presented in the fifth section. The final part lists possible additions and improvements for the apparatus to push further the understanding of the interaction between the particle and the cavity further.

### 4.1 Overview and general considerations

Figure 4.1 shows a schematic of the experimental apparatus in its current configuration. The main building blocks are highlighted using the following color code: red for the Fourier imaging part, green for visible and fluorescence imaging and orange for the confocal sensor. The large number of functionalities in the apparatus imposes the choice of infinity-corrected architecture. In this case, the optical assembly is such that the sample lies in the object focal plane of the microscope objective which forms an image at infinity. An image of the sample can be formed by introducing a tube lens of any arbitrary (though reasonable) distance. This geometry is particularly well-suited as it allows for the addition of a large number of non-dioptic optical elements (polarizers, beam splitters, prisms) in the optical train with minimal addition of aberrations and hence eliminates the need for any relay optics. The references, numerical apertures, and corrections of the microscope objectives used in the set-up are summarized in Table 4.1.



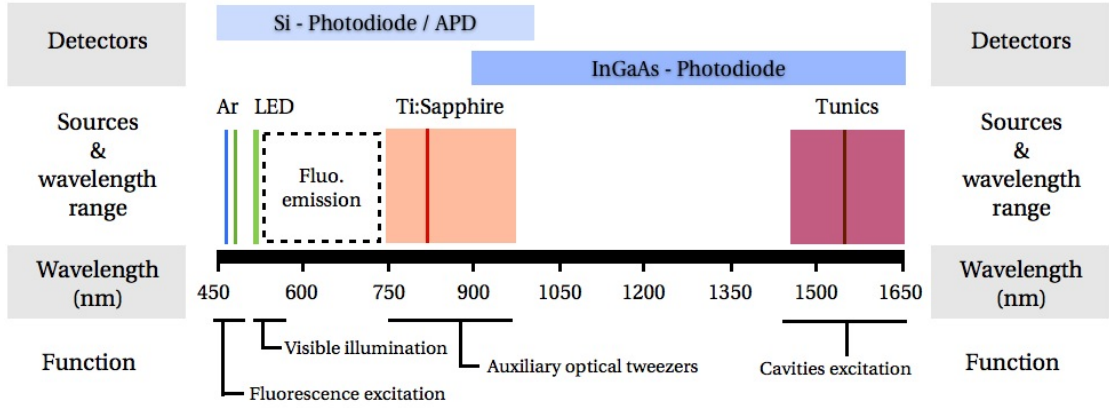


**Figure 4.2:** Overview of the spectral distribution of light sources and detectors. The schematic summarizes the different light sources that are used on the optical trapping experiment, their function and their wavelengths of emission. It also shows the spectral range of the Si and InGaAs detectors that are used. The spectral range that can be filtered out to separate the fluorescence emission of particles is indicated with the dashed rectangle.

The photonic crystal devices are fabricated on a Silicon On Insulator wafer. After the processing is complete, a thick layer (a few hundred micrometers) of silicon remains underneath the photonic crystal membrane and ensures mechanical cohesion of the chip. This comes with two consequences. Firstly, the underlying silicon layer is optically opaque at visible wavelengths because of the absorption in silicon. Therefore, illumination and imaging of the sample can only be performed in an Epi-illumination configuration, whereas a transmitted light illumination configuration could have been interesting for particle tracking [152]. The second consequence is that the large refractive index contrast between water and silicon makes the samples surface highly reflecting ( $R \approx 25\%$ ). This has strong implications in the setting up of fluorescence imaging and optical tweezers.

Figure 4.2 shows the final spectral distribution of the used laser sources used and their tunable wavelength ranges. The shorter wavelengths have been used for fluorescence excitation and visible illumination of the sample. The longer wavelengths are used for the photonic crystal cavities excitation and characterization along with the InGaAs photodiodes. The intermediate spectral region has been dedicated to the auxiliary optical tweezers. It also highlights the range of wavelengths that can be used for fluorescence emission and can be separated using appropriate filters. It can be seen that the 900 nm to 1400 nm window is still available and can be used for additional instruments in the future.

## 4.2 Fourier imaging

The propagation of electromagnetic radiations in a medium is described by the Helmholtz equation which links their spatial and temporal characteristics. The evolution of the spatial frequency of a mode versus its temporal frequency is generally known as the dispersion rela-

## Chapter 4. Experimental set-up

Manuf./Ref.	NA	M	Correction	Immersion	Coverslip (mm)	W.D. (mm)
<b>Spin.-Hoyer</b>	0.25	10x	$\infty$	-	0.16	-
<b>Olympus</b> Plan N	0.4	20x	$\infty$	-	0.17	1.2
<b>Leica</b> PL Fluotar	0.75	100x	$\infty$	-	0	4.7
<b>Lomo</b> APO	1.23	70x	160 mm	Water ( $n = 1.33$ )	0.17	0.07
<b>Leica</b> PL APO	1.4	100x	$\infty$	Oil ( $n = 1.47$ )	0.17	0.09

**Table 4.1:** Characteristics of microscope objectives that are used in the trapping experiment. The numerical aperture (NA), magnification (M), working distance (WD) of the microscope objectives used are summarized. Correction indicates whether the objective is design to work at infinite conjugates, Coverslip indicates the thickness of the coverslip to use for optimized correction. The smaller numerical aperture objectives are used for the coupling of the lensed fibers to the waveguides and the monitoring of the flow of particles. Resonant optical trapping experiments are only performed with the oil immersion objective. The water immersion objective presented here has been used for local infiltration experiments performed in the early stages of this thesis.

tion. The ability to experimentally retrieve the dispersion relation of a wave propagating in a medium is therefore a powerful tool for understanding and developing advanced photonic devices. Over the last few years, the Fourier imaging technique has been developed and optimized by previous collaborators. It allows for the direct experimental recording of dispersion properties of photonic crystal lattices, waveguides and cavities. The extensive description of its principles and main results have been published and can be found in the EPFL thesis of J. Jágerská [33]. The following section constitutes a short summary of the technique.

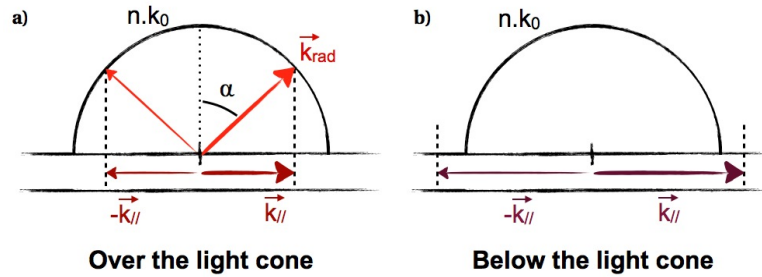


**Figure 4.3:** (a) Coupling of a guided mode to radiative modes above the light line and  $k$ -vector conservation at the waveguide interface. (b) The condition of conservation of the  $k$ -vector cannot be achieved below the light line resulting in the absence of coupling to the radiative continuum.

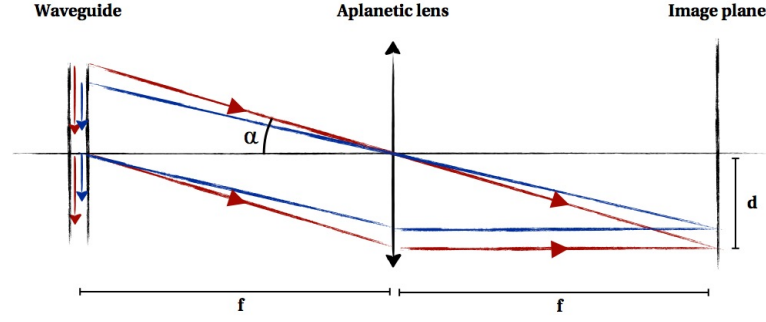


**Figure 4.4:** Principle of the Fourier Imaging technique. Radiative modes are collected using an aplanetic lens at an angle  $\alpha$  that is related to the wave vector of the propagating through the waveguide. The escaping rays are focus in the Fourier plane of the lens at a distance  $d$  from the optical center. The measurement of this distance allows for the retrieving of the original properties of the mode in the photonic structure. The extent of the region where escaping rays are focused in the Fourier plane depend on the numerical aperture of the objective and the dimensions of the investigated photonic structure.

#### 4.2.1 k-vector conservation

A wave propagating in an isotropic medium can be described with the help of a wave vector  $\vec{k}$  that carries the information on the spatial periodicity of the wave and the direction of propagation, and a pulsation  $\omega$  that indicates its temporal frequency. When it reaches the vicinity of a planar interface, the wave can couple to a propagating mode in a second medium provided that the in-plane wave vector  $k_{//}$  be conserved, as illustrated in Figure 4.3. This condition imposes a unique direction of propagation on the wave escaping from the first medium which corresponds to the intersection between an hemisphere of radius  $k = n.k_0$ , where  $n$  is the refractive index of the surrounding medium, and a line perpendicular to the interface located at a distance  $k_{//}$  from the center of the hemisphere. It should be mentioned that this constitutes nothing else but a simple description of Snell-Descartes law of refraction applied to a guided mode. In this case the relationship writes:

$$k_{//} = \|\vec{k}_{//}\| = \sin(\alpha) \cdot \|\vec{k}_{rad}\| = \sin(\alpha) \cdot nk_0 \quad (4.1)$$

By recording the angle at which a radiation of known frequency is leaking out of a waveguide, it is therefore possible to retrieve the in-plane  $k$  vector of the mode, and by tuning the excitation frequency, to reconstruct the dispersion curve. This can be performed optically by collecting the radiation using a lens and positioning an image acquisition system (CCD or CMOS) in the back focal plane of the lens, see Figure 4.4. A well-corrected lens (without field curvature or spherical aberration) focuses a set of rays with similar incoming angle ( $\vec{k}$ ) onto a single spot at a distance  $d$  of the optical axis, such that:

$$d = \left( \frac{2\pi k_{//}}{\lambda_0} \right) \cdot \frac{f}{\sqrt{1 - \left( \frac{2\pi k_{//}}{\lambda_0} \right)^2}} \quad (4.2)$$

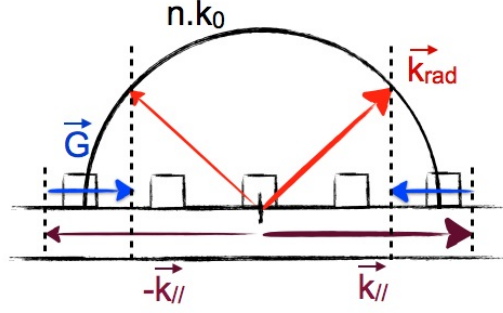


**Figure 4.5:** A periodic modulation of the refractive index near the waveguide permits the folding of a lossless mode above the light cone. The weak modulation acts as a grating with a reciprocal vector  $\vec{G}$ . A fraction of the guided light is in contact with the grating is scattered out of the structure following Laue's equation.

where  $f$  is the back-focal length of the lens,  $\lambda_0 = \frac{2\pi}{k_0}$  is the excitation wavelength in vacuum .

As such, the Fourier Imaging technique is very efficient but is inherently limited to the study of modes propagating above the light cone. It can be understood though that the region above the light cone is not the most interesting region of a waveguide since intrinsically lossy. It is possible to get around this limitation by introducing a small periodic perturbation of the refractive index in the vicinity of the waveguide (Figure 4.5). The periodic perturbation introduced acts as a grating with reciprocal vector  $\vec{G}$ . The multiple scattering induced by the perturbations gives rise to a diffracted wave whose wave-vector satisfies Laue's equation:

$$\vec{k}_{rad} = \vec{k}_{||} + \vec{G} \quad (4.3)$$

From this equation one can understand how the small perturbation "folds" the wave-vector of a guided-mode and creates new conditions for its coupling to radiative modes. These radiative modes can then be collected using the standard Fourier optics configuration and recorded in order to reconstruct the otherwise inaccessible experimental dispersion curve. It is important that the perturbation remains negligible not to alter the properties of the guided mode investigated. This so-called "weak-probe" technique has been developed and described by previous collaborators. [153].

### 4.2.2 Optical arrangement

In practice, the photonic crystal structure is excited by a tunable laser diode at  $1.55 \mu\text{m}$  (Tunics 100S) through a polarization controller and a lensed optical fiber (Nanonics) in an end-fire setup. The light transmitted through the PhC structure is collected through a second lensed fiber and directed towards an InGaAs module. The accurate positioning of the input and output fiber (spot diameter  $2 \mu\text{m} \pm 0.3$ , working distance  $6 \mu\text{m} \pm 1$ ) in front of the coupling ridge waveguides ( $32 \mu\text{m}$  wide and  $0.22 \mu\text{m}$  high) is a critical aspect of the experiment. It is

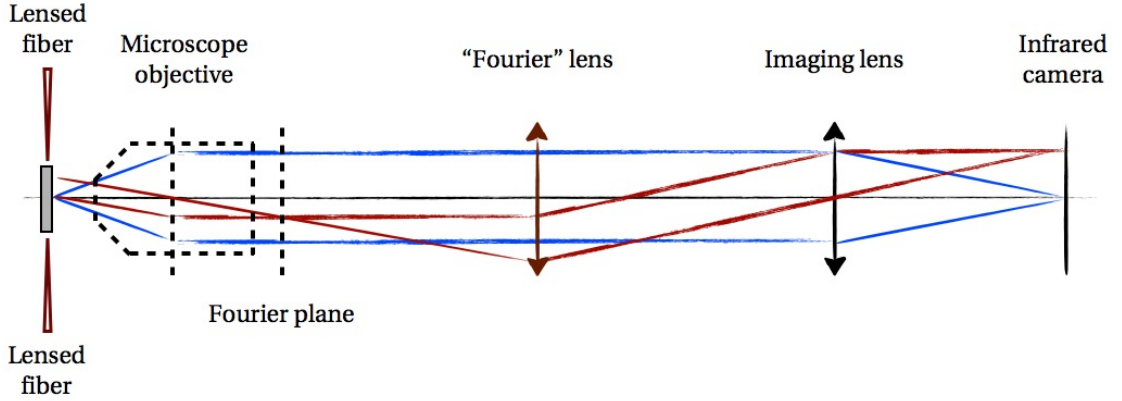


**Figure 4.6:** Schematic of the Fourier Imaging optical setup. The high numerical aperture objective realizes the optical Fourier transform of the surface scattered light in its back-focal plane. The Fourier lens / Imaging lens system relays this image onto an infrared camera where it is recorded. Alternatively, the Fourier lens can be removed and an image of the light scattering centers can be recorded.

ensured with the aid of three-stages Luminos positioners and fiber-supporting mechanics. The light radiating out of the device is collected through a high numerical aperture microscope objective and directed toward an infrared camera (SU320 - Sensor Unlimited, Polytec Inc). The optical arrangement is illustrated in Figure 4.6. In the described configuration the addition or removal of the central lens (in brown color) allows for the convenient switching between "real" and "Fourier" imaging. In the Fourier imaging configuration (dark red rays) an image of the exit pupil of the microscope objective is formed onto the infrared camera. In the real imaging configuration (blue rays, central lens removed) an image of the photonic structure is formed onto the camera showing the regions of light scattering. A complete Labview routine has been developed by previous collaborators that can simultaneously reconstruct the experimental dispersion curve of a structure and monitor the associated transmission.

#### 4.2.3 Example of characterization of a photonic crystal structure

This paragraph shows the characterization of a coupled-cavity waveguide (CCW) using the Fourier Imaging technique for illustration of its capabilities. A CCW can be seen as a succession of single PhC cavities positioned next to each other. When the first cavity of the chain is excited, the evanescent field of the confined mode can overlap with the neighboring cavity and couple to its eigenmode. The hybridization of each individual cavity mode due to the presence of the identical neighboring cavities leads to the appearance of a propagating CCW mode. The latter can achieve very slow group velocity and CCWs have been widely studied as possible candidates for optical delay lines [154], [36].

Figure 4.7 shows a scanning-electron micrograph (left) of a coupled-cavity waveguide designed and fabricated in order to study the influence of the W1 waveguide as a building-block for these cavities. A single cavity consists of 3 missing holes in a triangular lattice

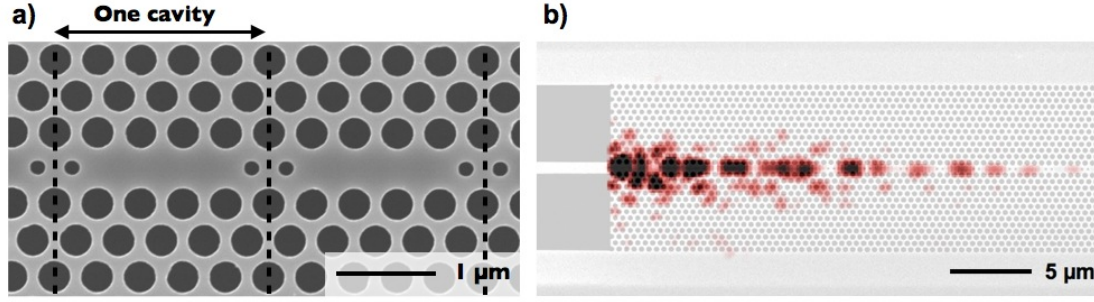


**Figure 4.7:** (a) SEM micrograph of a coupled-cavity waveguide. The dashed lines indicate the dimension of one unit cavity. The total structure composes of up to 50 coupled cavities. (b) The superimposition of the near infrared image recording the light that is scattered out of the CCW when excited in its propagation bandwidth and the lower magnification SEM image.

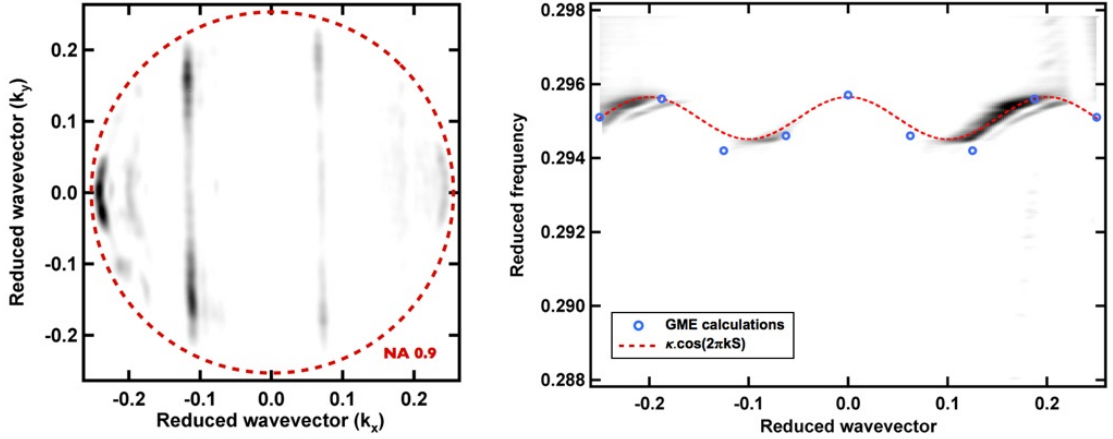
( $a = 440 \text{ nm}$ ,  $f = 38.5\%$ ) and two smaller side holes (140 nm in the diameter compared to 310nm for lattice holes). The total length of one cavity "S" is five in lattice constant unit ( $a$ ). The picture on the right of figure 4.7 shows the superimposition of the field scattered out of the photonic crystal structure over a SEM micrograph of smaller magnification. To obtain the "real" image of the scattered field, the central "Fourier" lens has been removed.

Figure 4.8 shows the image recorded in the infrared camera plane in the presence of the Fourier lens (left). Two vertical lines, associated to two propagating modes of reduced wave vectors  $k_1$  and  $k_2$  can be observed. The red dashed circle represents the maximum value for  $\|\vec{k}\|$  that can be recorded given the finite numerical aperture of the objective. On the right is the reconstruction of the dispersion curve for the CCW. It is obtained by changing step-by-step the excitation wavelength of the tunable laser diode, recording for each step the far-field pattern and summing the pixels in columns. The left axis represents the reduced energy, or in other words, the excitation wavelength  $u = \frac{\omega a}{2\pi c} = \frac{va}{c} = \frac{a}{\lambda_0}$ . The bottom axis corresponds to the reduced wave-vector  $\frac{ka}{2\pi}$ . The dark regions correspond to the recording of light being scattered at a given excitation wavelength and propagating with the associated reduced wavevector. Guided Mode Expansion (GME) calculations performed with an in-house tool [32] are superimposed on the recording showing the close agreement between experimentally measured and theoretically expected values. The red dashed curve corresponds to a tentative fit based on a tight-binding approach [31]. The central reduced frequency and amplitude  $\kappa$  are retrieved from the experimental data,  $k$  corresponds to the reduced wave-vector,  $S$  is the size of the super-cell in lattice constant units. Note that the periodic nature of the CCW here makes it possible to record the dispersion of the mode below the light cone without having to use an external weak probe.

### 4.3 Fluorescence excitation and imaging

A major challenge when studying the interaction of an electromagnetic field with individual submicron particles is the ability to observe and track the displacements of the particles.





**Figure 4.8:** Experimental recording of the dispersion properties of a CCW. (a) An image that is recorded on the NIR camera in the Fourier imaging mode. The vertical lines indicate the existence of two counter propagating modes in the CCW and gives access to their wave vector: The forward propagating mode is observed for the darkest line on the left. The negative value for the  $k$ -vector is due to the negative magnification of the complete imaging path. (b) The experimental dispersion curve for the CCW structure after reconstruction. The dark lines indicate the shape of the dispersion curve and the amount of light coupling to the mode for a given  $(k,u)$  couple. The blue markers superimposed on the experimental curve correspond to Guided Mode Expansion calculations performed with an internally developed routine using the SEM parameters of the structure investigated. It illustrates the good understanding, accurate prediction and fabrication capabilities of the laboratory. The red dashed line corresponds to a sine fit as predicted by the tight-binding model and using only *ab-initio* parameters apart from the coupling constant  $\kappa$  which is experimentally measured.

This requires the use of imaging techniques capable of providing good contrast between the particles and the background over a large field of view. Standard epi-illumination and imaging configurations are very efficient in this regard for dielectric objects in air down to a few hundred nanometers at visible wavelengths. It is non-trivial to obtain good contrast images when the particles under investigation are in suspension in an aqueous medium. In this case, the refractive index contrast of the particles with the aqueous medium can be very small (down to  $\approx 0.1$  RIU for biological objects or polymer particles) and the use of contrast-enhancing techniques like Polarized Light or Dark Field imaging is required.

A possible solution to this issue is the use of fluorescence imaging. In this case, the particles under investigation should either fluoresce naturally or be marked with fluorescent molecules (fluorophores). When they are excited with a suitable bright light source, typically a laser, fluorophores absorb incoming photons of high energy and re-emit photons of lower energy as they relax to their original state. This mechanism is illustrated in Figure 4.9. The fluorescence emission mechanism involves various non-radiative relaxation processes and the absorption and emission spectra are usually very large, covering hundreds of nanometers. Similarly, the peak excitation and emission wavelength can be separated by up to several tens of nanometers. Table 4.2 records the excitation and emission peak wavelengths for some common fluorescent markers commercially available.

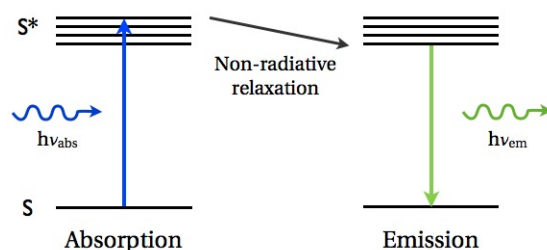


**Figure 4.9:** Schematic of absorption and fluorescence emission mechanism. A high energy photon (blue) is absorbed by the fluorescent molecule and drives it from a non-excited state (S) to an excited state (S\*). Non-radiative relaxation mechanism lead the molecule to a lower energy excited state before it finally emits a lower energy photon (green) and return to the non-excited state.

The light emitted by the fluorophores can be collected through a microscope objective and imaged onto a camera. In this manner, particles with a size smaller than the resolution limit appear as point-like individual emitters and can be imaged with high contrast over non-fluorescent backgrounds. This naturally requires that the quantity of light emission is sufficient and that the weak fluorescent emission is discriminated from the strong excitation radiation. This can be achieved easily by carefully choosing a combination of excitation laser, fluorescent markers and dichroic filters.

#### 4.3.1 Particles, fluorescent markers and laser excitation

As it can be seen in Table 4.2, it is possible to find fluorophores with excitation peaks ranging from UV to NIR wavelength. Conveniently, a large number of them can be excited using standard Argon (Ar, emission lines at 457, 488 and 514 nm) lasers or doubled Nd:YAG Diode Pumped Solid State (DPSS, emission line at 532 nm) lasers. The advantage here is that even fluorophores with large spectral separations between the excitation and emission peaks will fall into the absorption range of silicon array detectors like CCD and CMOS. Having a powerful Ar laser in the lab (Innova 90, Coherent Inc.) emitting simultaneously at 488 and 514 nm allowed us to broaden the range of fluorophores available for our experiment. It is also very interesting to possess two separate excitation lines since sub wavelength particles cannot

Fluorescent dye	Absorption peak(s) (nm)	Emission peak (nm)	Spectral region
Alexa Fluor 350	345	440	UV
R-Phycoerythrin	497 and 565	575	Yellow
Fluorescein	498	517	Green
Allophycocyanin	630 and 650	660	Red
APC-Cy7	650 and 730	785	NIR

**Table 4.2:** Absorption and emission characteristics of some common fluorescent molecules. The wavelengths of the main absorption peaks, the main emission peak and the corresponding "color" are recorded. Source: [155] and [156].



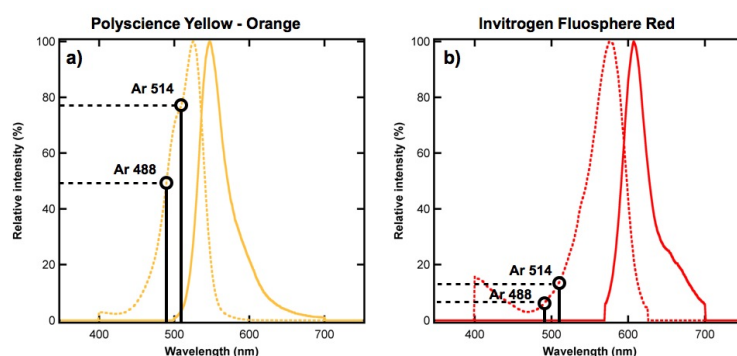


**Figure 4.10:** Excitation efficiency of Invitrogen Fluosphere Red (a) and Polysciences Yellow-Orange (b) using one or two lines of an Argon laser. These two markers have been chosen for the dyeing of the polymer beads used in the resonant trapping experiments.

be distinguished by their diameter on the recorded images. Two types of particles with two slightly different sizes can be distinguished though if their fluorescent markers are excited by different lines and one of them is modulated at low frequency (below the exposure time of the CCD) for example. This is of special importance as we intend to demonstrate the sharp size specificity of our resonant trapping devices.

Polymer beads like latex or polystyrene nanospheres are well-known substitutes to biological entities which are generally cumbersome during the early stages of the development of novel optical trapping schemes. It is possible to purchase highly concentrated suspensions of the beads which are used for example for the calibration of flow-cytometers. These beads come with reference fluorescent markers diluted inside the polymer matrix. Taking into account the need for an auxiliary optical tweezer in the far red or NIR region that sets a higher limit to the maximum peak emission wavelength, two types of markers have been retained. Figure 4.10 shows the absorption (dashed lines) and emission spectra (solid lines) of Polyscience Yellow-Orange (PYO) and Invitrogen Fluosphere Red (IFR) markers along with the position of the two Ar emission lines. On this figure it appears that PYO is approximately 7 times more sensitive to the 514 nm Ar line. High performance (OD 4 or more) off-the-shelf dichroic filters, required to filter out the fluorescence emission from the excitation radiation are typically available in steps of 25 to 50 nm for the cut-off frequency with a tolerance of approximately 1% (5 nm for a 500 nm specification). The typical cut-off slope is of the order of 1 to 3% (another 5 to 10 nm of lower optical density for a 500 nm cut-off). An efficient rejection of the 514 nm Ar line can only be obtained with a high pass filter with a cut-off frequency roughly 15 nm higher, that is 530 nm. Two filters have been acquired for this purpose. One is the 84–738 filter from Edmund optics (cut-off 525 nm, cut-off slope 1%, OD > 4), the second one is the FEL550 from Thorlabs (cut-off 550 nm, cut-off slope 3%, OD > 4). Qualitative analysis of the fluorescence imaging of particles marked with PYO has proven the rejection capability of our 525 nm filter to be insufficient and imposes to work with the 550 nm filter. Unfortunately this filter turns to also reject half of the fluorescent emission of PYO markers. Conversely the IFR marker, though less efficiently pumped with the argon lines is perfectly adapted to the imaging

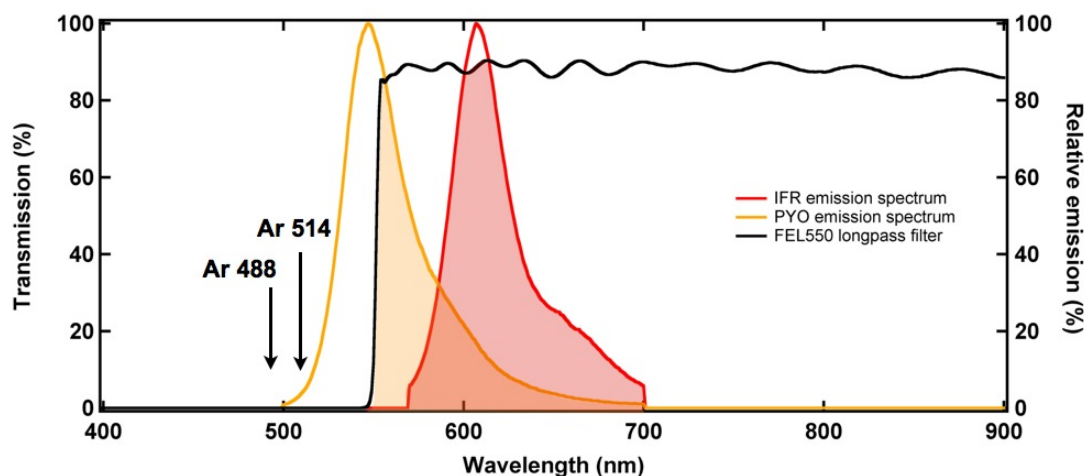


**Figure 4.11:** Transmission properties of a long-pass dichroic filter used for fluorescence excitation separation. The black curve shows the rejection (OD 4 below 550 nm) and the transmission of the FEL 550 filter from Thorlabs. The emission spectra of IFR and PYO are superimposed on the transmission data, showing the rejection of half of the PYO emission but almost complete transmission of the IFR one. Source: [157]

through a 550 nm high pass filter since all the fluorescence emission occurs after 570 nm. This justifies the utilization of both this markers.

### 4.3.2 Optical arrangements

The fluorescence/visible imaging block comprises of three parts: the fluorescence excitation arm, the visible illumination arm that can be dimmed or switched off to maximize the contrast of fluorescent particles and finally the imaging arm. The different beams are directed into and extracted out of the central microscope objective using 50/50 pellicle beamsplitters.

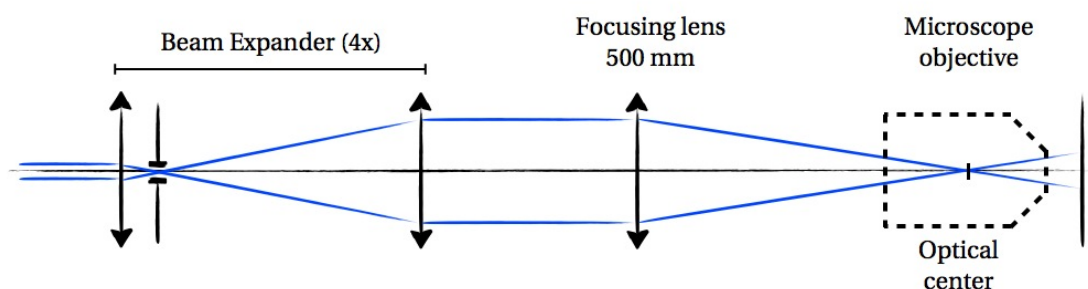


**Figure 4.12:** Optical arrangement of the fluorescence excitation path. The beam of an Argon laser is spatially filtered and expanded. It is finally loosely focused onto the optical center of the microscope objective. This configuration allows for a maximized fluorescence excitation area.

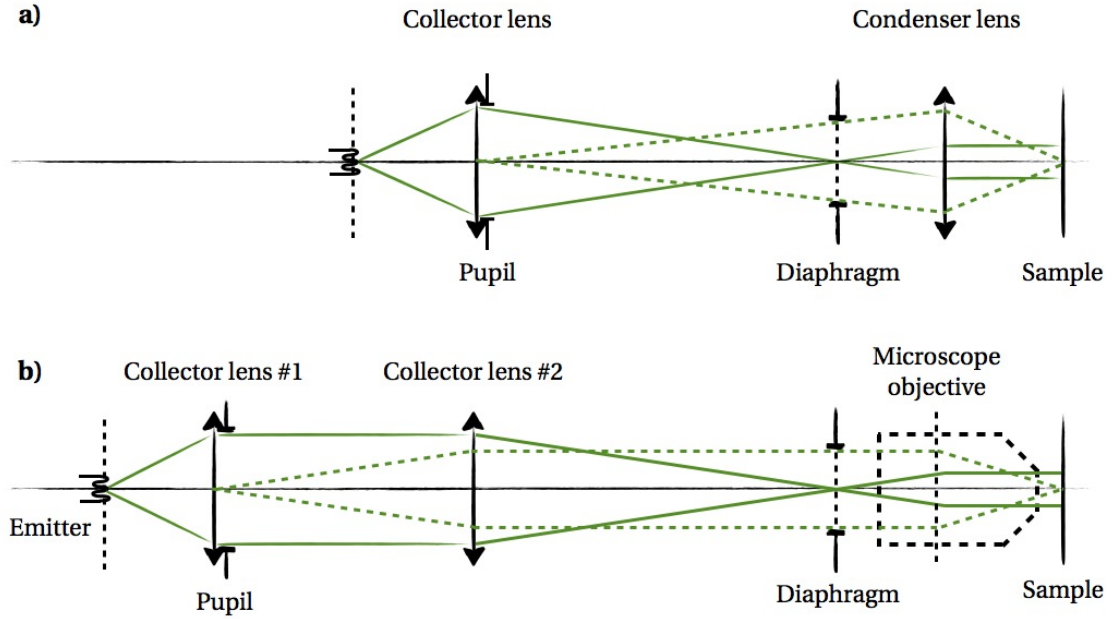


**Figure 4.13:** Optical arrangement of the visible illumination. (a) The optical configuration of a typical Köhler illumination using a collector lens, a condenser lens and a diaphragm controlling the amount of light and the degree of homogeneity of the illumination. (b) Configuration of the modified Köhler illumination implemented in the case of the trapping bench. This configuration is motivated by the length of the optical train imposed by the large number of instruments on the bench and the use of the microscope objective as the condenser lens.

Within the fluorescence illumination path, the Argon beam is first expanded using a Keplerian beam expander. The quality of the beam is controlled with the help of a pinhole located at the intermediate focus. The expanded collimated beam is then focused near the optical center of the microscope objective using a long focal length lens. The microscope objective has therefore little influence on the diverging beam. This configuration is advantageous because it permits to obtain uniform fluorescence excitation over a large area. The extent of this area is limited by the divergence  $\alpha$  of the incoming beam (diameter  $D$  of the collimated beam and focal length  $f$  of the last lens). Here  $D = 30$  mm and  $f = 500$  mm leading to a divergence angle  $\alpha = \arctan(\frac{D}{2f}) = 0.03$  rad = 1.7 deg at the entrance of the objective. In reality, the large optical thickness of a microscope objective causes the divergence of the fluo-excitation beam to be smaller than in principle. The fluorescence excitation field in the case of the oil immersion objective is a disk of  $45 \mu\text{m}$ . The power of the Ar beam entering the objective is  $40 \mu\text{W}$ . The average power density for the fluorescence excitation can be calculated to be of the order of  $6 \text{ nW}/\mu\text{m}^2$ . No photobleaching of the particles has been observed at these powers. One drawback of this configuration is that the power density then depends on the front-focal length (FFL) of the objective and different densities of excitation are produced whenever the objective is changed. Considering a uniform fluorescent excitation, exchanging a microscope objective with another with FFL that is twice as long will cause a reduction in power density by a factor 4.

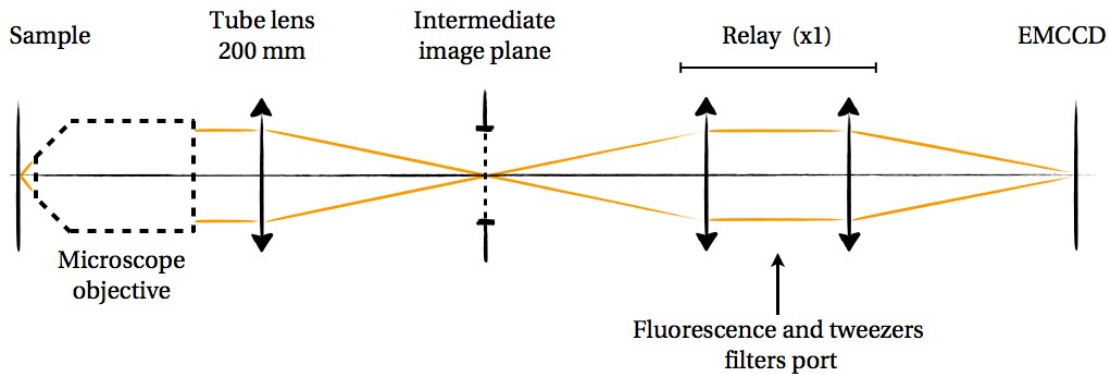


**Figure 4.14:** Optical arrangement of the visible imaging. It corresponds to the standard optical path of an infinity-corrected microscope with 200 mm reference length, with the introduction of an extra relay system. The latter gives a lot of freedom in the choice of the total magnification of the imaging path without affecting other instruments. It also provides a port for the insertion of fluorescence and optical tweezer rejection filters.

The design of the visible illumination block is probably the less demanding part of the optical bench. The main goal is to provide good uniformity illumination over the full-field of observation. The Köhler illumination is a typical architecture for this purpose as illustrated in Figure 4.13. It makes use of a collector lens that gathers the light from the source, an aperture stop, an intermediate diaphragm and a condenser lens that makes an image of the aperture stop on the sample [74]. The main constraints in this case come from the epi-illumination architecture, which imposes the microscope objective to play the role of the condenser lens, and the length of the optical train imposed by the large number of instruments to be combined. A modified version of Köhler's illumination described in Figure 4.13 has been assembled, where an extra lens is inserted between the first collector (CL1) and condenser lenses. The role of this lens is to make an image of the aperture stop (pupil) that is not at a finite conjugate like in the standard Köhler illumination but at infinity. The infinity-corrected microscope objective then forms a real image of the aperture stop in its focal plane illuminating the sample uniformly. The main advantage here is that there can be a very long distance between the second lens (CL2) and the microscope objective, by choosing CL2 with a long focal length. This gives a lot of freedom in the position and assembly of the illumination block. Conversely, the main drawback comes from the extra light losses associated with rays going through the second collector lens but missing the diaphragm aperture or the entrance pupil of the microscope objective. This can give rise to apodization effects and a smaller effective aperture stop.

The visible and fluorescence imaging arm is composed of two groups of lenses. The first group comprises of the microscope objective and an achromatic tube lens of 200 mm focal length. This group is based on the standard optical arrangement of Leica microscopes. The 200 mm tube lens forms a real image in its focal plane whose magnification corresponds to that of the indicated value on the microscope objective. On the contrary, a correction factor has to be

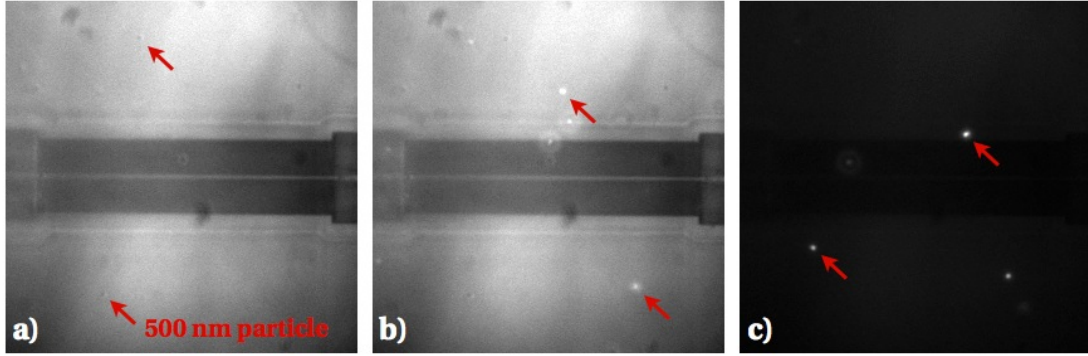


**Figure 4.15:** Imaging of 500 nm polystyrene particles with and without fluorescence. (a) An image of a photonic crystal structure and 500 nm beads recorded on the camera with visible illumination but no fluorescence excitation. Red arrows indicate the position of particles. (b) A similar image recorded with visible imaging and fluorescence excitation. (c) Another similar image recorded with dimmed visible illumination and fluorescence excitation. These images show the clear contrast enhancement obtained when going from pure visible imaging to pure fluorescent imaging.

applied according to the reference focal length, see Table 4.3. The second lens group serves as a relay and allows for extra magnification or demagnification of the final image by simply replacing the final lens. A variable aperture diaphragm is positioned in the intermediate image plane and serves two main purposes: stray light rejection and focus control. Separately, the infinite conjugate region between the two lenses of the second group is well adapted to position fluorescence excitation and optical tweezer rejection filters.

The theoretical resolution limit for the imaging path is set by the numerical aperture (NA) of the microscope objective when working at appropriate (finite or infinite) conjugates, with the appropriate coverslip thickness (if any) and in absence of any aberrating surfaces. Following Rayleigh's criterion for the resolving power of an image forming instrument of circular aperture and incoherent illumination [74], the theoretical resolution limit is given by:

$$r = 0.61 \frac{\lambda_0}{NA} \quad (4.4)$$

This quantity corresponds to the first minimum of the Airy distribution of light that can be observed in the object plane of a microscope objective of circular aperture illuminated by a bright point-like object located at infinity. For a very small fluorescent particle (typ. <100nm), the size of the first Airy disk observed in the image plane of the imaging path is  $M.r$  where  $M$  is the magnification of the objective/tube lens system (Figure 4.18) .

Table 4.4 summarizes the theoretical (minimum) values for the resolution limit as seen in the object space and Airy disk diameters, as seen in the image space, for different numerical apertures and total magnification. A discussion of the influence of the coverslip correction and deviation from its design thickness will be provided in Chapter 5.

Manufacturer	Reference focal length (mm)	Correction factor to apply
Leica	200	1
Linos	200	1
Mitutoyo	200	1
Nachet	200	1
Nikon	200	1
Olympus	180	0.9
Zeiss	165	0.825

**Table 4.3:** Record of reference tube lens length for most common microscope objective manufacturers. This table shows how most of the manufacturers decided to adopt the same tube lens reference except Olympus and Zeiss. The experimental test bench makes use of a 200 mm tube lens and in most cases the total magnification can be obtained by directly reading the magnification specified on the objective and multiply it by the relay magnification. In the case of Zeiss and Olympus an extra correction factor must be applied.

All units $\mu\text{m}$	NA 0.25	NA 0.4	NA 0.75	NA 0.9	NA 1.23	NA 1.4
Resolution limit (object space)	1.34	0.84	0.45	0.37	0.27	0.24
Airy disk diameter (image space)						
M=50x	134	84	45	37	27	24
M=100x	268	168	90	74	54	48
M=150x	402	250	134	110	80	72

**Table 4.4:** Tabulated values of the resolution limit for various numerical aperture objectives. The first line indicates the order of magnitude of the smallest object that can be distinguished in the object plane assuming good contrast with the immersion medium. The following lines indicate the apparent size of this object when recorded in the image plane of the imaging path for different magnification values.

### 4.3.3 Detection and choice of camera

The choice of the detector is critical when it comes to the imaging the fluorescence of small particles. The sensitivity and low background noise of the device are of considerable importance due to the low light levels involved. Nevertheless, read-out speeds must also be taken into account if the application requires particle tracking. The maximum speed at which an object can be tracked depends on the minimum exposure required to obtain an image with acceptable contrast and the maximum speed of the read-out. This tracking speed value can be improved by reducing the size of the matrix from the full-sensor down to a region of interest.

Current Charge-Coupled Devices (CCDs) and Complementary Metal-Oxide Semiconductor (CMOS) technologies were investigated before narrowing down to the appropriate choice. Current state of the art in CCD and CMOS sensors typically achieve Quantum Efficiencies (QE) of the order of 70 % (with the notable exception of back-thinned CCDs which can achieve



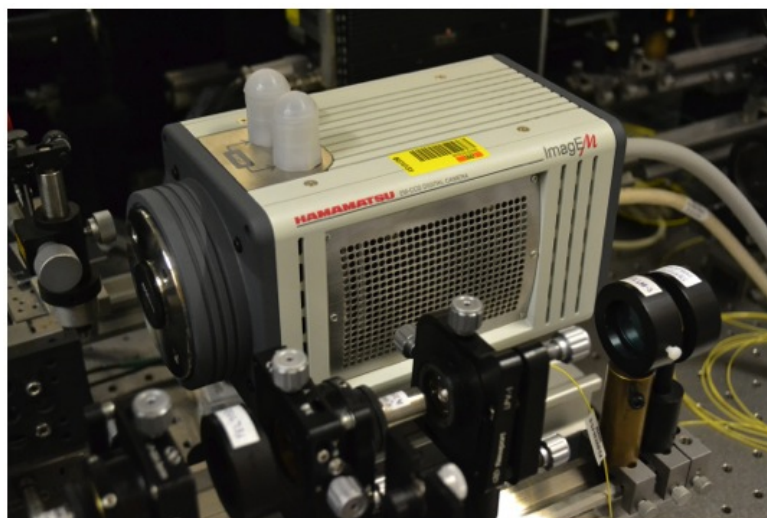


**Figure 4.16:** Picture of EMCCD camera Hamamatsu ImagEM 512 on the optical trapping bench. The EMCCD detector can be cooled either with a forced air mechanism (side grid) or with a water cooling system (white ports on the top). In our case only the forced-air system reaching up to  $-75^{\circ}\text{C}$  is used.

up to 90 % QE). Therefore, the exposure times required to obtain a image of a particle with a good contrast will be of the same order for both technologies. It is known that CCDs are better performing than their CMOS counterparts in terms of noise levels. This is inherent to the architecture of the CMOS sensor where each pixel possesses a set of transistors along with the photo-sensing region, providing on-site photo-current to photo-voltage conversion and amplification. The additional noise comes predominantly in the form of dark current, reset noise and  $1/f$  noise. Conversely, the peculiar architecture of CMOS pixels makes the read-out much faster and the setting-up of Regions Of Interest (ROI) easier than in CCD devices, allowing for greater frame rates. The limited ROI capability of CCD comes from the line-by-line read-out and amplification of CCD sensors.

While both technologies are efficient in tracking 500 nm fluorescent particles, the detection of 100 nm particles in real experimental conditions is a more complicated challenge. Indeed, during fabrication, fluorophores are diluted in the matrix of the polymer (here polystyrene). For an equal concentration in fluomarker, the amount of fluorophores therefore scales with the cubic power of the diameter. Hence 100 nm particles are expected to be approximately 125 times less bright than 500 nm particles. For this reason it has been decided to acquire an Electron-Multiplying (EM) CCD camera (C9100-13 ImagEM 512, Hamamatsu) which possesses a back-thinned CCD sensor and a  $-75^{\circ}\text{C}$  air cooler. On top of having a higher sensitivity than standard sensor, the camera possesses a high-voltage register that provides gain through impact ionization of the accelerated electrons. This process is somewhat similar to the avalanche effect in Avalanche Photodiodes (APD) but occurs outside of the photosensitive area. The EMCCD gain can be selected from 0 to its maximum value through a computer graphical interface.

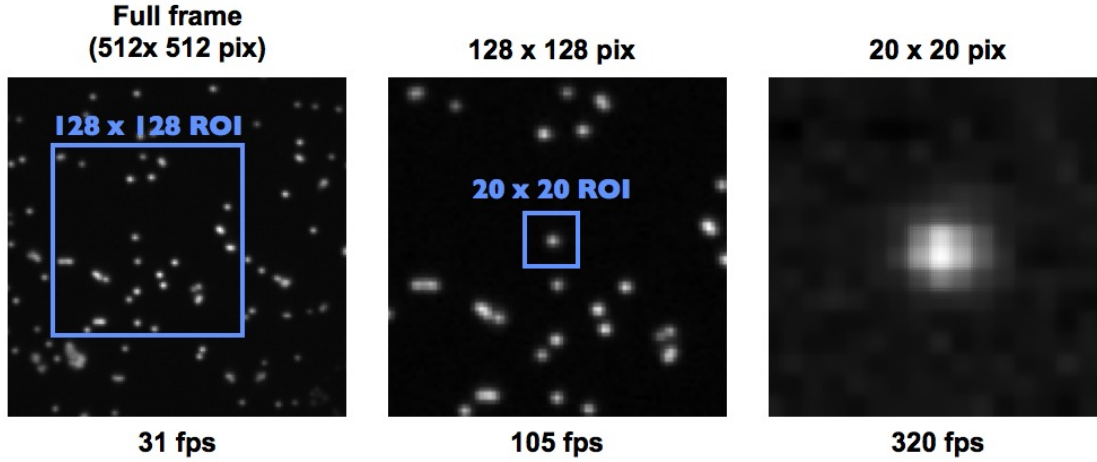


**Figure 4.17:** Snapshots showing image acquisitions of fluorescent polystyrene particles with a constant acquisition time of 3 ms. Decreasing the size of the ROI allows increasing the frame rate from 31 fps (left) to 105 (center) and 302 fps (right). The dynamic of the camera for these images covers approximately 3000 grey levels (out of 65536 possible)

The camera stills suffers from two main drawbacks. First the pixel size for EMCCD cameras is large (16  $\mu\text{m}$  in this case) which improves the sensitivity through larger collecting area but artificially decreases the resolution in the image plane. Second, as mentioned earlier, CCD-type sensors are limited in their possibility to use ROIs. In this case, the minimum ROI corresponds to a 16 lines regions and allows for a 315 fps frame rate with no pixel binning and assuming good lightening conditions. Figure 4.17 shows the imaging of 500 nm polystyrene particles with a 3 ms exposure time and no EMCCD gain. The frame rate is gradually increased from 31 fps (full-frame) to 302 fps by reducing the ROI.

## 4.4 Auxiliary optical tweezers

Submicron particles undergo Brownian motion when they are brought in suspension in the vicinity of a PhC cavity. If the suspension is steady (no macroscopic flow) the particles displace randomly above the silicon slab. It can take very large amounts of time for a 100 to 500 nm particle to randomly enter the 700 nm hole of the cavity, even with large concentrations of particles. Standard optical tweezers (OT) can be used to address this issue by either pushing or dragging isolated particles into the cavity.

### 4.4.1 Optical arrangement

The optical train for a single OT beam is straightforward. A laser beam is first expanded using a Keplerian beam expander (see Figure 4.19). The magnification of the telescope is 2. The collimated beam is then directed towards the high numerical aperture objective where it slightly overfills the entrance pupil. The beam is finally focused onto the sample



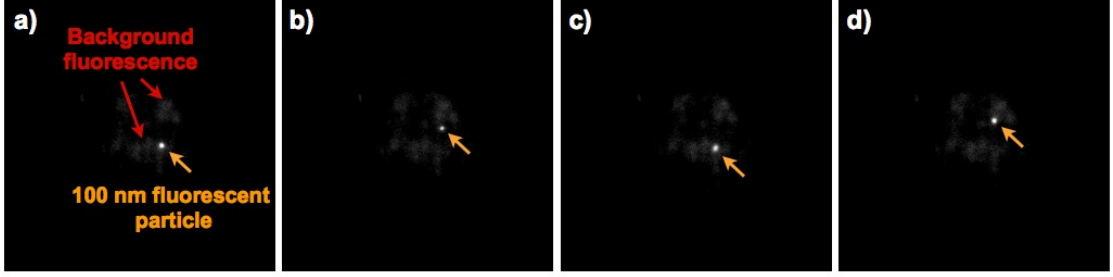


**Figure 4.18:** Tracking of a 100 nm fluorescent particle in Brownian motion using the EMCCD camera. Figures (a), (b), (c) and (d) show snapshots acquired with the EMCCD camera while observing a 100 nm bead in Brownian motion inside a microfluidic channel with no EMCCD gain. Dynamic contrast levels of the camera have been adjusted in order to improve the visibility of the particle and cover approximately 1000 grey levels. The yellow arrow points at the fluorescent particle. The red arrow shows a faint cloud-like structure with correspond to some background fluorescence in the channel.

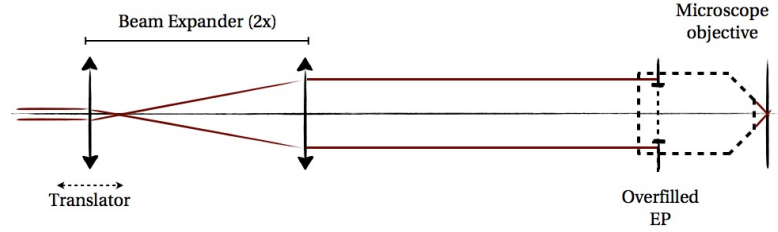


**Figure 4.19:** Optical arrangement of the auxiliary optical tweezers. The OT beam is first expanded in order to slightly overfill the Entrance Pupil (EP) of the microscope objective. The beam is then focused in the plane of the sample and can be displaced by gently moving the objective off the optical axis using piezo positioners.

plane. Fine adjustment of the beam waist position along the optical axis is obtained by translating the first lens of the telescope using an electronically driven micrometre translation stage. The optical set-up is such that the OT beam is always at the center of the microscope objective field. Displacement of the OT beam is obtained by translating the microscope objective perpendicularly to the optical axis using piezoelectric actuators. This configuration has provided acceptable working conditions during the time of this thesis but might need improvement (see last section of this chapter) if a constant and accurately optimized optical quality is required as in the case of the confocal sensor.

#### 4.4.2 Trapping wavelength

The OT beam requires high optical intensities, of the order of several tens of milliwatts and focused on wavelength-scale regions, which is in stark contrast to the fluorescence excitation beam. This leads to large local power densities which might perturb the optical properties of the neighboring photonic crystal cavities. The choice of the trapping wavelength requires careful analysis. Attempts to optimize the performance of the OT lead to two contradicting

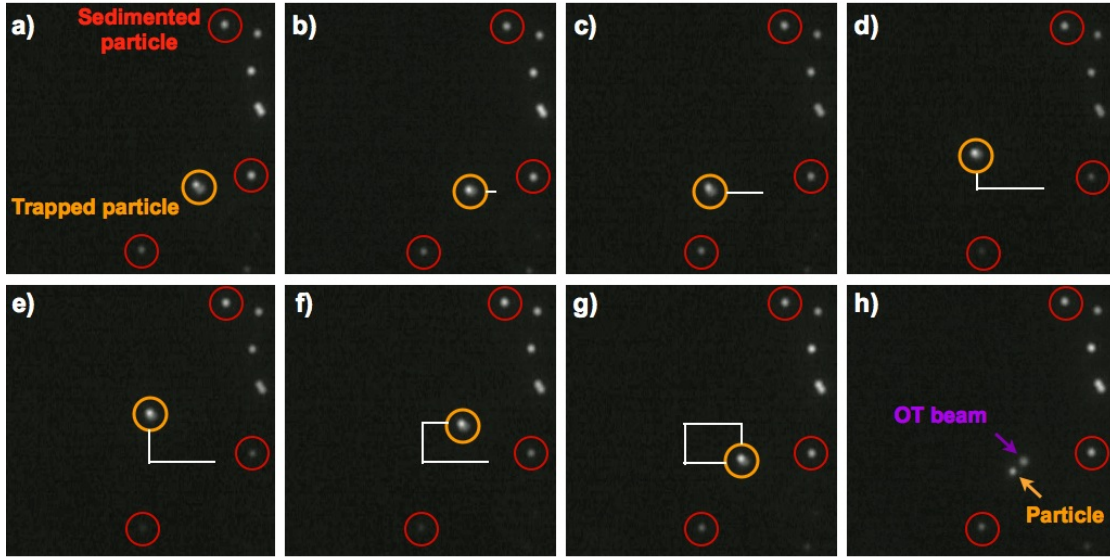


**Figure 4.20:** Demonstration of optical trapping and displacement of a 500 nm polystyrene particle. A 500 nm fluorescent particle is captured with the auxiliary tweezers (a). The particle is then displaced inside the microfluidic channel by describing a rectangular path (b to g) with the piezo actuated microscope objective. (h) Finally the OT beam is quickly disrupted in order to release the particle. The yellow arrow indicates the fluorescent particle while the purple arrow shows the residual reflection of the OT beam on the silicon substrate.

trends. First, as described in Chapter 3, the focusing of the OT beam scales linearly with the wavelength and it is therefore desirable to use shorter wavelengths to obtain tighter traps. Secondly, the bandgap of silicon is 1.1 eV and wavelengths shorter than 1100 nm start being absorbed proportionally to the density of state in the semiconductor. This will lead to increasing carrier and thermal effects as the wavelength is shortened.

Initial attempts have been made using the 514 nm line of an Argon laser which had the advantage of providing large amounts of optical powers and small beam waists in the sample plane. This configuration was given up rapidly as significant resonance wavelength drifts and collapsing of the quality factors of the cavities have been observed. A reasonable alternative has been found by using an Argon pumped - Ti:Sapphire laser (Coherent 890) equipped with medium wave (MW) optics. This combination gives access to a range of emission wavelength between 760 and 930 nm by adjusting the Liot filter. The maximum output power achievable at this wavelength and in the current set-up configuration is approximately 150 mW for a 5.7 W pumping power. Higher output powers are possible with this laser but the introduction of a glass plate in the pump beam (used to separate the fluorescent excitation beam) introduces significant perturbation and limits the maximum possible value.

The estimated optical power entering the microscope objective for a 130 mW laser output is 25 mW. Large amounts of power are lost due to the numerous beam splitters required. This power is then concentrated on a 700 nm diameter region leading to an average power density

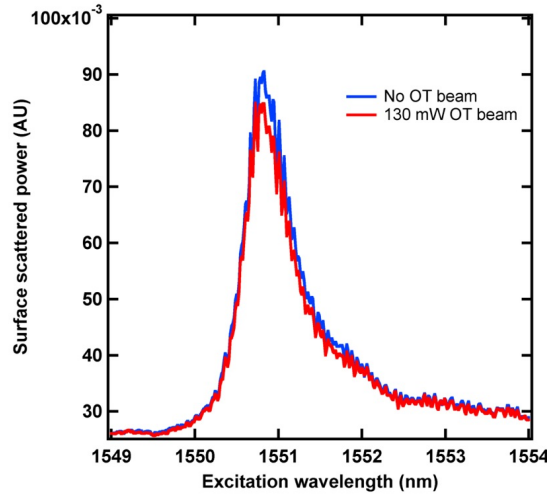


**Figure 4.21:** Influence of tweezers beam on cavity mode. The light that is scattered out of the surface of a photonic crystal cavity is recorded as a function of the excitation wavelength. The scan is performed in the absence of the OT beam (blue curve) and when a 130 mW output power beam is focused onto the cavity with an emission wavelength of 850 nm. The experiment shows almost no difference in the radiated energy nor in the spectral position of the cavity mode.

of  $65 \text{ mW}/\mu\text{m}^2$  (this value is obtained for a lossless and diffraction-limited objective). For this value, it is possible to attract, immobilize or displace 500 nm polystyrene particle with ease. Nevertheless, the stiffness of the trap is not very large and the particles still undergo significant constrained Brownian motion. If the size of particle is decreased down to 200 nm, it is still possible to attract particles towards the focus but the trap becomes too shallow to retain the particle for more than a few seconds. 100 nm particles are usually not affected by the trapping beam.

Figure 4.21 shows the evolution of the quality factor of a hollow photonic crystal cavity in water before (blue) and during the time (red) when the optical tweezers beam is positioned on top of it. This experiment is performed at maximum output power. It can be clearly seen that it does not impact neither the quality factor nor the position of the resonance wavelength.

Another advantage of working at these wavelengths rather than deeper in the visible range is that it is possible to discriminate the strong Ti:Sapphire radiation from the fluorescence emission before it reaches the silicon detectors (EMCCD and confocal APD) with OD4 short pass filters. Hence, a good imaging contrast is preserved.

## 4.5 Confocal sensing

The large forces involved in the optical trapping of neutral particles near photonic nanostructures constitute one of the main reasons behind the extensive investigation efforts by the scientific community. Although the demonstration of the optical trapping of a specimen is reasonably straightforward with any "hold and release" method, the experimental

quantification of the trapping stiffness is a non-trivial task. Common methods make use of either statistics over the spatial distribution of the position of the particle[67] or analysis of its temporal behavior[94]. Centroid tracking methods using a camera can provide up to sub-pixel resolution (typically 0.1 pixel) using good algorithms and sampling rates as high as allowed by the frame rate and exposure time of the camera. In the case of this experiment, this corresponds to a spatial resolution of approximately 16 nm and a sampling rate of up to a maximum of 300 Hz. In these conditions, the largest measurable stiffness for a one dimensional trap is of the order of 10 fN/nm (as estimated for a one-dimensional trap using the equipartition method), while numerical calculations predict stiffnesses of over 1 pN/nm at milliwatt excitation in the vicinity of a PhC cavity. Measurement of such large values required the anticipated development of an instrument capable of tracking the displacement of a particle on much smaller scales (typically 1 nm) and on much larger bandwidths (typically tens of kHz).

The method that has been explored to aim at these performances makes use of a confocal sensor. These types of detectors are capable of associating large light intensity variations with displacements of an object of the order of an optical wavelength. The monitoring of these variations using a fast, low-noise light photodetector and appropriate electronics can then be related the displacement of the object, sometimes achieving sub-nanometer sensitivity. Implementations of confocal sensors can be found in Atomic Force Microscopes (AFM) to measure the motion of the AFM tip at the proximity of the sample. The principle has also already been employed for the monitoring of small particles in an optical tweezers beam but in a configuration that was not limited by the opacity of the sample like in the case of our experiment [152].

The development of the confocal sensor has gone through a lot of progress during the time of this thesis and allowed us to evidence the first signs of particle-cavity back action as described in Chapter 6. Nevertheless, the performance of the sensor itself has not reached the nanometer-scale and tens of kHz bandwidth yet and further effort should be perform. This paragraph will describe the working principle, required optical apparatus and current performances for the developed sensor. A discussion of the various paths that are considered to achieve the desired sensitivity and speed will also be provided.

### 4.5.1 Principle

A confocal sensor is a very simple instrument in its basic implementation. It makes use of two lenses, although one would be enough in principle, a pinhole and a single point detector as shown on Figure 4.22. In this configuration, the object focal plane of the first lens (P1) and the image focal plane of the second lens (P2) are conjugated. The pinhole is located in P2 with the aperture on the optical axis. In accordance with the reversibility principle of light, any light that propagates through the two-lenses system and the pinhole aperture must have been emitted in a tiny region around the intersection of P1 and the optical axis. This region is called

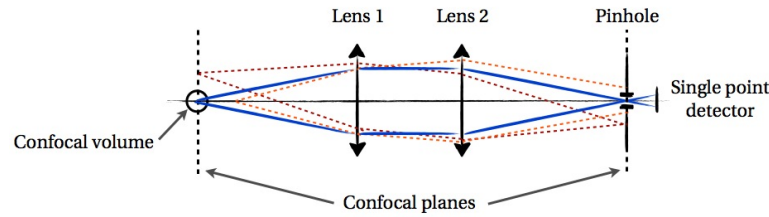


**Figure 4.22:** Principle of the confocal sensor. A two-lens system conjugates the object focal plane of the first lens to the image focal plane of the second lens. A small aperture located in the image plane of the second lens prevents any light that has not been emitted from a restricted region at the intersection of the optical axis and the conjugated plane to reach the single point detector. This configuration gives access to large signal to noise ratio measurements of light emitted in localized region of the object plane.

the confocal region or volume. The confocal volume (CV) is typically an ellipsoid whose long axis is along the optical axis of the system. The size of the CV can be controlled by adjusting the diameter of the pinhole down to the diffraction limit. The diameter of the pinhole can be even further reduced for some applications but at the expense of lesser light levels and the introduction of strong coherence related effects. This case will not be considered here.

The advantage of such an architecture lies in the large signal to noise ratio that can be achieved. Indeed, any light that is emitted outside the confocal region like illumination, fluorescence excitation or background fluorescence get automatically rejected by the pinhole. On the contrary, for any light originating from the CV a large fraction of the energy is directly focused onto the single point detector (SPD) which can be a photodiode, an avalanche photodiode or a photo multiplier tube, depending on the light level requirements.

In a standard confocal microscope the principle just described is applied and the sample to be imaged is positioned on top of a three stage (X,Y,Z) piezo stage. A light intensity measurement is then performed point by point as the stage move the sample through the confocal volume. A 3D image can then be reconstructed with a computer for a transparent specimen. The principle of the confocal sensor is somewhat different. In this case, the confocal volume is located on top of the trapping volume (here a hollow photonic crystal cavity). A fluorescent particle is emitting light at the center of the confocal volume and gives raise to a maximum in the photovoltage recorded on the sensor. If the particle drifts towards the edge of the CV, part of the emitted light is now vignettted by the pinhole, up to the point where no light is captured anymore. The monotonous and quasi-linear relationship between the position of the particle with respect the center of the CV provides us with a light intensity level that is proportional to the excursion of the particle. The sensitivity of the detector in terms of displacement of the particle is then dictated by the photovoltage dynamics divided by the radius of the confocal volume (a few hundred nanometers) and the accuracy on the voltage read-out (limited by the various noise processes existing in the system).

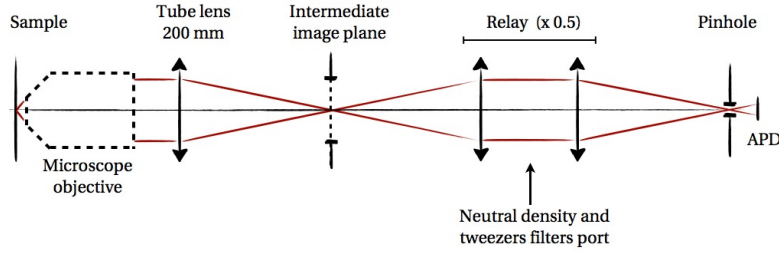


**Figure 4.23:** Optical arrangement of the confocal sensor. The optical arrangement is similar to the visible imaging with the microscope objective and the tube 200 mm lens forming an intermediate image. A 0.5 magnification relay reproduces the intermediate image onto the pinhole plane. Any ray bundle that focused on the aperture of the pinhole is free to reach the avalanche photodiode. Any other ray is absorbed and therefore does not contribute to noise in the sensor read-out.

### 4.5.2 Optical arrangement

The optical arrangement for the confocal sensor is similar to the one of the visible imaging. The light emitted by the fluorescent particle is collected through the microscope objective, collimated and refocused through the tube lens in an intermediate image plane. Then a two-lens relay of magnification 0.5 re-images the intermediate focus on the confocal pinhole. The infinity-conjugated region in between the two relay lenses is used to insert the various dichroic filters used for the rejection of the Ti:Sapphire beam and the residual fluorescent excitation beam. The final lens before the pinhole has a focal length of 200 mm while the incoming beam has a pupil of 15 mm in the diameter. The diffraction limited spot in the plane of the pinhole is therefore  $40\ \mu\text{m}$  (calculated for a 600 nm wavelength). In a diffraction limited configuration, an optimized choice for pinhole diameter would therefore be around  $40\ \mu\text{m}$ . In our case the pinhole diameter has been chosen to be  $80\ \mu\text{m}$  and accounts for increase in Point Spread Function (PSF) due to the microfluidic layer (mainly in the form of spherical aberration). Different trials with pinholes between 30 and  $100\ \mu\text{m}$  have been performed before reaching to this value. The single point detector is finally located at a distance such that the beam diffracted through the pinhole aperture covers almost completely the photosensitive area.

In a similar manner, different single point detectors have been experimented, starting from a standard silicon photodiode, to a silicon APD in Geiger mode (EG&G, SPCM- 200-PQ and Hamamatsu HM8122 counter) and finally a standard silicon APD in linear mode (Hamamatsu, C4777-01). Silicon photodiodes are interesting candidates because of the ease of use they provide and the large achievable bandwidths (10 - 100 MHz with appropriate electronics). Nevertheless, the small responsivity (typically 0.5 A/W for a Si photodiode) and elevated noise-equivalent-powers (NEP, typically 100 to 500 fW/ $\sqrt{\text{Hz}}$ ) make them inappropriate to the low-light levels involved. On the contrary, silicon avalanche photodiodes have a much larger responsivity and lower NEPs allowing for the detection of much smaller amounts of light. The Hamamatsu C4777-01 module displays for example a 25 A/W responsivity for an



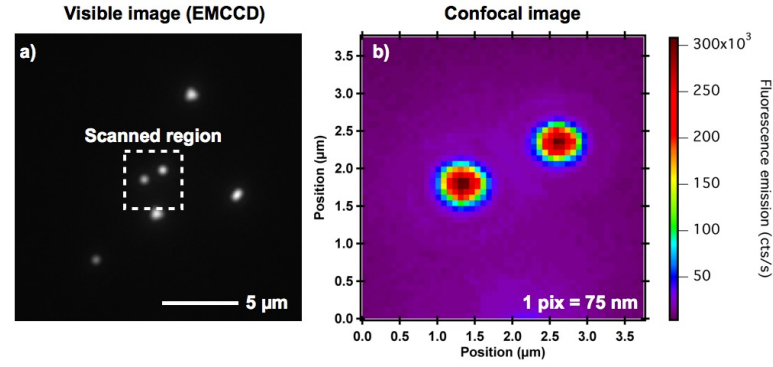


**Figure 4.24:** Fluorescence confocal imaging of two separated sedimented particles. (a) Visible image of the sedimented particles as recorded with the EMCCD camera. The full field is approximately 20  $\mu\text{m}$  wide. The area marked with the purple dashed line indicates the region scanned by the confocal microscope. (b) Fluorescence confocal image of the two particles recorded with the EG&G photometer. The full field measures 3.75  $\mu\text{m}$  and is composed of 50 x 50 square pixels of 75 nm each. The measurement dynamic has approximately 300 000 levels (counts per seconds) in the case of the confocal sensor compared to 3000 grey levels in the case of the EMCCD camera.

internal gain of 50, and a NEP as low as  $2 \text{ fW}/\sqrt{\text{Hz}}$ . The motivation to go from the EG&G single photon counting module (SPCM) to the linear-mode Hamamatsu APD is not related to sensitivity but comes from the requirements in terms of bandwidth and analog output related to noise spectra related methods. Although the SPCM can be operated with gate times as small as 20  $\mu\text{s}$ , the GPIB communication between the counter and the recording computer limits the practical sample rate to slightly above 30 Hz. In addition, the output of the counter is a digital value corresponding to the number of photocounts recorded during the precedent gate time. An APD module that operates "linearly" delivers a continuous voltage and is more appropriate for noise spectra analysis. The Hamamatsu C4777-01 module has been chosen for this purpose. It has a measured cut-off frequency at 3 dB is 10 kHz and is expected to be sufficient to measure trapping stiffnesses of the order of 0.1 pN/nm (as estimated for a 500 nm polystyrene particle in standard optical tweezers).

#### 4.5.3 Performance

One method to evaluate the performance of the confocal detector and to calibrate it is to record the confocal image of a sedimented fluorescent particle. A set of 500 nm polystyrene particles is let free to bond to the surface of a sample. Figure 4.24 (a) shows a fluorescence image of 3 individual particles and 3 clusters as recorded on the EMCCD camera. The piezoelectric-transducers (PZT) are then driven to scan the confocal volume over a subset of the field (purple frame), centered on two of the individual particles. The scan records a 50 x 50 array of photocounts per seconds measurement, each "pixel" being separated by 75 nm. The minimal sampling achievable with the current PZTs and driving electronics is 25 nm. The confocal image is finally reconstructed on the computer and is shown in Figure 4.24 (b). The performances presented here are those taken with the EG&G photo counter. The gate time is

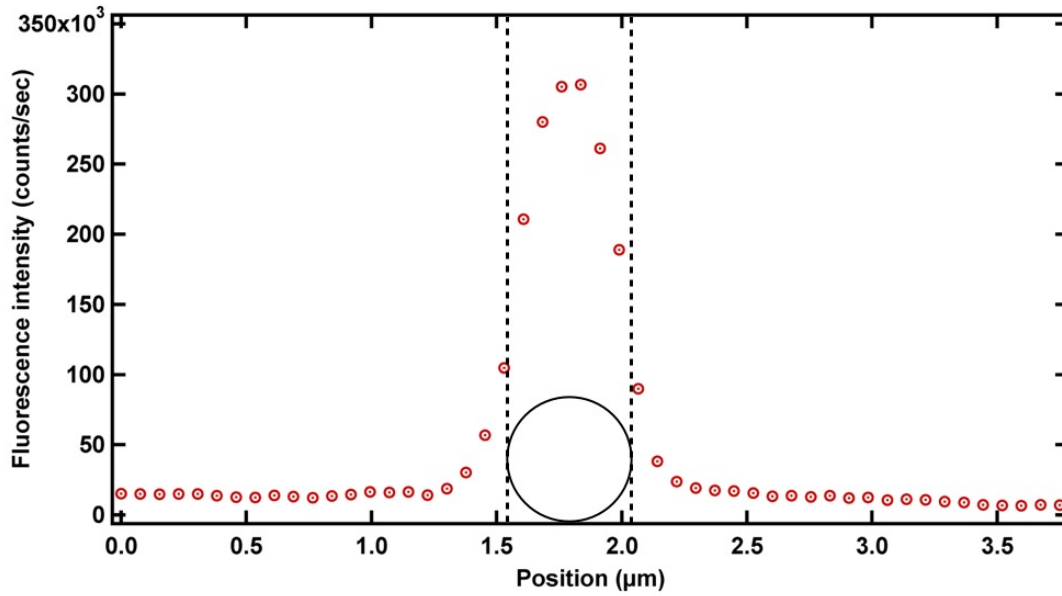


**Figure 4.25:** Calibration of the confocal sensor for a 500 nm fluorescent particle. The calibration is based on the cross-section of the confocal image shown in Figure 4.24. The graph shows the evolution of the photocounts recorded when scanning the confocal volume across the center of a fluorescent particle of 500 nm in the diameter. The circle represents the up-to-scale size of the particle in order to illustrate the sharpness of the measurement. From the dependence of the light intensity compared to the displacement of the particle from the optical axis, an experimental sensitivity of 5 nm can be deduced for the sensor.

set at 20 ms. Future performance estimation and calibration using the C477-01 module will be performed by M. Tonin over the coming months. It can be observed that both particles, approximately 1  $\mu\text{m}$  away, are clearly resolved by the detector. Since the size of the observed particle is of the order of magnitude of the diffraction limited Airy disk at these wavelengths, what Figure 4.24 (b) shows is the convolution product of the cross-section of the confocal volume and the local density of fluorophores (proportional to the thickness of the particle).

From the confocal image, it is possible to retrieve the sensitivity of the detector in terms of excursion of the particle with respect to the optical axis of the sensor. Figure 4.25 shows a cross-section of the photocounts per seconds (cts/s) when scanning one of the sedimented particles. The bell-shaped signal observed reached over 300 000 cts/s at its maximum, a background noise level of approximately 15 000 cts/s and has a full-width at half-maximum of 450 nm. Using these values, it is possible to derive a displacement sensitivity of 2.5 pm/cts/s, which is limited in practice by the fluctuations in time of the fluorescence emission. These fluctuations are measured to be lesser than 1% in amplitude of the average measured intensity. For a conservative 2000 cts/s experimental read-out accuracy, this corresponds to a detector with a real-time 5 nm in-plane displacement resolution at 50 Hz. This corresponds to an improvement by a factor 3 of the displacement resolution compared to the centroid tracking approach with the EMCCD but at the cost of a factor 6 in the sampling rate.



**4.5.4 Limitations**

As mentioned earlier in this section, the confocal sensor has been developed as a side apparatus in anticipation of the need for a mean to measure large optical forces. It is a tool that has proven useful already in several occasions but which does not perform yet to its fullest capacity in terms of sensitivity and bandwidth. One step has been made already to improve the bandwidth from 50 Hz to 10 kHz by acquiring the C477-01 Hamamatsu module which is awaiting to be tested. Regarding the displacement sensitivity, the correction of optical aberrations (see Chapter 5 for details) in the optical path will be beneficial on two aspects simultaneously. First a finer Point Spread Function concentrates more light in the main central lobe, leading to an increased signal on the photodetector. Second, a finer PSF allows for the use of a smaller pinhole, without extra light losses, which leads to a confocal volume with narrower lateral dimensions. The combined effects of the increased light levels and sharper lateral dimensions should bring the apparatus closer to the 1 nm resolution target.

A second important limitation comes from the three dimensional nature of the confocal volume. In the previous paragraphs, the dependence of the position of the particle has been only considered in the plane that is perpendicular to the optical axis. In reality, the signal that is recorded on the sensor depends on the position of the particle in the three dimensions. The current configuration does not permit the discrimination between in-plane and out-of-plane displacements of the particle which will be necessary for a rigorous analysis of the resonant optical forces.

**4.6 Possible additions and improvements**

The current configuration of the optical test bench has proven to be successful in setting up all the appropriate conditions for the operation and characterization of photonic crystal cavity, the optical manipulation of sub-micron polymer particles and the demonstration of resonant optical trapping. The complexity of a resonant trapping experiment (cavity coupling and particle injection monitoring, single particle isolation and manipulation, surface-scattered infrared light collection, transmitted light measurement, etc ...) makes it complicated to use the developed functionalities of the bench simultaneously by one or even two users. A large number of highly interesting experiments can still be performed without any addition or modification of the bench. Nevertheless a few aspects might be considered in order to improve the practicality of operations.

The use of the Ti:Sapphire as the optical tweezer beam makes a lot of sense in the early stage of such an experiment. It provides a well separated wavelength that can be easily filtered out and benefits from a large tunability range which proved to be important for the non-perturbation of the PhC cavity mode. On a separate aspect, Ti-Sapphire lasers are known not to be very practical, especially in terms of maximization of their performances. The complexity of the cavity and the large number of element it comprises of make it very sensitive to external perturbations and requires frequent adjustments. The optically-pumped nature also comes

with a few drawbacks like the dependency of the Ti:Sapphire output on the stability of the pump laser and on the quality of its beam. The replacement of the Ti:Sapphire laser by a diode-pumped solid-state Neodymium-doped Yttrium Aluminum Garnett (Nd:YAG) laser emitting at 1064 nm would have several benefits. It would decouple the fluorescence excitation beam from the OT beam removing at the same time the need for a large number of optical elements and therefore saving a lot of optical bench space. It would also give access to larger output powers (of the order of 300 mW) when the current OT beam reaches a maximum of 150 mW which is just enough. Finally, it would operate nearer to the silicon transparency window and remove any risk for residual interaction between the OT beam and the cavity mode.

The current PhC coupling configuration based on lensed optical fibers imposes that sample remains fixed at all time and that the microscope objective is displaced to adjust the observation field and the position of the OT spot. One weakness of this approach is that the amount of light coupled into a PhC structure can vary when experiments occur over extended periods of time. A second weakness is that the optical quality of both the visible imaging and the confocal sensor are affected by the displacement of the objective outside of the optical axis. One way around these issues would be the use of bonded fibers for the cavity excitation rather than lenses fibers. As a consequence, the amount of light coupled to the structure would remain constant over time. It would also enable the possibility of mounting the sample on a three dimension piezo stage and freeze the position of the microscope objective on the optical axis. This would ensure constant and optimized optical performances for the imaging and the confocal sensor.

Finally, as mentioned in the previous section, an important limitation of the confocal sensor is its incapacity to discriminate between in-plane and out-of-plane displacements of the particle. It would be possible to circumvent this issue by replacing the single-point-detector by a four-quadrant detector and appropriate electronics. In this case, an in-plane displacement of the particle would cause a displacement of the image spot of the quadrant. A differential measure of the light intensity on each quadrant would not only indicate an in-plane displacement of the particle, but would also give an information on the direction of the motion. Similarly, any out-of-plane displacement of the particle would generate a homogeneous decrease of the light impinging on each quadrant.

## 5 The optofluidic chip

This chapter is dedicated to the description of the technique developed during the time frame of this thesis and is based on a microfluidic approach. In the first part, a general description of the requirements imposed by the experimental conditions is provided followed by the preliminary approaches that have been investigated in the early stages of this work along with their limitations. In the second part, a quick introduction to microfluidics is provided, before the main design aspects for the device we developed are explained. In the third part, the detailed fabrication procedure for the optofluidic chip is provided. In the fourth part the pneumatic system used for the actuation of the chip and a description of the performance in usage are shown. Finally in the last part, the development of alternative approaches that has been carried out in parallel to the fabrication of the chip is described.

### 5.1 Motivation and early experiments

The ability to bring colloidal particles in the vicinity of a photonic crystal cavity in a way that is compatible with high resolution imagery is a critical requirement to successfully demonstrate resonant optical trapping. The small dimensions imposed by the photonic crystal samples, the sensitivity to mechanical damage or contamination, and the need for an optimized optical coupling to an external laser source constitute the many difficulties in the design of the appropriate technique.

Classical trapping experiments usually make use of large immersion chambers whose dimensions are of the order of a centimeter in width and several millimeters in height. These glass chambers are typically sealed and therefore are isolated from the outer environment. Their top surface consist of a thin microscope coverslip in accordance with the correction of the microscope objective in use. The implementation of this approach for resonant trapping experiment makes the PhC sample completely immersed inside the chamber thus rendering the coupling to lensed fibers rather impossible. This approach is therefore not considered.

A successful immersion technique should verify two important requirements: It should have

a total footprint that is smaller than the photonic crystal sample in order to leave the input facets free for coupling. It should maintain high numerical aperture imaging from the top of the sample. Out of these two requirements two preliminary approaches were investigated. The first one is a local infiltration method where a drop of the solution containing the colloidal particles is deposited on the PhC sample while serving as the microscope immersion medium. The second is the addition of a thin glass reservoir on top of the PhC structures.

### 5.1.1 Local infiltration approach

Immersion microscope objectives for high numerical aperture imaging exist in a variety of configurations depending on the immersion liquid they are designed for. The latter can either be water, glycerol or oil. In most cases, a small drop of the liquid is deposited on the coverslip of the sample to be studied and the front lens of the microscope objective is brought in contact with the droplet. In some cases, the specimen under study is directly in aqueous medium and a water immersion objective can be brought in direct contact with the medium, without any intermediate coverslip. This is generally referred to as a "dipping" configuration.

The use of a water immersion objective in a dipping configuration where a low concentration of nanoparticles is added to the immersion water is a simple and straight forward way to bring a particle in the vicinity of the PhC cavity. A solution of colloidal particles is diluted in deionized water. A small quantity of the diluted solution is then collected in a 1 mL syringe equipped with a needle. A droplet is then formed at the tip of the needle and deposited in the center of the photonic crystal sample before the microscope objective is brought in contact with the meniscus of the droplet (see Figure 5.1). Fine focus is finally obtained by adjusting the distance between the silicon surface and the front lens of the objective. As the thickness of the water layer decreases during focus, a small over pressure is formed, which pushes out the air bubbles underneath the PhC membranes. Complete infiltration of the structures (see Chapter 6) is usually obtained within seconds.

This approach offers many advantages. On top of its simplicity, it inherently deals with very small and steady quantities of solution (of the order of 10 to 50  $\mu\text{L}$ ) and hence removes the need for any pumping or injection circuitry. Besides, optical performance in dipping configuration is very high, even in the case of a coverslip-corrected water immersion objective (see Table 4.1 on page 52). Figure 5.1 shows an image of a hollow photonic crystal cavity imaged in the dipping configuration. The 400 nm periodicity of the photonic crystal lattice can be resolved with high contrast as well as the 700 nm hollow cavity in the center.

Conversely, the local infiltration method comes with a large number of prohibitive disadvantages. As mentioned earlier the solution is composed mostly of water and therefore evaporates over time. This has two consequences. Firstly, the experimental working time is very limited. It takes approximately 25 minutes for a droplet to evaporate completely from the moment it is positioned on the PhC sample. In these 25 minutes, decent imaging conditions can only be obtained for 15 minutes mainly due to the deformation of the droplet which degrades the

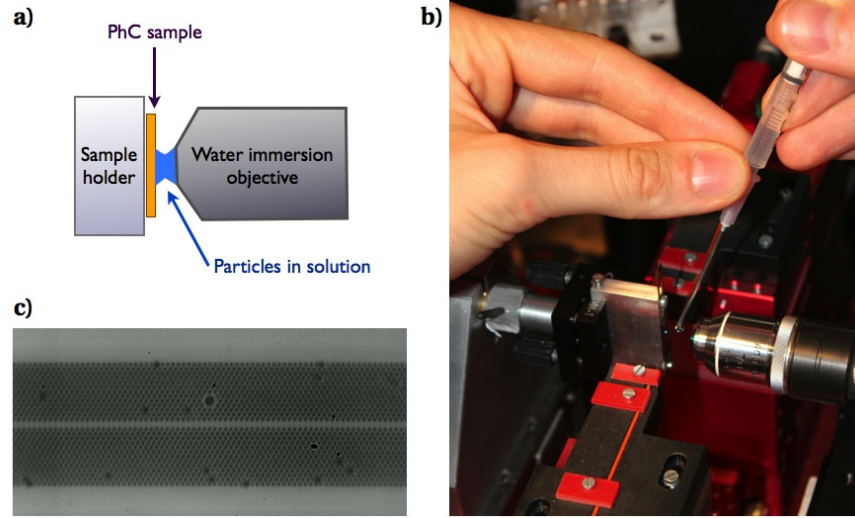


**Figure 5.1:** Local infiltration method. a) Schematic of the method: a water immersion objective is used in dipping configuration, the particles investigated are diluted in the immersion liquid. b) Photograph of the method as implemented in the lab. c) Optical micrograph of a hollow photonic crystal cavity as observed with the local infiltration method.

optical quality. After a reasonable focus is achieved, it usually takes between 5 to 10 minutes to optimize the fiber coupling to the PhC device and fine adjustment of the various detectors. The average working time is therefore approximatively 7 minutes long which is largely insufficient when it comes down to isolating randomly moving nano particles. Some results presented in Chapter 6 have been achieved after several hours of continuous measurement. Secondly, each droplet that is let to dry on the photonic crystal sample leaves small amounts of particles and other compounds on the silicon surface. Repeated local infiltrations rapidly lead to the deterioration of the photonic structure operation through lower light coupling, extra scattering losses and linewidth broadening. A fresh PhC sample needs to be cleaned after 20 to 30 infiltrations on average using a demanding cleaning procedure which is not always 100% successful. Photonic crystal samples investigated with this method suffer from a very limited lifetime. Finally the non-constrained displacement of the water drop on the surface of the sample can be problematic if the meniscus reaches the input / output facets. In this case the coupling performance can be dramatically affected and will be changing over time as the water drop recesses through drying.

### 5.1.2 Glass reservoir approach

A second possibility that has been investigated makes use of a thin glass reservoir deposited on top of the PhC structures. The reservoir consists of a 6 mm long, 1 mm wide, 10  $\mu\text{m}$  high channel etched in a 6 mm long, 3 mm wide glass piece diced off a microscope coverslip (see Figure 5.2). The fabrication of the glass piece is described in the following part as carried out by Hans-Jörg Bühlmann.

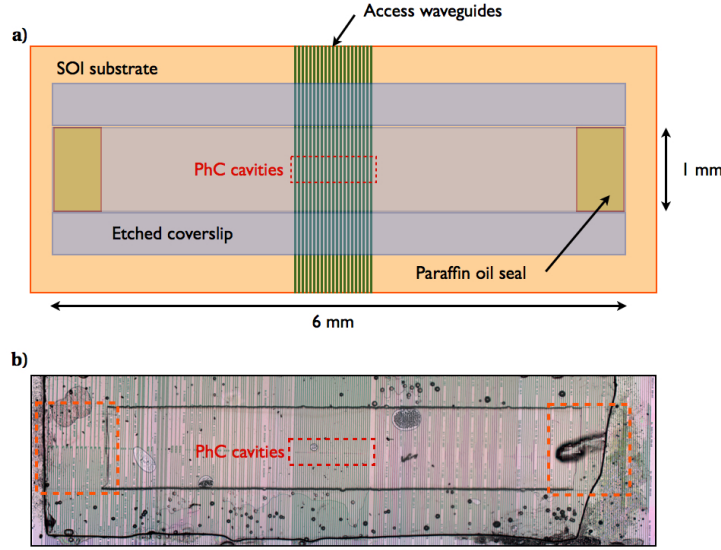


**Figure 5.2:** Glass reservoir approach. a) Schematic of the fabricated device. A 1 mm x 6 mm channel is etched in a glass coverslip. The coverslip is then cut, positioned above the PhC cavities and bonded with optical epoxy resin. The channel is finally filled with the particles solution and sealed with paraffin oil. b) Assembly of low numerical aperture optical micrographs showing the final structure.

A float glass microscope coverslip is first cleaned and coated with a  $\approx 900$  nm aluminum layer. A shadow mask vapor deposition method is used to define the channel location, leaving a 6 x 1 mm rectangular area uncoated on one of the faces of the coverslip. The aluminum-coated piece of glass is then immersed in a buffered hydrofluoric acid solution (90:10) for three and a half hours. A measured  $3 \mu\text{m}/\text{hour}$  etching speed leads to the formation of the  $10 \mu\text{m}$  high channel in the coverslip. The coverslip is finally rinsed in water and left for a few minutes in a  $\text{H}_3\text{PO}_4$  (1:1) and  $\text{HNO}_3$  (1:5) solution in order to remove the Al layer. The measured etching speed is approximately  $0.3 \mu\text{m}/\text{min}$ .

The piece of glass is then rinsed in water and carefully diced using a diamond knife to its final dimensions. The channel is carefully deposited by hand on top of the devices. An optical epoxy resin is deposited on the long-edges of the glass part and let to migrate through capillary action in between the glass - silicon interface. An overnight baking in an oven at  $50^\circ\text{C}$  leaves the glass reservoir bound to the silicon surface. The reservoir is then filled with the colloidal solution with a micropipette through capillary action before both ends of the channel are sealed using "in-house thickened" paraffin oil.

This approach is interesting because it allows to work in almost perfect imaging conditions with respect to the coverslip correction of an immersion microscope objective. It also removes the risks of residual aberrations that are still being introduced by the water layer in the etched channel. Nevertheless, it comes at the price of large drawbacks in terms of complexity of the fabrication process. The dicing of such a small and fragile glass piece is highly uncertain and usually requires several attempts before one valid channel can be glued to the PhC sample. The

capillary migration of the epoxy resin is another complicated step since a too little quantity of resin will lead to a non-working device while a too large quantity will lead to a lifted coverslip with lower optical quality. The last major impediment to this technique is that it limits the use of the PhC sample to one type of particle. The presence of paraffin oil and epoxy resin makes the sample almost impossible to clean without any significant damage either to the photonic crystals or the glass/silicon assembly. The lifetime of the sample is therefore that of the time before sedimentation of the particles (up to a few months in some cases) or the time before drying of the injected colloidal solution through residual pores (typically a few days).

## 5.2 Microfluidic circuit and chip design

In this section, a short introduction to microfluidics is provided along with a limited state-of-the-art. The main design parameters for the microfluidic chips that were fabricated during this thesis are detailed.

### 5.2.1 Introduction to microfluidics

Microfluidics originally relates to the study of fluids in very small volumes, typically of the order of nanoliters or smaller. At these scales, the small volumes of the fluids involved and their interaction with the environment lead to flow behaviors or chemical reaction kinetics that can be very different from those that of the once experienced in bulk volumes. This can be partially understood with the fact that the lengths of the intermolecules and the surface-to-molecules interactions are not negligible anymore compared to the physical lengths of the systems considered (typically less than a few tens of micrometers). As an illustration of the power of handling fluids at the micro and nano scale, a large variety of biological systems and organisms actually rely on microfluidic systems. For example, the uniform distribution of water to the leaves of the trees is based on a complex system of capillaries ranging from a few tens of nanometers to a few tens of microns [158]. Similarly, the fast synthesis of extremely robust protein silks by a spider is an impressive example of microfluidic chemical reaction [158].

Hence, the understanding and mastering of these phenomena is of a major interest and holds promise in many fields of science. [159]. Microfluidics is a fast and effective way to isolate, detect and study ensembles of few or even single molecules, [160], [161], [162] which makes them highly suited for analysis applications. The small system footprint, tiny quantities of reactants required and quick reaction times make it very adapted for the control and detection of chemical reactions [163]. In a similar manner to microelectronics, the small dimensions of microfluidic features allows for massive parallelization of operations [164] (see Figure 5.3.b). This feature is crucial for applications in genetics [165], protein manipulations [166], and more generally to bio-assays [167], [168] where repeatable and reproducible conditions are required over large number of specimen simultaneously. The combination of all these amazing characteristics have led researchers to imagine new generations of microfluidic chips including

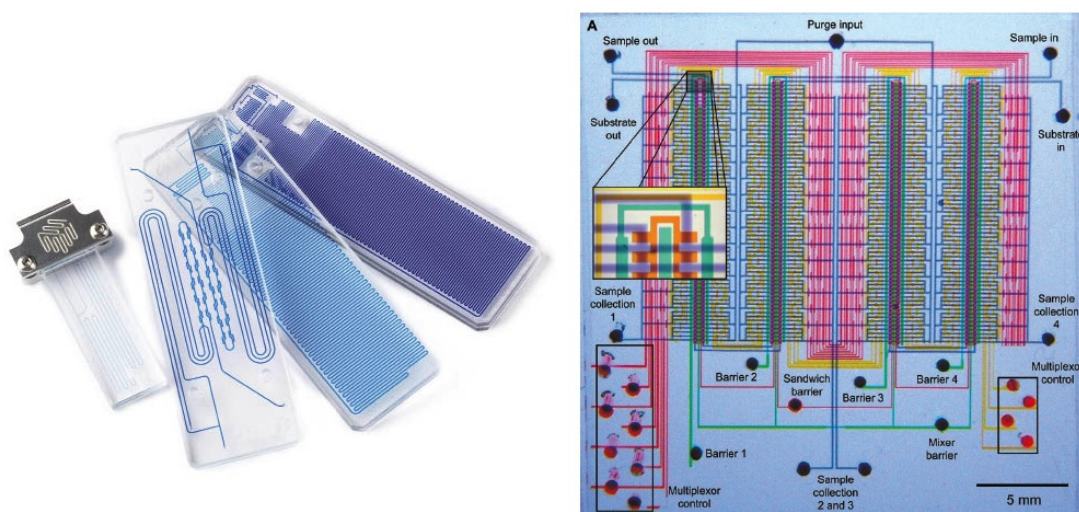


**Figure 5.3:** Examples of microfluidic chips. *a)* A set of mixer and reactor chips from Dolomite Microfluidics. *b)* Demonstration of a highly integrated microfluidic chip comprising of 1000 independent compartments and over 3500 microvalves as published by Thorsen and co-workers. [169]

numerous functionalities simultaneously under the title of "Lab-on-Chip" or "Micro-Total-Analysis Systems". It is possible to find a few commercial version of reactor chips on the market already (see Figure 5.3.a) but the long standing goal of wide-spread, inexpensive, Lab-on-Chip device for Point-of-Care diagnostic is still to be achieved.

The progresses in microfluidics have been limited by the ability to fabricate structures with micro or nanometer scales dimensions for a long time. The fast development of microelectronics and micro-electro-mechanical systems (MEMS) in the 1990's has permitted the fast growth of microfluidic related research [158]. The early microfluidic fabrication processes involved silicon and glass substrates. These materials benefit from the very-well established and accurate photolithographic processes for the realization of microfluidic channels. Unfortunately these two materials also suffer from a few limitations. Firstly, these are two very rigid materials and though it is technically interesting to have robust devices, the control of microfluidic flows requires the presence of deformable pieces for the realization of pumps and valves. Secondly, both these materials are completely impermeable to oxygen. This prevents their use in cell culture applications which represents a large fraction of the applications of microfluidic chips [167]. Finally, it is important to note that silicon is opaque to visible and UV radiation. This limits its use for any application where classical optical diagnostic methods like microscopy and spectrometry are required.

These issues have been largely circumvented with the development of new generations of polymer-based [170] and especially elastomer-based microfluidic systems [171], [172]. The so-called soft lithography process relies on a replica molding technique. A master (negative preform of the circuit) is first fabricated through either micromachining or standard pho-



tolithography. A liquid-phase elastomer, usually poly(dimethylsiloxane) or PDMS, is then deposited and cured on top of it. The microfluidic circuit is then peeled off the master and is placed on its final substrate. The advantages of this method are numerous, mainly in term of practicality and cost, as it does not require clean-room conditions or expensive equipment. The PDMS itself is an inexpensive material and is widely used in the agribusiness. More importantly, layers of soft lithography fabricated channels can be assembled together and create advanced microfluidic functions like the widely used Quake valves [171]. In this configuration, a first channel is fabricated in a thin PDMS membrane and a second channel is fabricated in a much thicker PDMS layer and is positioned perpendicularly. The top channel can then be injected with a higher pressure fluid which causes a temporary deformation of the thin membrane and compresses the lower channel until complete closure thus realizing a valve. This operation is allowed by the elastic properties of PDMS. A variety of combinations of these valves can then be implemented and can be used to perform peristaltic pumping or fluid mixing [173]. Another great advantage of PDMS is that it is actually permeable to oxygen. This property makes it an ideal material for on-chip cell growth and bioassays.

In continuation of all the progresses achieved in the last ten to twenty years, microfluidics is still at the heart of scientific research today. Important developments are still being reported not only on the physics of fluid at the micro and nano scale [174], [175], [176], but also on the technological aspects of microfluidics like materials, interconnects [177], and integration of flow controls [178]. It also includes using microfluidics as an experimental technique like in the field of medicine for drugs discovery, in the field of genetics, for the replication of RNA [179], or in the field chemistry for the photoelectrocatalytic purification of water [180]. Large efforts are also dedicated to the merging of other technologies with microfluidics, which recently has given birth to new sub-fields like optofluidics [181],[182], [183]. Optofluidics covers the development and investigation of devices such as microfluidic waveguides [184], [185], light sources [186], [187], [188], modulators [189], integrated opto-chemical sensors [190], [191], [192], biosensors [193], [194], and optical manipulators [195], [136], [149].

### 5.2.2 Design of the optofluidic chip

The chips that were designed and fabricated during this thesis consist of two parts: a silicon-on-insulator substrate comprising of photonic crystals devices and a PDMS microfluidic membrane. The primary objective of using microfluidics is the transport and control of nanoparticles in aqueous solution. This constitutes a rather humble target with respect to the current state of microfluidics technology. Nevertheless, the presence of an individually fabricated silicon PhC sample as a substrate imposes two supplementary objectives. Firstly, the opacity of silicon to visible wavelength requires that the microfluidic design is compatible with high numerical aperture imaging from the top. Secondly, the complexity and of fabrication for the photonic crystal sample impose the choice of a microfluidic design that reduces the risk of damage during assembly and ensures a lifetime of at least of few weeks.

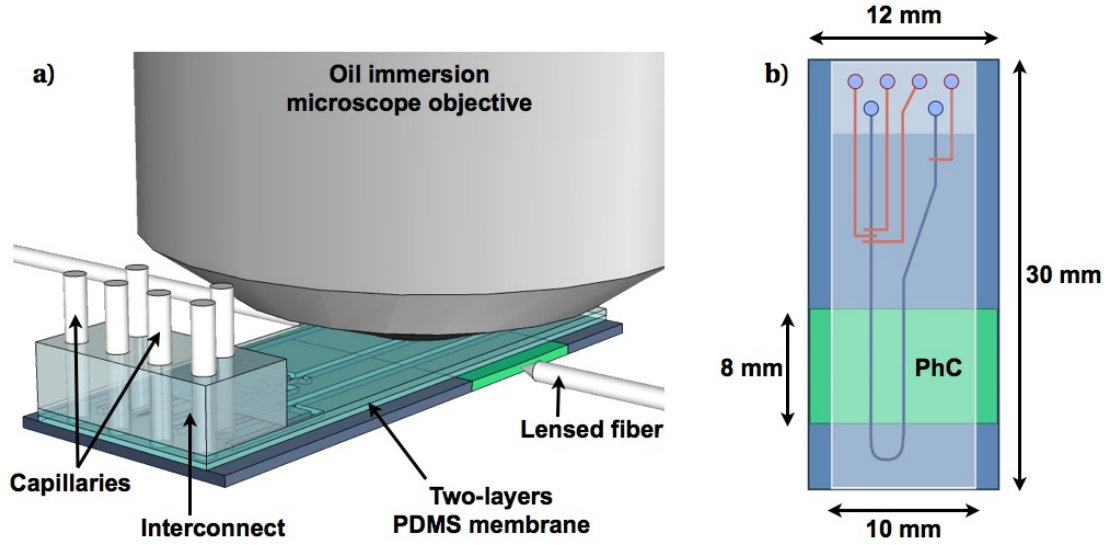


**Figure 5.4:** Design of the optofluidic chip. a) 3D rendering of the optofluidic chip when placed underneath the oil-immersion microscope objective. The rendering shows how the design allows for displacement of the objective above the photonic crystal region without being limited by the presence of the interconnect. b) The chip consists of a 30 mm by 12 mm SOI substrate including the PhC structures and a 30 mm by 12 mm PDMS membrane including a transport channel and four control channels.]

The dimensions of the optofluidic chip have been mainly dictated by the necessity to work with an oil immersion objective. Usually, photonic crystal samples fabricated in the laboratory measure 3 to 4 mm in the width and 10 mm in the length. The cleaving is performed manually. The "active" region of the sample where photonic devices are implemented can measure up to 8 mm in the length and contain over a hundred structures. In the case of the resonant optical trapping sample, an active region with comparable dimensions is desired. The sample should also include an interconnect (necessarily a few millimeters thick) for the injection capillary while maintaining enough space for displacement of the microscope objective from the first to the last PhC device. The design that was chosen is based on a 30 mm long and 12 mm wide SOI substrate (see Figure 5.4). A 10 mm wide PDMS membrane is placed above the substrate leaving a 1 mm region free from PDMS on each side of the chip. This is to prevent any influence of the PDMS layer on the light coupling from the lensed fibers (Figure 5.4.a). The 1 mm value is chosen conservatively and includes large tolerances for the manual positioning of the membrane. A U-shaped channel, 200  $\mu\text{m}$  wide, is designed to transport the flow of particles in suspension to the active region. This approach has been preferred to a straight channel in order to concentrate all the connections to the injection capillaries on one side of the sample and thus limit the total size of the chip. A straight approach would have led to a sample length of the order 40 to 50 mm in the length (as imposed by the 30 mm outer diameter of the microscope objective) rendering the cleaving of the facet very complicated and risky. The width of the substrate is chosen mainly for mechanical stability of the chip.

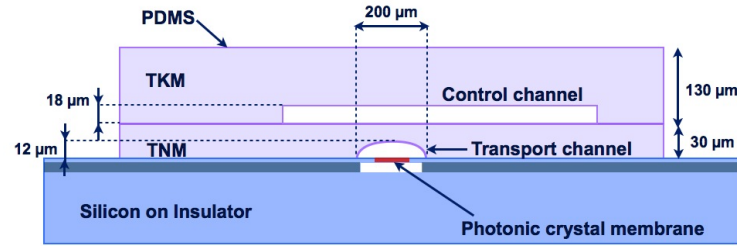


**Figure 5.5:** Design of the two-layers microfluidic membrane. The 160  $\mu\text{m}$  membrane consists of an assembly of two thinner membranes. A thin (TNM) membrane - 30  $\mu\text{m}$  - contains the transport channel and is in direct contact with the silicon substrate. A thicker (TKM) membrane - 130  $\mu\text{m}$  - contains the control channels.]

A set of Quake valves [171] is placed at the entrance and exit of the transport channel in order to control the flow as shown of Figure 5.4.b. They consists of 200  $\mu\text{m}$  wide channels (in orange) distributed perpendicularly to the transport channel in a second PDMS layer. (see Chapter "Actuation and performance"). Three valves are located on the input to form a peristaltic pump. The last valve at the output of the transport channel is designed to act like a brake or flow stopper.

The thickness of the lower membrane including the transport channel is chosen to be 30  $\mu\text{m}$ . This value was retained as it seems to be commonly used in the microfluidics community. The height of the transport channel is designed to be 12  $\mu\text{m}$  in height and must have a rounded shape in order to achieve perfect closure at the valves level. The main difference in the design of the resonant trapping chips comes in the choice of the top PDMS membrane thickness. In most cases found in the literature, the upper layer is several millimeters thick. This probably renders the PDMS assembly very robust and it most likely help concentrating the pressure-induced deformation of PDMS on the thin membrane, thus making the valving more efficient. Conversely, it prevents high-numerical aperture imaging from the top. The thickness of the top layer was designed to be 130  $\mu\text{m}$  in order to reach a total height of PDMS close to 160  $\mu\text{m}$  and mimic the thickness of glass coverslips for which immersion microscope objectives are corrected. The height of the control channels is 18  $\mu\text{m}$ .

Figure 5.5 shows a cross-section (not to scale) of the PDMS membrane and photonic crystal chip. It is important to note that there are no PhC membranes located underneath the Quake valves on the chips. The presence of both on Figure 5.5 is for illustration purposes only. The thin PDMS (30  $\mu\text{m}$ ) membrane is referred to as TNM and the thicker membrane (130  $\mu\text{m}$ ) above is labeled TKM.

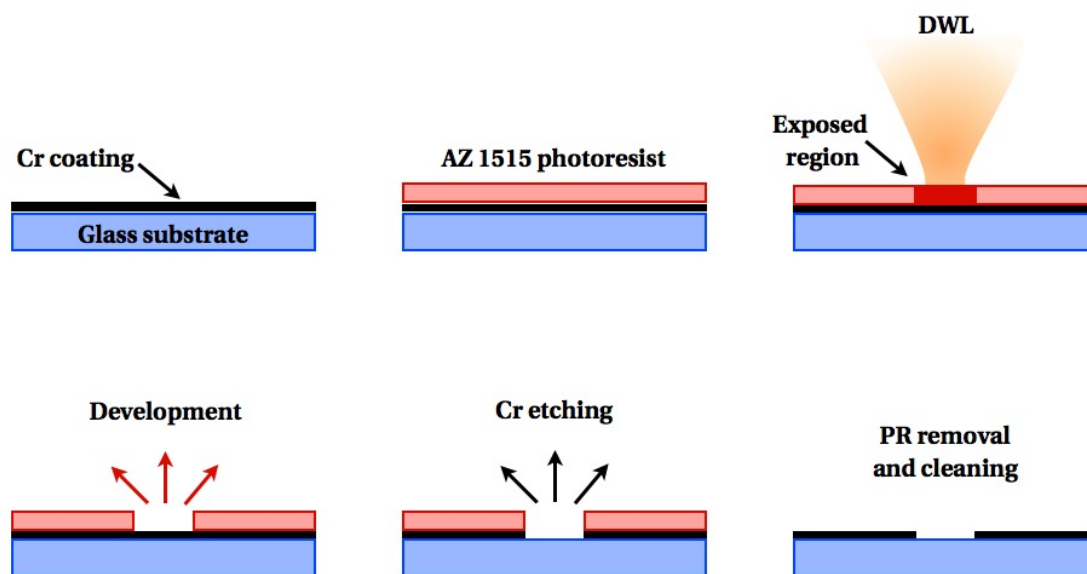


**Figure 5.6:** Fabrication of the chromium mask. A chromium (Cr) mask plate is coated with a positive photoresist (AZ1512) and exposed with a laser scanning system (Heidelberg DWL200). The development of the photoresist is then performed and the unprotected Cr regions are removed in a Cr etchant.]

### 5.3 Fabrication of the optofluidic chip

The optofluidic chip assembly follows the aforementioned steps.

- Design and etching of the photolithography mask
- Photolithography of the master moulds
- Membranes replica molding
- Chip assembly

#### 5.3.1 Design and etching of the photolithography mask

The microfluidic channel design is first drawn on a layout editor (L-Edit, Tanner EDA) and is exported to the GDSII format. The layout file is then imported into an optical pattern generator (Direct laser writing - Heidelberg DWL200) at the CMi. The chromium (Cr) blank mask plates, which consist of a 5 x 5 inches glass pieces coated with a Chromium layer, are available directly from the CMi. The CMi provides blank plates that are already coated with AZ 1512 (positive) photoresist and that are ready to be exposed with the laser scanning system. The diameter of the laser beam in the low resolution mode is 2  $\mu\text{m}$ , which sets the limit for the smallest features that can be included in the layout. The exposure of a full 5 inches chromium mask can take up to one hour in the low resolution mode and up to 3 hours in the high resolution mode. The

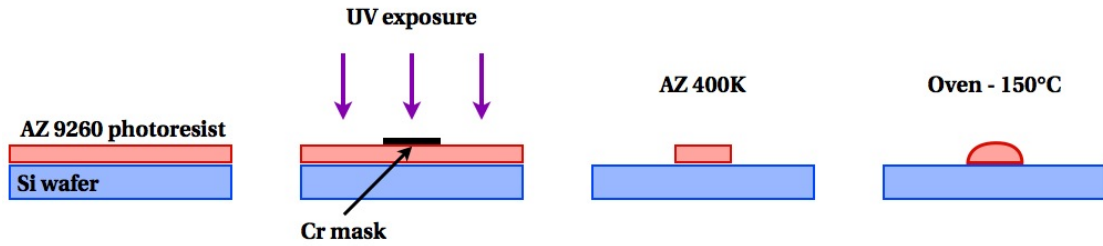


**Figure 5.7:** Schematic of the photolithography process of the transport layer master. The positive photoresist is spin-coated on a Si wafer and exposed to UV radiation through a Cr mask. The photoresist is then developed in a AZ400K solution. The wafer is finally placed in an oven to obtain a rounded structure.

large dimensions of the features in our designs (typically 100 to 200  $\mu\text{m}$ ) allow us to work in the low resolution mode and therefore limit the fabrication times and costs. After the optical pattern is exposed, the photoresist coated chromium mask is developed in the Süss DV10 machine. The regions of the mask that are irradiated with the laser diode are removed during the development process. In the next step, the plate is rinsed and is dried before it is put in a Cr-etchant solution. The regions of the Cr plate that are not protected by the photoresist are oxidized until the chromium layer is fully removed and is transparent to light. The sample is finally rinsed, dried, and spin coated with a protective AZ5214 resist layer and is diced into 4 smaller pieces of 2.5 x 2.5 inches each. The design and layout were performed by myself while the Cr mask exposure and etching were realized by my colleague Zhaolu Diao. The dicing of the mask plate was performed by Yvan Deillon at CMi.

#### 5.3.2 Photolithography of the master moulds

Each layer of the PDMS membrane is fabricated using a dedicated master made out of either positive (transport layer) or negative photoresist (control layer). The masters fabrication is entirely carried out by myself in the IPEQ clean rooms. A 5 inch silicon wafer is first oxidized for one minute in a low power  $\text{O}_2$  plasma (50W, 0.3 mbar). The wafer is then rinsed in deionized water (DI), dried with  $\text{N}_2$ , dehydrated on a hot plate at 90°C for 5 minutes and is left to cool down for 5 more minutes.

##### Transport layer master

The cleaned wafer is positioned on the spin coater. It is then covered with hexamethyldisilazane (HDMS) which acts as an adhesion promoter and spin coated for 10 seconds at 5000 rpm. A large drop of AZ9260 is then gently poured onto the wafer, avoiding the formation of bubbles, and is let to spread for a few seconds. A spin coating program is started that includes a 9 seconds ramp and a 60 seconds dwell time at 1800 rpm. The target layer thickness is 7  $\mu\text{m}$  in the central region of the wafer, which is rather thick for standard photolithography. It is

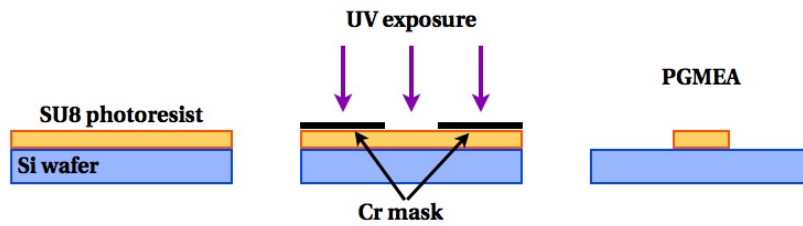


**Figure 5.8:** Schematic of the photolithography of the control layer master. The SU8 photoresist is spin-coated on a Si wafer and is exposed to UV radiation through a Cr mask. The photoresist is finally developed in PGMEA.

therefore important that the spin coating occurs in a vibration-free environment. The failure to do so leads to a wavy AZ9260 surface that prevents from achieving sharp and uniform exposure and thus high quality channels. After the spin coating step is finished, the coated wafer is placed on a hot plate for 200 seconds at 115°C for soft baking. The resist is let to cool down for a few minutes before the wafer is loaded in a Süss mask aligner. A UV exposure is performed for 80 seconds through the appropriate chromium mask fabricated as described in the previous section. Since AZ9260 is a positive photoresist, all the regions that are being exposed to the UV radiation are dissolved during development. Hence, the chromium mask is mainly transparent except for the transport channel region. The development of the photoresist is obtained by leaving the exposed wafer in a diluted AZ400K (4:1) solution for 6 minutes while continuously stirring the petri dish. The wafer is then rinsed in DI water and is dried with  $N_2$ . At this point in time, the edges of the newly formed photoresist structures are square in shape. The wafer is then put in an oven at 150°C for 90 minutes. This operation allows for the gentle softening of the photoresist, which leads to the rounding of the edges due to surface tension effects. The choice of baking temperature and time is important as a longer baking time leads to damages and cracks in the photoresist structure and shorter baking times prevent a fully rounded aspect. Further attempts to perform the reflowing of the photoresist on hot plates for various temperatures have failed to achieve good quality structures, possibly due to the non-uniform temperature distribution.

### Control layer master

A GM1060 SU8 (Gersteltec) patch is poured onto the wafer following the same precautions as in the case of the positive photoresist. The spin coating consists of a 9 seconds ramp and a 40 seconds dwell time at 1080 rpm. The targeted layer thickness is 20  $\mu\text{m}$  in the central region of the wafer. The photoresist is then let to rest for 5 minutes under the hood. The soft baking of the resist occurs in two steps. First, the coated wafer is placed on a hot plate for 180 seconds at 65°C. It is then moved onto a second hot plate at 95°C for 9 minutes. The resist is finally let to cool down for a few minutes. A UV exposure is performed for 75 seconds. The SU8 is a negative photoresist and all the regions that are being exposed to the UV radiation is preserved during development. The chromium mask for the control layer looks like narrow

transparent patterns on a mirror-like substrate. A two step hard bake is then performed, first for 1 minute on a 65°C hot plate and then for 7 minutes on a 95°C hot plate. The photoresist is then developed for 5 minutes in Propylene Glycol Monomethyl Ether Acetate (PGMEA) while maintaining continuous stirring. Finally, the wafer is rinsed in Isopropanol (IPA). Milky white suspensions can sometimes be observed around the structure. These are symptomatic of underdevelopment of the resist. In this case, rinsing in water and drying of the wafer can be performed before the wafer is placed in PGMEA for an extra 30 seconds to 1 minute time period.

#### 5.3.3 Membranes replica molding

The thin (TNM) and thick (TKM) membranes are fabricated simultaneously in the CMI+ PDMS area. Two mixtures (10.5 g and 12 g) of PDMS base and curing agent (20:1 and 5:1 concentrations) are prepared, mixed and defoamed. These operations can be performed either manually or with an automatic mixer. A typical program includes 1 minute of mixing at 2000 rpm and 2 minutes of defaming at 2200 rpm. In the case of manual mixing, an approximate 20 minutes of defoaming time must be planned in the process flow. This time can also be reduced by placing the PDMS mixtures in an ultrasonic bath. The PDMS preparations are finally degassed in a vacuum desiccator for a few minutes. In the meantime, the surfaces of the two photoresist masters are conditioned with Trimethyl-chloro-silane (TMCS) in a desiccator. The exposure to a few drops of TMCS for 15 minutes is generally enough to prevent the strong adhesion of the PDMS membranes on the silicon or photoresist surfaces. The AZ9260 master is placed on a spincoater and covered with the 20:1 PDMS mixture. The spin coating program includes a 10 seconds ramp and a 40 seconds dwell time at 2500 rpm. The coated master is then placed in an oven at 80°C for 30 minutes. Similarly, the SU8 master is spin coated with the 5:1 mixture for 40 seconds at 500 rpm. It is then placed in the same oven for 30 minutes.

#### 5.3.4 Chip assembly

A large patch of the TKM surrounding the control channels is carefully cut with a scalpel and is peeled off the wafer. The flexible membrane is then gently deposited on top of the TNM following alignment marks. It is important that any bubble between the two membranes is removed. This is usually facilitated by the excellent conformal adhesion of the two surfaces. The superimposed membranes are then placed in the 80°C oven again for another 30 minutes time period. The difference in curing agent concentrations between the two mixtures used leads to the bonding of the two layers due to residual migration of the agent. It is therefore very important that the superimposition operation is carried out as soon as possible after the mixtures are prepared.

A 10 mm long, 5 mm wide and approximately 4 mm high piece of bulk PDMS is prepared while the membranes are cooling down. Both the bulk PDMS piece and the two layers assembly are

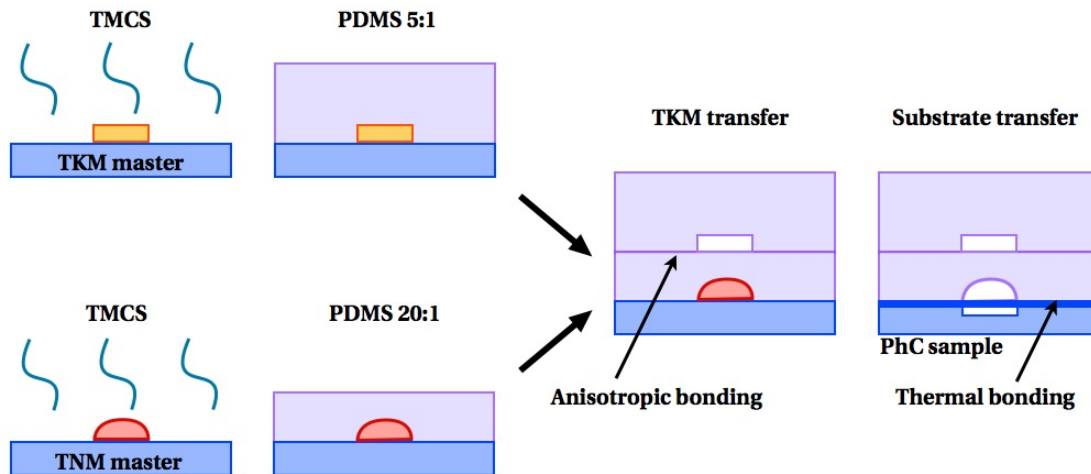


**Figure 5.9:** Schematic of the assembly of the PDMS membranes. The TNM and TKM are prepared separately on TMCS treated masters. The TKM is then cut and transferred onto the TNM. The difference in curing agent concentrations allows for a strong binding between the two membranes. The assembled 170  $\mu\text{m}$  membrane is finally cut, peeled and manually transferred onto the PhC sample.

placed in an oxygen plasma chamber for a low power oxidation (50W, 0.3 mbar, 1 minute). The bulk PDMS block is then positioned on top of the control channels ends in such a way that the oxidized face is in contact with the top surface of the membrane. The bonding that is obtained through oxygen plasma oxidation is permanent and almost instantaneous. The positioning of the block must therefore be as accurate as possible. The full assembly is then placed in the oven at 80°C for 30 minutes.

The wafer carrying the two superimposed membranes and the PDMS interconnect is let to cool down for 10 to 15 minutes. The membrane is then cut, under binoculars, using a razor blade to the exact dimensions (10 mm x 30 mm). It is then carefully lifted-off from the wafer and is flipped upside-down before it is placed on a Polytetrafluorethylene (PTFE) substrate. Two main precautions should be taken during the lift-off operation. First, it is important to verify that the razor blade has effectively cut the PDMS down to the silicon wafer and separated the membrane from the rest of the PDMS layers. Incomplete separation can lead to the tearing or deformation of the final membrane when it is lifted off. Second, the lift-off should be performed by maintaining the membrane as flat as possible and without pulling it too strongly to avoid irreversible stretching of the polymer.

Injection holes are finally punched through the membrane and PDMS block using Harris Unicore biopsy punches at the end of each channel. After this last operation is performed, the final microfluidics device is manually positioned on top of the silicon substrate under binoculars. Alignment tolerances are  $\pm 70 \mu\text{m}$  in the width and  $\pm 1.5^\circ$  for the axis angle formed by the PhC structures and the transport channel. This operation is very delicate especially due to the fragile nature of the PhC membranes. The stiction of the PDMS membrane is strong enough to snatch the silicon nano structures in case of an attempt to peel a badly aligned



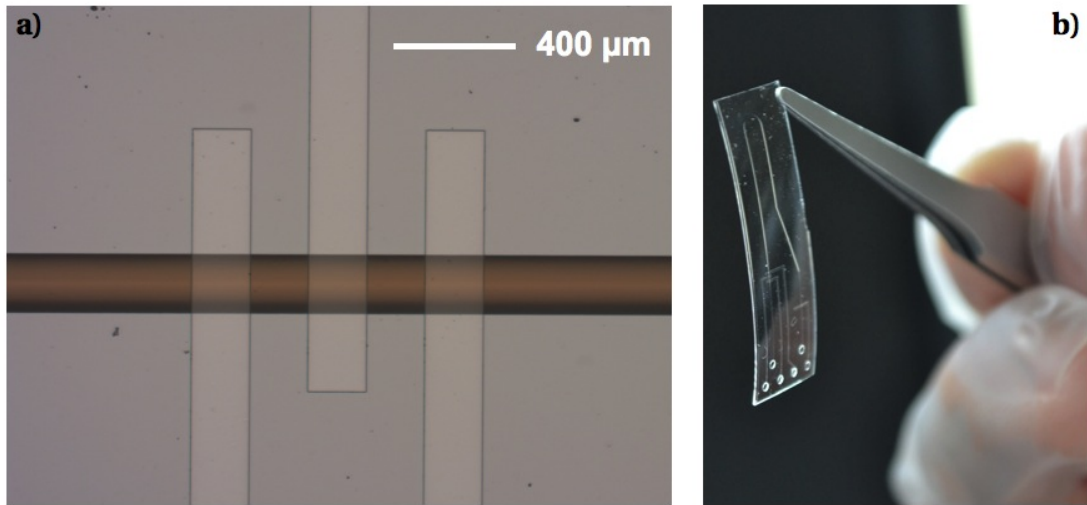


**Figure 5.10:** Assembly of the two-layers PDMS membrane. a) Optical micrograph of the control valves after manual positioning of the TKM on top of the TNM. The horizontal brown structure corresponds to the rounded AZ9260 master. The centering of the control channels above the transport channel is accurate to approximately 100  $\mu\text{m}$  during the manual process. b) Photograph of the two-layers PDMS membrane during substrate transfer.

channel. Once the positioning is finished, the completed sample is placed for an hour in the 80°C oven and is finally left to rest overnight before any connection attempt.

#### 5.3.5 Some important aspects in fabrication

The successful assembly of a chip not only relies on the accurate following of the recipe described in this chapter but also involves a number of details and methods that have been acquired through trial and error over the time of this thesis. Most of these details are related to the great care that should be taken when manipulating the membrane in order to avoid tearing or contamination for example. The manipulation of the spin coated wafers to ensure flat PDMS surfaces necessary to good conformal contact between the layers and thus efficient bonding is another important aspect. It also concerns the atmospheric conditions in the clean room which have been found to be of significant importance on the polymerization conditions of PDMS and the electrostatic behavior of the membrane. It is not possible to report on all the details in this thesis. Nevertheless, the choice of the height of the channels and the bonding of the PDMS interconnect is of critical importance and is described.

Originally, the height for both the transport and control channels was chosen to be 10  $\mu\text{m}$ . Unfortunately, a large fraction of the prototypes that have been fabricated with these values turned out to be non-functional. Two types of defects were observed on almost 60 % of the devices, all of which were located near the control valves: PDMS/PDMS stiction points and Si/PDMS stiction points (see Figure reffig:stiction). In the case of a PDMS/PDMS stiction point, the thin membrane is stuck onto the upper face of a control channel within a valve. As a

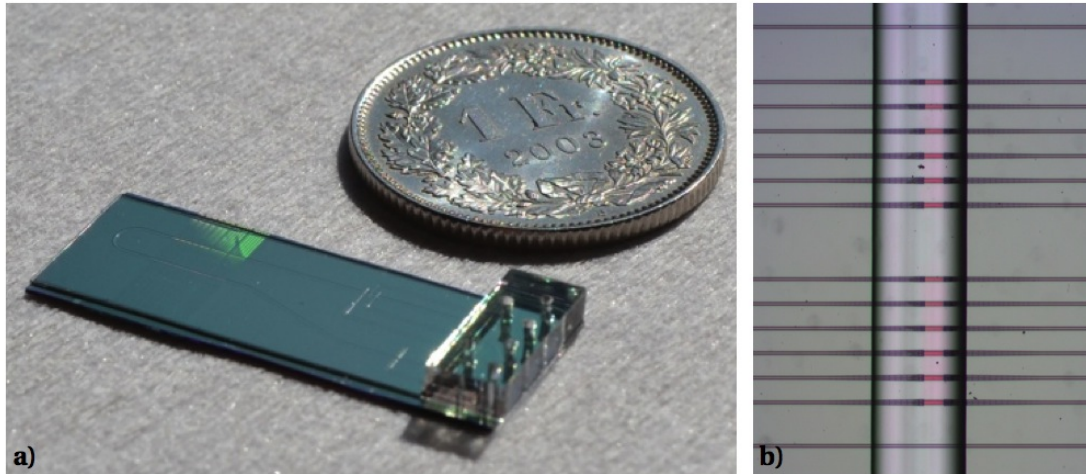


**Figure 5.11:** Assembled optofluidic chip. a) Photograph of the assembled optofluidic chip. The chip is composed of the Si-PhC substrate (green iridescence can be observed from the input waveguides), the thin two-layers PDMS membrane including transport and control channels, and finally a bulk PDMS interconnect. The chip is 30 mm long, 12 mm wide and 4 mm high. b) Optical micrograph of the PhC structures inside the transport channel after manual deposition of the two-layers membrane. The picture shows an offset of the PhC devices (in red) less than 50  $\mu\text{m}$  from the channel axis.

consequence, the affected valve cannot be closed using pressure values below the delimitation threshold of the two-layers membrane. Although the presence of one faulty valve in the peristaltic pump can be overcome, a faulty brake valve could prevent any resonant optical trapping experiment to be performed since the residual flow in the transport channel might be too large. This defect usually appears either when peeling the two-layers membrane off the AZ9260 master or during Plasma oxidation of the membrane before the positioning of the interconnect. Many methods have been investigated in order to release the TNM either manually or by injecting high pressure (up to 0.07 MPa / 10 PSI) surfactant solutions in the control channel for several hours, with little success. Similarly, Si/PDMS stiction points can appear inside the transport channel either at the integrated valves or near the PDMS interconnect. This defect results in an increased injection pressure and might prevent injection completely. The failure to notice the presence of the defect can end up in the lifting of the microfluidic membrane off the silicon substrate. In order to avoid these defects, a variety of combinations for the transport and control channels heights have been attempted. The final values of 12  $\mu\text{m}$  (transport) and 18  $\mu\text{m}$  (control) have shown the best results by allowing the fabrication of defect free devices while maintaining the height of the channels as small as possible.

Another aspect responsible for the failure of a large number of prototype samples is the partial or complete lifting of the two-layers membrane off the substrate. This lifting can be caused by two mechanisms (see Figure 5.12). First, the weight of the 6 injection capillaries, though small, along with their rigidity exerts a torque on the interconnect (Fig. 5.13.a) Even though several attempts to cancel this torque using various types of mounts have been made, the residual

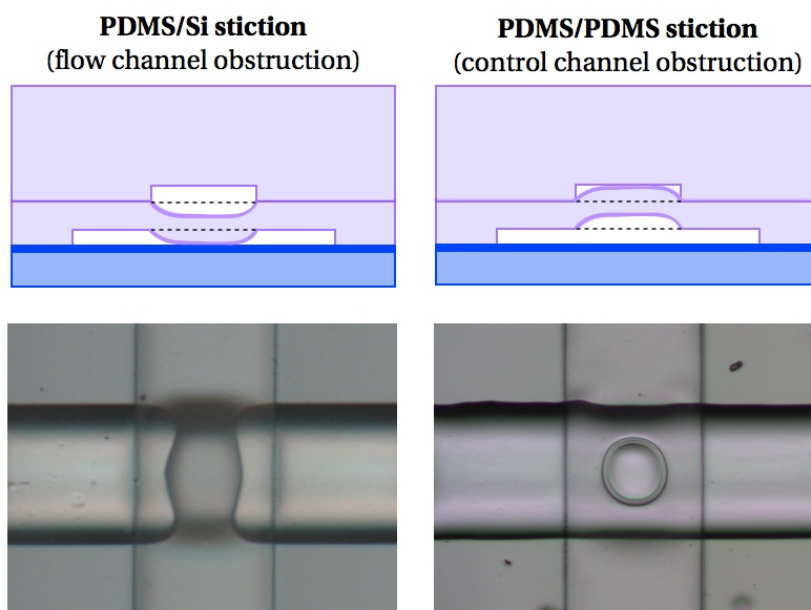


**Figure 5.12:** Valve failure due to PDMS membrane stiction. **Left.** The thin membrane collapses inside a valve and sticks to the silicon substrate underneath. This issue prevents any transport of fluid in the transport channel. **Right.** The thin membrane lifts and sticks to the above thick membrane inside a valve. The control channel is obstructed and the valve fails to completely squash the underlying transport channel. This issue prevents the control of the transported solution.

torque is usually large enough to peel the thin membrane off the substrate within minutes. Second, the outer diameter of the capillaries must be slightly larger than the inner diameter of the cored hole in the interconnect. This is to ensure the perfect sealing of the interconnect even at pressures greater than 10 PSI. This efficient sealing is possible because the PDMS is quite elastic, and hence tightly surrounds the capillaries. This comes with the associated downside that the 6 capillaries, which are quite densely distributed (6 capillaries of 1 mm diameter on a 5 mm x 10 mm rectangular surface), results in the fact that the bottom surface of the PDMS block is also slightly deformed (Fig. 5.13.b). These deformations are small and hardly noticeable with the naked eye. Nevertheless, they are sufficient to prevent a conformal contact between the PDMS surface and the silicon substrate weakening the thermal bonding. The most frequent cases of failure come from leakages between two adjacent channels, although cases of complete lift-off of the membrane have also been observed. A method to prevent these issues is the addition of an intermediate step after the final substrate transfer, just before the final baking in the oven. The two-layers membrane and bulk PDMS interconnect assembly is carefully lifted of the PhC substrate under binoculars using a pair of tweezers. It is important that the membrane is lifted over the entire length of the interconnect and a few millimeters further without being folded in order to not damage the membrane. The sample is then leaned forward in such a way that both the naked silicon region and the naked PDMS surface point towards the roof. This is realized using a specially designed mechanical mount. The sample is then placed in the plasma oxygen chamber and is oxidized for 1 minute (50 W, 0.3 mbar). After

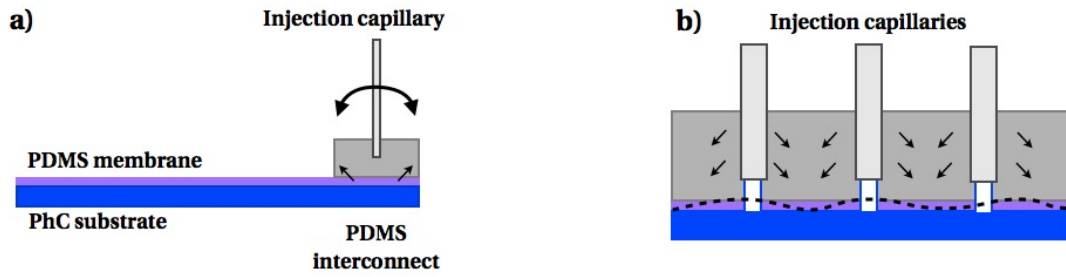


**Figure 5.13:** Interconnect induced membrane lifting. a) The torque exerted by the injection capillary causes the partial or complete lifting of the PDMS membrane underneath the interconnect. b) The deformation of the PDMS block induced by the presence of 6 capillaries in a compact distribution causes the local lifting of the membrane underneath the interconnect. This issue can result either in channel to channel leakages or partial lifting of the membrane.

the oxidation, the membrane is gently placed again on the PhC substrate. This operation is critical and must be successful from the first attempt since the oxidized Si to PDMS bonding is irreversible. The sample is finally placed in the oven as described in the previous section. The main benefit of this operation is that the interconnect is very robust, can withstand pressures much larger than 10 PSI without lift-off and prevents the lifting of the membrane through torque or deformation of the bulk PDMS. However, it comes with two major drawbacks. First, it adds a complicated manual operation to the process flow which can result in the loss of the PhC sample if unsuccessful. Second, it prevents the PhC substrate to be reused after the microfluidic circuit stops being operational.

## 5.4 Actuation and performance

### 5.4.1 Pneumatic control system

The developed optofluidic sample includes 6 ports: two ports for the input and output of the colloidal nanoparticles or flushing agents and four ports for the pneumatic control of the flow inside the channel. A pressure source common to both the injection and control systems is used and it derives from the liquid nitrogen evaporation circuit of the Physics department. This circuit provides a consistent 10 bar pressure of  $N_2$ . This pressure source is then distributed over three different pressure regulators (Bellofram, Type 10) as illustrated on Figure 5.14. The first one sets the injection pressure in the transport channel. Some over pressure (from atmospheric pressure) is necessary when injecting a new sample due to the hydrophobicity of both the silicon and the PDMS. This over pressure can be very small and it has been found that a few tens of centimeters in height difference between the plane of the sample and the plane of the fluid reservoir is often enough to infiltrate the transport channel. In working conditions, the injection over pressure is minimized in order to eliminate any residual flow during resonant trapping experiments. The 0.01 to 0.17 MPa (2 to 25 PSI) range of pressures available (above atmospheric pressure) in the injection circuit is therefore not

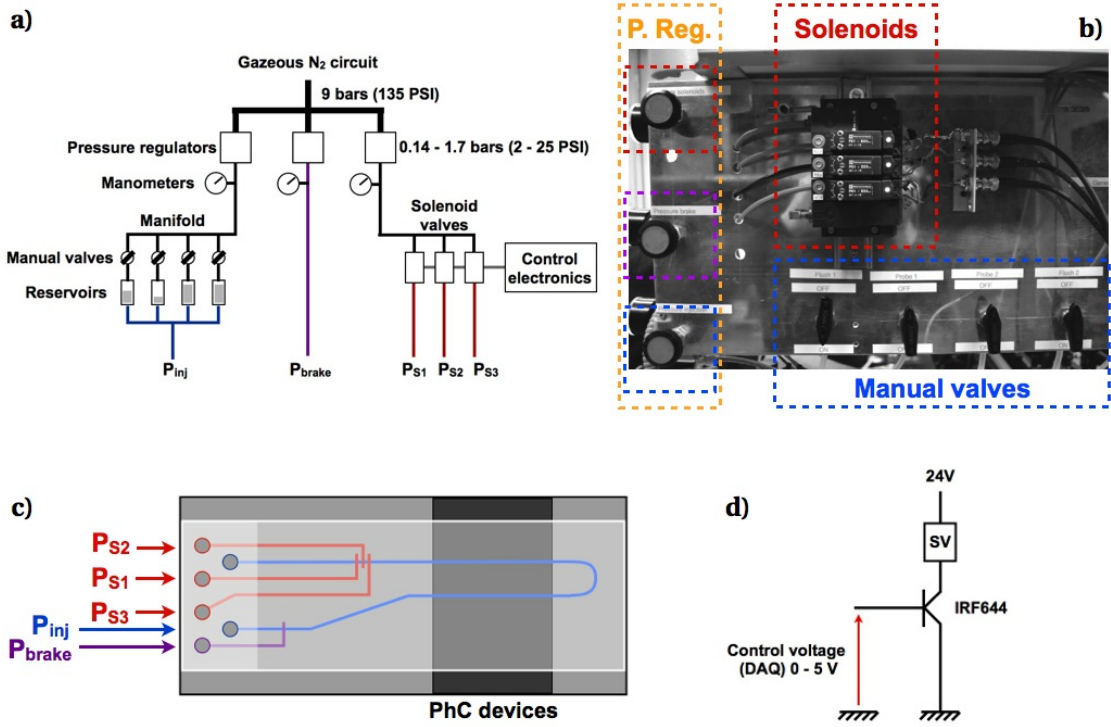


**Figure 5.14:** Description of the injection and pneumatic control system. a) Schematic of the three different pressure controlled circuits regulating the injection within the transport channel, the input to the solenoid valves and the "brake" valve. b) Photograph of the pressure control board as implemented on the optical trapping test bench. c) Schematic of the microfluidic circuit and input ports for the trapping samples. d) Diagram showing the electronic control of one solenoid valve (SV).

absolutely required for the operation of the device but it turns out to very practical for flushing and decontamination operations.

The second pressure regulator sets the pressure that drives the control channels. The typical working pressures are in the 0.03 MPa (5 PSI) to 0.05 MPa (7 PSI) range. The pressure is input in a set of normally-closed solenoid valves (PS1E11 and PS1E23, Telemecanique). An in-house electronic board with a DAQ (USB 6009, National Instruments) is used to control the opening and closing of the electro-valves from a Labview program (Figure 5.14 .d). The three control channels can be operated simultaneously. In their OFF state, the output of the solenoid valves is at atmospheric pressure. In their ON state, the regulated input pressure is injected inside the control channels causing a squashing of the transport channel and hence realizing a valve. Activated in a sequence, the three control channels act as a peristaltic pump that allows for the injection of very small and repeatable quantities of fluid inside the transport channel. Various sequences can be implemented which are usually referred to as "60, 90 or 120 degrees" cycles (in the case of three valves) depending on the dephasing between each valve. The main difference between them is the number of steps, the volume pumped per cycle and the possibility of some reflux flow during the switching of the state of the valves. The 120 degrees



cycle was used during this work

The third regulator is directly connected to the fourth control valve located at the output of the transport channel. It allows for the manual adjustment of the pressure in the valve and therefore acts either as a flow brake or a flow stopper. This component is very useful in resonant trapping experiments since it permits the isolation of the fluid containing the particles investigated from the outside world. In particular, it allows to reach a zero residual flow state in the transport channel for several tens of minutes.

### 5.4.2 Valving and flow speeds

The realization of a thin PDMS transport channel above the photonic crystal devices concerns only one of the objectives to be achieved. The demonstration of the resonant optical trapping also imposes the ability to stop or reduce the speed of the particles traveling through the channel, at least in the region near the PhC cavities. Following the precious inputs from Prof. Sebastian Maerkl, a set of integrated valves have been added to the design of the microfluidic circuit.

If the transport channel is injected with the smallest over pressure necessary, particles move at approximately  $150 \mu\text{m/s}$  in the transport channel that corresponds to flow speeds of the order of  $500 \text{ pL/s}$ . Although this value seems reasonably small, it means that it takes less than a second for a particle to cross the entire field of the oil-immersion microscope objective imaged on the EMCCD camera. At these speeds, fluorescent particles appear as very faint lines on any recorded video, and reveal the laminar nature of the flow in the transport channel. It is therefore impossible that a particle gets randomly captured in the resonant trap. Similarly the drag force of the flow on a particle is orders of magnitude stronger than what would be achievable with the auxiliary optical tweezers.

Figure 5.15 shows the optical micrograph of a pneumatic valve being operated. The transport channel (in blue) carries the colloidal particles between the TNM and the silicon substrate towards the PhC region. The control channel in red is filled with an aqueous solution whose pressure is controlled by the solenoid valves and the Labview program. When the pressure in the transport channel is higher than that of the control channel, ( $P_{inj}=P_{control}+0.03 \text{ MPa}$ ) the solution containing the particles crosses the integrated valve freely (Figure 5.15, left frame) . If the solenoid valve is activated, the control channel receives a pressure of  $0.05 \text{ MPa}$  above the atmospheric pressure that deforms the TNM up to the point where the flow in the transport channel is completely disrupted (right frame of Figure 5.15). It is also possible to observe that the TNM is being squashed against the silicon substrate on the picture.

The use of a single integrated valve allows for the control of the transport flow from a few nanoliters per second down to almost zero. This is important for the flushing of the photonic structure, and the calibration of optical forces. This is also a way to diagnose whether the channel is not becoming obstructed. Nevertheless, it is not efficient enough to reach zero flow

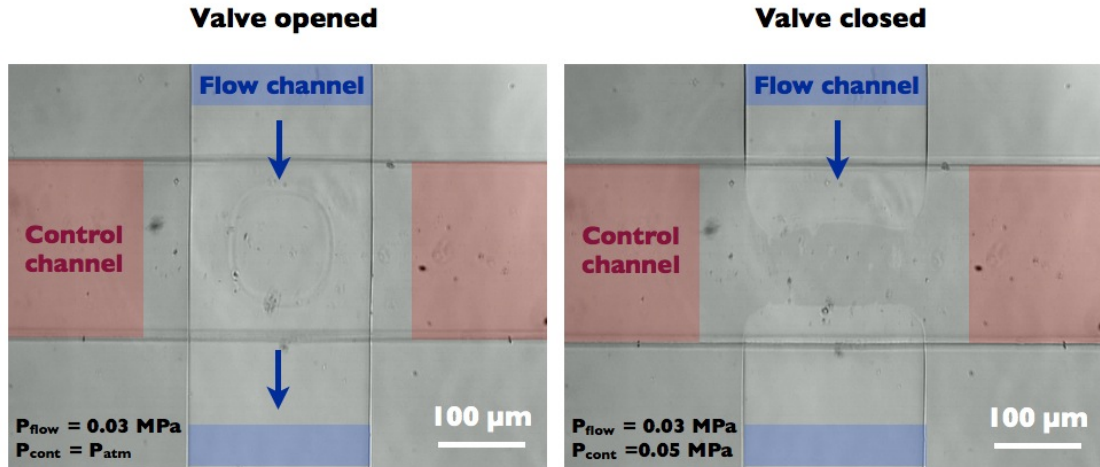


**Figure 5.15:** Actuation of the integrated valves. Optical micrographs of an integrated valve composed of a control channel (red) positioned above and perpendicularly to the transport channel (blue). For control pressures lesser than or equal to the transport pressure, the valve is open (left frame). For pressures higher than the transport pressure, typically 0.02 MPa above, the TNM is deformed and squeezed against the silicon substrate, thus closing the transport channel (right frame).

or residual flow values that are compatible with the resonant optical trapping experiment. Figure 5.16 shows the influence of the injection pressure on the speed of the particles within the transport channel and the associated estimated flow through the channel (blue markers). The experimental points correspond to the average speed of a set of particles, while the error bars indicate the minimum and maximum values recorded. A large dispersion can be observed due to the hydrodynamic dispersion of speeds in the channel, which make particles closer to the surface of the channel travel slower than those located at a further distance. The blue and red dashed lines only constitute a guide for the eye. The red markers indicate the possibility to use one control channel to slow down the solution through the transport channel by compressing it down to complete closure.

One closed valve is not enough because of the dynamic effects that are observed if only one side of the channel is closed. The dynamical effects include oscillating flows (changing direction) and very large particle speeds (of the order of a millimeter per second). There are several explanations possible for these effects, such as the elasticity of the PDMS and channel resistance leading to oscillations, inertia of the fluid in the long capillaries, and evaporation pumping. These effects have not yet been investigated. Dynamic effects can be minimized by:

- Working with low injection pressures
- Leaving long relaxing times between flow control operations and trapping experiments
- Having the capillaries as flat as possible
- Having the end of the output capillary plunged in water

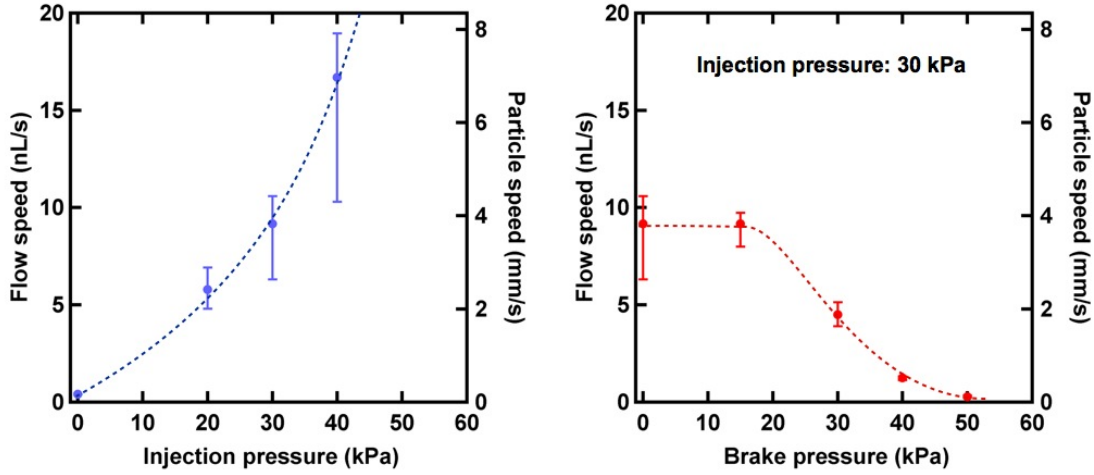


**Figure 5.16:** Typical flow speed achievable in free injection and slowed injection modes. Experimental measurement of the influence of injection pressure (blue) and control valve pressure (red) over the flow speed in the transport channel. Flow speed are estimated by measuring the speed of a set of particles in the fluid over a distance of 15 mm corresponding to traveling times between 2 to 45 seconds. The error bars presented correspond to the slowest and fastest particles recorded for a given injection and control pressure, while the marker corresponds to the average velocity of the set. The blue curve is recorded by increasing the injection pressure in steps. Pressure in the four control channels are kept equal to the the injection pressure. The red curve is recorded by setting the injection pressure and the three input (peristaltic) control channel at 0.03 MPa. The pressure within the output (brake) control channel is then gradually increased until closing of the valve is achieved (around 0.05 MPa).

The current solution for this problem is obtained by the simultaneous closing of all the valves (peristaltic pump and brake). In this case, the solution located in the PhC region is completely isolated from the outside input/output circuitry and the particles recover standard Brownian motion. Figure 5.17 shows the tracking of three separated 500 nm particles in the transport channel a few seconds after the four valves have been closed. The tracking is performed using a free centroid tracking software [196]. Figure 5.17 corresponds to the calculated position of circa 900 centroids obtained from a 30 seconds video acquisition at a frame rate of 30 fps. On these figures, it is clearly possible to observe the random walk of the particles. The position (0,0) corresponds to the relative centroid position of each particle as calculated for the first frame (also indicated as Starting Position - SP). A closer analysis indicates a small but consistent drift of the three particles, not perceivable directly on the video, which tends to demonstrate the existence of a minor residual flow. The distance between the starting and finishing points (FP) allows for an estimation of the drift to roughly 150 nm/s corresponding to a residual flow of lesser than 0.4 pL/s. This value is 1000 times smaller than the slowest flow achievable in the non-controlled configuration (no use of the valves). Earlier experiments have shown that residual flows lesser than  $\approx 5$  pL/s still provides acceptable working conditions.



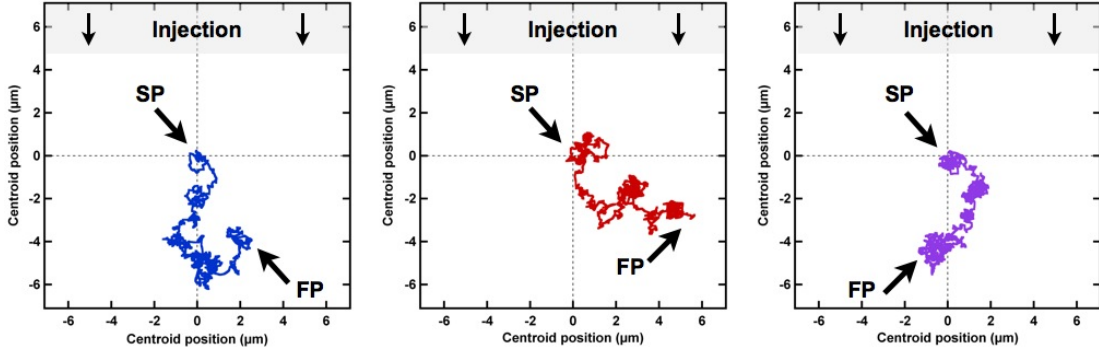


**Figure 5.17:** Residual flow in isolated mode. A set of three fluorescent particles has been tracked for over 30 seconds at 30 fps using a centroid algorithm after the three (peristaltic) input valves and the output (brake) valve have been closed. The random walk of the three particles over 1000 positions can be clearly observed validating the usefulness of this configuration for resonant optical trapping experiments.

### 5.4.3 Sample lifetime

The lifetime of the sample is the last important criterion in terms of performances. As previously mentioned, the main reason for this is the necessity to repeatedly perform trapping experiments over long time periods of several weeks or months with the same devices. Despite the high quality and precision with which PhC structures that have been fabricated, small variations exist from one sample to the next. This makes comparison of the trapping experiments with different samples very complex. The ability to work with the devices on the same sample for several days is therefore critical. The need for long lifetime samples is also imposed by the large fabrication times required for each sample. Using current procedures, it takes approximately two weeks for Z. Diao or M. Tonin to obtain a state-of-the-art 30 mm x 12 mm membraned photonic crystal sample. It then takes two to three days to fabricate, deposit and connect a fully functional microfluidic circuit on top of it. These times include the machine calibration times for e-beam lithography and dry-etching steps, as well as the fabrication times of dummy microfluidic samples that are a close to the designed parameters.

During this work, two complete optofluidic samples have been fabricated. Their design parameters are almost identical, the only difference lies in the height of the control channels, which are higher (20  $\mu\text{m}$ ) for the latest sample. The first of these samples remained functional for almost 6 months, from February 2012 to July 2012, while the second sample was connected on January of this year (2013) and is still functional (May 2013). The longevity of these samples is a great success of the design but also comes at the expense of great care and demanding maintenance.

The lifetime of an optofluidic sample can get shortened either through direct damages to the photonic devices or through impairment of the microfluidic membrane which is by far the most sensitive part. In most cases, the direct damages to the photonic crystal is caused by the collapsing of the PDMS membrane, which is described in the following paragraphs.

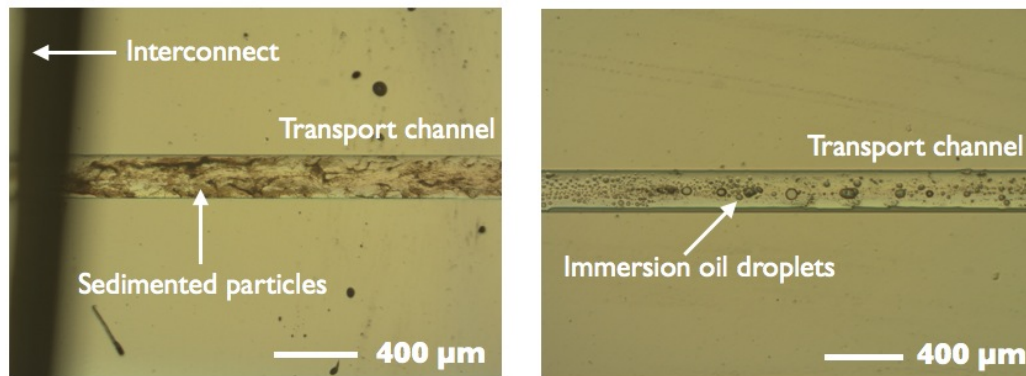


**Figure 5.18:** Example of contaminations in the microfluidic transport channel. **Left** Optical micrograph of a transport channel showing massive sedimentation of nanoparticles near the interconnect. Sedimented particles form extended agglomerates that prevent the good progression of the fluid in the channel. **Right** Optical micrograph of a transport channel contaminated with immersion oil. Droplets of various sizes can be observed at the top of the channel.

Damages to the membrane are usually related to an obstruction in the transport channel. Obstructions occur mostly due to agglomerates of nanoparticles in critical regions like valves or underneath the interconnect (see Figure 5.18 -left). They can also occur due to bacterial contamination of the microfluidic circuitry, in which case debris of various sizes (several microns sometimes) rapidly clog the channel. Alternatively oil immersion contamination can happen after long measurement times as shown in Figure 5.18 on the right panel. Although the mechanism is not clear, oil immersion seem capable to migrate through the PDMS membrane and form droplets in the transport channel. These droplets do not dissolve in water and can rapidly form a congestion.

The appearance of an obstruction in the transport channel leads to a decrease of the flow and can prevent injection completely. The failure to notice the obstruction during operations might lead the user to increase the injection pressure and can lead to the lifting of the membrane from the silicon substrate. The consequences are the irreversible distortion of the PDMS membrane and leakage. If the obstruction appears when the sample is not operated, or at least when not under observation, depressions can appear in the channel downstream from the agglomerate. It is not clear whether the depression is due to evaporative pumping at the end of the output capillary or if it occurs due to the weight of the fluid within the capillary. The effect of this depression is a slow but almost irreversible collapsing of the transport channel onto the silicon substrate. If too extended, the region where the membrane is stuck to the silicon substrate cannot be lifted again using higher injection pressures. The only solution available in this case is the manual peeling, drying and repositioning of the membrane. This operation has worked once but generally leads to the damaging of the photonic devices. Moreover, the new PDMS to silicon bond is much weaker than the original one.

Unfortunately, at this point of time, there is not a single solution to the formation of agglomerates in the channel but there are a set of measures that can be taken to prevent them.

- The addition of 0.1 to 1% surfactant (Triton X100) in the solution carrying the nanoparticles has proven to be very successful at reducing sedimentation. Long, high injection pressure (0.05 MPa), flushing times of the transport channel with a DI water and 1% surfactant solution have also shown to be useful after operations are finished.
- It is important that the entire fluidic circuit (reservoirs, pipes, capillaries, valves) are kept free for bacterial and or fungal contamination. This can be achieved by regularly cleaning the circuit with a 70% isopropanol solution or a 10% chlorine solution. The latter has been used once successfully but the 70% IPA solution is usually preferred as the effect of chlorine on PDMS is not known.
- No solution has been found yet regarding the prevention of immersion oil contamination. One idea to get rid of this issue would be to either replace the TKM with a glass layer or replace the TKM by another thin PDMS membrane and an extra glass layer, approximately 100  $\mu\text{m}$  thick. This would add rigidity and robustness to the microfluidic assembly, improve optical imaging (see next chapter) and suppress the oil permeability issue of PDMS. Nevertheless, when the channel is contaminated, long flushing times (typically overnight) of the channel with an IPA and DI water solution have shown good results so far. On the contrary, surfactant solutions and DI water solutions are usually quite inefficient.

## 5.5 Limitations and alternative approaches

The microfluidic membrane developed over the time of this thesis has proven to fulfill all the experimental requirements necessary to the successful demonstration of resonant optical trapping. Samples can now be fabricated and operated consistently following the described procedure within a few weeks from the PhC mask design. Nevertheless, a few downsides still exist for this method for which a variety of improvements or replacements have been envisaged. In this paragraph, the three most important aspects that are believed to deserve further investigations will be presented. A description of the current limitation along with the means that have been imagined and/or developed is provided regarding namely:

- The optical quality through the PDMS membrane
- The difficulty linked to the addition of the interconnect
- The large size of the samples used

### 5.5.1 Optical quality

The quality of optical imaging through the microfluidic circuit is obviously one of the most important parameters. It not only impacts the imaging and characterization of the PhC devices but also dictates the accuracy in the position tracking of nanoparticles and the efficiency of

Characteristics	Leica PL APO (specified)	US 6519092 B2 (computed)
Numerical aperture	1.4	1.4
Magnification	100x	100x
Eq. focal length	2 mm	1.998 mm @ 588 nm
Working distance	0.15 mm	0.148 mm @ 588 nm
Coverslip correction	0.17 mm	0.17 mm

**Table 5.1:** Comparison of manufacturer specifications and modeled characteristics for the oil immersion objective

the optical tweezers. The original design of the thin PDMS membrane was chosen to mimic the thickness of a standard microscope glass coverslip. This approach has turned out to be successful offering high quality imaging conditions along with optical trapping and sub- 20 nm tracking of fluorescent 500 nm particles. Nevertheless, the difficulties encountered to trap smaller dielectric particles of the order of 250 nm diameter led us to investigate in further details the influence of a 170  $\mu\text{m}$  layer of PDMS on the optical quality.

One method to perform this study is to model the optical train using a ray tracing software and monitor the variations of the optical quality when varying the refractive index and thickness of the microfluidic layer. The modeling of a microscope objective is usually made complicated by the absence of public documentation regarding the fabrication data available from the manufacturers. Nevertheless, high performance designs are generally patented before the industrialization phase mentioning explicitly radii of curvature, distances, refractive indices and Abbe numbers used for the ray tracing calculations. It is therefore possible to reconstruct models that have the exact or at least very close specifications compared to the purchased objectives.

For this work, data from US Patent 6519092 B2 assigned by Nikon have been used to reconstruct a model having exact specifications (with respect to fabrication tolerances) to the oil-immersion Leica Plan Apochromat objective used in experiments. These performances are summarized in Table 5.1. The computed values are obtained from the ray tracing software after inputting the optical parameters from the patent without any further operation or modification.

Based on this model, it is possible to study the influence of the PDMS thickness on the quality of the imaging. A light source is located at infinity (in the sense of the ray tracing software) and rays are collected through the entrance pupil of the modeled microscope objective. For the sake of simplicity, calculations are performed only for a monochromatic illumination at 588 nm and for incoming rays parallel to the optical axis. The simplicity of the model constructed imposes the choice of a simple figure of merit for the optical quality. A common criterion to evaluate the amount of aberration existing in an optical system is the "ray aberration" and the principle is quite straightforward. A ray is launched from the entrance pupil (EP) of the modeled system. The position is given in EP normalized units where (0,0) indicate the

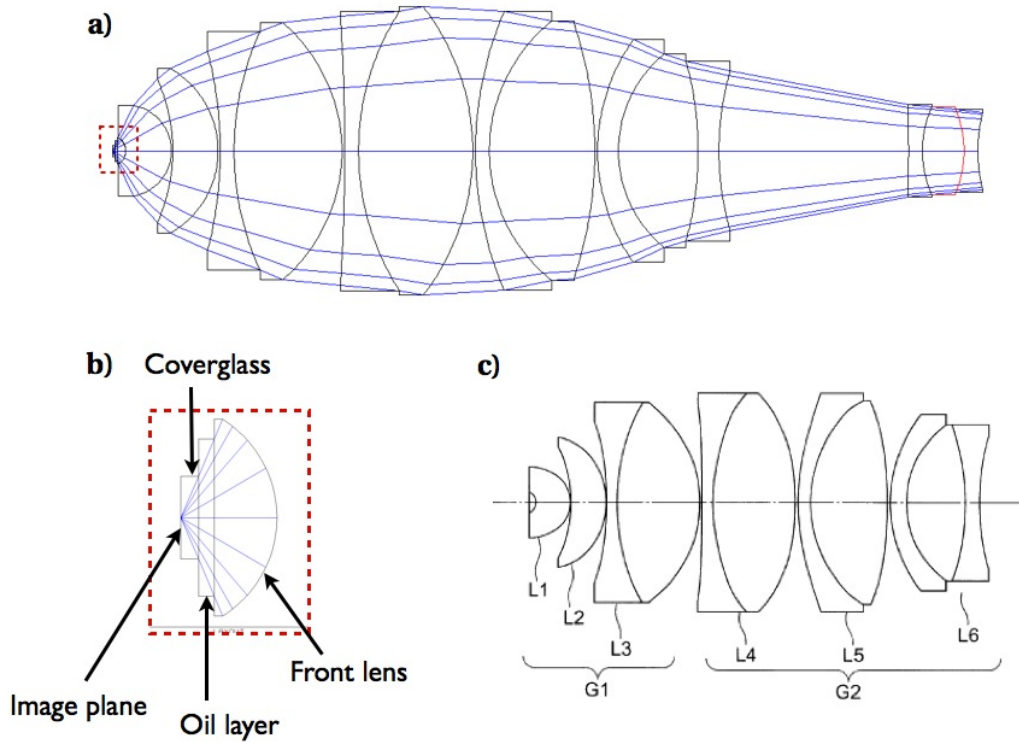


**Figure 5.19:** Description of the modeled microscope objective. a) Layout of the ray tracing model. Light propagation is taken from right to left. b) Detailed schematic of the front lens, oil immersion layer and cover glass region as simulated in the model. c) Layout of the microscope objective as published in the original patent displaying a clear similarity to the reconstructed model.

optical axis and the unit circle indicates the set of the farthest points from the optical axis from which a ray can be launched that will reach the image plane after having travelled through the entire system. Rays emerging from the EP unit circle will reach the image plane with the largest angle of incidence (as taken from the optical axis). Simultaneously, the theoretical (ideal) impact position for that ray is determined for the ideal aberration-free system with equivalent characteristics. In the case of paraxial rays like in this model, this position is (0,0) in coordinates of the image plane. All incoming rays should intersect with the optical axis in the image plane according to the exact stigmatism principle. The ray aberration corresponds to the distance between the ideal (geometric) impact position of a ray and the impact position of the real ray determined by the ray tracing software. For example, a real diffraction limited system will see all the paraxial rays emitted from its entrance pupil intersect the image plane at a distance close to or smaller than the Airy radius calculated for the corresponding wavelength. It should be noted that in the case of a non-rotational symmetric optical system (including folding mirrors or cylindrical lenses), both the sagittal and tangential ray aberrations should be plotted in order to evaluate the optical quality of the system. In this case, the system has an axial symmetry and only a single ray aberration diagram is sufficient.

Figure 5.20 a) shows the ray aberration calculated for a variety of PDMS layer thicknesses after

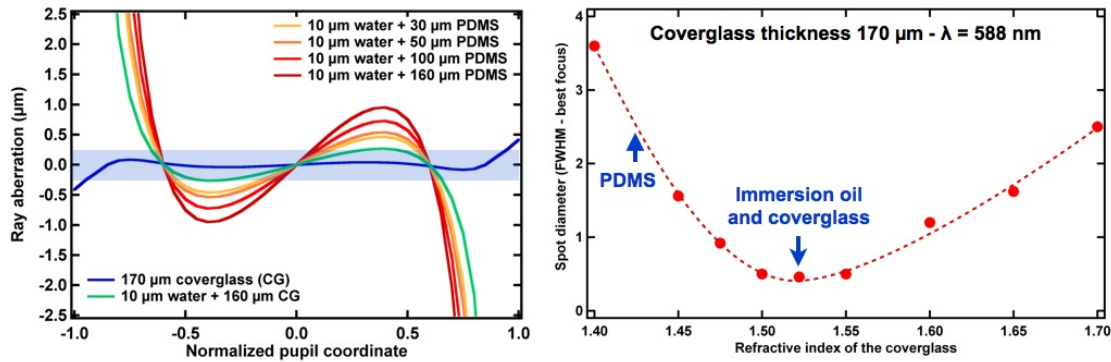


**Figure 5.20:** Influence of the PDMS layer thickness on the quality of optical imaging. Left - Calculation of the ray aberration for a variety of PDMS thicknesses and a 10  $\mu\text{m}$  water channel. The calculated aberrations are compared to the levels obtained for the diffraction limited objective when imaging through a 170  $\mu\text{m}$  borosilicate coverslip (blue curve) and to a 10  $\mu\text{m}$  water channel covered with a 160  $\mu\text{m}$  borosilicate coverslip (green curve). Right - Influence of the refractive index contrast of a 170  $\mu\text{m}$  layer on the diameter of a spot formed in the image plane of the modeled oil-immersion microscope objective.

the correction of the defocus (optimization of the coverglass to front lens distance). The merit function used for the focus optimization is the same for all the configurations calculated and consists of a basic 10 points RMS centroid minimization. Figure 5.20-left shows the 170  $\mu\text{m}$  float glass coverslip ray aberration (blue curve) displaying diffraction limited performance. The blue area shows the theoretical diffraction limited Airy diameter at 588nm. The green curve corresponds to the introduction of a 10  $\mu\text{m}$  high channel immersed with water inside the coverslip. It can be noticed that the presence of this thin layer of water, that can hardly be avoided in a microfluidic experiment, has a detrimental effect on the imaging quality. Although it is possible to find a focusing position where the low numerical aperture rays (below 0.6 normalized pupil coordinates) can be considered as limited by diffraction, the introduction of a low refractive index material layer underneath the higher refractive index cover glass or polymer leads to total internal refraction of the larger angle rays and a reduced effective numerical aperture. It can be intuitively understood that the effective numerical aperture is limited by the last immersion medium, in this case water, giving a maximum NA of approximately 1.3 for a perfectly corrected system. Nevertheless, Fig. 5.20-left) shows that the large amount of spherical aberration introduced at the glass/water interface prevent rays of normalized pupil coordinates (NPC) larger than 0.6 to reach the image plane within a reasonable distance from their ideal target. This corresponds to a significant reduction of imaging quality that can be roughly associated with a lower effective numerical aperture of the order of 0.8 (compared to 1.4 expected with the oil immersion objective).

The 160  $\mu\text{m}$  glass layer is then replaced by a PDMS layer of increasing thickness, from 30 to 160  $\mu\text{m}$  (yellow to dark red curves). A 10  $\mu\text{m}$  of water and 160  $\mu\text{m}$  of PDMS situation corresponds to the actual configuration implemented on the resonant optical trapping sample. It can be observed that the addition of this layer contributes only further to the decreasing of

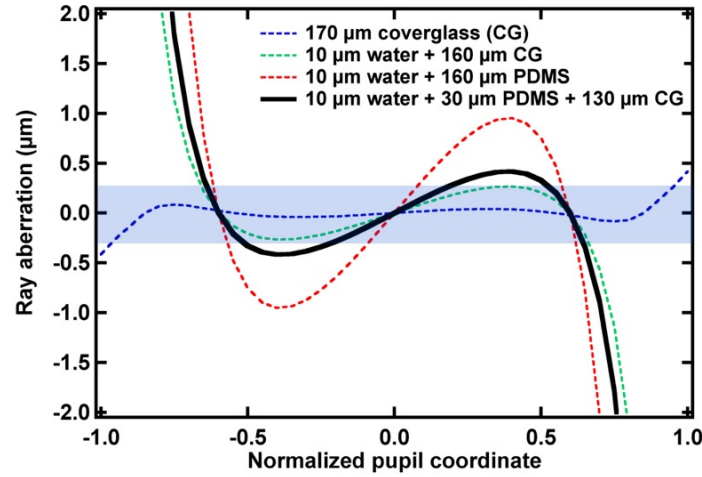


**Figure 5.21:** Comparison of the calculated ray aberration between the current PDMS/PDMS structure and the proposed Glass/PDMS approach. The red dashed curve corresponds to the ray aberration calculated for the 160  $\mu\text{m}$  PDMS membrane while the solid black line corresponds to the 30  $\mu\text{m}$  PDMS / 130  $\mu\text{m}$  glass structure.

the optical quality and hence the lowering of the effective numerical aperture. This can be intuitively understood with the help of Figure 5.20-right. This figure shows the evolution of the spot diameter, taken at its full width at half maximum, of a uniform beam of light coming from infinity through the modeled objective and filling the entrance pupil as a function of the refractive index of the 170  $\mu\text{m}$  coverglass. For a cover glass of 1.52 refractive index like standard float glass (borosilicate) microscope coverslips, there is no refractive index contrast between the last surface of the front lens (Figure 5.19), the immersion oil (refractive index 1.52) and the coverglass. The rays exiting from the microscope objective therefore see virtually no change in propagating medium leading to the introduction of no first order aberration. It should be noted that the Abbe number of the borosilicate glasses and the immersion oil are different, which leads to chromatic aberration and must be taken into account in the design of the lens. If the refractive index of the cover glass is now changed to a different value, refraction of rays hitting the newly formed diopter will lead to angle dependent optical path differences between the rays and loss of stigmatism. The decrease in optical quality will become more dramatic for media with smaller refractive indices with the appearance of TIR for the rays with largest angles of incidence (reduced effective numerical aperture).

A solution that is envisaged to counter this issue is to fabricate a hybrid glass/PDMS microfluidic circuit. The idea is to keep the same thin PDMS membrane as in the current PDMS/PDMS approach, 30  $\mu\text{m}$  in height, but to replace the "thick" 130  $\mu\text{m}$  PDMS with a cover glass of the same thickness. Figure 5.21 shows the ray aberration calculated using the model described earlier and a 10  $\mu\text{m}$  water/ 30  $\mu\text{m}$  PDMS/ 130  $\mu\text{m}$  glass structure (black solid line). The results obtained with the hybrid approach are compared with the current 10  $\mu\text{m}$  water/ 160  $\mu\text{m}$  PDMS structure (red dashed line), the 10  $\mu\text{m}$  water/ 160  $\mu\text{m}$  glass structure (green dashed line) and the "as-designed" 170  $\mu\text{m}$  glass coverslip (blue dashed line). This simulation shows



a conclusive improvement of the glass/PDMS compared to the PDMS/PDMS approach. As expected, the achieved optical quality in this case is very close from the "water-limited" level and should permit clear improvements both in terms of imaging and efficiency of the optical tweezers if implemented. These results also illustrate that it would be interesting to reduce the height of the water channel above the photonic crystal, which is a major contributor in terms of optical aberrations.

Borosilicate coverslip are readily available commercially for thicknesses down to 80  $\mu\text{m}$  (Grade 0, Schott D263M, Ted Pella). Etching of the control channels could fairly be achieved by etching in BHF as described in Section 1 of this chapter. Drilling of the injection holes seems slightly more complicated. Two methods can be envisaged: firstly, diamond drilling which requires a dedicated drill, a water bath and might require to machine a batch of coverslip stuck together for mechanical stability. Secondly, laser drilling, which is probably the most adapted method.

The first benefit of this approach is obviously the reduction of the aberration-inducing PDMS layer and its replacement by an index-matched glass layer. The second benefit lies in the robustness that the device would gain from a glass top layer. It is expected that pressure induced membrane lifting or deformation should be much lesser due to a better repartition of the forces applied to the channel. Finally, this device would be a very efficient solution to get rid of any immersion-oil contamination described in the previous section.

### 5.5.2 Fabrication and reusability

One of the most critical steps of the fabrication process is the addition of the PDMS interconnect. It makes the manipulation of the membrane complicated due to the weight imbalance between the lightweight membrane and the heavy interconnect. The various deformation issues discussed in the corresponding section renders necessary the local plasma oxidation of the membrane in order to guarantee good performances and lifetime from the sample. Unfortunately this later operation prevents any possibility of completely peeling the PDMS assembly from a used and contaminated PhC substrate, which would constitute the first step towards cleaning of the PhCs in strong solvents or acids and deposition of a new microfluidic circuit.

One solution that has been envisaged to circumvent that issue is to replace the irreversibly plasma-oxygen bonded interconnect by a clamped interconnect system. Several attempts have been carried out using mechanical pieces made out of aluminum or plexiglas with mitigated results. Although flow injection has been achieved in a few cases using these approaches, the goal of obtaining a leakage-free connection through the six ports of the sample has been achieved only once on a dummy sample. The major issue comes from the difficulty of obtaining an homogeneous force distribution from the interconnect on the PDMS membrane that withstand over 0.05 MPa of pressure without squeezing the channels underneath.



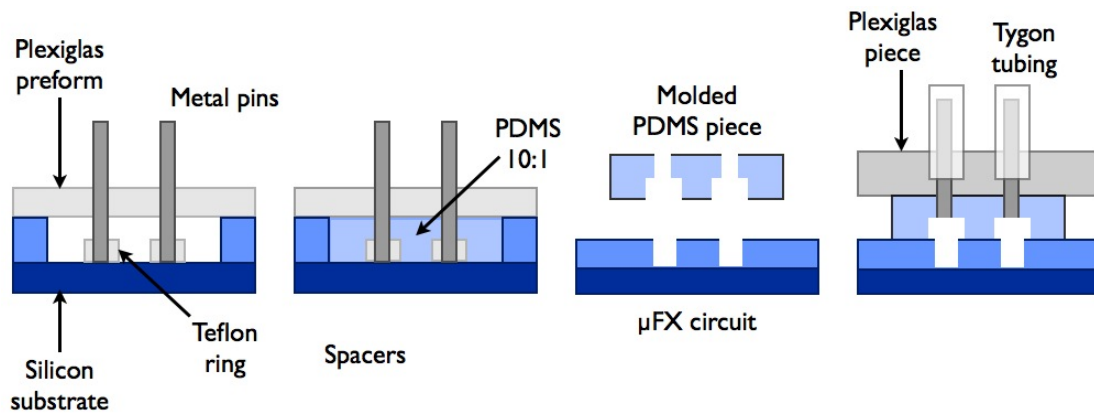


**Figure 5.22:** Fabrication of the clamped interconnect. From left to right: a plexiglass preform is held 3 mm above a silicon wafer using spacers and maintains 6 metal pins vertically. 10:1 PDMS is poured onto the wafer and fills the volume left between the wafer and the plexiglass preform. After baking the molded PDMS piece is removed from the wafer and cleaned. It is finally placed underneath a second plexiglass preform, equipped with new hollow metal pins, injection capillaries and clamped to the optofluidic chip.

Finally, a mixed PDMS - Plexiglass approach has been taken with the aim of benefitting simultaneously from a rigid piece to evenly distribute the clamping force and an intermediate elastic piece to improve the contact between the PDMS membrane and the interconnect while preventing squashing of the channels. The fabrication of the hybrid interconnect is relatively straightforward as described on Figure 5.22. A plexiglass "preform" consisting of a flat plexiglass piece where six holes have been drilled at the appropriate positions to match the sample input/output ports is positioned on a silicon wafer, separated by 2 to 3 mm high spacers. In each of the holes of the preform, a metal pin is held vertically (the holes of the preform have a diameter allowing a tight fit of the pins). The lower end of each tip is surrounded by a 1 mm high teflon ring, in contact with the silicon wafer. A 2 to 3 mm thick 10:1 PDMS layer is poured onto the silicon wafer in accordance with the height of the spacers. The wafer is then placed in a 80°C oven for an hour. The plexiglass preform, spacers and metal pins are then carefully removed before the molded PDMS piece is cut using a razor blade to the 5 mm x 10 mm dimensions described in the previous paragraphs. The optofluidic chip is finally placed on its mechanical mount and the molded PDMS piece is positioned on top of the input ports of the two-layers membrane. A second plexiglass piece carrying six holes of 1 mm diameter at the appropriate position to face the input/output of the sample is located on top of the PDMS piece. One millimeter outer diameter Tygon capillaries are equipped with hollow metal pins at their ends and plugged into each of the six holes of the plexiglass piece. The metal pins are adjusted in such a way that they cross the molded PDMS interconnect and reach the two-layers PDMS membrane level. The clamping of the top plexiglass piece is then ensured using two side screws connected to the mechanical mount of the sample.

The final assembly can be observed on Figure 5.23. A complete sample is assembled except that the silicon substrate does not carry photonic crystal devices (left frame). The molded

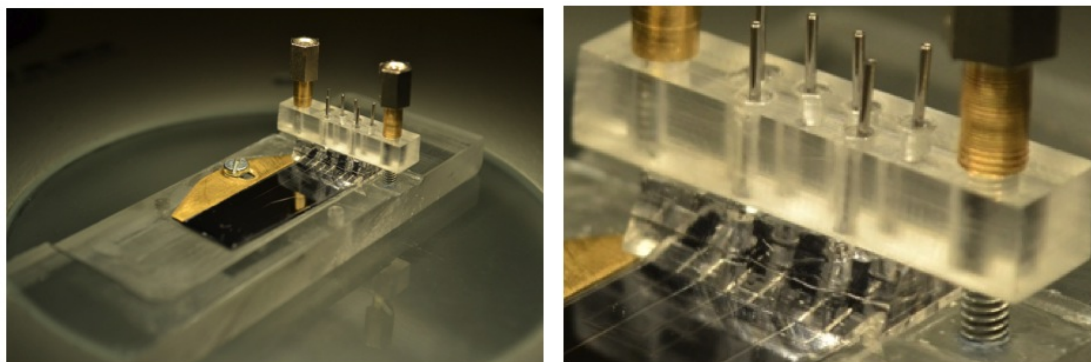


**Figure 5.23:** Photograph of the PDMS/Plexiglass interconnect. **Left.** Picture of a fully assembled microfluidic chip including a silicon substrate, a two-layers PDMS microfluidic membrane and a clamped PDMS/Plexiglass interconnect. **Right.** Zoomed picture on the PDMS/Plexiglass interconnect showing the 6 channels being clearly opened.

PDMS piece and plexiglass piece can be easily distinguished on the right frame. It is possible to observe the transport and control channels through the PDMS piece with good optical contrast confirming that these channels are not compressed by the above interconnect. The total height of the system is approximately 7 mm in this first version, but the rigidity and good manufacturability of plexiglass should allow decrease the height down to 5 mm or less. Similarly, the height of the screws used in this experiment is related to practicality rather than necessity. They could easily be replaced with smaller versions. The mechanical support mount was made in a large plexiglass for practical reasons but serves no particular purpose and could be made much smaller and in other materials.

The system presented on Figure 5.23 successfully demonstrated flow injection and peristaltic actuation of the control valves at pressures up to 0.07 MPa (10 PSI) without any leakage. Injection and operation of the sample has been performed for several days before the PDMS/-Plexiglass interconnect is unmounted, leaving no damages to the two-layers PDMS membrane. The thin microfluidic circuit could then be peeled of the silicon substrate and the substrate be cleaned in acetone. In comparison, this latest operation could not have been performed with a permanently bonded PDMS interconnect. The thin microfluidic circuit would have been permanently damaged by the acetone bath while the plasma activated region would have prevented any removal of the damaged membrane thus making its replacement impossible. The use of the mixed PDMS/Plexiglass interconnect has not yet been implemented on a PhC sample but this last step should be possible without any further development work apart from the design of a mechanical mount that is compatible with the optical test bench. A replica of the mechanical mounts currently used with the addition of two holes for the clamping screws would be sufficient in the first instance.

### 5.5.3 Smaller sized chips

The size of the sample currently used (30 mm x 12 mm x 1 mm without the interconnect) is another aspect that has received a lot of attention. These dimensions could be appealing in the prospect of developing a biomedical-type device with a footprint similar to a SD card. Nevertheless, at this early stage where the physical phenomena involved are still to be completely described and where the advanced techniques available in the laboratory allow for some degrees of freedom in the design of the chip, smaller devices would be desirable. The main reasons behind this come from the photonic crystal fabrication side. Electron-beam exposure is time consuming, relatively expensive and requires long-term planning due to the large demand for e-beam reservation slots. In addition to this, SOI substrates used for the fabrication of our PhCs are back-thinned in order to facilitate sharp cleaving of the facets. Unfortunately, larger samples require thicker substrates for mechanical stability and therefore imply further difficulties in the cleaving. Finally, on the experimental side, the sub-micron scale alignment of lensed fibers for the coupling of IR light into the cavities is made much more complicated with a large sample due to the long mechanical ranges required for the displacements of either the sample mount or the microscope objective mount.

A convenient width for a PhC chip given the fabrication and characterization methods in our lab is approximately 4 mm, for a 8 to 10 mm length. The difficulties linked to the replication of a microfluidic circuit as described in the previous sections on such a small devices are straightforward, going from the small dimensions of the PDMS membrane and the associated difficulties to manipulate it, the absence of room for interconnect, or the reduced PDMS/Silicon contact area to balance pressure induced lifting.

A flexible, two layers, microfluidic approach has been proposed and implemented to enable working with small PhC samples while maintaining the functionalities of the thin microfluidic circuit. Schematics of the design are presented on figure 5.24. This configuration relies on two distinct substrate, one can be glass, silicon, or any other material with good bonding to PDMS properties, while the second one is a 4 mm x 10 mm SOI PhC chip. A T-shaped two PDMS layers assembly is fabricated to connect them. The dimensions of the assembly are 14 mm x 14 mm for the upper part of the T and a stripe of 3.5 mm x 28 mm for the basis. The lower layer is made out of 5:1 PDMS and carries a 6 mm, 200  $\mu\text{m}$  long straight channel at the end of the stripe, that is designed to be located above the photonic devices. The upper layer is made out of 20:1 PDMS and has the exact same dimensions as the lower layer. Each of the layers is 70 to 80  $\mu\text{m}$  thick in order not to exceed 170  $\mu\text{m}$  and preserve good optical imaging quality above the PhCs. A large square PDMS piece is positioned on top of the square part of the assembly and serves two purposes. First it serves as a robust interconnect capable of holding a large number of input capillaries and second it carries control channels are located above the transport channels inside the upper layer. The large PDMS piece is relatively straightforward to manipulate manually and can be plasma activated for higher robustness.

In practice the 3D layout and Cr mask fabrication for this device have been performed by our

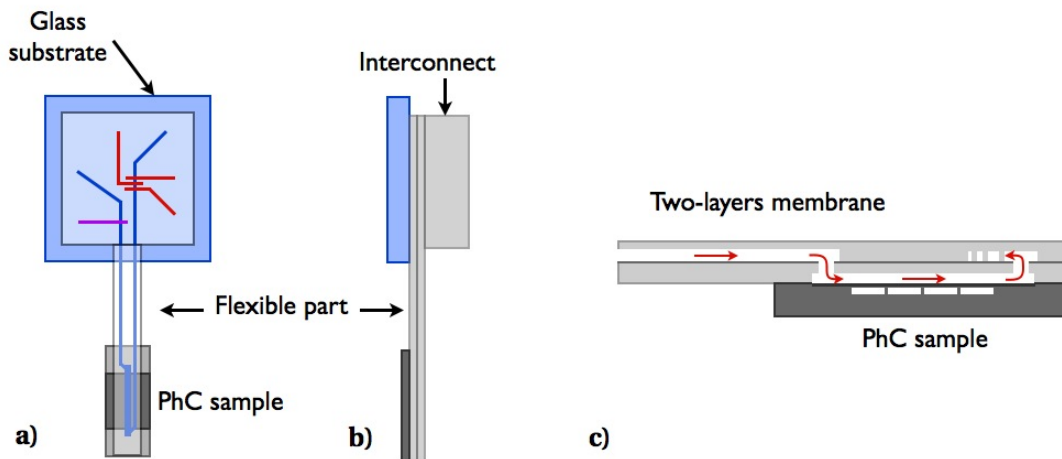


**Figure 5.24:** Design of the flexible microfluidic approach. a) Top view of a flexible microfluidic sample. A glass substrate carries the two 80  $\mu\text{m}$  thick PDMS membranes and a large PDMS interconnect also including control channels. The two-layers assembly carries the transport channel on a free-standing flexible strip to a 4 mm x 10 mm photonic crystal sample. b) Side view of the sample illustrating the free-standing region of the PDMS structure. c) Description of the path followed by the immersion liquid from the free standing region to the photonic crystal area.

colleague Mario Tonin. The assembly and test of the final device have been performed by both of us. Figure 5.25 shows pictures of the flexible microfluidic device fabricated. A glass substrate has been used for the interconnect side. The PhC sample can be observed on the left of the figure, separated by a 1 cm flexible region, that can be bent at 90 degrees angles without obstructing the flow through the channel. The picture on the right shows the sample as placed on the Fourier Imaging lab before characterization. This sample has enabled the study of water infiltration in PhC slot cavities by my colleagues M. Tonin and U. Dharanipathy.

The major benefit of the flexible microfluidic approach is that it separates the interconnect region from the "photonic" region. In this manner, the microfluidic control and interconnect region can be irreversibly bonded to the glass substrate giving a lot a freedom in terms of torque from the capillaries, density of input/output and control pressures inside the valves. It also allows for more room for fluidic functions like integrated mixers or filters. Finally the PhC cavities can be positioned underneath a microscope objective without any mechanical limitation from the size of the interconnect or the presence of rigid capillaries. Reversible thermal bonding is sufficient to maintain good adhesion from the PDMS membrane onto the sample since no major mechanical constraints are exerted. This allows for the peeling off of a used or defective microfluidic circuit and its replacement by a newly fabricated one after cleaning of the photonic devices.

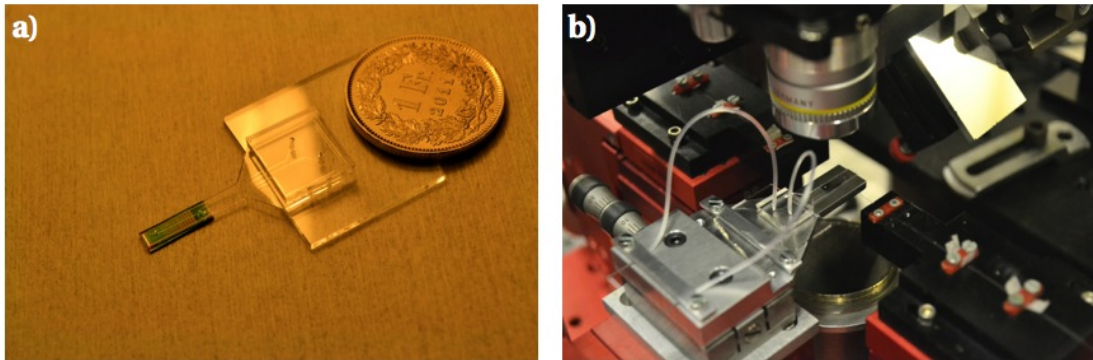


**Figure 5.25:** Photograph of the fabricated flexible microfluidic device. a) Picture of the device after fabrication illustrating the small photonic crystal chip (bottom left), the Y-shaped free-standing region and the thick PDMS interconnect on a square glass substrate (top right). b) Picture of the same device when mounted of the Fourier Imaging bench.



## 6 Resonant optical trapping and back-action effects

This chapter summarizes the main experimental results obtained regarding the resonant optical trapping (ROT) of dielectric particles in hollow photonic crystal cavities. It is divided into four sections:

- Properties of the circular cavities
- Demonstration of resonant optical trapping
- Particle induced eigenfrequency shift
- Demonstration of back-action effects

The results described here have been reported in the following journals: Physical Review Letters, 110, 123601 (2013) and Lab on Chip, 13 (16), 3268 (2013).

### 6.1 Properties of the circular cavities

The hollow photonic crystal cavities that have been used during the work of this thesis consist of a large circular defect in a two-dimensional triangular lattice [55]. The possibility of using cavities based on slot waveguides has also been envisaged but currently suffers from the large decrease of quality factor occurring when immersed in water. The hole in the HPhC measures 700 nm in diameter and is coupled evanescently by a W1 waveguide located on the side, as shown in Figure 6.1.a. The lattice constant is typically 420 nm and the lattice holes are of 250 nm in the diameter. The characteristics of the photonic crystal are designed by U. Dharanipathy using Guided Mode Expansion (GME) such that the TE band gap overlaps with the excitation range of the tunable laser diode (1470 - 1660 nm) and that the cut-off wavelength of the W1 waveguide occurs within the second half of that range (see Figure). The diameter of the large hole is then adapted so that the resonance wavelength is located between the light line and the W1 cut-off. This ensures maximum light guiding through the PhC waveguide and quality factor for the cavity mode. Finally the distance between the cavity

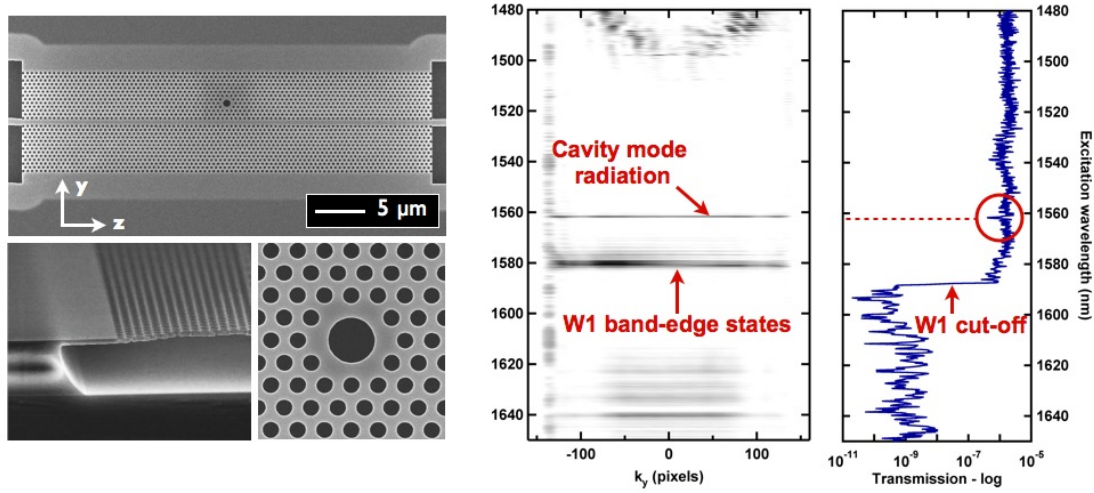


**Figure 6.1:** Structure of the circular cavity and light coupling. **Left.** Set of scanning electron micrographs showing the full photonic crystal structure including the coupling W1 waveguide and the circular cavity. A side view of the structure is also presented illustrating the suspended nature of the photonic crystal membrane. **Right.** Experimental recording of the spatially resolved out-of-plane light scattering from the cavity (grey levels) and transmission through the structure (blue curve) over a large wavelength range. The combination of this two recording allow for the accurate understanding of the various features of the structure.

and the waveguide is set to either 3, 4, or 5 lattice rows. These three configurations give access to three different loads from the waveguide on the cavity and therefore three different experimental Q factors [197]. Conversely, the amount of energy coupled to the eigenmode is expected to be exponentially decreasing as the coupling distance increases in the assumption of a simple, weak, evanescent coupling mechanism [198]. The dimensions of a full photonic crystal device are approximately  $10\ \mu\text{m} \times 60\ \mu\text{m}$  excluding the access ridge waveguides.

### 6.1.1 Hollow cavity in air

The cavities are first fabricated as described in Chapter 2 and characterized in air before the microfluidic circuit is deposited. Characterization is performed using the Fourier imaging technique. Figure 6.1.b and 6.1.c show an example of experimental measurement obtained for a well designed device. The surface scattering (left) and transmission through the PhC devices (right) are simultaneously recorded for each device. The left graph shows the amount of light radiated from the cavity, as recorded in the Fourier space and integrated along the column of the CCD array. The columns are perpendicular to the direction of propagation of light in the PhC sample. Two main features can be observed on this spectrum. A first sharp and bright line is present near 1560 nm. It corresponds to the cavity mode losses through scattering. A second broader and non-uniform line exists near 1580 nm. The later is attributed to the scattering of the W1 mode in the slow light regime by the large circular defect. This hypothesis is in good agreement the presence of the W1 cut-off before 1590 nm as seen on the transmission record.



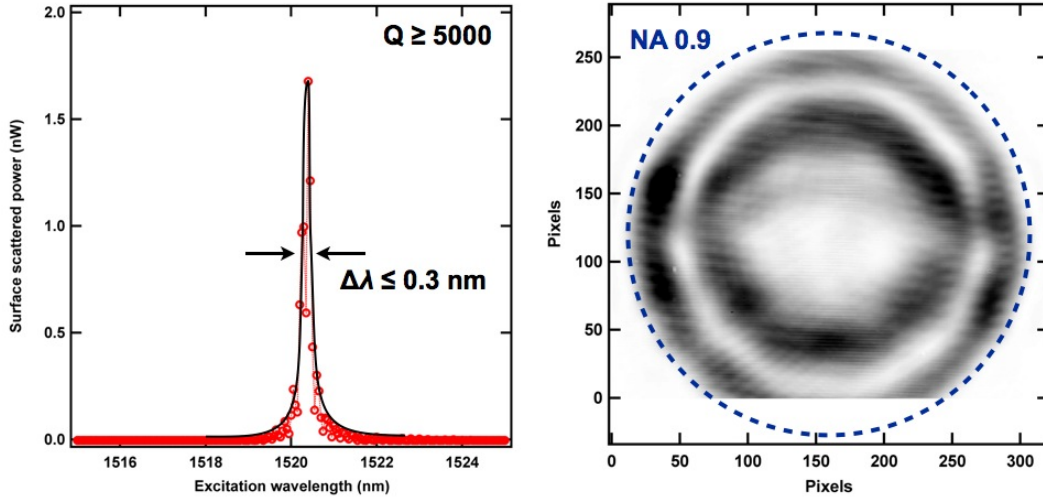


**Figure 6.2:** Experimental characterization of the circular cavity in air. **Left.** Record of the light intensity scattered out of the circular cavity in the vicinity of the cavity resonance when excited with a tunable laser diode. **Right.** Inverse grey-level image of the far-field pattern recorded for the cavity mode. A close look at the light distribution reveals a 6-fold symmetry that could be a signature of the hexapole field distribution of the eigenmode.

The confocal collection of the light scattered out of the plane from the circular cavity can be performed in the vicinity of the resonance wavelength. An example of such a record is shown in Figure 6.2.a. The red circles correspond to the experimentally measured values while the black solid line is a guide for the eye. A Lorentzian-type envelope can be clearly observed on the measurement along with a fast modulation of the intensity that is due to the Fabry-Perot interferences between the facets of the sample. The measured full-width at half-maximum (FWHM) is smaller than 0.3 nm for this cavity corresponding to a quality factor of above 5000 at 1520 nm. As it has been mentioned earlier, the experimental value of the quality factor does not correspond to the intrinsic (unloaded) quality factor of the cavity but it also take into account the coupling (losses) to the waveguide resulting in a smaller value. Typical structures display quality factors of the order of 3000 for 3 rows coupling and above 5000 for 4 and 5 rows coupling in air (see Figure 6.2). The largest value measured was  $7000 \pm 500$ , corresponding to a linewidth of circa 0.22 nm at 1550 nm and a cavity photon lifetime of approximately 5 ps. In comparison, the numerical quality factors obtained by U. Dharanipathy using 3D Finite Element Method (COMSOL) is 8800 in air (no waveguide). This good agreement between the experimentally measured and numerically computed values is satisfying and illustrates the good quality of the both the photonic crystal fabrication process and the 3D modeling.

	Mode volume - $\mu m^3$	Mode volume - $(\frac{\lambda}{n})^3$
Definition 1	0.21	2.3
Definition 2	0.36	4

**Table 6.1:** Computation of the mode volume of the circular cavity using Finite Element Method

Other interesting characteristics of the mode can be retrieved from the 3D simulations. For example, the field distribution of the eigenmode is found to be hexapolar (see Chapter 2), with electric field maxima located along the edges of the large hole. Similarly, the cavity mode volume can be estimated following one of the following definitions:

$$V_{\text{mode1}} = \frac{\iiint \epsilon(\mathbf{r}) |\mathbf{E}(\mathbf{r})|^2 d^3\mathbf{r}}{\max[\epsilon(\mathbf{r}) |\mathbf{E}(\mathbf{r})|^2]} \quad (6.1)$$

which is the most widely used definition for the mode volume of an optical micro cavity [199] or:

$$V_{\text{mode2}} = \frac{(\iiint \epsilon(\mathbf{r}) |\mathbf{E}(\mathbf{r})|^2 d^3\mathbf{r})^2}{\iiint (\epsilon(\mathbf{r}) |\mathbf{E}(\mathbf{r})|^2)^2 d^3\mathbf{r}} \quad (6.2)$$

which has also been proposed [46],[199] and which offers the advantage of being less sensitive to field distribution discontinuities as in the case of slot cavities for example. The values obtained for the volume of the eigenmode are expressed both in  $\mu m^3$  and fraction of  $(\frac{\lambda}{n})^3$  and summarized in Table 6.1 for record purpose. The obtained mode volumes are relatively large for 2D -point defect- photonic crystal cavities in silicon where record values as low as  $0.23 (\frac{\lambda}{n})^3$  have been reported [43]. Nonetheless, the large volume occupied by the hollow region ( $0.085 \mu m^3$ ) illustrates how adapted this type of cavity is to study interactions with nanoparticles. For comparison, a 500 nm diameter particle has a volume of  $0.065 \mu m^3$  which corresponds to almost the same volume as the hollow region of the cavity and at the same time corresponds to almost 1/6 of the total estimated mode volume (Definition 2).

The experimental confirmation of these computations was not performed during this thesis but it could be realized, for example, with the help of a phase-resolved near field technique like the one presented in the work of Burresi *et al.*[200]. Nevertheless, the observation of the far-field pattern of the cavity scattering (Figure 6.2) allows for the observation of 3 planes of symmetry. The later is believed to be a signature of the hexapolar field distribution expected from 3D FEM. Finally, the overlap of the electric field with the low refractive index medium (air) is computed to be over 30% and the fraction of the mode overlapping with the air within the cylindrical volume of the hole (700 nm in diameter, 220 nm high) is of the order of 10%.

The combination of high quality factor, small mode volume and large overlap give the circular cavity a clear advantage in terms of particle sensing and trapping in the principle.

## 6.1. Properties of the circular cavities

	Q in air	Q in water	Water induced shift (nm)
Experimental	7000	2500	46.7
Numerical	8800	3300	47.5

**Table 6.2:** Experimental and numerical quality factors and resonance wavelength shifts for a water infiltrated circular cavity

### 6.1.2 Hollow cavity in water

Prior to the resonant trapping experiments, the hollow cavities are integrated in the transport channel and immersed in water. The immersion of the PhC devices in an aqueous solution modifies their properties due to the decrease in refractive index contrast. The two main consequences are a decrease of the light confinement within the waveguide and cavity (hence a smaller quality factor) and a displacement of the cavity eigenfrequency towards the dielectric band edge resulting in a redshift of the resonance wavelength. Figure 6.3 shows the experimental shift induced on a circular cavity when the transport channel is infiltrated with water.

Experimental measurements indicate a resonance wavelength shift of 46 nm after immersion of a cavity. This value compares very well with FEM simulations which predict a 47 nm redshift for a fully immersed photonic crystal structure (see Table 6.2). In terms of refractive index sensing, this corresponds to an experimental of 130 nm/RIU sensitivity. It can also be used as an accurate indicator on whether the device is only partially or fully infiltrated with the immersion solution. For example, a partially infiltrated device (water only above the device and air underneath the membrane) produces a shift of only 25 nm numerically and about 20 nm experimentally.

The experimental values for the quality factors, both in air and water and for the water-induced resonant frequency shift are recorded in Table 6.2. These corresponds to the largest values observed over a set of three samples. The experimental quality factors values have errors of approximately  $\pm 500$ . The water-induced shift is known with a certainty of  $\pm 0.1$  nm. It should be noted that the largest quality factors and resonance wavelength shift were not recorded for the same cavity. The FEM values for these characteristics, as computed by my colleague, are added to the table for comparison. A very close agreement can be observed between the computed and measured figures which highlights both the accuracy of the model and the high quality of the sample fabrication that have been developed.

A broadening of the linewidth can be observed when the cavity is placed in aqueous medium, typically from 0.3 to 0.6 nm. This broadening can be attributed to the increase in radiation losses associated with the smaller refractive index contrast in the presence of water. This phenomenon can be understood by the presence of a larger number of spatial components of the eigenmode lying above the "water" light cone than under the "air" light cone. A larger number of spatial components is associated to larger out-of-plane radiation losses which in

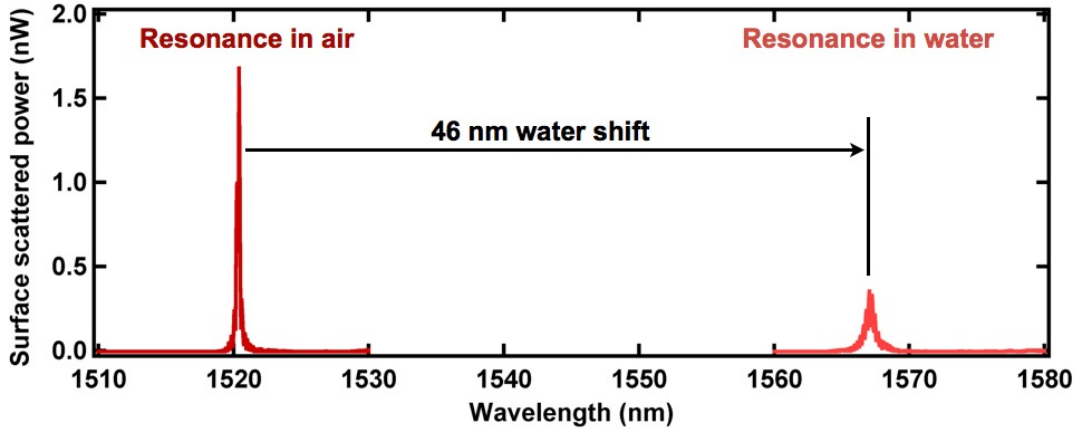


**Figure 6.3:** Water induced resonant wavelength shift. Experimental record of the light scattered out of the cavity as a function of wavelength before and after immersion in water. The presence of water induces a redshift of approximately 45 nm of the resonance wavelength.

turn lead to a shorter cavity-photon lifetime and a larger cavity linewidth. Further explanations about this mechanism can be found in the work of J. Jágerská *et al.*[36]. The possible influence of the large water absorption band in the 1500 to 1600 nm region on the broadening of the linewidth has been discarded by performing quality factor measurements in a 99% deuterium dioxide solution ( $D_2O$ ) showing no noticeable difference. The latter is form of water where the standard hydrogen atoms are replaced by deuterium ones (containing one neutron more than standard hydrogen). Though similar in many aspect to standard water (including refractive index), the heavier mass of deuterium causes the absorption spectrum of deuterium dioxide to differ. For instance,  $D_2O$  does not display the large absorption bands of  $D_2O$  around  $1.5\ \mu\text{m}$  ([201]). This stability constitutes a great advantage of the circular cavity design compared to other types of hollow cavities. For example, slot-type cavities have been investigated during the time of this work [47], [51], [45]. These types of cavities have been regarded as very promising candidates to demonstrate resonant optical trapping of particles due to the large field overlap with the low refractive index medium (around 90%) and the large quality factors achievable (over 25 000) [45]. Unfortunately two main difficulties come with these cavities. Firstly the large resonance wavelength shift associated with the large field overlap render the tracking of the cavity mode very complicated during infiltration. The reported refractive index sensitivity are of the order of 500 nm/RIU which corresponds to a 165 nm shift going from air to water infiltration. For comparison, the range of tuneability of our external cavity laser diode is 170 nm and a photonic crystal cavity fabricated as per design has a resonance wavelength within  $\pm 10$  nm of the targeted value. This implies using lithographic tuning techniques and adding a cavity-to-cavity uncertainty when measuring properties. Secondly, the slot cavity design that is widely used in the group and that is based on two narrower regions to act as barriers shows no robustness to the water infiltration. Sets of cavity modes with quality factors above 20 000 have been observe to completely vanish after infiltration. The mechanism behind this phenomenon is still to be understood. Nevertheless, the explanation where this disappearance would be related only to water absorption around 1550 nm has been discarded

in a set of experiments in Deuterium dioxide which have shown no recovery of the mode. Other researchers have managed to maintain a slot cavity mode in a sugar solution [51] or hexane [202] using a heterostructure type slot cavity. In their case, the quality factor drops from 50 000 to 4 000 during infiltration.

## 6.2 Resonant optical trapping

This section summarizes the main experimental results that constitute the optical trapping of sub-wavelength dielectric particles with the confined electromagnetic field in a hollow photonic crystal cavity.

### 6.2.1 Resonant trapping of 500 nm polystyrene particles

The procedure for this experiment is as follows. The optofluidic chip is aligned on the optical test bench and a hollow cavity is coupled to a tunable laser diode. Hollow cavities with four rows of separation from the W1 waveguide are usually preferred for resonant optical trapping (ROT) experiments since they provide a good compromise between quality factor and amount of energy coupled to the eigenmode. A deionized water solution containing 0.1% of Triton X-100 surfactant is injected in the microfluidic channel. After an hour, a diluted polystyrene bead solution is injected into the channel. The choice of the dilution is quite important as too small a dilution will result in large concentrations of particles and thus rendering the trapping of a single particle complicated. On the contrary, too large a dilution might lead to long waiting times before a particle can be captured. The velocity of particles in the channel at this time can reach up to several hundreds of microns per second. The set of pneumatic valves described in Chapter 5 is used to completely arrest the flow, leaving the individual particles in unconstrained Brownian motion. The hollow cavity is excited near the water resonance with the tunable diode. The auxiliary tweezer beam is positioned on top of the large hole and acts as a funnel for particles hovering in the neighborhood of the structure (see Figure 6.4). When a particle enters the beam of the Ti:Sapphire laser, it is propelled towards the center of the large hole. The auxiliary tweezers beam is then switched off leaving the particle to interact with only the resonant excitation.

Figure 6.5 demonstrates the optical trapping of a 500 nm particle using the field confined in the hollow photonic crystal cavity. It consists of four snapshots extracted from a single video recorded with the fluorescence EMCCD camera. Time  $t = 0$  (Snapshot a.) corresponds to the time of extinction of the auxiliary tweezers. The fluorescent particle (bright white spot) can be observed in the center of the hollow cavity (yellow dashed circle). A set of other free fluorescent particles can be observed on the right hand side of the cavity. As time passes (snapshots b. and c.), one can observe how the fluorescent particle remains firmly held inside the hollow cavity after  $t = 5$  min and  $t = 10$  min respectively. In comparison, it is possible to observe that the other particles have been moving freely in and out of the field of the microscope objective. Finally after ten minutes of continuous trapping, the resonant excitation is turned

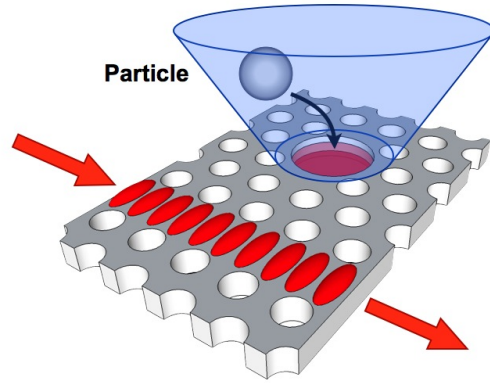


**Figure 6.4:** Schematic of resonant optical trapping experiment procedure. The hollow cavity is excited near its resonance wavelength. The excitation of the cavity is provided through the W1 waveguide. The auxiliary tweezers beam is positioned above the hollow cavity and acts as a funnel to guide a free particle in suspension in the vicinity. After the particle has entered the cavity, the auxiliary beam is switched off.

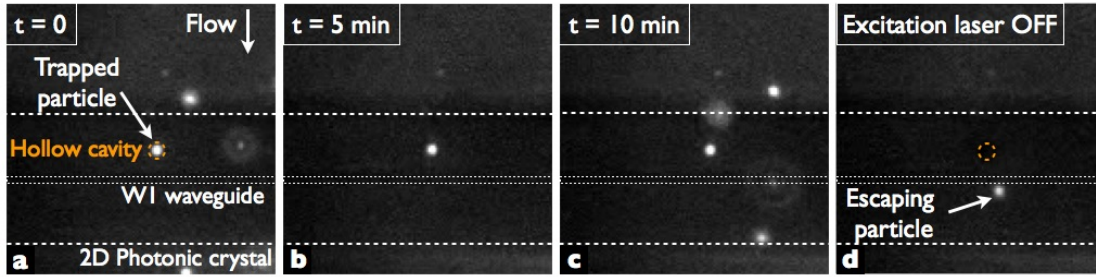


**Figure 6.5:** Video snapshots demonstrating the resonant optical trapping of a 500 nm polystyrene particle in a hollow photonic crystal cavity. a. The particle is guided inside the hollow cavity using auxiliary optical tweezers. The auxiliary tweezers are switched off at  $t=0$ . b. The particle remains trapped in the resonant field after 5 minutes. c. The particle is still trapping within the cavity after 10 minutes despite the existence of a small residual flow. d. The resonant excitation is switched off and the particle is free to escape and recover unconstrained Brownian motion

off. This operation releases the particle from the resonant trap instantaneously as shown in snapshot d. The particle then recovers unconstrained Brownian motion and escapes rapidly from the region of cavity. The full video recording of this experiment can be found on the Supplementary Material page of [203]. A second descriptive video showing a 500 nm particle being trapped for one minute can also be viewed at the following link: [204].

The resonant nature of the trap is ascertained by performing trapping attempts at a range of wavelengths around the water resonance. The result of which shows that trapping is only possible for a limited wavelength span (typically one to two linewidths) after the water resonance. The most stable trapping cases (for a constant laser input power) are recorded for a detuning of about one linewidth. Resonant trapping times exceeding twenty minutes have been achieved in this spectral region for 2 mW laser output powers, without any sign of apparent structural damage or photobleaching of the particle. It is believed that this feature

could be of the highest interest for the biology and medicine communities for example where it is important to be able to isolate and immobilize single specimens for extended time periods without damages or alteration.

### 6.2.2 Particle confinement and suspended nature of the trap

Having demonstrated that the hollow cavity is capable of resonantly trapping particles, it is now of the highest interest to investigate the behavior of these particles within the trap. The video recordings of trapping experiments show that the residual Brownian motion of the trapped particle is extremely small (not visible with naked eye). One major concern, for example, is the possibility that the particle could actually be stuck on the silicon membrane rather than being suspended like in the case of standard optical tweezers.

There are several ways to be convinced that the particle is not stuck on the silicon surface during trapping experiments. Firstly, the fact that a trapped particle recovers unconstrained Brownian motion immediately after the cavity excitation is stopped, is a convincing explanation. Indeed, all the experiments showed that small polystyrene particles, once deposited on the silicon surface never return to their colloidal state. This observation motivated the usage of surfactants and flushing methods as described in Chapter 5 in the first place. Therefore the quick escape of the particle from the trap suggests that there is no extended contact between the specimen and the silicon membrane. Another explanation can be inferred from the study of the temporal evolution of the light transmitted through the photonic crystal structure. This point is a very interesting subject of study on its own and will be developed in the Section 6.3.

Finally, the most convincing method to prove the suspended nature of the cavity trap is the direct study of the position of the particle over time. As mentioned earlier, the displacements of the fluorescent particle are very small and can hardly be noticed on the recorded image. Nevertheless, it is possible to use centroid measurement methods to resolve subpixel displacements of objects with good contrast with their background. A freely available software "Video Spot Tracker" ([196]) developed by the University of North Carolina and supported by the National Institute for Biomedical Imaging and Bioengineering has been used for this purpose.

Before the resonant trapping experiments are performed, a two minute video recording of a sedimented particle is acquired. Centroid calculations are then made for the 2000 recorded frames. The position of each centroid is then plotted on a quadrant graph (Figure 6.6.a). The (0,0) coordinates point corresponds to the mean values for the X and Y positions of the cloud of points as measured on the EMCCD matrix. It is possible to see that the entire cloud of points (except for 4 points out of 2000) can be circumscribed within a circle of 0.2 pixel in the radius. This gives an upper limit for the error in centroid position which includes the centroid measurement error and any vibration existing within the optical system. A less pessimistic error value can be determined by calculating the radial standard deviation from (0,0) of the 2000 centroid positions. The radial excursion is therefore calculated for each centroid. A standard deviation of 0.045 is found and the distribution of excursions is plotted as

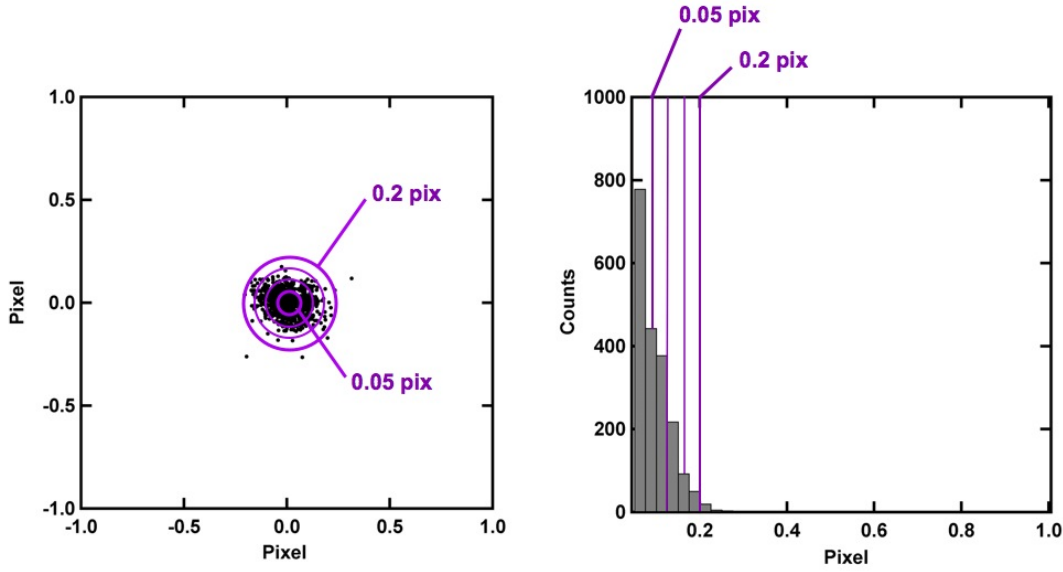


**Figure 6.6:** Determination of the resolution of the centroid tracking method. **Left.** A 2000 frames video acquisition is performed of a sedimented fluorescent particle. The centroid is calculated for each of these frames and placed on the quadrant plot. Purple circles indicate the radial excursion of the measured centroids from the real position of the particle. **Right.** The occurrences of the radial excursions of the centroids are plotted in a histogram. Purple lines indicate the standard deviation (0.045 pixel) and maximum significant recorded excursions (0.2 pixel).

an histogram in Figure 6.6.b. The 0.05 pixel line indicates the rounded value for the standard deviation and the 0.2 pixel line indicates the largest circle shown on Figure 6.6.a.

Two trapping experiments are now performed. In the first one, a 500 nm polystyrene particle is trapped in the resonant field with a laser output power of 1.5 mW. In the second one, a second identical particle is trapped with a laser output power of 3 mW. The particle is captured for over 30 seconds in each case while a video recording is performed at a frame rate of 30 fps. The two sets of points are then plotted on a quadrant graph and superimposed (Figure 6.7.a). The acquisition obtained for a 1.5 mW laser power is depicted using blue markers while the 3 mW one is depicted in red. Each marker has a radius of 0.05 pixel corresponding to a  $1\sigma$  radial error bar, as obtained in the previous paragraph. One pixel on the graph corresponds to a distance of 160 nm in the plane of the photonic crystal cavity, therefore the  $\pm 0.05$  pixel standard deviation corresponds to a  $\pm 8$  nm uncertainty on the position of the particle. Similarly, a 500 nm spherical particle in a 700 nm diameter cylinder has a free displacement range of  $\pm 100$  nm in all direction. The black dotted circle (0.6 pixel in the radius) indicates this free displacement range of the particle within the cavity plane. The center of the circle has been arbitrarily positioned on (0,0) which corresponds to the mean values of the centroid clouds in X and Y. Figure 6.7.b. and c. show the histograms of the centroid distribution projected in X and Y. The same color code as Figure 6.7.a applies.

Several observations can be made from the set of graphs presented in Figure 6.7.



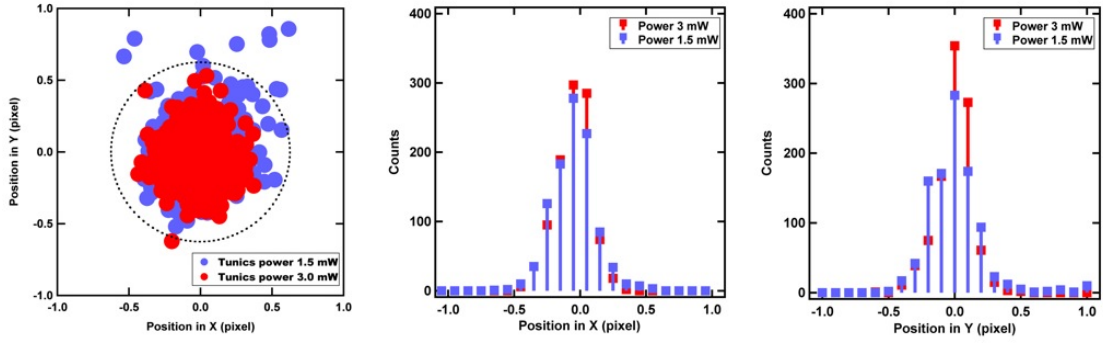


**Figure 6.7:** Particle tracking using the centroid method for different optical powers. **Left.** Positions of the calculated centroids for the 1000 frames acquisitions of two particles being resonantly trapping at 1.5 mW laser output power (blue) and 3 mW output power (red) respectively. The diameter of the markers correspond to a  $1\sigma$  error bar as determined experimentally. The black dotted circle corresponds to the free displacement range of a 500 nm particle in a 700 nm cavity. **Center and Right.** Histograms of the centroid positions projected on the X and Y axis for the two different power values.

- A clear difference can be observed between the cloud of centroids recorded for a resonantly trapped particle and a sedimented particle (Figure 6.6.a). The extent of the recorded clouds is much larger than the 0.2 pixel circle associated with the largest deviations recorded on a sedimented particle. The hypothesis of stiction of the particle on the membrane is therefore definitively invalidated.
- Both clouds of centroids can be circumscribed with a 100 nm radius circle corresponding to the free displacement range of the 500 nm particle within the cavity. Although the relative centering of the circle with respect to the centroids is approximate, this observation constitutes a good hint that the motion of the particle is happening mainly within the plane of the silicon membrane.
- The increase in excitation power from 1.5 mW to 3 mW leads to a constriction of the centroid cloud around its center. This expected power dependency of the motion of the particle is the sign of a reduction of the trapping volume of the cavity.

Though very efficient, the centroid method as employed here operates near its resolution limit. A study of the trapping volume with respect to input power is made complicated in the current configuration by small difference existing between 1.5 mW (trapping threshold) and 3 mW. For powers above 3 mW, the dimensions of the centroid cloud get close to that of a sedimented particle. Future work could make use of a camera of the type of the Hamamatsu Orca Flash 4.0 which is sensitive enough for 500 nm particle despite not being EMCCD but which has pixels that are  $6.5 \mu\text{m}$  each side, therefore, automatically a factor 2 in the centroid resolution. Similarly, it would be interesting to develop a technique where the relative centering of the centroid clouds and free displacement circles (related to the position of the particle) could be ascertained. This could involved for example using a set of reference sedimented beads on the image, whose positions could be monitored simultaneously with that of the trapped particle.

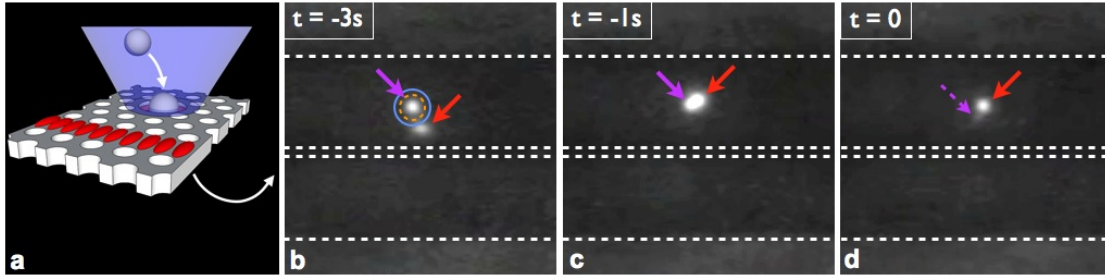


**Figure 6.8:** Experimental demonstration of the exclusivity of the resonant trap. a) Schematic of the experiment performed. A first particle is captured in the resonant trap while a second particle is forced inside the cavity with the help of the auxiliary tweezers beam. b) Snapshot of the video-recording of the experiment. The first particle, in the resonant trap, is labeled with a purple arrow, while the second particle guided with the auxiliary beam is labeled with a red arrow. c) The second (red) particle enters the cavity from the top while being accelerated by the Ti:Sapphire beam. d) The first particle (purple) is pushed away from the resonant trap and escapes underneath the membrane while the second particle replaces it.

This method would also bring the additional benefit of subtracting vibration related errors on the centroid measurement.

### 6.2.3 Exclusivity and trapping volume

Another very interesting property can be attributed to our trapping mechanism: the circular cavity allows for the trapping of only one particle at a given time. This feature, referred to as "exclusivity" is a remarkable feature in the prospect of particle sorting on a chip and is not achievable with standard optical tweezers techniques [95]. This property can be demonstrated by performing an experiment where a first particle is being held in the resonant trap, while a second particle is forced inside the cavity using the auxiliary tweezers beam (Figure 6.8.a). The snapshots on figure 6.8.b, c. and d. show a video recording obtained during one of these experiments. Snapshot b. shows the first particle (purple arrow) immobilized in the cavity (yellow dashed circle) and the second particle (red arrow) entering the cone of the ATB (blue circle). On snapshot c. the second (red) particle starts entering the cylindrical cavity volume and starts pushing the first particle (purple). The second particle finally pushes the first one through the cavity (snapshot d.). The later gets released from the resonant trap and escapes underneath the silicon membrane (dashed purple arrow) and recovers unconstrained Brownian motion while the incoming particle replaces it inside the cavity trap.

Exclusivity arises from two main reasons. The first one is the obvious geometrical limitation for the largest particles (above 700 nm) due to the diameter of the hole. The second comes from the very localized nature of the eigenstate. This is depicted in the Plane Wave Expansion (PWE) and 3D FEM calculations of the cavity eigenmode shown in Figure 6.9. The left panel is a general view of the system showing the access W1 waveguide providing resonant excitation to the cavity mode and the particle being trapped within the hollow volume. The right panels present the top and side views of the cavity field as calculated by my colleague U. Dharanipathy

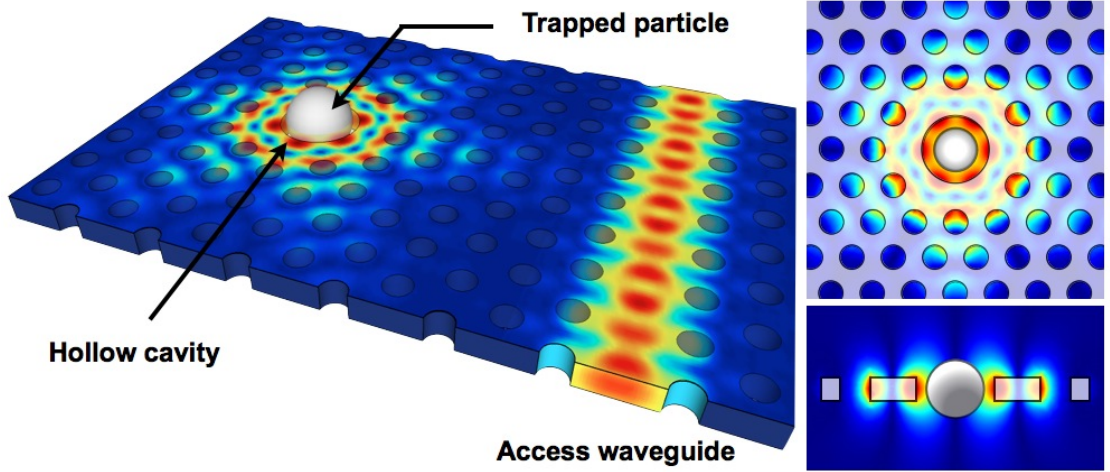


**Figure 6.9:** Electric field distribution calculated by PWE and 3D FEM. **Left.** Corner view of the photonic crystal cavity showing the W1 waveguide, the cavity mode and the particle being trapped within the hollow volume. Field distribution in the waveguide and cavity were calculated separately using Plane Wave Expansion. **Right.** Top and side views of the electric field distribution within the cavity in the presence of a particle.

using 3D FEM. The hexapolar field distribution mentioned in the previous section can be clearly observed on the top view rendering. The bottom right rendering shows the cross section of the  $|E_{xy}|$  field component within the circular cavity. It is possible to understand from this distribution that the extent of the field in the vertical direction is limited to a few hundred nanometers. A closer observation shows that the largest part of the field is confined within the 220 nm ( $\pm 110$  nm) height of the silicon slab, similarly, the  $|E_{xy}|$  has almost completely faded after  $\pm 250$  nm from the center of the slab (approximately the size of the 500 nm particle). As a consequence, for a 700 nm diameter cavity, exclusivity is expected for particles reaching from 350 nm to 650 nm.

#### 6.2.4 Estimation of the trapping power

The amount of light coupled to the cavity is a very important aspect of this experiment for two main reasons. Firstly it is a mean to quantify the efficiency of our trapping technique in comparison to other existing methods such as optical tweezers or nano-antennae traps. Secondly it is an important data that people may consider before choosing to apply our technique to trap light sensitive particles such as cells and viruses but also light absorbing particles like gold colloids. An accurate estimation of the power guided in the W1 waveguide near the cavity has been performed based on experimentally measured parameters like reflection coefficients at the facets and propagation losses in the ridge and W1 waveguides. The parameters that have been used are listed in Table ???. All the parametric values have been chosen in order to obtain a conservative value. The coupling from the W1 waveguide to the cavity eigenmode has not been estimated.

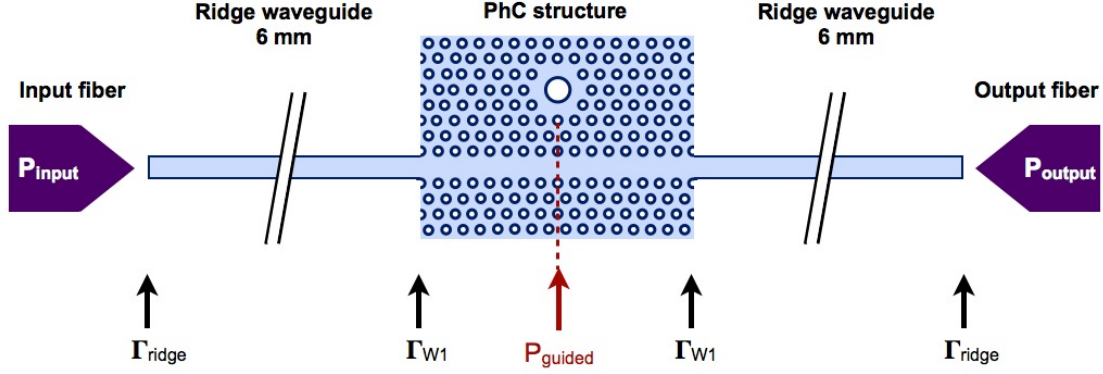


**Figure 6.10:** Schematic of the end-fire setup used for the estimation of the guided power.

The estimation, was consistently performed following two separate methods. **The first method** consists in considering the reflections and propagation losses undergone by the initial input power all along its way to the detector. Following the schematic shown in figure 6.10, the power  $P_{guided}$  that is guided near the cavity can be written:

$$P_{guided} = \sqrt{\alpha_{W1} L_{W1} \Gamma_{W1}} \sqrt{\alpha_{Ridge} L_{Ridge} \Gamma_{Ridge}} P_{input} \quad (6.3)$$

For a 1 mW input power, the values listed in Table 6.3 give a 62  $\mu$ W guided power near the hollow cavity.

**The second method** relies on the symmetry of the end-fire setup, which imposes that the power that is guided exactly in the middle of the system (and thus near the cavity) writes:

$$P_{guided} = \sqrt{\frac{P_{output}}{P_{input}}} \cdot P_{input} = \sqrt{P_{output} \cdot P_{input}} \quad (6.4)$$

For a 4  $\mu$ W transmitted power through the end-fire setup (Table 6.3 ) associated with a 1 mW input power, this method directly gives a 63  $\mu$ W guided power near the cavity.

Parameter	Symbol	Value	Comment
Optical power in the input fiber	$P_{input}$	1 mW	measured
Coupling fraction at air/ridge interface	$\Gamma_{ridge}$	0.13	measured
Length of side ridge waveguides	$L_{ridge}$	6 mm	by design
Losses in ridge waveguide	$\alpha_{ridge}$	0.3 dB/mm	measured - best case
Length of PhC W1 waveguide	$L_{W1}$	60 $\mu$ m	by design
Coupling fraction at ridge/W1 interface	$\Gamma_{W1}$	0.65	measured
Losses in W1 waveguide	$\alpha_{W1}$	2.4 dB/mm	measured - best case
Optical power in the output fiber	$P_{output}$	4 $\mu$ W	measured

**Table 6.3:** List of parameters used in the estimation of the guided power near the cavity

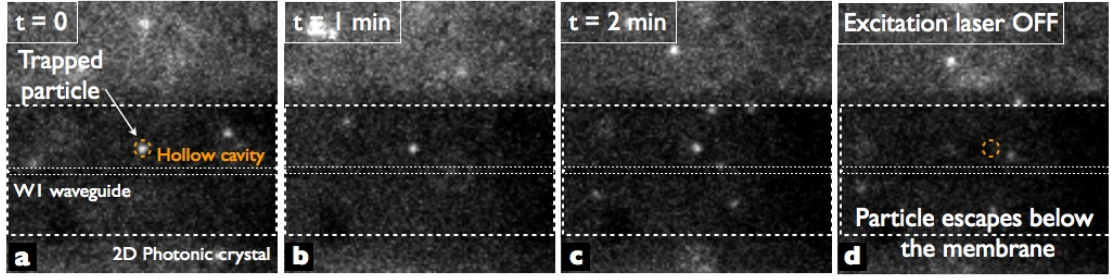


**Figure 6.11:** Resonant optical trapping of 250 nm polystyrene particles. Snapshots demonstrating the resonant optical trapping of a 250 nm particle in the hollow cavity. The particle is first captured within the cavity using the weak influence of the auxiliary beam a). The particle remains trapped for above 2 minutes b) and c) until the resonant excitation is switched off and the particle recovers unconstrained Brownian motion d).

Each of these methods independently provides a consistent value circa  $63 \mu\text{W}$  of guided power near the cavity plane for a 1 mW laser diode output. Following this estimation, it can be retrieved that the trapping of a 500 nm polystyrene particle for over ten minutes has been obtained for a cavity power lesser than  $120 \mu\text{W}$ . In comparison with standard optical tweezers, this corresponds to a decrease in trapping power of over two orders of magnitude [205]. This comes as a consequence of making use of a strongly localized field but also accessing the inner part of the cavity field. The later constitutes the biggest difference between our technique and previously reported near-field techniques. It should be stressed that owing to the resonant nature of the trap, the effective optical power confined within the cavity can be much superior to that of the net power propagating through the adjacent coupling waveguide.

### 6.2.5 Resonant trapping of 250 nm polystyrene particles

On top of reaching for lower trapping powers, one strong motivation behind optical trapping in small mode volume cavities is the possibility to trap smaller individual particles. The reason comes from the fact that small dielectric particles have a polarizability that scales with their volume. Assuming a trapping force that is purely a gradient force, a spherical particle sees a gradient force that scales down with the third power of its radius, while the same force only increases with the first power of the intensity of the field. One straight forward solution to achieve smaller particles trapping is therefore to use sub wavelength confining structures such as photonic crystal cavities.

Figure 6.11 shows the resonant optical trapping of a single 250 nm polystyrene particle. This size of particle is of particular interest to us. It is still large enough not to require demanding low-light fluorescent imaging techniques but it is small enough for our auxiliary tweezers beam not to be able to trap it through the thin PDMS layer, even at our maximum input power. It is also a size of particle characteristic of large viruses such as the Mosaic Tobacco Virus (MTV) [84].



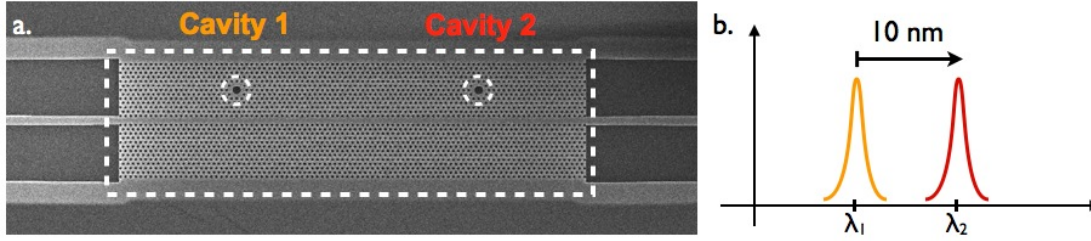


**Figure 6.12:** Design and fabrication of individually addressable traps on a single photonic crystal structure. **Left.** SEM micrograph of the fabricated device containing two distinct circular cavities. **Right.** Schematic of the 10 nm resonance wavelength separation between the two cavities.

The experimental procedure is the same as in the case of the trapping of 500 nm particles except that the auxiliary tweezers beam is too weak to trap the 250 nm particle. A particle is pushed towards the hollow cavity using the Ti:Sapphire beam and captured in the resonant field. The particle remains strongly held for two minutes before the resonant excitation is turned off, leaving it free to escape. It can be observed on Figure 6.11 that the contrast between the fluorescent particles and the background is lesser than in the case of Figure 6.5. This is due to the fact that the number of fluorophores within the particles that scales with their volume. Therefore 250 nm particles emit about 8 times less light than their 500 nm counterparts. The resonant trapping of the 250 nm particle is achieved with an estimated power of 360  $\mu$ W. As a very rough comparison, in their 1987 Science paper, Ashkin and Dziedzic achieved optical trapping of individual Mosaic Tobacco viruses at 300 mW optical powers using optical tweezers operating at 514.5 nm. Mosaic Tobacco viruses are cylindrical specimens, 320 nm in the length, 20 nm in the width and with an approximate refractive index of 1.57.

### 6.2.6 Application to multiple addressable traps

In the previous paragraphs, the principle behind a single hollow cavity trapping single particles has been demonstrated. From an application and integration point of view, it could very advantageous to have several individually addressable cavities on a single photonic crystal structure (i.e. with a common input waveguide). These multiple cavities could either be used for parallel investigation of individually trapped specimen or used in complex on-chip functions like particle sorting.

In order to demonstrate the feasibility of such a PhC structure and, most importantly, the individual addressing of resonant traps, a two-cavities structure has been designed and fabricated. A standard photonic crystal lattice (same length as individual cavity structure) was divided in two, and a cavity has been positioned in the center of each of these halves (see Figure 6.12.a). The diameter of each cavity was chosen such that their designed resonance wavelength are separated by 10 nm around 1550 nm (Figure 6.12.b). Table 6.4 records the exact design diameters, design resonance wavelength and their measured counterparts. The comparison between the design and experimental values show that, despite the small over-

## 6.2. Resonant optical trapping

	Cavity diameter (nm)	Design resonance (nm)	Experimental resonance (nm)
Cavity 1	720	1550	1568.3
Cavity 2	700	1560	1577.0

**Table 6.4:** Experimental and numerical quality factors and resonance wavelength shifts for a water infiltrated circular cavity

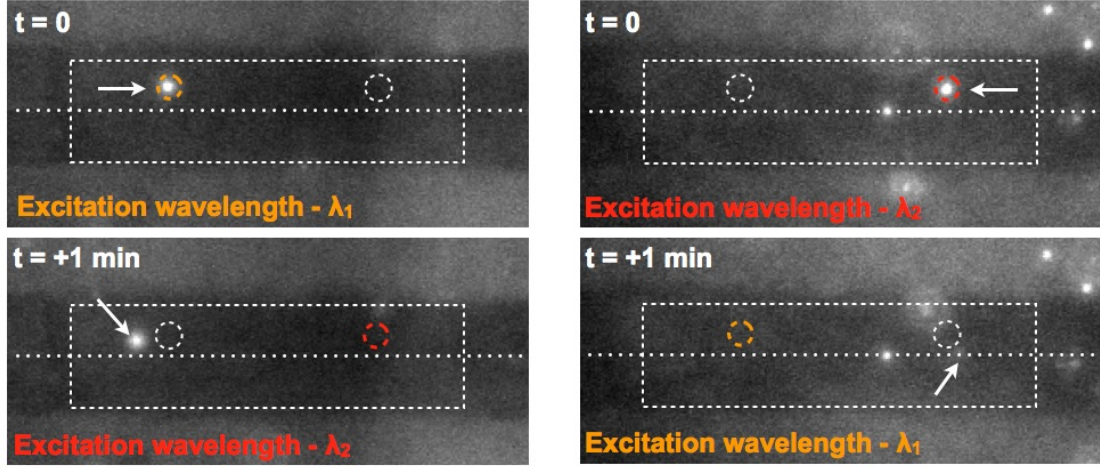


**Figure 6.13:** Experimental demonstration of the addressability of individual resonant traps on a single photonic crystal structure. **Left.** The first cavity is resonantly excited (1568 nm) and traps a particle for above one minute. The resonant excitation is then switched to that of the second cavity (1578 nm) which causes the particle to escape. **Right.** The reverse experiment is performed, where a second particle is help in the second cavity. The resonant excitation is set to 1578 nm. After one minute of continuous trapping, the excitation wavelength is switched to that of the first cavity (1568 nm) which causes the particle to escape.

shoot in resonance wavelength attributed to a minor under etching of the cavity, the 10 nm spectral separation is well-maintained during fabrication.

Figure 6.13 shows the separate trapping operation of the two neighboring cavities. The first cavity is excited at its resonance wavelength (1568 nm). A particle is directed towards the cavity using the auxiliary tweezers beam and remains stably trapped for over 1 minute as seen on the left frame. After this one minute time period, the excitation wavelength is switched to that of the second cavity (1578 nm). As a consequence, the particle is immediately released from the resonant trap and recovers Brownian motion. Similarly, the second particle is excited at its resonance wavelength (1578 nm). A second particle is captured and immobilized in the resonant trap for over 1 minute as seen (right frame). At the end of the one minute time span, the excitation wavelength is switched to that of the first cavity (1568 nm). As in the case of the first cavity, the second particle leaves instantaneously the second resonant trap, thus completing the demonstration of addressability of each trap. The simultaneous trapping of two particles, one in each cavity with the help of two tunable laser diodes and a fiber coupler would have constituted a nice complement to this experiment.

## Chapter 6. Resonant optical trapping and back-action effects

---

Regarding the design of photonic crystal devices with more than one cavity, the main parameters are mainly:

- the minimum spatial separation between two cavities in order to avoid coupling
- the minimum spectral separation between two eigenstates (including fabrication tolerances) in order to achieve true individual addressing
- the bandwidth of the access waveguide. In the case of a standard W1 waveguide, the bandwidth is limited by the presence of the light cone on the short-wavelength (high reduced energy) end and by presence of the band-edge on the long-wavelength end (low reduced energy).
- the length of the coupling waveguide and the propagation losses. This will influence the discrepancy in energy coupled between the first and the last cavities along the waveguide.
- the mechanical stability of the device

Our current understanding of the device and the experimental data available allow us to make predictions on the maximum number of cavities based on the the three first parameters only. On that basis, a standard device, 100  $\mu\text{m}$  long, could potentially hold up to 20 individually addressable cavities, separated in wavelength spectrum by more than a full cavity linewidth. This prediction is still to be demonstrated.

### 6.2.7 Summary

In this section the first experimental demonstration of a resonant optical trap in a 2D hollow photonic crystal cavity has been demonstrated. This result, on top of behind the original goal of this thesis work, constitutes a very important and exciting result. The properties of this novel trapping mechanism are numerous and is believed to open the door to new generations of devices capable of trapping individual particles whether mineral or biological in parallel at low optical powers. The following is a list of the currently identified properties of our resonant trap.



- The hollow nature of the cavity allows the particle to access the inner part of the field rather than just the evanescent tail as in the case of nanobeam cavities for example [149]. This feature greatly optimizes the interaction of the particle with the cavity field.
- The strongly localized nature of the cavity field, along with the access to the inner field give rise to large field gradients enabling ultra low power trapping.
- The trapped particle is held in suspension within the hollow volume, which minimizes the interaction with the silicon surface. This feature is of particular interest for biological particles applications where surface chemistry effects are not desirable.
- Unlike standard optical tweezers, which can trap simultaneously a large number of particles with a diversity of sizes and refractive indices, the hollow cavity trap is exclusive for particles whose size is of the order of that of the cavity.

## 6.3 Particle-induced eigenfrequency shift

The previous section is dedicated to the study of the influence of the cavity confined electromagnetic field on the mechanics of a dielectric particle in colloidal suspension. This section is dedicated to the study of the converse effect, that is the modification of the cavity eigenmode properties as an effect of the presence of a particle in its vicinity. In the first paragraph, a short explanation of how the presence of a particle is expected to have an influence on the cavity mode. In the second paragraph, a description of the experiment that has been performed is provided. In the third paragraph the main experimental results are shown and discussed. In the last paragraph, an application of this phenomenon for the counting or the tracking of the particle within the cavity is proposed and implemented.

### 6.3.1 Mechanism of the perturbation

As explained earlier, the presence of the large circular defect in the photonic crystal lattice introduces a "defect" or "cavity" state in the photonic bandgap (see Figure 6.2). The cavity state is associated to both an eigenfrequency (in practical terms, a resonance wavelength) and a spatial field distribution. Both these quantities are a function of the dielectric landscape of the cavity. It has been shown in Section 1 of this Chapter that the replacement of the low refractive index material of the periodic structure from air to water induces a resonance wavelength shift of approximately 45 nm. This can be equivalently understood in terms of a decrease of the refractive index contrast of the PhC structure or an increase of polarizability of the low refractive index material which induces a shift of the band structure towards lower reduced energies (longer wavelengths). As a result the eigenfrequency/resonance wavelength is displaced, along with the band-edges of both the "dielectric" and "air" bands. Nevertheless, no significant alteration of the field distribution is predicted by the 3D FEM model in the case of water immersion.

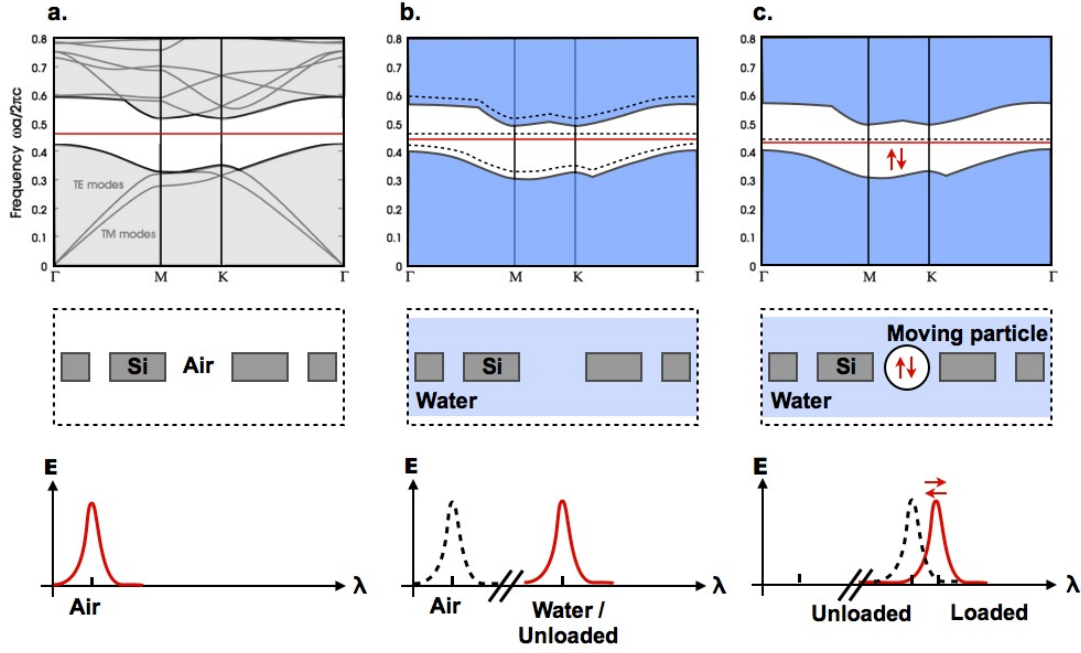


**Figure 6.14:** Illustration of the dynamic eigenfrequency shift. *a.* Band diagram of a two-dimensional triangular lattice (Si/air) and eigenstate of the circular cavity mode (red line). The amount of energy coupled to the eigenstate follows a Lorentzian law as dictated by the finite cavity photon lifetime. The eigenfrequency can be associated to a corresponding excitation wavelength in air. *b.* Water infiltration of the PhC structure displaces the band diagram towards lower energies. The associated resonance wavelength is red-shifted from the air resonance wavelength. *c.* The intracavity perturbation induced by the presence of the particle further red-shifts the resonance wavelength due to the increase in polarizable material. The amount of perturbation is a function of the position of the particle and therefore varies with time when the particle is in Brownian motion.

Following a similar principle, the replacement of a small volume of water within the circular cavity with a particle of higher polarizability is expected to displace further the cavity frequency (Figure 6.14.c). The noticeable difference here with water infiltration is that it constitutes a very localized intracavity perturbation. This phenomenon gets even more interesting in the case of a colloidal particle in Brownian motion. In this case, a dynamic change of the cavity eigenfrequency / resonance wavelength with time is expected. Small colloidal particles in standard optical traps have characteristic times (as estimated from the inverse of the cut-off frequencies of their power spectrum of motion) down to a few tens or hundreds of microseconds [67] [94]. In comparison, the cavity photon lifetime is of the order of 1 ps which justifies that eigenfrequency shift is considered instantaneous. The set of values taken by the resonance wavelength is expected to be between the "empty" or "unloaded" water resonance and a maximum value corresponding to the largest perturbation a given particle can create in the cavity mode, referred to as "loaded" resonance. The maximum perturbation is expected to occur when the overlap of the cavity confined field with the particle is maximum.

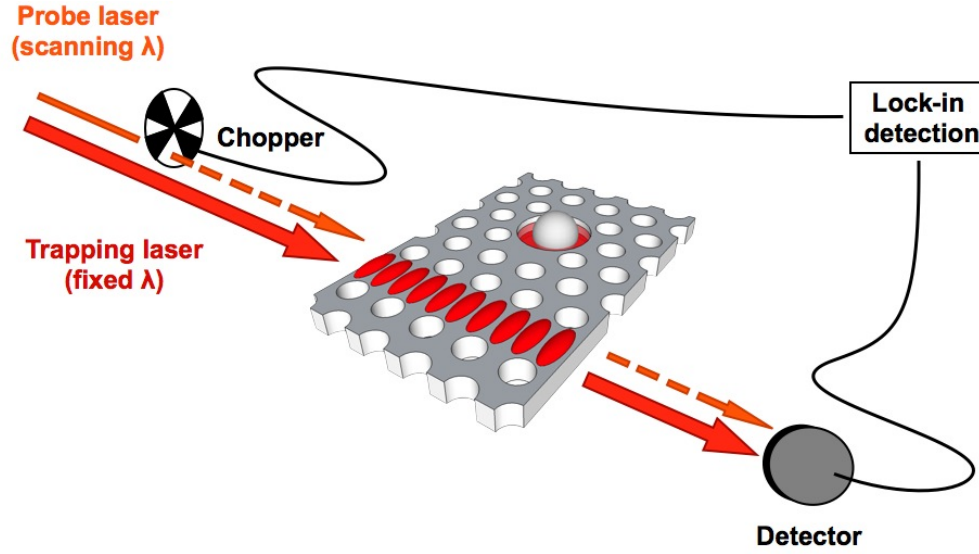


**Figure 6.15:** Schematic of the eigenfrequency shift measurement. Two tunable laser diodes are injected in a 90/10 fiber coupler. The first diode emits a high power excitation and serves as a trapping laser. The second diode emits a low power excitation, is modulated in amplitude and serves as a probe laser. Both emissions are coupled to the photonic crystal structure and the total transmission is monitored and sent to a lock-in amplifier. The probe laser wavelength is continuously scanned and records the variation of the resonance wavelength of the cavity under the influence of a resonantly trapped particle.

### 6.3.2 Description of the experiment

In order to demonstrate the existence of the eigenfrequency shift, a new resonant optical trapping experiment was set-up. In the same manner as in Section 2, a first tunable laser diode is used as the trapping laser. A 500 nm particle is captured in the resonant trap. Then, a second tunable laser diode is added on the set-up and is also coupled to the PhC structure under investigation using a 90/10 fiber coupler (Figure 6.15). This laser, operated at lower powers is used as a probe to monitor the spectral position of the resonance wavelength. The excitation wavelength of the second laser is set to periodically scan a 10 nm spectral range centered near the unloaded resonance wavelength of the cavity. The scanning period is 1 second long and includes a forward scan (100 nm/s), a backward scan (100 nm/s) and a dead time (0.8 s) for the self-referencing of the tuneable diode.

The light transmitted through the PhC structure is monitored using a fast NIR module (Hamamatsu G6122). The quantity of interest is the light intensity from the probe laser that is transmitted as a function of the probe wavelength. Nevertheless, this intensity is kept much smaller than the intensity from the trapping beam in order not to alter the displacement of the particle. A lock-in detection scheme is used in order to separate the probe signal from stronger trapping laser signal. The scanning laser is modulated at 1 kHz and a lock-in amplifier (Stanford Research) with a 1 ms integration time measures the evolution of the probe signal through the PhC device.

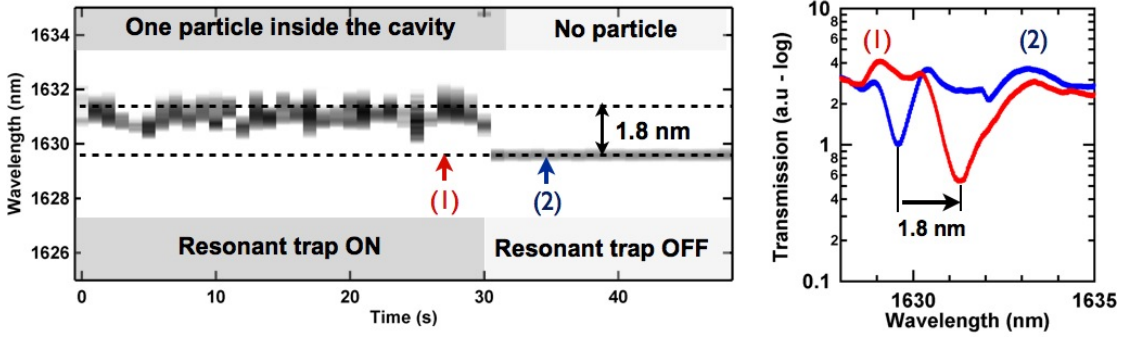


**Figure 6.16:** Experimental demonstration and measurement of the dynamic resonance wavelength shift. **Left.** Evolution of the transmission spectrum of the photonic crystal structure in the presence and absence of a resonantly trapped particle. **Right.** Two transmission spectra are superimposed (1) when a particle is trapped in the cavity (2) after the particle has left. A 1.8 nm red-shift can be measured. The apparent broadening of the cavity mode is attributed to an averaging effect of the measurement apparatus.

### 6.3.3 Experimental measurement

Following the procedure described in the previous paragraph, the transmission spectrum of a hollow cavity is measured in the presence or absence of a particle. The evolution of the spectrum in time (horizontal axis) is displayed in Figure 6.16.a with a scanning rate of 1 Hz. The vertical axis shows the range of wavelengths scanned by the probe laser. The transmitted power is plotted in gray levels. A dark region indicates a dip in the transmitted signal while a white region corresponds to a high transmission level.

During the first 30 seconds of the experiment a polystyrene bead is held in the resonant trap. The graph in Figure 6.16.a shows fluctuations of the position of the resonance wavelength between 1630.5 nm and 1631.5 nm. After 30 seconds, the resonant trap is turned off and the particle escapes from the cavity volume. It can be observed that the resonance wavelength instantaneously recovers a steady value near 1629.8 nm. The fluctuations of the cavity spectrum are directly attributed to the constricted residual Brownian motion of the particle within the stable trap region. This observation not only constitutes another proof of the suspended nature of the resonant trap, it also opens the door to the intracavity tracking of the position of the particle assuming that some calibration method could be designed.

On top of confirming the anticipated existence of the dynamic eigenfrequency shift, the experiment presented in Figure 6.16.a allows for the quantification of the perturbation induced by the particle. As mentioned earlier on in this section, the dynamic resonance wavelength shift is expected to be bounded by the unloaded resonance wavelength ( $\lambda_U$ ) on the short wavelengths side and by a maximum value, dictated by the maximum overlap achievable between the cavity field and the particle, on the long wavelength side. This maximum value is therefore intrinsically particle specific or, to be more accurate, polarizability specific.

Two "snapshots" of the dynamic spectrum, labelled (1) and (2), are superimposed and com-

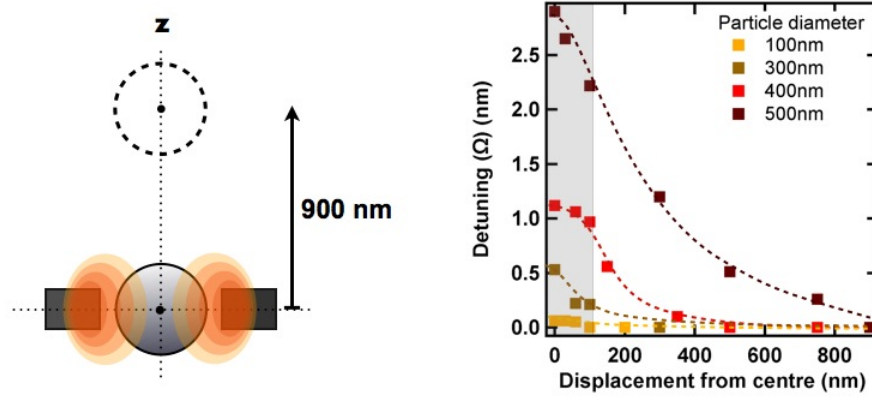


**Figure 6.17:** Computation of the resonance wavelength shift with Finite Element Method. **Left.** Schematic of the displacement of a 500 nm particle as performed in the computations. **Right.** Resonance wavelength shift induced by a range of particle of increasing diameter as a function of their position. The range of particles goes from 100 nm to 500 nm diameter. A maximum shift is observed for the largest particle when located in the center of the cavity.

pared in Figure 6.16.b. The spectrum (1) corresponds to the largest recorded shift while (2) corresponds to the unloaded resonance wavelength. An maximum resonance shift of 1.8 nm from the unloaded cavity resonance is measured and corresponds to a variation as large as twice the linewidth ( $\Delta\lambda = 0.75$  nm) of the unloaded mode. The apparent broadening of the cavity mode visible on spectrum (2) is attributed to an averaging effect of the slow acquisition time of the measurement set-up compared to the fast motion of the particle in the trap, rather than a decrease of quality factor.

The measurement performed in this experiment is in reasonable agreement with the FEM simulations performed and shown on Figure 6.17. In these simulations, the change in the eigenfrequency of the system is computed as a particle is moved from the center of the cavity to a far away position (left panel). The calculations are repeated for four different sizes of polystyrene particles ranging from 100 nm to 500 nm (right panel). A maximum shift of 2.8 nm is expected in the case of a 500 nm bead. As expected, this value decreases rapidly with the diameter of the particle under the simultaneous influence of the decrease in polarizability of the particle and the reduced overlap with the field. A maximum shift of 0.1 nm ( $\frac{\Delta\lambda}{8}$ ) is obtained in the case of a 100 nm particle, which sets of lower limit for the detection of single particles using the circular cavity at 1550 nm.

The discrepancy between the measured (1.8 nm) and computed (2.8 nm) shift values could be attributed to three factors.

- The slow scanning time of the laser diode prevents us from capturing truly instantaneous resonance spectra with respect to the position of the particle. In the current configuration it takes approximately 7.5 ms to scan the full cavity linewidth. This is of the same order of magnitude or larger than the "characteristic" time of a particle moving in an optical trap. The largest shift events, which also the less probable, are therefore possibly averaged out in the recorded signal.
- The colloids used in our experiments have a statistical distribution of sizes around the central 500 nm value with a standard deviation of 5% i.e.  $\pm 25$  nm. It is fairly possible that the measured particle was smaller than 500 nm. Such small differences in size are out of the reach of the fluorescence microscope and could not be spotted during the experiment.
- The FEM simulation is based on a refractive index of 1.59 for the particles. This value corresponds to the bulk refractive index of polystyrene at 588 nm. It would be interesting to obtain a value for the refractive index at  $1.5 \mu\text{m}$  before this simulation is performed again. The validity of the refractive index concept is also to be considered for a ( $\frac{\lambda}{3}$ ) particle in a sub wavelength optical nanocavity.

### 6.3.4 Application to single particle detection, tracking and analysis

The particle-induced resonance wavelength shift is a very exciting phenomenon which offers lots of possibilities related to the detection of individual nanoparticles. For example, a very efficient particle counter can be designed by appropriately detuning the excitation wavelength of the cavity and monitoring the intensity transmitted through the PhC device. If the cavity is excited near its unloaded resonance wavelength, the amount of light transmitted through the coupling waveguide will remain at a low value. In these conditions, a particle that crosses swiftly the hollow cavity will induce a rapid dynamic shift (Figure 6.18 - left). This generates a sharp spike in the transmission signal that can then be integrated with a simple digital counter thus providing a very efficient platform for single particle detection and enumeration. An experimental example of a particle induced transmission peak can be observed on the central panel of Figure 6.18. Following this scheme, single particle detection can be achieved at very low powers, typically of the order of the microwatt in the W1 waveguide.

It would be possible to use the same method as a way to track the intracavity displacements of a particle. Figure 6.18 (right panel) shows a typical record of the transmission through the PhC structure before and after a particle enters the cavity and remains resonantly trapped. As such, statistical and spectral analysis of these signals are believed to carry significant information on the motion of the particle within the resonant trap. These analysis will be carried on by M. Tonin who is continuing the work on resonant optical trapping. The prior knowledge of the relationship between the position of the particle and the induced perturbation would also

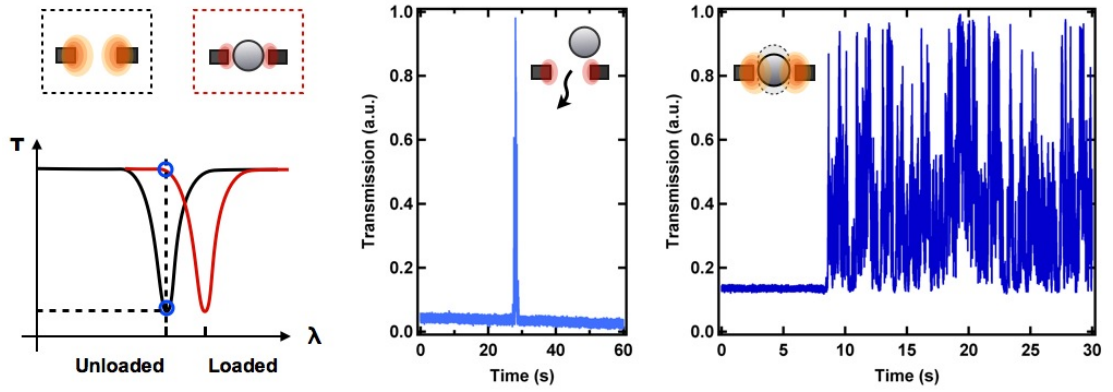


**Figure 6.18:** Experimental demonstration of single particle detection and tracking. **Left.** Schematic of the resonance-shift induced transmission variation. For a cavity excitation near the unloaded resonance wavelength, the transmitted power is very low. A particle entering the cavity induces a resonance shift that changes the transmitted power from a low value to a high value. **Center.** Experimental recording of a transmission peak caused by a particle swiftly crossing the cavity. **Right.** Record of the transmitted power in the absence and in the presence of a resonantly trapped particle. The large variations in transmitted power are attributed to the variations in resonance wavelength shift due to the particle being in Brownian motion.

open the door to the tracking of the position of the particle in real-time. Current investigations regarding the cooling of the center of mass of a particle (in vacuum) could potentially benefit from this type of sensing method.

Finally the circular cavity could be used to differentiate objects in complex solutions. It has been shown in the precedent paragraph that it is possible to distinguish particles of similar refractive index but different sizes (Figure 6.17). The maximum shifts computed (particle in the center of cavity) have been reported in a separate figure (6.19.a) as a function of the diameter of the particle. It can be seen on this figure that the perturbation induced increases rapidly with the size of the object (taken spherical). The trend observed could be that of a cubic function of the radius, as expected from the expression of the polarizability of a small dielectric particle [57]. The largest sensitivity would therefore be obtained for particles comparable in size with the cavity, here 700 nm. Based on the last two calculated points (400 and 500 nm) and assuming a conservative resolution limit of half a linewidth ( $Q_{\text{numerical}} = 3300$  i.e.  $\Delta\lambda = 0.45$ ), the hollow cavity could possibly distinguish particles that are bigger or smaller than 500 nm by 15 nm. Nevertheless the true behavior of the shift should be a function of both the radius of the particle and the overlap integral with the cavity field. In this case, a saturation of the perturbation might be observed for objects larger than 500 nm since the overlap will stop increasing despite the increase in polarizability.

A similar graph as Figure 6.19.a can be made for the dependence of the cavity perturbation as a function of the refractive index of the object (Figure 6.19.b). The modeled particle is kept with a diameter of 500 nm while its refractive index is increased from 1.33 (water) to 1.65. For this range of values the induced perturbation shows a linear response and a "single particle



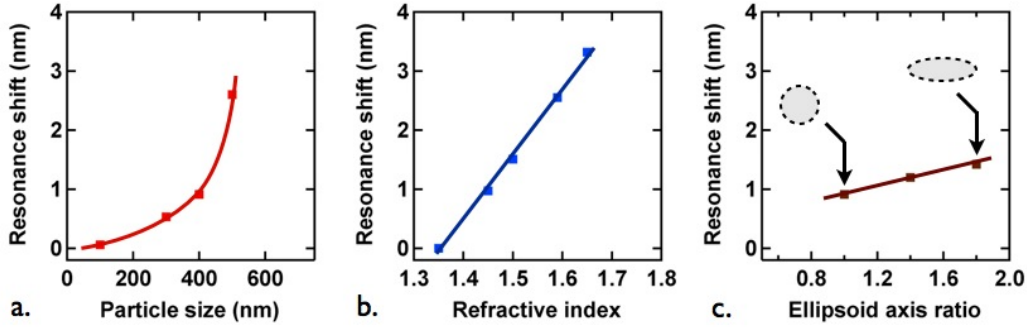


**Figure 6.19:** Influence of the diameter, refractive index and form factor on the resonance shift. *a.* FEM computation of the resonance wavelength shifts induced by polystyrene particles of 100, 300, 400 and 500 nm diameters. *b.* FEM computation of the resonance wavelength shifts induced by particles, 500 nm in the diameter, with refractive indices ranging from 1.33 to 1.65. *c.* Computations for particle of constant volume ( $0.065 \mu\text{m}^3$ ) but shapes going from a sphere to an elongated ellipsoid.

sensitivity" of 11 nm/RIU for the detection of 500 nm particles of various refractive indices. Following the same idea as for the sensitivity to the size of the object, the minimum refractive index change that could possibly be measured with the cavity lies in the order of 0.02 RIU. Finally, a third calculation shows that our system might also be capable of separating particles that are identical in volume ( $0.065 \mu\text{m}^3$ ) and refractive index (1.59) but with different form factors. In Figure 6.19.c, a spherical particle is elongated in an ellipsoid and the resonance shift induced is reported versus the ellipsoid axis ratio. It can be seen that an extra 0.4 nm shift is expected for an oblong particle lying in the plane of the silicon membrane, providing a clearly distinguishable signal on the monitoring system used.

By giving access to the inner resonant field, the circular hollow cavity opens the door to a wide variety of single particle detection, tracking and analysis applications. The principle is based on refractive index / polarizability measurement, which has the great advantage of being completely label-free. It is believed these applications could be of interest in many fields of science going from physics, biology, medicine or chemistry.

## 6.4 Back-action: mutual interaction between the particle and the cavity mode

This section is dedicated to the experimental evidences of mutual interaction between the mechanics of a particle resonantly trapped and the cavity eigenmode. This highly exciting phenomenon arises from the combined existence of sufficient optical trapping forces (shown in Section 6.2) and renormalization of the optical mode (Section 6.3). One very interesting consequence of the back-action in our system is the existence of two distinct trapping regimes, which was experimentally reported for the first time.



### 6.4.1 Introduction to back-action

In the historical point of view, the term "back-action" is related to the impossibility to perform measurements (by classical means) on an object (typically its position) with arbitrary precision owing to the Heisenberg Uncertainty Principle. As the sensitivity of the measurement is increased, the act of measuring itself influences the position of the object often referred to as "Quantum Back-action". This phenomenon introduces a source of noise in the measurement, of quantum origin, which contributes to the saturation of the precision at which the measurement can be made. This is referred to as "Standard Quantum Limit". One extensively studied manifestation of the Quantum Back-action is the radiation pressure induced oscillations of cavity mirrors in Fabry-Perot interferometers especially when applied to the detection of gravitational waves. In this case, the quantized nature of photons used for the measurement and their statistical distribution in time when emitted from a classical light source is responsible for the fundamental noise level achievable [206].

More recently, a second related phenomenon called "Dynamical Back-action" has been widely investigated [207], [208]. The latter is similar in the sense that it also describes the coupling of an optical oscillator (an optical cavity mode) and a mechanical oscillator (a cavity mirror), but differs in the fact that it is a classical effect rather than quantum. This phenomenon becomes perceivable when the cavity photon lifetime becomes comparable or larger than the period of the mechanical oscillator [207]. One very interesting consequence of this effect is the possibility to dynamically control the motion of the mechanical oscillator either in a positive (amplification) or negative (dampening) manner. A variety of optomechanical systems have been developed and studied recently demonstrating the optical cooling of the oscillator in its degree of freedom [209], [210].

In most of these work, the mechanical oscillator consists of a partially suspended cavity like a microtoroid [209] or a photonic crystal membrane in 1D [211], [210], or 2D [212]. In these cases, the optically driven oscillations of the suspended cavity are provided by the radiation pressure of the cavity mode radiation. The mechanical oscillator can also consist of an immobile cavity that excites a vibrating structure positioned in the near field of the cavity [213]. In this case the optical driving forces are more gradient-like (or dipole-like) [214] assuming that the common dipole force / radiation pressure separation for the Lorentz force on a polarizable element remains valid [RUBIN 2011].

The investigation of the interaction between the mechanics of a completely isolated nanoparticle and a high finesse optical cavity has also been the object of theoretical work [151], [215], [216]. Nevertheless no experimental demonstration of the optomechanical coupling between two such objects has not been reported to this day. The physics of this type of system is highly exciting because it is noticeably different from the previously published devices. A free nanoparticle (in vacuum or in a colloidal suspension) does not constitute a mechanical oscillator itself. However, when the same particle is placed in an optical field that induces a restoring force, it is common to describe the mechanics of the particle as that of an oscillator

[67]. The most common case is that of a particle trapped in a tightly focused gaussian laser beam where the optical gradient force follows Hooke's law for small displacements of the particle and can be associated to a spring constant. It is important to note that in the later case, the properties of the optomechanical oscillator are only little dependent on the wavelength of the trap through the maximum focusing achievable with standard optics.

In the case of our system, the motion of the centre of mass of the particle and the cavity field are mutually coupled. The strong optical trapping forces exert a restoring force that retains the particle within the hollow cavity while the position dependent eigenmode perturbation dynamically renormalizes the amount of energy coupled to the cavity. The trapping forces experienced by the particle are therefore expected to vary in a non trivial manner with the excitation wavelength. Moreover, phenomena where the particle itself contributes to the build-up or stiffening of the optical trap are expected to be observable. This phenomenon was first predicted in the work of Barth and Benson [5] and was referred to as "Self-induced trapping" (SIT). Further theoretical investigation of this effect was also published in the work of Hu *et al* [151]

### 6.4.2 Escape threshold power experiment

The coupling between the particle and the optical field is expected to manifest in several ways. One of them is a non-trivial dependency of the trapping strength with the excitation wavelength. This behavior is investigated by monitoring the trapping threshold power for a range of wavelengths centered on the unloaded resonance wavelength.

A given detuning value ( $\delta$ ) is chosen and coupled to the cavity with a large laser output power (typically 8 to 10 mW). A 500 nm particle is captured and held in the resonant trap. The excitation power is then decreased by a small amount (typically 0.1 mW) every 10 seconds. This operation is repeated until the resonant trap is not strong enough anymore to retain the particle and the particle escapes. After the particle has left, the laser output power is recorded as the "escape threshold power". Finally the complete operation is repeated for a large number of detuning values. This experiment is made possible by the very sharp transition that exists between the escape threshold power and the precedent higher power. That is to say that once the escape threshold power is reached, the particle escapes almost instantaneously.

Figure 6.20 shows the evolution of the escape threshold power for a range of wavelengths detuned from  $\delta = -1$  to  $\delta = +3$  nm from the unloaded resonance. The ETP is reported simultaneously on the right axis in units of the laser output power and on the left axis in unit of power in the W1 waveguide. The black circles indicate the escape threshold power for each detuning. The gray area constitutes a guide for the eye and separates the region where it is possible to resonantly trap a particle from the region where resonant trapping is not possible.

Three striking observations can be made from Figure 6.20.

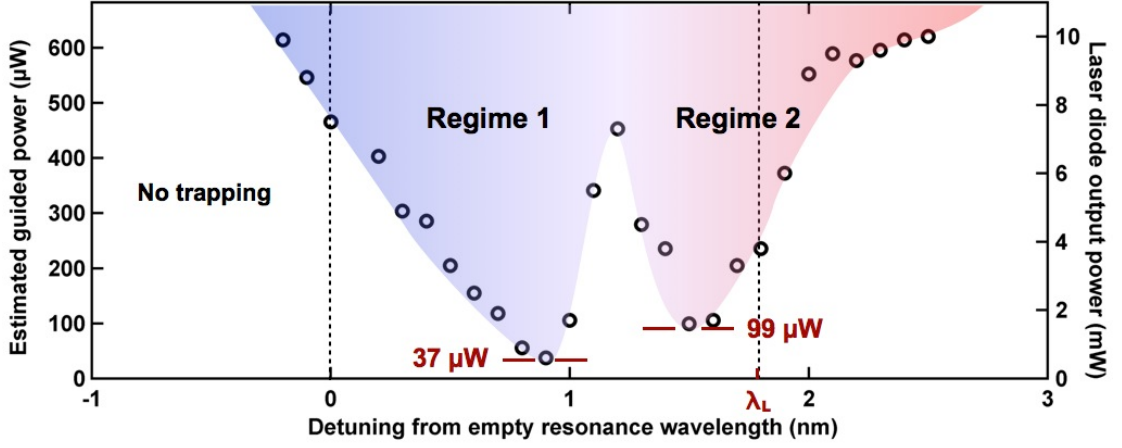


**Figure 6.20:** Measurement of the escape threshold power. Experimental record of the minimum optical power in the access waveguide (left axis) and out of the laser (right axis) at which a particle escapes the resonant trap as a function of detuning. The black circles correspond to escape trapping times of the order of ten seconds or less.

- The resonant nature of the trap is clearly illustrated by the existence of a restricted range of wavelengths only for which it is possible to observe trapping.
- The spectral extent of the trapping region is not centered on the unloaded resonance wavelength but on a redshifted value ( $\delta \approx 1.2$  nm). This observation constitutes the first manifestation of back-action.
- The evolution of the ETP with the detuning is non trivial and does not resemble the unloaded cavity line shape. On the contrary, two distinct minima, that we associate to two trapping regimes, can be observed. The guided optical powers corresponding to these minima are reported on Figure 6.20. They indicate the possibility to trap particles from 40  $\mu$ W in the waveguide.

### 6.4.3 Trapping regimes

The nature of the two trapping regime can be understood with the help of Finite Element modeling. The optical forces acting on a 500 nm spherical dielectric particle have been computed for a variety of positions and a large range of detunings. Calculations are performed using the Maxwell Stress Tensor (MST) formalism integrated over the surface of the spherical particle. Energy is coupled to the empty hollow cavity through a plane wave and the coupling process is checked to be independent of the detuning.

The optomechanical forces calculated are presented in Figure 6.21 as a function the position of the particle (horizontal axis) and for a set of meaningful detunings. The displacements of the particles are divided into two components: in-plane and out-of-plane (see Figure 6.21.a). The set of detuning starts from  $\delta = 0$  (unloaded resonance) up to  $\delta = 2.9$  (computed loaded

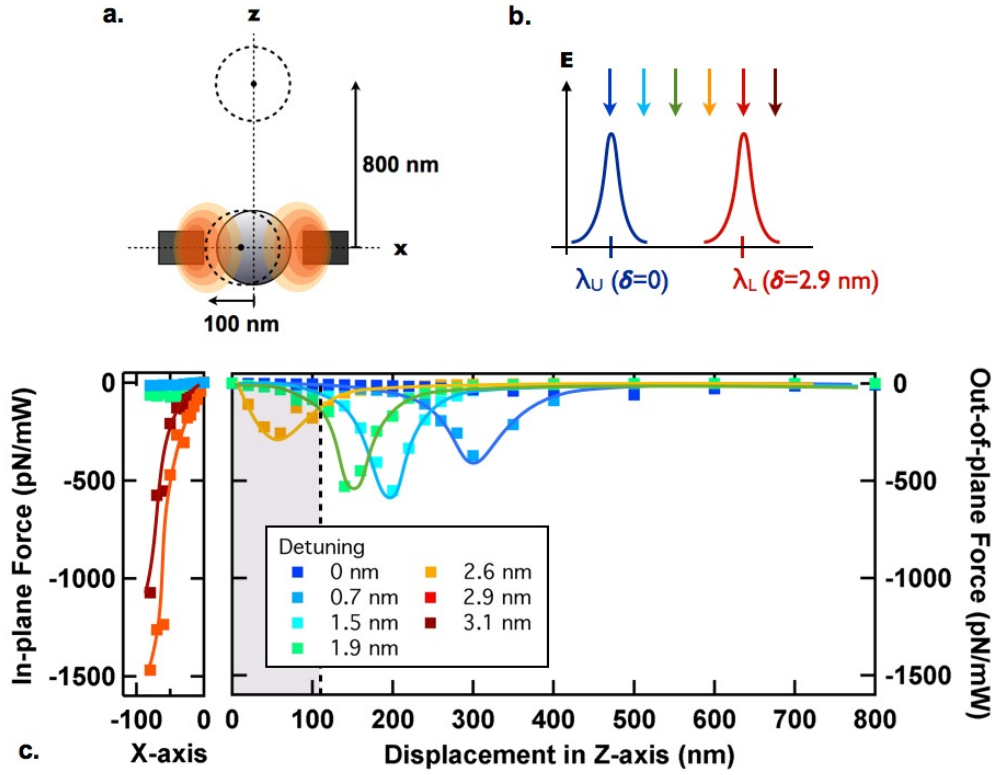


**Figure 6.21:** Optical forces calculated with Finite Element Method. *a.* Schematic of the various positions of the particle modeled in the calculations. Two sets of position, one along the horizontal axis (from -100 nm to 0) and one along the vertical axis (0 to 800 nm) have been chosen. *b.* Illustration of the detuning values that have been used for the calculation of the forces. *c.* Trapping forces as a function of the position of the particle for the indicated detuning values along the horizontal axis inside the cavity (left panel) and along the vertical axis (right panel). The computations are performed for a 500 nm particle and include the particle-cavity renormalization. The shaded area indicated corresponds to the half-thickness of the silicon slab.

resonance) and includes a further detuned value of  $\delta = 3.1$  (Figure 6.21.b). The projection of the total optical force applying on the particle when moving in the plane are shown on the small panel of Fig. 6.21.c on the left. The out-of-plane component of the force calculated for an out-of-plane displacement is shown on the large panel on the right. The axis of both panels are shown on the same scale (displacement and force) to give a more accurate vision of the phenomena. The solid lines drawn of the Fig. 6.21.c are guides for the eye.

As expected, large variations in the magnitude of the out-of-plane and in-plane force components are observed when changing the detuning. More interestingly, the study of the out-of-plane component indicates that the position of the point of maximum force is also a detuning dependent quantity. Besides, the restoring force profile displays a large degree of anharmonicity for the smallest detuning which is in strong contrast with the case of "standard" gaussian beam optical tweezers. Finally, one can notice that the out-of-plane and in-plane components get sequentially predominant as the amount of detuning increases. The later

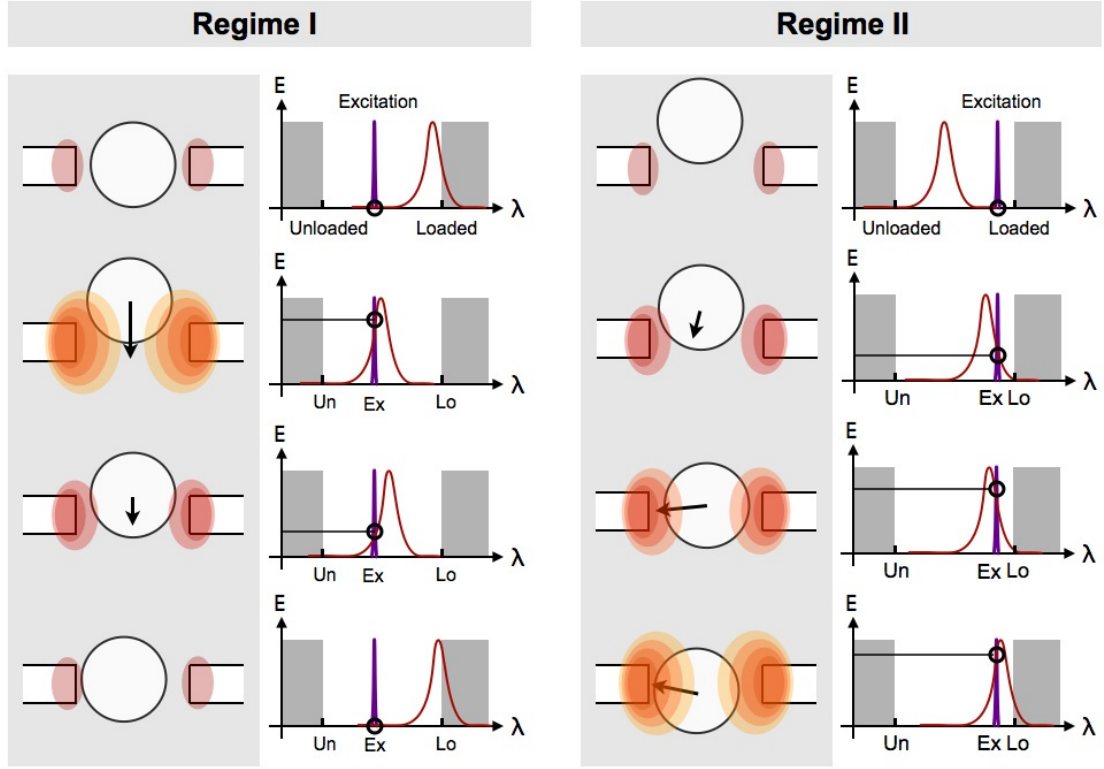


**Figure 6.22:** Illustration of the resonant optical trapping regimes. **Left.** Illustration of the first trapping regime. The eigenmode of the cavity is weakly coupled to the excitation laser in the presence of the particle. An out-of-plane displacement reduces the shift induced on the resonance and couples the eigenmode to the excitation. This results in strong gradient forces that pull the particle back inside the cavity. **Right.** Illustration of the second trapping regime. The absence of a particle in the cavity causes the eigenmode to be weakly coupled to the excitation laser. An incoming particle renormalizes the eigenmode which couples strongly to the excitation and hence increases the trapping strength.

is believed to be responsible for the existence of the two regimes observed experimentally. On a separate aspect, a maximum in-plane force of 1.5 nN is computed near the sidewall of the cavity for an input power of 1 mW. This value corresponds to a three orders of magnitude increase in terms of optical forces compared to previous studies involving evanescent field trapping [149].

As a consequence of these observations, the first trapping regime (shorter detunings) can be conceptualized as a quasi-1D trap where the particle is held within the hollow volume under the influence of mainly out-of-plane forces. In these detuning values, the in-plane forces are considerably weaker than their out-of-plane counterparts. The relatively weak but spatially extended out-of-plane forces reach their maximum value when the center of the particle is actually a few tens or hundreds of nanometer above the surface of the silicon membrane. This phenomenon is the direct consequence of the particle-induced eigenmode renormalization: the presence of the particle within the cavity prevents the coupling of energy

from the waveguide to the eigenmode for small detuning excitations. A deviation of the position of the particle towards the outside reduces the spectral separation between the excitation and resonance wavelength which causes a build up of the intracavity field and the appearance of a strong restoring force. The particle is then pulled back towards the central region. This phenomenon is illustrated in Figure 6.22 on the left panel.

Conversely, the second regime (farther detuning values) can be seen as a fully 3D trap where the stable position is located near the inner sidewalls of the cavity. For these positions the in-plane force component is much larger than the out-of-plane one and can be seen on Figure 6.21. They also correspond to the region where the electric field reaches its maximum amplitude. In this regime, the separation between the unloaded resonance wavelength and the greatly detuned excitation ( $\delta > \Delta\lambda$ ) prevents the optical energy from being coupled to the cavity mode in the absence of a particle. This is coherent with the fact that the out-of-plane force component is negligible when the particle is located outside of the silicon membrane (small induced shift). On the contrary, the presence of a particle inside the cavity reduces the separation between the excitation and the shifted resonance wavelength, thus contributing to the build up of the cavity field. This phenomenon is illustrated on Figure 6.22, on the right panel.

It is interesting to note that the second regime constitutes a clear case of Self Induced Trapping as described in Ref [5]. The displacement of the particle towards the inside of the cavity stiffens the optical trap, which in turn, drags the particle deeper in the cavity. The stable trapping of the particle is achieved at the end of this positive feedback mechanism, at which a maximum of energy is being coupled to the optical mode on average. More interestingly, the first regime can also be described as another case of Self-Induced Trapping with a negative feedback mechanism. In this case, the particle experiences almost no optical energy and therefore no optomechanical forces for as long as it is located inside the volume of the cavity. This case of SIT, which was not described in the paper from Barth and Benson, is mainly a consequence of the planar symmetry of the hollow cavity and the silicon membrane.

### 6.5 Summary

The work performed and the techniques developed during the time of this project have permitted the achievement of a set of very exciting experimental results. The most significant ones are:

- The first demonstration of resonant optical trapping in a hollow photonic crystal cavity has been demonstrated. The intrinsic properties of the hollow cavity allowed for the optical manipulation of dielectric particles of 250 nm and 500 nm at powers of the order of 300 and 100  $\mu\text{W}$ .
- The dynamic eigenmode perturbation of the particle on the cavity has been evidenced in the form of a redshift of the resonance wavelength. A 1.8 nm shift, which corresponds

to more than twice the linewidth of the unloaded cavity, was measured for a 500 nm particle.

- The existence of back-action between the particle and the cavity mode has been observed through the wavelength dependency of the minimum power required to trap a particle. The observation of two distinct Self Induced Trapping regimes is reported for the first time.

Nevertheless, these results constitute only a first step in the study of interactions between a hollow cavity and single particles. It would be highly interesting to pursue these investigations with a range of complementary experiments. First of all, to further the understanding of the physics of the resonant trap and the back-action effects. Second to confirm the wide possibilities in terms of application offered by our hollow cavity approach.

On the physics of the resonant trap, one point of interest is the effect of particles inducing larger renormalization on the cavity eigenmode. In the case of a 500 nm polystyrene particle, the "optical volume" of the perturbation is rather small compared to the mode volume of the cavity. The spatial field distribution can be considered constant and only the eigenfrequency shift due to the increase in polarization energy is noticed. The presence of a particle of higher polarizability such as a silicon nanocrystal and/or featuring absorption such as metallic colloids or suitably tuned quantum dots is expected to have a more dramatic impact. For example, dynamic variations of the quality factor should be observable.

The nature of the two Self-Induced Trapping regimes, though intuitively understood, is still to be confirmed experimentally. One method envisaged to distinguish their properties is the study of the power spectra of the displacements of the particle [94]. In the current understanding, the second regime corresponds to a tight trap with a narrow trapping volume and stiff restoring forces (Fig. 6.21). Not taking into account the presence of the silicon membrane, the power spectrum recorded for a trapped particle is expected to be somewhat similar to that of a stiff optical tweezers trap. On the contrary, the first regime corresponds to a looser trap, with an extended anharmonic region and an extended trapping volume. The power spectrum of displacements of the particle is therefore expected to be noticeably different from that of the second regime.

Finally, the existence of a maximum in the escape threshold power around 1.2 nm detuning (Fig. 6.20) is still to be understood. The current understanding and simulations suggest that the transition from Regime 1 to Regime 2 should be smooth. Based on the latter, no apparent reason seems to justify why the resonant trap should be less stable (corresponding to a higher escape threshold power) for an intermediate detuning. The current direction of investigation focuses on the calculation of the work produced by a particle to escape from the resonant trap. Early simulations using FEM and a phenomenological in-house model indicate that the energy required for the particle to escape could be dependent on the escape path, thus weakening the tacit hypothesis of conservativity of the system. The possibility of optical forces

displaying some degree of non-conservativity has already been pointed out in the theoretical work of Rubin and Deych [64] in the specific case of a whispering-gallery mode resonator trapping small dielectric particles.

On the application aspect of the resonant optical trapping technique, three main directions need to be developed. First of all, the size and refractive indices of particles used in our experiment easily falls within the category of a variety of biological entities such as viruses[84] [113] [110], cell organelles [108] and small bacteria [105], [106]. Nevertheless, an experimental demonstration of biological specimen handling within our resonant trap has not been performed yet. The benefits of the suspended nature and ultra low power isolation, though intuitive, are thus still to be confirmed.

Similarly, the size of the smallest particles than can be trapped in the hollow cavity with reasonable power is still to be determined experimentally. This number is estimated around 100 nm for a dielectric particle like polystyrene and could be smaller for metallic colloids or high refractive index quantum dots. Nevertheless the exclusivity of the trap will not be guaranteed at these scales and the possibility that several particles can be captured simultaneously should be take into account. The experimental sensitivities of the circular cavities in term of particle diameter, refractive index and form-factor are also to be determined.

Finally, owing to the scaling laws of Maxwell equations, one direct possibility in the quest of trapping smaller and smaller particles is to make use of a scaled down circular HPhC structure. The translation from near-infrared wavelengths in a silicon membrane to visible wavelengths in a gallium-nitride membrane could potentially offer a direct factor 3 reduction of the circular hole diameter. Assuming that the cavity properties are conserved despite the loss in vertical confinement, the new structure could offer exclusive trapping of particles in the range of 100 to 200 nm without the need for further development than what those already demonstrated [217].



## 7 Conclusion and Outlook

The work presented in this thesis has pursued the experimental demonstration of resonant optical trapping of dielectric nanoparticles in a planar photonic crystal cavity. In order to achieve this goal, a complete experimental setup has been assembled and a pneumatically controlled optofluidic chip has been designed, fabricated and finally used as a platform for the resonant trapping experiment.

**Conclusions** The investigations have been focused on two-dimensional hollow photonic crystal cavities, which feature a central region where the confined field overlaps with the low refractive index region. Hence, the cavity field is free to interact with an external object. The main design that has been studied consists of a large circular cavity, 700 nm in the diameter in a triangular lattice of a silicon membrane, operating in the near-infrared (around 1.55  $\mu\text{m}$ ). These cavities have been found to maintain a large quality factor through water immersion ( $\approx 2000$ ) which makes them very suitable for aqueous working conditions as required by colloidal or biological suspensions.

The characterization and monitoring of the cavities has been performed using a combined End-fire and Fourier imaging technique. The experiments have been performed using fluorescent polystyrene particles ranging from 100 to 500 nm in the diameter. Low light fluorescent imaging of these particles has been achieved using an Argon laser beam for the photoexcitation of the fluorophores and an EMCCD camera. Fine manipulation of the microspheres around the photonic crystal cavities has been made possible with the implementation of auxiliary optical tweezers. The latter relies on a Ti:Sapphire laser focused through an oil-immersion microscope objective. Finally, position sensing of the particles was achieved using a confocal-type sensor.

The reliable and repeatable injection of colloidal particles has required the development of a two-layer, ultra-thin microfluidic membrane in polydimethylsiloxane. The first, thinner, layer allows for the transportation of the particles in solution to the photonic crystal cavities. The second, thicker, layer includes peristaltic valves that enable the accurate control of the

flow of particles. The fabrication and assembly of the two-membranes and later, the merging of the photonic crystal chip with the complete microfluidic membrane has been performed in the Center of Micro-nano-technology of EPFL, and in the cleanrooms of the Institute of Condensed Matter Physics. Two complete optofluidic chips have been assembled during the time of this thesis. Both of these samples have produced repeatable working conditions continuously for up to six months.

All of these developments have permitted to bring together the appropriate conditions required to observe the optical trapping of nanoparticles in the resonant field of the cavities. The demonstration of resonant trapping has been realized with polystyrene particles of two sizes, 250 nm and 500 nm in the diameter. The particles have been kept in the cavity trap for time ranging up to twenty minutes, with optical powers as low as 120  $\mu\text{W}$  (500 nm) and 360  $\mu\text{W}$  (250 nm). These trapping powers correspond to an improvement of more than two orders of magnitude compared to standard optical tweezers. In addition, several features inherent to the circular cavity designs have been identified. The suspended nature of the resonant trap has been demonstrated, along with its exclusivity. The latter corresponds to the fact that only one particle is allowed within the trap for a given range of sizes. Finally, the possibility to form arrays of individually addressed resonant traps has also been shown. This definitely constitutes a significant advantage in the view of realizing on-chip detection and manipulation systems.

A further investigation has been conducted on the influence of the presence of a particle on the cavity mode. It has been found that a dielectric particle induces a dynamic resonance wavelength shift of the cavity mode. The magnitude of the shift is position dependent and particle dependent. A maximum redshift of 1.8 nm has been found in the case of a 500 nm polystyrene particle within the cavity. This corresponds to more than twice the linewidth of the cavity mode in water. Based on this observation, a simple method to detect and count particles has been proposed. It is expected that this scheme will allow the differentiation of particles according to their size, refractive index and possibly their shape. It is interesting to highlight that this detection method is based on the polarizability of the particle and thus label-free.

Finally, the existence of a mutual interaction between the particle and the resonant mode has been evidenced. This phenomenon manifests in the form of a wavelength dependent escape threshold power. The measurement of the aforementioned quantity for a 500 nm particle has revealed the existence of two distinct trapping regimes. The aid of finite element method analysis has allowed to get an insight into the nature of these regimes. In the first regime, a particle in the center of the cavity experiences almost no optical force. A deviation of the particle from the center increases the energy coupled into the cavity mode and induces a restoring force that brings the particle back into the cavity. In the second regime, the absence of a particle inside the cavity implies that no energy is coupled to the cavity mode. Upon arrival of a particle in the vicinity of the cavity, a large build up of the field is induced which attracts the particle further down inside the hollow cavity. The spectral position of these two

---

regimes is understood to be inherently particle specific and opens the door to particle specific trapping. In addition, the nature of the first regimes indicates that a trapped particle is actually exposed to very little optical power. This can be of great interest for the optical manipulation of light sensitive biological particles.

**Outlook** The achievement of optical trapping in a planar photonic crystal cavity holds great promises both in terms of understanding further the physics of resonant optical forces and in terms of applications. The work presented in this thesis constitutes only a small step towards the demonstration of the full potential of photonic crystal cavities for the optical manipulation of nano-objects. A lot of directions that have been envisaged over the last remain unexplored.

The resonant trapping of particles outside of the range of standard optical tweezers, for example, has not been performed within the hollow cavity yet. In the current understanding, the trapping of 100 nm polystyrene particles should be achievable with guided powers of the order of 2 to 3 mW. Similarly, although theoretically straightforward, the manipulation of biological entities is yet to be demonstrated. It would also be of the highest interest to compare the evolution of the trapped entity over prolonged exposure to the resonant trap with that of an identical specimen trapped in optical tweezers.

The investigation of other hollow cavity designs is yet to be made. The circular cavity used in this work did not receive through any attempt of optimization. It is strongly believed that appropriate tailoring of the first rows of holes could possibly lead to high quality factors and/or large overlaps with the immersion medium. Also, a variety of other cavities architectures could be envisaged, with other geometries. Finally, the scalability of Maxwells equation, and thus photonic crystals, implies that the circular cavity design should be be transposable to a material with transmission in the visible, such as GaN. The approximate factor three reduction of the size of the cavity ( $\approx 200$  nm) would open the door to the trapping of virus and large biomolecules.

The capacity of the cavity mode to discriminate particles of distinct sizes, refractive indices or shape is also to be demonstrated experimentally. In particular, it would be very interesting to compare the experimental sensitivities to each of these parameters to that obtained by U. Dharanipathy using finite elements. The optical sorting of specimen in a complex solution of mixed particles would constitute a compelling achievement.

The nature of the trapping regimes, though intuitively understood, need to be confirmed experimentally. This can be performed through a set of investigations. The strong differences in the optical forces in terms of magnitude, direction and spatial distribution must have consequences on the constrained Brownian motion of the particles. It should be possible to point out these differences between the two regimes either in the spatial domain through a more accurate particle tracking method, or in the time domain through the analysis of the power spectra of the particles displacements. The evolution of the escape threshold power plot with the polarizability of the particle should also provide insightful information. For

example, in the current understanding, it is expected that the first regime should progressively vanish in the limit of high polarizability particles, leaving only a far redshifted second regime of narrower bandwidth and deeper potential. Conversely, in the low polarizability particles limit, both regimes are expected to merge and remain centered at the empty resonance wavelength.

The achievement of most of these results requires the fine optimization of a variety of parameters from the experimental point of view. For example, further improvements in terms of low light imaging and optical tweezers assisted manipulation could be obtained through the replacement of the thick PDMS layer with a glass counterpart. This approach would also simultaneously solve oil immersion contamination issues and thus facilitate the maintenance of the optofluidic chip. Amelioration of the interconnect scheme would also be greatly beneficial. Finally, additional microfluidic functions could be implemented in order to more efficiently direct the particles towards the photonic crystal cavities, prevent external contaminations, or allow the separation of sorted particles.

## Bibliography

- [1] J. D. Thompson, T. G. Tiecke, N. P. de Leon, J. Feist, A. V. Akimov, M. Gullans, A. S. Zibrov, V. Vuleti, and M. D. Lukin, "Coupling a single trapped atom to a nanoscale optical cavity," *Science*, vol. 340, no. 6137, pp. 1202–1205, 2013.
- [2] Y. Takahashi, Y. Inui, M. Chihara, T. Asano, R. Terawaki, and S. Noda, "A micrometre-scale raman silicon laser with a microwatt threshold," *Nature*, vol. 498, pp. 470–474, 06 2013.
- [3] E. Gavartin, P. Verlot, and T. J. Kippenberg, "A hybrid on-chip optomechanical transducer for ultrasensitive force measurements," *Nat Nano*, vol. 7, no. 8, pp. 509–514, 2012. 10.1038/nnano.2012.97.
- [4] A. Ashkin, J. M. Dziedzic, J. E. Bjorkholm, and S. Chu, "Observation of a single-beam gradient force optical trap for dielectric particles," *Optics Letters*, vol. 11, no. 5, pp. 288–290, 1986.
- [5] M. Barth and O. Benson, "Manipulation of dielectric particles using photonic crystal cavities," *Applied Physics Letters*, vol. 89, no. 25, p. 253114, 2006. Cited By (since 1996): 22 Export Date: 28 June 2012 Source: Scopus Art. No.: 253114.
- [6] G. Cosendey, J.-F. Carlin, N. A. K. Kaufmann, R. Butte, and N. Grandjean, "Strain compensation in AlInN/GaN multilayers on GaN substrates: Application to the realization of defect-free bragg reflectors," *Applied Physics Letters*, vol. 98, no. 18, pp. 181111–3, 2011.
- [7] U. Gruning, V. Lehmann, and C. M. Engelhardt, "Two-dimensional infrared photonic band gap structure based on porous silicon," *Applied Physics Letters*, vol. 66, no. 24, pp. 3254–3256, 1995.
- [8] Y. A. Vlasov, X.-Z. Bo, J. C. Sturm, and D. J. Norris, "On-chip natural assembly of silicon photonic bandgap crystals," *Nature*, vol. 414, no. 6861, pp. 289–293, 2001. 10.1038/35104529.
- [9] K. M. Ho, C. T. Chan, C. M. Soukoulis, R. Biswas, and M. Sigalas, "Photonic band gaps in three dimensions: New layer-by-layer periodic structures," *Solid State Communications*, vol. 89, no. 5, pp. 413–416, 1994.

## Bibliography

---

- [10] E. Yablonovitch, T. J. Gmitter, and K. M. Leung, "Photonic band structure: The face-centered-cubic case employing nonspherical atoms," *Physical Review Letters*, vol. 67, no. 17, pp. 2295–2298, 1991. PRL.
- [11] J.-M. Lourtioz, H. Benisty, V. Berger, j.-M. Gérard, D. Maystre, and A. Tchebnokov, *Les cristaux photophoniques ou la lumière en cage*. Hermès Science, 2003.
- [12] J. D. Joannopoulos, S. G. Johnson, J. N. Winn, and R. D. Meade, *Photonic crystals: molding the flow of light*. Princeton university press, 2011.
- [13] K. M. Ho, C. T. Chan, and C. M. Soukoulis, "Existence of a photonic gap in periodic dielectric structures," *Physical Review Letters*, vol. 65, no. 25, pp. 3152–3155, 1990. PRL.
- [14] E. Yablonovitch, "Inhibited spontaneous emission in solid-state physics and electronics," *Physical Review Letters*, vol. 58, no. 20, pp. 2059–2062, 1987. PRL.
- [15] J. R. Wendt, G. A. Vawter, P. L. Gourley, T. M. Brennan, and B. E. Hammons, "Nanofabrication of photonic lattice structures in gaas/algaas," in -, vol. 11, pp. 2637–2640, AVS, 1993.
- [16] T. Krauss, Y. Song, S. Thoms, C. Wilkinson, and R. DelaRue, "Fabrication of 2-d photonic bandgap structures in gaas/algaas," *Electronics Letters*, vol. 30, no. 17, pp. 1444–1446, 1994.
- [17] D. Labilloy, H. Benisty, C. Weisbuch, T. F. Krauss, R. M. De La Rue, V. Bardinal, R. Houdré, U. Oesterle, D. Cassagne, and C. Jouanin, "Quantitative measurement of transmission, reflection, and diffraction of two-dimensional photonic band gap structures at near-infrared wavelengths," *Physical Review Letters*, vol. 79, no. 21, pp. 4147–4150, 1997. PRL.
- [18] E. Purcell, "Spontaneous emission probabilities at radio frequencies," *Physical Review*, vol. 69, p. 681, 1946.
- [19] D. Englund, D. Fattal, E. Waks, G. Solomon, B. Zhang, T. Nakaoka, Y. Arakawa, Y. Yamamoto, and J. Vučković, "Controlling the spontaneous emission rate of single quantum dots in a two-dimensional photonic crystal," *Phys. Rev. Lett.*, vol. 95, p. 013904, Jul 2005.
- [20] W.-H. Chang, W.-Y. Chen, H.-S. Chang, T.-P. Hsieh, J.-I. Chyi, and T.-M. Hsu, "Efficient single-photon sources based on low-density quantum dots in photonic-crystal nanocavities," *Phys. Rev. Lett.*, vol. 96, p. 117401, Mar 2006.
- [21] J. P. Dowling, M. Scalora, M. J. Bloemer, and C. M. Bowden, "The photonic band edge laser: A new approach to gain enhancement," *Journal of Applied Physics*, vol. 75, no. 4, pp. 1896–1899, 1994.
- [22] J. O'Brien, O. Painter, R. Lee, C.-C. Cheng, A. Yariv, and A. Scherer, "Lasers incorporating 2d photonic bandgap mirrors," *Electronics Letters*, vol. 32, no. 24, pp. 2243–2244, 1996.

- 
- [23] O. Painter, R. K. Lee, A. Scherer, A. Yariv, J. D. O'Brien, P. D. Dapkus, and I. Kim, "Two-dimensional photonic band-gap defect mode laser," *Science*, vol. 284, no. 5421, pp. 1819–1821, 1999.
- [24] A. Mekis, J. C. Chen, I. Kurland, S. Fan, P. R. Villeneuve, and J. D. Joannopoulos, "High transmission through sharp bends in photonic crystal waveguides," *Phys. Rev. Lett.*, vol. 77, pp. 3787–3790, Oct 1996.
- [25] T. F. Krauss, "Why do we need slow light?," *Nat Photon*, vol. 2, pp. 448–450, 08 2008.
- [26] D. Marcuse, "Theory of dielectric optical waveguides," *New York, Academic Press, Inc.*, 1974. 267 p., vol. 1, 1974.
- [27] P. R. Villeneuve, S. Fan, J. D. Joannopoulos, K.-Y. Lim, G. S. Petrich, L. A. Kolodziejski, and R. Reif, "Air-bridge microcavities," *Applied Physics Letters*, vol. 67, no. 2, pp. 167–169, 1995.
- [28] W. Zhang, L. Huang, C. Santschi, and O. J. F. Martin, "Trapping and sensing 10 nm metal nanoparticles using plasmonic dipole antennas," *Nano Letters*, vol. 10, no. 3, pp. 1006–1011, 2010.
- [29] Z. Diao, *Investigation of 2D Photonic Crystals and Their Applications on Terahertz Quantum Cascade Lasers, Optical Trapping and Sensing*. PhD thesis, Ecole Polytechnique Fédérale de Lausanne, 2009.
- [30] M. Plihal and A. A. Maradudin, "Photonic band structure of two-dimensional systems: The triangular lattice," *Phys. Rev. B*, vol. 44, pp. 8565–8571, Oct 1991.
- [31] D. Leuenberger, *Experimental and numerical investigation of two-dimensional photonic crystals for application in integrated optics*. PhD thesis, Ecole Polytechnique Fédérale de Lausanne, 2004.
- [32] V. Zabelin, *Numerical investigation of two-dimensional photonic crystal optical properties, design and analysis of photonic crystal based structures*. PhD thesis, Ecole Polytechnique Fédérale de Lausanne, 2009.
- [33] J. Jágerská, *Dispersion Properties of Photonic Crystals and Silicon Nanostructures Investigated by Fourier-Space Imaging*. PhD thesis, Ecole Polytechnique Fédérale de Lausanne, 2011.
- [34] S. McNab, N. Moll, and Y. Vlasov, "Ultra-low loss photonic integrated circuit with membrane-type photonic crystal waveguides," *Opt. Express*, vol. 11, no. 22, pp. 2927–2939, 2003.
- [35] J. Vuckovic, M. Loncar, H. Mabuchi, and A. Scherer, "Optimization of the q factor in photonic crystal microcavities," *Quantum Electronics, IEEE Journal of*, vol. 38, no. 7, pp. 850–856, 2002.

## Bibliography

---

- [36] J. Jágorská, H. Zhang, N. Le Thomas, and R. Houdré, “Radiation loss of photonic crystal coupled-cavity waveguides,” *Applied Physics Letters*, vol. 95, no. 11, pp. 111105–3, 2009.
- [37] T. Tanabe, M. Notomi, E. Kuramochi, A. Shinya, and H. Taniyama, “Trapping and delaying photons for one nanosecond in an ultrasmall high-q photonic-crystal nanocavity,” *Nat Photon*, vol. 1, no. 1, pp. 49–52, 2007. 10.1038/nphoton.2006.51.
- [38] S. Nakayama, S. Ishida, S. Iwamoto, and Y. Arakawa, “Effect of cavity mode volume on photoluminescence from silicon photonic crystal nanocavities,” *Applied Physics Letters*, vol. 98, no. 17, pp. 171102–3, 2011.
- [39] M. Loncar, A. Scherer, and Y. Qiu, “Photonic crystal laser sources for chemical detection,” *Applied Physics Letters*, vol. 82, no. 26, pp. 4648–4650, 2003.
- [40] E. Kuramochi, M. Notomi, S. Mitsugi, A. Shinya, T. Tanabe, and T. Watanabe, “Ultrahigh-q photonic crystal nanocavities realized by the local width modulation of a line defect,” *Applied Physics Letters*, vol. 88, no. 4, pp. 041112–3, 2006.
- [41] T. Asano, B.-S. Song, and S. Noda, “Analysis of the experimental q factors (  $> 1$  million) of photonic crystal nanocavities,” *Opt. Express*, vol. 14, no. 5, pp. 1996–2002, 2006.
- [42] Y. Takahashi, H. Hagino, Y. Tanaka, B.-S. Song, T. Asano, and S. Noda, “High-q nanocavity with a 2-ns photon lifetime,” *Opt. Express*, vol. 15, no. 25, pp. 17206–17213, 2007.
- [43] M. Nomura, K. Tanabe, S. Iwamoto, and Y. Arakawa, “High-q design of semiconductor-based ultrasmall photonic crystal nanocavity,” *Opt. Express*, vol. 18, no. 8, pp. 8144–8150, 2010.
- [44] Y. Akahane, T. Asano, B.-S. Song, and S. Noda, “High-q photonic nanocavity in a two-dimensional photonic crystal,” *Nature*, vol. 425, no. 6961, pp. 944–947, 2003. 10.1038/nature02063.
- [45] J. Jágorská, H. Zhang, Z. Diao, N. Le Thomas, and R. Houdré, “Refractive index sensing with an air-slot photonic crystal nanocavity,” *Optics Letters*, vol. 35, no. 15, pp. 2523–2525, 2010.
- [46] U. Dharanipathy and R. Houdré, “Numerical modelling of optical trapping in hollow photonic crystal cavities,” *Optical and Quantum Electronics*, vol. 44, no. 3-5, pp. 161–167, 2012.
- [47] V. R. Almeida, Q. Xu, C. A. Barrios, and M. Lipson, “Guiding and confining light in void nanostructure,” *Optics Letters*, vol. 29, no. 11, pp. 1209–1211, 2004.
- [48] T. Baehr-Jones, M. Hochberg, C. Walker, and A. Scherer, “High-q optical resonators in silicon-on-insulator-based slot waveguides,” *Applied Physics Letters*, vol. 86, no. 8, pp. 081101–3, 2005.



- 
- [49] A. H. J. Yang, S. D. Moore, B. S. Schmidt, M. Klug, M. Lipson, and D. Erickson, "Optical manipulation of nanoparticles and biomolecules in sub-wavelength slot waveguides," *Nature*, vol. 457, no. 7225, pp. 71–75, 2009. 10.1038/nature07593.
  - [50] A. Di Falco, L. O'Faolain, and T. F. Krauss, "Photonic crystal slotted slab waveguides," *Photonics and Nanostructures - Fundamentals and Applications*, vol. 6, no. 1, pp. 38–41, 2008. Cited By (since 1996): 14 Export Date: 28 June 2012 Source: Scopus.
  - [51] A. Di Falco, L. O'Faolain, and T. F. Krauss, "Chemical sensing in slotted photonic crystal heterostructure cavities," *Applied Physics Letters*, vol. 94, no. 6, 2009. Cited By (since 1996): 47 Export Date: 28 June 2012 Source: Scopus Art. No.: 063503.
  - [52] T. Sunner, T. Stichel, S. H. Kwon, T. W. Schlereth, S. Hofling, M. Kamp, and A. Forchel, "Photonic crystal cavity based gas sensor," *Applied Physics Letters*, vol. 92, no. 26, pp. 261112–3, 2008.
  - [53] M. R. Lee and P. M. Fauchet, "Two-dimensional silicon photonic crystal based biosensing platform for protein detection," *Opt. Express*, vol. 15, no. 8, pp. 4530–4535, 2007.
  - [54] S. Noda, A. Chutinan, and M. Imada, "Trapping and emission of photons by a single defect in a photonic bandgap structure," *Nature*, vol. 407, pp. 608–610, 10 2000.
  - [55] M. R. Lee and P. M. Fauchet, "Nanoscale microcavity sensor for single particle detection," *Optics Letters*, vol. 32, no. 22, pp. 3284–3286, 2007.
  - [56] P. Lebedev, "The experimental study of the pressure of the light," *Ann. Phys*, vol. 6, p. 433, 1901.
  - [57] J. Jackson, "Classical electrodynamics," *JOHN WILEY AND SONS (NewYork)*, 1962.
  - [58] L. Novotny and B. Hecht, *Principles of nano-optics*. Cambridge university press, 2006.
  - [59] M. B. Stephen, "Optical angular-momentum flux," *Journal of Optics B: Quantum and Semiclassical Optics*, vol. 4, no. 2, p. S7, 2002.
  - [60] B. T. Draine, "The discrete-dipole approximation and its application to interstellar graphite grains," *The Astrophysical Journal*, vol. 333, pp. 848–872, 1988.
  - [61] P. W. Smith, P. J. Maloney, and A. Ashkin, "Use of a liquid suspension of dielectric spheres as an artificial kerr medium," *Optics Letters*, vol. 7, no. 8, pp. 347–349, 1982.
  - [62] J. P. Gordon, "Radiation forces and momenta in dielectric media," *Physical Review A*, vol. 8, no. 1, pp. 14–21, 1973. PRA.
  - [63] A. Rohrbach and E. H. K. Stelzer, "Optical trapping of dielectric particles in arbitrary fields," *J. Opt. Soc. Am. A*, vol. 18, pp. 839–853, Apr 2001.
  - [64] J. T. Rubin and L. Deych, "On optical forces in spherical whispering gallery mode resonators," *Optics Express*, vol. 19, no. 22, pp. 22337–22349, 2011.

## Bibliography

---

- [65] P. C. Chaumet and M. Nieto-Vesperinas, "Time-averaged total force on a dipolar sphere in an electromagnetic field," *Optics Letters*, vol. 25, no. 15, pp. 1065–1067, 2000.
- [66] M. Dienerowitz, M. Mazilu, and K. Dholakia, "Optical manipulation of nanoparticles: a review," *Journal of Nanophotonics*, vol. 2, no. 1, pp. 021875–021875–32, 2008.
- [67] K. C. Neuman and S. M. Block, "Optical trapping," *Review of Scientific Instruments*, vol. 75, no. 9, pp. 2787–2809, 2004. Cited By (since 1996): 692 Export Date: 29 June 2012 Source: Scopus.
- [68] K. Svoboda and S. M. Block, "Optical trapping of metallic rayleigh particles," *Optics Letters*, vol. 19, no. 13, pp. 930–932, 1994.
- [69] Y. Harada and T. Asakura, "Radiation forces on a dielectric sphere in the rayleigh scattering regime," *Optics Communications*, vol. 124, pp. 529–541, 1996.
- [70] P. Zemánek, A. Jonáš, L. Šrámek, and M. Liška, "Optical trapping of rayleigh particles using a gaussian standing wave," *Optics Communications*, vol. 151, no. 4–6, pp. 273 – 285, 1998.
- [71] S. Chu, J. E. Bjorkholm, A. Ashkin, and A. Cable, "Experimental observation of optically trapped atoms," *Physical Review Letters*, vol. 57, no. 3, pp. 314–317, 1986. PRL.
- [72] S. Chu, "Laser manipulation of atoms and particles," *Science*, vol. 253, no. 5022, pp. 861–866, 1991.
- [73] A. Ashkin and J. M. Dziedzic, "Observation of optical resonances of dielectric spheres by light scattering," *Appl. Opt.*, vol. 20, pp. 1803–1814, May 1981.
- [74] M. Born and E. Wolf, "Principles of optics, seventh (expanded) edition," *Cambridge, England*, 1999.
- [75] W. M. IRVINE, "Light scattering by spherical particles: Radiation pressure, asymmetry factor, and extinction cross section," *J. Opt. Soc. Am.*, vol. 55, pp. 16–19, Jan 1965.
- [76] B. T. Draine and P. J. Flatau, "Discrete-dipole approximation for scattering calculations," *J. Opt. Soc. Am. A*, vol. 11, pp. 1491–1499, Apr 1994.
- [77] A. G. Hoekstra, M. Frijlink, L. B. F. M. Waters, and P. M. A. Sloot, "Radiation forces in the discrete-dipole approximation," *J. Opt. Soc. Am. A*, vol. 18, no. 8, pp. 1944–1953, 2001.
- [78] W. H. Wright, G. J. Sonek, and M. W. Berns, "Radiation trapping forces on microspheres with optical tweezers," *Applied Physics Letters*, vol. 63, no. 6, pp. 715–717, 1993.
- [79] T. Li, S. Kheifets, and M. G. Raizen, "Millikelvin cooling of an optically trapped microsphere in vacuum," *Nature Physics*, vol. 7, no. 7, pp. 527–530, 2011. 10.1038/nphys1952.
- [80] A. Ashkin, "Forces of a single-beam gradient laser trap on a dielectric sphere in the ray optics regime," *Biophysical Journal*, vol. 61, no. 2, pp. 569–582, 1992.

- 
- [81] Y. Li, O. V. Svitelskiy, A. V. Maslov, D. Carnegie, E. Rafailov, and V. N. Astratov, "Giant resonant light forces in microspherical photonics," *Light Sci Appl*, vol. 2, pp. e64–, 04 2013.
- [82] A. V. Maslov, V. N. Astratov, and M. I. Bakunov, "Resonant propulsion of a microparticle by a surface wave," *Phys. Rev. A*, vol. 87, p. 053848, May 2013.
- [83] A. Ashkin, "Acceleration and trapping of particles by radiation pressure," *Physical Review Letters*, vol. 24, no. 4, pp. 156–159, 1970. PRL.
- [84] A. Ashkin and J. Dziedzic, "Optical trapping and manipulation of viruses and bacteria," *Science*, vol. 235, no. 4795, pp. 1517–1520, 1987.
- [85] H. He, M. E. J. Friese, N. R. Heckenberg, and H. Rubinsztein-Dunlop, "Direct observation of transfer of angular momentum to absorptive particles from a laser beam with a phase singularity," *Physical Review Letters*, vol. 75, no. 5, pp. 826–829, 1995. PRL.
- [86] L. Allen, M. W. Beijersbergen, R. J. C. Spreeuw, and J. P. Woerdman, "Orbital angular momentum of light and the transformation of laguerre-gaussian laser modes," *Phys. Rev. A*, vol. 45, pp. 8185–8189, Jun 1992.
- [87] N. B. Simpson, K. Dholakia, L. Allen, and M. J. Padgett, "Mechanical equivalence of spin and orbital angular momentum of light: an optical spanner," *Opt. Lett.*, vol. 22, pp. 52–54, Jan 1997.
- [88] M. E. J. Friese, T. A. Nieminen, N. R. Heckenberg, and H. Rubinsztein-Dunlop, "Optical alignment and spinning of laser-trapped microscopic particles," *Nature*, vol. 394, no. 6691, pp. 348–350, 1998. 10.1038/28566.
- [89] J. E. Curtis, B. A. Koss, and D. G. Grier, "Dynamic holographic optical tweezers," *Optics Communications*, vol. 207, no. 1–6, pp. 169 – 175, 2002.
- [90] D. G. Grier, "A revolution in optical manipulation," *Nature Photonics*, vol. 424, no. 6950, pp. 810–816, 2003. 10.1038/nature01935.
- [91] K. Dholakia and T. Cizmar, "Shaping the future of manipulation," *Nat Photon*, vol. 5, no. 6, pp. 335–342, 2011. 10.1038/nphoton.2011.80.
- [92] H. J. H. Clercx and P. P. J. M. Schram, "Brownian particles in shear flow and harmonic potentials: A study of long-time tails," *Phys. Rev. A*, vol. 46, pp. 1942–1950, Aug 1992.
- [93] B. Lukic, S. Jeney, C. Tischer, A. J. Kulik, L. Forró, and E.-L. Florin, "Direct observation of nondiffusive motion of a brownian particle," *Phys. Rev. Lett.*, vol. 95, p. 160601, Oct 2005.
- [94] K. Berg-Sorensen and H. Flyvbjerg, "Power spectrum analysis for optical tweezers," *Review of Scientific Instruments*, vol. 75, no. 3, pp. 594–612, 2004.

## Bibliography

---

- [95] K. C. Neuman and A. Nagy, "Single-molecule force spectroscopy: optical tweezers, magnetic tweezers and atomic force microscopy," *Nature Methods*, vol. 5, no. 6, pp. 491–505, 2008. 10.1038/nmeth.1218.
- [96] S. Tan, H. A. Lopez, C. W. Cai, and Y. Zhang, "Optical trapping of single-walled carbon nanotubes," *Nano Letters*, vol. 4, no. 8, pp. 1415–1419, 2004.
- [97] A. Irrera, P. Artoni, R. Saija, P. G. Gucciardi, M. A. Iatì, F. Borghese, P. Denti, F. Iacona, F. Priolo, and O. M. Maragò, "Size-scaling in optical trapping of silicon nanowires," *Nano Letters*, vol. 11, no. 11, pp. 4879–4884, 2011.
- [98] L. Jauffred, A. C. Richardson, and L. B. Oddershede, "Three-dimensional optical control of individual quantum dots," *Nano Letters*, vol. 8, no. 10, pp. 3376–3380, 2008.
- [99] A. Ashkin and J. M. Dziedzic, "Internal cell manipulation using infrared laser traps," *Proceedings of the National Academy of Sciences*, vol. 86, no. 20, pp. 7914–7918, 1989.
- [100] L. Sacconi, I. M. Tolic-Nørrelykke, C. Stringari, R. Antolini, and F. S. Pavone, "Optical micromanipulations inside yeast cells," *Appl. Opt.*, vol. 44, no. 11, pp. 2001–2007, 2005.
- [101] M. P. MacDonald, L. Paterson, K. Volke-Sepulveda, J. Arlt, W. Sibbett, and K. Dholakia, "Creation and manipulation of three-dimensional optically trapped structures," *Science*, vol. 296, no. 5570, pp. 1101–1103, 2002.
- [102] T. L. Min, P. J. Mears, L. M. Chubiz, C. V. Rao, I. Golding, and Y. R. Chemla, "High-resolution, long-term characterization of bacterial motility using optical tweezers," *Nat Meth*, vol. 6, no. 11, pp. 831–835, 2009. 10.1038/nmeth.1380.
- [103] T. Franosch, M. Grimm, M. Belushkin, F. M. Mor, G. Foffi, L. Forro, and S. Jeney, "Resonances arising from hydrodynamic memory in brownian motion," *Nature*, vol. 478, no. 7367, pp. 85–88, 2011. 10.1038/nature10498.
- [104] J. A. Valkenburg and C. L. Woldringh, "Phase separation between nucleoid and cytoplasm in escherichia coli as defined by immersive refractometry," *Journal of Bacteriology*, vol. 160, no. 3, pp. 1151–1157, 1984.
- [105] J. Tully, R. Cole, D. Taylor-Robinson, and D. Rose, "A newly discovered mycoplasma in the human urogenital tract," *The Lancet*, vol. 317, no. 8233, pp. 1288–1291, 1981.
- [106] A. Katz, A. Alimova, X. Min, E. Rudolph, M. K. Shah, H. E. Savage, R. B. Rosen, S. A. McCormick, and R. R. Alfano, "Bacteria size determination by elastic light scattering," *Selected Topics in Quantum Electronics, IEEE Journal of*, vol. 9, no. 2, pp. 277–287, 2003.
- [107] J. R. Mourant, J. P. Freyer, A. H. Hielscher, A. A. Eick, D. Shen, and T. M. Johnson, "Mechanisms of light scattering from biological cells relevant to noninvasive optical-tissue diagnostics," *Appl. Opt.*, vol. 37, pp. 3586–3593, Jun 1998.

- [108] S. Bassnett, "On the mechanism of organelle degradation in the vertebrate lens," *Experimental Eye Research*, vol. 88, no. 2, pp. 133–139, 2009.
- [109] A. Claude and E. F. Fullam, "An electron microscope study of isolated mitochondria: method and preliminary results," *The Journal of experimental medicine*, vol. 81, no. 1, p. 51, 1945.
- [110] J. A. G. Briggs, T. Wilk, R. Welker, H.-G. Krausslich, and S. D. Fuller, "Structural organization of authentic, mature hiv-1 virions and cores," *The EMBO Journal*, vol. 22, no. 7, pp. 1707–1715, 2003. 10.1093/emboj/cdgl43.
- [111] D.-Q. Wei, Q.-S. Du, H. Sun, and K.-C. Chou, "Insights from modeling the 3d structure of {H5N1} influenza virus neuraminidase and its binding interactions with ligands," *Biochemical and Biophysical Research Communications*, vol. 344, no. 3, pp. 1048 – 1055, 2006.
- [112] H. B. Donald and A. Isaacs, "Counts of influenza virus particles," *Journal of General Microbiology*, vol. 10, no. 3, pp. 457–464, 1954.
- [113] B. L. Scola, S. Audic, C. Robert, L. Jungang, X. de Lamballerie, M. Drancourt, R. Birtles, J.-M. Claverie, and D. Raoult, "A giant virus in amoebae," *Science*, vol. 299, no. 5615, p. 2033, 2003.
- [114] L. P. Ghislain and W. W. Webb, "Scanning-force microscope based on an optical trap," *Optics Letters*, vol. 18, no. 19, pp. 1678–1680, 1993.
- [115] R. Simmons, J. Finer, S. Chu, and J. Spudich, "Quantitative measurements of force and displacement using an optical trap," *Biophysical Journal*, vol. 70, no. 4, pp. 1813 – 1822, 1996.
- [116] A. Pralle, E. L. Florin, E. H. K. Stelzer, and J. K. H. Hörber, "Local viscosity probed by photonic force microscopy," *Applied Physics A*, vol. 66, no. 1, pp. S71–S73, 1998.
- [117] A. Rohrbach, C. Tischer, D. Neumayer, E.-L. Florin, and E. H. K. Stelzer, "Trapping and tracking a local probe with a photonic force microscope," *Review of Scientific Instruments*, vol. 75, no. 6, pp. 2197–2210, 2004.
- [118] A. D. Mehta, M. Rief, J. A. Spudich, D. A. Smith, and R. M. Simmons, "Single-molecule biomechanics with optical methods," *Science*, vol. 283, no. 5408, pp. 1689–1695, 1999.
- [119] J. Liphardt, B. Onoa, S. B. Smith, I. Tinoco, and C. Bustamante, "Reversible unfolding of single rna molecules by mechanical force," *Science*, vol. 292, no. 5517, pp. 733–737, 2001.
- [120] M. J. Lang, P. M. Fordyce, A. M. Engh, K. C. Neuman, and S. M. Block, "Simultaneous, coincident optical trapping and single-molecule fluorescence," *Nat Meth*, vol. 1, no. 2, pp. 133–139, 2004. 10.1038/nmeth714.

## Bibliography

---

- [121] E. A. Abbondanzieri, W. J. Greenleaf, J. W. Shaevitz, R. Landick, and S. M. Block, "Direct observation of base-pair stepping by rna polymerase," *Nature*, vol. 438, no. 7067, pp. 460–465, 2005. 10.1038/nature04268.
- [122] L. Novotny, R. X. Bian, and X. S. Xie, "Theory of nanometric optical tweezers," *Physical Review Letters*, vol. 79, no. 4, pp. 645–648, 1997. PRL.
- [123] M. Righini, A. S. Zelenina, C. Girard, and R. Quidant, "Parallel and selective trapping in a patterned plasmonic landscape," *Nature Physics*, vol. 3, no. 7, pp. 477–480, 2007. 10.1038/nphys624.
- [124] L. Huang, S. J. Maerkl, and O. J. Martin, "Integration of plasmonic trapping in a microfluidic environment," *Optics Express*, vol. 17, no. 8, pp. 6018–6024, 2009.
- [125] Y. Pang and R. Gordon, "Optical trapping of 12 nm dielectric spheres using double-nanoholes in a gold film," *Nano Letters*, vol. 11, no. 9, pp. 3763–3767, 2011.
- [126] K. Wang, E. Schonbrun, P. Steinvurzel, and K. B. Crozier, "Trapping and rotating nanoparticles using a plasmonic nano-tweezer with an integrated heat sink," *Nat Commun*, vol. 2, p. 469, 09 2011.
- [127] A. N. Grigorenko, N. W. Roberts, M. R. Dickinson, and ZhangY, "Nanometric optical tweezers based on nanostructured substrates," *Nature Photonics*, vol. 2, no. 6, pp. 365–370, 2008. 10.1038/nphoton.2008.78.
- [128] M. Righini, P. Ghenuche, S. Cherukulappurath, V. Myroshnychenko, F. J. García de Abajo, and R. Quidant, "Nano-optical trapping of rayleigh particles and escherichia coli bacteria with resonant optical antennas," *Nano Letters*, vol. 9, no. 10, pp. 3387–3391, 2009.
- [129] C. Genet and T. W. Ebbesen, "Light in tiny holes," *Nature*, vol. 445, no. 7123, pp. 39–46, 2007. 10.1038/nature05350.
- [130] M. L. Juan, R. Gordon, Y. Pang, F. Eftekhari, and R. Quidant, "Self-induced back-action optical trapping of dielectric nanoparticles," *Nature Physics*, vol. 5, no. 12, pp. 915–919, 2009. 10.1038/nphys1422.
- [131] S. Kawata and T. Tani, "Optically driven mie particles in an evanescent field along a channeled waveguide," *Optics Letters*, vol. 21, no. 21, pp. 1768–1770, 1996.
- [132] L. N. Ng, M. N. Zervas, J. S. Wilkinson, and B. J. Luff, "Manipulation of colloidal gold nanoparticles in the evanescent field of a channel waveguide," *Applied Physics Letters*, vol. 76, no. 15, pp. 1993–1995, 2000.
- [133] K. Grujic, O. G. Hellesø, O. G., J. S. Wilkinson, and J. P. Hole, "Optical propulsion of microspheres along a channel waveguide produced by cs<sup>+</sup> ion-exchange in glass," *Optics Communications*, vol. 239, pp. 227–235, 2004.

- 
- [134] S. Gaugiran, S. Gétin, J. Fedeli, G. Colas, A. Fuchs, F. Chatelain, and J. Dèrouard, "Optical manipulation of microparticles and cells on silicon nitride waveguides," *Opt. Express*, vol. 13, no. 18, pp. 6956–6963, 2005.
- [135] G. Brambilla, G. S. Murugan, J. S. Wilkinson, and D. J. Richardson, "Optical manipulation of microspheres along a subwavelength optical wire," *Optics Letters*, vol. 32, no. 20, pp. 3041–3043, 2007.
- [136] B. S. Schmidt, A. H. Yang, D. Erickson, and M. Lipson, "Optofluidic trapping and transport on solid core waveguides within a microfluidic device," *Optics Express*, vol. 15, no. 22, pp. 14322–14334, 2007.
- [137] B. S. Ahluwalia, P. McCourt, T. Huser, and O. G. Hellesø, Olav Gaute, "Optical trapping and propulsion of red blood cells on waveguide surfaces," *Opt. Express*, vol. 18, no. 20, pp. 21053–21061, 2010.
- [138] K. J. Vahala, "Optical microcavities," *Nature*, vol. 424, no. 6950, pp. 839–846, 2003. 10.1038/nature01939.
- [139] F. Vollmer and S. Arnold, "Whispering-gallery-mode biosensing: label-free detection down to single molecules," *Nat Meth*, vol. 5, no. 7, pp. 591–596, 2008. 10.1038/nmeth.1221.
- [140] F. Vollmer, S. Arnold, and D. Keng, "Single virus detection from the reactive shift of a whispering-gallery mode," *Proceedings of the National Academy of Sciences*, vol. 105, no. 52, pp. 20701–20704, 2008.
- [141] S. Arnold, D. Keng, S. I. Shopova, S. Holler, W. Zurawsky, and F. Vollmer, "Whispering gallery mode carousel—a photonic mechanism for enhanced nanoparticle detection in biosensing," *Optics Express*, vol. 17, no. 8, pp. 6230–6238, 2009. Research Support, Non-U.S. Gov't, Research Support, U.S. Gov't, Non-P.H.S.
- [142] S. Lin, E. Schonbrun, and K. Crozier, "Optical manipulation with planar silicon microring resonators," *Nano Letters*, vol. 10, no. 7, pp. 2408–2411, 2010.
- [143] A. H. J. Yang and D. Erickson, "Optofluidic ring resonator switch for optical particle transport," *Lab Chip*, vol. 10, pp. 769–774, 2010.
- [144] H. Cai and A. W. Poon, "Optical manipulation and transport of microparticles on silicon nitride microring-resonator-based add-drop devices," *Optics Letters*, vol. 35, no. 17, pp. 2855–2857, 2010.
- [145] S. Lin, J. Hu, L. Kimerling, and K. Crozier, "Design of nanoslotted photonic crystal waveguide cavities for single nanoparticle trapping and detection," *Optics Letters*, vol. 34, no. 21, pp. 3451–3453, 2009.

## Bibliography

---

- [146] Y.-F. Chen, X. Serey, R. Sarkar, P. Chen, and D. Erickson, "Controlled photonic manipulation of proteins and other nanomaterials," *Nano Letters*, vol. 12, no. 3, pp. 1633–1637, 2012.
- [147] T. van der Sar, J. Hagemeier, W. Pfaff, E. Heeres, S. Thon, H. Kim, P. Petroff, O. Tjerk, D. Bouwmeester, and R. Hanson, "Effect of a nanoparticle on the optical properties of a photonic crystal cavity: theory and experiment," *J. Opt. Soc. Am. B*, vol. 29, no. 4, pp. 698–703, 2012.
- [148] A. Rahmani and P. C. Chaumet, "Optical trapping near a photonic crystal," *Optics Express*, vol. 14, no. 13, pp. 6353–6358, 2006.
- [149] S. Mandal, X. Serey, and D. Erickson, "Nanomanipulation using silicon photonic crystal resonators," *Nano Letters*, vol. 10, no. 1, pp. 99–104, 2009.
- [150] C. Renaut, J. Dellinger, B. Cluzel, T. Honegger, D. Peyrade, E. Picard, F. De Fornel, and E. Hadji, "Assembly of microparticles by optical trapping with a photonic crystal nanocavity," *Applied Physics Letters*, vol. 100, no. 10, 2012. Export Date: 28 June 2012 Source: Scopus Art. No.: 101103.
- [151] J. Hu, S. Lin, L. C. Kimerling, and K. Crozier, "Optical trapping of dielectric nanoparticles in resonant cavities," *Physical Review A*, vol. 82, no. 5, p. 053819, 2010. PRA.
- [152] L. P. Ghislain, N. A. Switz, and W. W. Webb, "Measurement of small forces using an optical trap," *Review of Scientific Instruments*, vol. 65, no. 9, pp. 2762–2768, 1994.
- [153] J. Jágorská, N. Le Thomas, R. Houdré, J. Bolten, C. Moormann, T. Wahlbrink, J. Ctyroky, M. Waldow, and M. Först, "Dispersion properties of silicon nanophotonic waveguides investigated with fourier optics," *Optics Letters*, vol. 32, no. 18, pp. 2723–2725, 2007.
- [154] M. Notomi, E. Kuramochi, and T. Tanabe, "Large-scale arrays of ultrahigh-q coupled nanocavities," *Nat Photon*, vol. 2, no. 12, pp. 741–747, 2008. 10.1038/nphoton.2008.226.
- [155] "<http://www.micro-shop.zeiss.com>."
- [156] "<http://www.bdbiosciences.com>."
- [157] "<http://www.thorlabs.com>."
- [158] P. Tabeling, *Introduction à la microfluidique*. Belin, Paris, 2003.
- [159] G. M. Whitesides, "The origins and the future of microfluidics," *Nature*, vol. 442, no. 7101, pp. 368–373, 2006. 10.1038/nature05058.
- [160] M. B. Wabuyele, S. M. Ford, W. Stryjewski, J. Barrow, and S. A. Soper, "Single molecule detection of double-stranded dna in poly(methylmethacrylate) and polycarbonate microfluidic devices," *Electrophoresis*, vol. 22, no. 18, pp. 3939–3948, 2001.



- [161] E. T. Lagally, I. Medintz, and R. A. Mathies, "Single-molecule dna amplification and analysis in an integrated microfluidic device," *Analytical Chemistry*, vol. 73, no. 3, pp. 565–570, 2001.
- [162] H.-P. Chou, C. Spence, A. Scherer, and S. Quake, "A microfabricated device for sizing and sorting dna molecules," *Proceedings of the National Academy of Sciences*, vol. 96, no. 1, pp. 11–13, 1999.
- [163] A. J. deMello, "Control and detection of chemical reactions in microfluidic systems," *Nature*, vol. 442, no. 7101, pp. 394–402, 2006. 10.1038/nature05062.
- [164] P. S. Dittrich and A. Manz, "Lab-on-a-chip: microfluidics in drug discovery," *Nat Rev Drug Discov*, vol. 5, no. 3, pp. 210–218, 2006. 10.1038/nrd1985.
- [165] S. Einav, D. Gerber, P. D. Bryson, E. H. Sklan, M. Elazar, S. J. Maerkl, J. S. Glenn, and S. R. Quake, "Discovery of a hepatitis c target and its pharmacological inhibitors by microfluidic affinity analysis," *Nat Biotech*, vol. 26, no. 9, pp. 1019–1027, 2008. 10.1038/nbt.1490.
- [166] S. J. Maerkl and S. R. Quake, "A systems approach to measuring the binding energy landscapes of transcription factors," *Science*, vol. 315, no. 5809, pp. 233–237, 2007.
- [167] J. El-Ali, P. K. Sorger, and K. F. Jensen, "Cells on chips," *Nature*, vol. 442, no. 7101, pp. 403–411, 2006. 10.1038/nature05063.
- [168] N. W. Choi, M. Cabodi, B. Held, J. P. Gleghorn, L. J. Bonassar, and A. D. Stroock, "Microfluidic scaffolds for tissue engineering," *Nat Mater*, vol. 6, no. 11, pp. 908–915, 2007. 10.1038/nmat2022.
- [169] T. Thorsen, S. J. Maerkl, and S. R. Quake, "Microfluidic large-scale integration," *Science*, vol. 298, no. 5593, pp. 580–584, 2002.
- [170] H. Becker and C. Gärtner, "Polymer microfabrication technologies for microfluidic systems," *Analytical and Bioanalytical Chemistry*, vol. 390, no. 1, pp. 89–111, 2008.
- [171] M. A. Unger, H.-P. Chou, T. Thorsen, A. Scherer, and S. R. Quake, "Monolithic microfabricated valves and pumps by multilayer soft lithography," *Science*, vol. 288, no. 5463, pp. 113–116, 2000.
- [172] D. C. Duffy, J. C. McDonald, O. J. A. Schueller, and G. M. Whitesides, "Rapid prototyping of microfluidic systems in poly(dimethylsiloxane)," *Analytical Chemistry*, vol. 70, no. 23, pp. 4974–4984, 1998.
- [173] H.-P. Chou, M. Unger, and S. Quake, "A microfabricated rotary pump," *Biomedical Microdevices*, vol. 3, no. 4, pp. 323–330, 2001.
- [174] C. I. Bouzigues, P. Tabeling, and L. Bocquet, "Nanofluidics in the debye layer at hydrophilic and hydrophobic surfaces," *Physical Review Letters*, vol. 101, no. 11, p. 114503, 2008. PRL.

## Bibliography

---

- [175] K. Ando, A.-Q. Liu, and C.-D. Ohl, "Homogeneous nucleation in water in microfluidic channels," *Physical Review Letters*, vol. 109, no. 4, p. 044501, 2012. PRL.
- [176] K. H. Jensen and M. A. Zwieniecki, "Physical limits to leaf size in tall trees," *Physical Review Letters*, vol. 110, no. 1, p. 018104, 2013. PRL.
- [177] A. Scott, A. K. Au, E. Vinckenbosch, and A. Folch, "A microfluidic d-subminiature connector," *Lab on a Chip*, 2013.
- [178] I. E. Araci and S. R. Quake, "Microfluidic very large scale integration (mvlsi) with integrated micromechanical valves," *Lab on a Chip*, vol. 12, no. 16, pp. 2803–2806, 2012.
- [179] L. Martin, M. Meier, S. M. Lyons, R. V. Sit, W. F. Marzluff, S. R. Quake, and H. Y. Chang, "Systematic reconstruction of rna functional motifs with high-throughput microfluidics," *Nat Meth*, vol. 9, no. 12, pp. 1192–1194, 2012. 10.1038/nmeth.2225.
- [180] N. Wang, X. Zhang, B. Chen, W. Song, N. Y. Chan, and H. L. W. Chan, "Microfluidic photoelectrocatalytic reactors for water purification with an integrated visible-light source," *Lab on a Chip*, vol. 12, no. 20, pp. 3983–3990, 2012.
- [181] D. Psaltis, S. R. Quake, and C. Yang, "Developing optofluidic technology through the fusion of microfluidics and optics," *Nature*, vol. 442, no. 7101, pp. 381–386, 2006. 10.1038/nature05060.
- [182] C. Monat, P. Domachuk, and B. J. Eggleton, "Integrated optofluidics: A new river of light," *Nature Photonics*, vol. 1, no. 2, pp. 106–114, 2007. 10.1038/nphoton.2006.96.
- [183] L. Pang, H. M. Chen, L. M. Freeman, and Y. Fainman, "Optofluidic devices and applications in photonics, sensing and imaging," *Lab on a Chip*, vol. 12, no. 19, pp. 3543–3551, 2012.
- [184] Y. Yang, A. Q. Liu, L. K. Chin, X. M. Zhang, D. P. Tsai, C. L. Lin, C. Lu, G. P. Wang, and N. I. Zheludev, "Optofluidic waveguide as a transformation optics device for lightwave bending and manipulation," *Nat Commun*, vol. 3, p. 651, 2012. 10.1038/ncomms1662.
- [185] A. J. Chung and D. Erickson, "Optofluidic waveguides for reconfigurable photonic systems," *Opt. Express*, vol. 19, no. 9, pp. 8602–8609, 2011.
- [186] D. V. Vezhenov, B. T. Mayers, D. B. Wolfe, and G. M. Whitesides, "Integrated fluorescent light source for optofluidic applications," *Applied Physics Letters*, vol. 86, no. 4, pp. 041104–3, 2005.
- [187] Z. Li, Z. Zhang, T. Emery, A. Scherer, and D. Psaltis, "Single mode optofluidic distributed feedback dye laser," *Opt. Express*, vol. 14, no. 2, pp. 696–701, 2006.
- [188] X. Zhang, W. Lee, and X. Fan, "Bio-switchable optofluidic lasers based on dna holliday junctions," *Lab on a Chip*, vol. 12, no. 19, pp. 3673–3675, 2012.

- [189] C. J. G., V. A. E., D. S. L., and P. D., "Optofluidic modulator based on peristaltic nematogen microflows," *Nat Photon*, vol. 5, pp. 234–238, 04 2011.
- [190] D. Erickson, D. Sinton, and D. Psaltis, "Optofluidics for energy applications," *Nat Photon*, vol. 5, no. 10, pp. 583–590, 2011. 10.1038/nphoton.2011.209.
- [191] S. Surdo, S. Merlo, F. Carpignano, L. M. Strambini, C. Trono, A. Giannetti, F. Baldini, and G. Barillaro, "Optofluidic microsystems with integrated vertical one-dimensional photonic crystals for chemical analysis," *Lab on a Chip*, vol. 12, no. 21, pp. 4403–4415, 2012.
- [192] E. Weber and M. J. Vellekoop, "Optofluidic micro-sensors for the determination of liquid concentrations," *Lab on a Chip*, vol. 12, no. 19, pp. 3754–3759, 2012.
- [193] A. A. Yanik, M. Huang, O. Kamohara, A. Artar, T. W. Geisbert, J. H. Connor, and H. Altug, "An optofluidic nanoplasmonic biosensor for direct detection of live viruses from biological media," *Nano Letters*, vol. 10, no. 12, pp. 4962–4969, 2010.
- [194] Y. Guo, H. Li, K. Reddy, H. S. Shelar, V. R. Nittoor, and X. Fan, "Optofluidic fabry-p[er]acute]rot cavity biosensor with integrated flow-through micro-/nanochannels," *Applied Physics Letters*, vol. 98, no. 4, pp. 041104–3, 2011.
- [195] J.-S. Kwon, S. P. Ravindranath, A. Kumar, J. Irudayaraj, and S. T. Wereley, "Opto-electrokinetic manipulation for high-performance on-chip bioassays," *Lab on a Chip*, vol. 12, no. 23, pp. 4955–4959, 2012.
- [196] "[http://www.cs.unc.edu/~nanowork/cismm/download/spottracker/video\\_spot\\_tracker.html](http://www.cs.unc.edu/~nanowork/cismm/download/spottracker/video_spot_tracker.html)."
- [197] Y. Akahane, T. Asano, B.-S. Song, and S. Noda, "Fine-tuned high-q photonic-crystal nanocavity," *Opt. Express*, vol. 13, no. 4, pp. 1202–1214, 2005.
- [198] G.-H. Kim, Y.-H. Lee, A. Shinya, and M. Notomi, "Coupling of small, low-loss hexapole mode with photonic crystal slab waveguide mode," *Opt. Express*, vol. 12, no. 26, pp. 6624–6631, 2004.
- [199] N. Masaya, "Manipulating light with strongly modulated photonic crystals," *Reports on Progress in Physics*, vol. 73, no. 9, p. 096501, 2010.
- [200] M. Burrese, R. J. P. Engelen, A. Opheij, D. van Oosten, D. Mori, T. Baba, and L. Kuipers, "Observation of polarization singularities at the nanoscale," *Physical Review Letters*, vol. 102, no. 3, p. 033902, 2009. PRL.
- [201] J. Bayly, V. Kartha, and W. Stevens, "The absorption spectra of liquid phase h<sub>2</sub>o, hdo and d<sub>2</sub>o," *Infrared Physics*, vol. 3, no. 4, pp. 211 – 222, 1963.

## Bibliography

---

- [202] S. H. Mirsadeghi, E. Schelew, and J. F. Young, “Photonic crystal slot-microcavity circuit implemented in silicon-on-insulator: High q operation in solvent without undercutting,” *Applied Physics Letters*, vol. 102, no. 13, p. 131115, 2013.
- [203] N. Descharmes, U. P. Dharanipathy, Z. Diao, M. Tonin, and R. Houdre, “Single particle detection, manipulation and analysis with resonant optical trapping in photonic crystals,” *Lab Chip*, vol. 13, pp. 3268–3274, 2013.
- [204] “[http://prl.aps.org/epaps/PRL/v110/i12/e123601/Descharmes\\_Supplementary\\_Movie.mov](http://prl.aps.org/epaps/PRL/v110/i12/e123601/Descharmes_Supplementary_Movie.mov).”
- [205] E. J. G. Peterman, F. Gittes, and C. F. Schmidt, “Laser-induced heating in optical traps,” *Biophysical Journal*, vol. 84, no. 2, pp. 1308–1316, 2003.
- [206] C. M. Caves, “Quantum-mechanical noise in an interferometer,” *Physical Review D*, vol. 23, no. 8, pp. 1693–1708, 1981. PRD.
- [207] T. J. Kippenberg and K. J. Vahala, “Cavity optomechanics: Back-action at the mesoscale,” *Science*, vol. 321, no. 5893, pp. 1172–1176, 2008.
- [208] V. Braginsky, S. Strigin, and S. Vyatchanin, “Parametric oscillatory instability in fabry-perot interferometer,” *Physics Letters A*, vol. 287, no. 5–6, pp. 331 – 338, 2001.
- [209] A. Schliesser, P. Del’Haye, N. Nooshi, K. J. Vahala, and T. J. Kippenberg, “Radiation pressure cooling of a micromechanical oscillator using dynamical backaction,” *Phys. Rev. Lett.*, vol. 97, p. 243905, Dec 2006.
- [210] J. Chan, T. P. M. Alegre, A. H. Safavi-Naeini, J. T. Hill, A. Krause, S. Groblacher, M. Aspelmeyer, and O. Painter, “Laser cooling of a nanomechanical oscillator into its quantum ground state,” *Nature*, vol. 478, pp. 89–92, 10 2011.
- [211] M. Eichenfield, R. Camacho, J. Chan, K. J. Vahala, and O. Painter, “A picogram- and nanometre-scale photonic-crystal optomechanical cavity,” *Nature*, vol. 459, no. 7246, pp. 550–555, 2009. 10.1038/nature08061.
- [212] E. Gavartin, R. Braive, I. Sagnes, O. Arcizet, A. Beveratos, T. J. Kippenberg, and I. Robert-Philip, “Optomechanical coupling in a two-dimensional photonic crystal defect cavity,” *Phys. Rev. Lett.*, vol. 106, p. 203902, May 2011.
- [213] G. Anetsberger, O. Arcizet, Q. P. Unterreithmeier, R. Riviere, A. Schliesser, E. M. Weig, J. P. Kotthaus, and T. J. Kippenberg, “Near-field cavity optomechanics with nanomechanical oscillators,” *Nat Phys*, vol. 5, no. 12, pp. 909–914, 2009. 10.1038/nphys1425.
- [214] D. Van Thourhout and J. Roels, “Optomechanical device actuation through the optical gradient force,” *Nat Photon*, vol. 4, no. 4, pp. 211–217, 2010. 10.1038/nphoton.2010.72.
- [215] Z.-q. Yin, T. Li, and M. Feng, “Three-dimensional cooling and detection of a nanosphere with a single cavity,” *Phys. Rev. A*, vol. 83, p. 013816, Jan 2011.

- [216] D. E. Chang, C. A. Regal, S. B. Papp, D. J. Wilson, J. Ye, O. Painter, H. J. Kimble, and P. Zoller, “Cavity opto-mechanics using an optically levitated nanosphere,” *Proceedings of the National Academy of Sciences*, vol. 107, no. 3, pp. 1005–1010, 2010. 10.1073/pnas.0912969107.
- [217] N. V. Triviño, G. Rossbach, U. Dharanipathy, J. Levrat, A. Castiglia, J. F. Carlin, K. A. Atlasov, R. Butté, R. Houdré, and N. Grandjean, “High quality factor two dimensional gan photonic crystal cavity membranes grown on silicon substrate,” *Applied Physics Letters*, vol. 100, no. 7, pp. 071103–3, 2012.



# Acknowledgements

The four years of my doctoral studies leave me deeply indebted to many people. First of all, I would like to sincerely thank my thesis advisor Prof. Romuald Houdré. By accepting me as a PhD student in his group, Romuald gave me a chance when I needed one. Romuald has an outstanding care for scientific rigor, preciseness and clarity of explanation. He is also one of the most knowledgeable person I was ever given to meet. The memories of my work under his direction will be those of the tough - but invaluable - lessons learned and, more importantly, the exceptional feeling of the goal that has been achieved through persistent efforts and commitment. He also shared with me his passion for mountaineering, and especially ski touring, which I hope we will be given to share again.

I also would like to thank my three amazing teammates without whom nothing would have been possible: Perumal, Zhaolu and Mario. Work is a different place when you share it with three passionate, hard-working, dedicated friends. In particular I would like to thank: Peru, for having been there for me on so many occasions, for our countless philosophical discussions, for our agitated scientific debates, and for introducing me to his legendary "big picture talk" technique. He also took the time to read and correct my entire manuscript. Zhaolu, for being such a great and inspiring man who has shown me that it is possible to treat life inside and outside of work with an equal degree of genuineness, humility and dedication. Mario, for the long hours spent with me in the clean rooms and in the lab, repeating the fabrication and experiments over and over again, without getting upset at me even once (that I know of).

I sincerely thank Prof. Sebastian Maerkl and his group for their precious help on the development of the microfluidic membrane.

I thank Prof. Nicolas Le Thomas who introduced me to the different experimental techniques related to the characterization of photonic crystal nanostructures at the Lab. of Quantum Optoelectronics. Nicolas also spent a lot of time sharing with me his vast knowledge of Physics.

I thank Dr. Omar Sqalli who, as my supervisor in Dublin, convinced me, motivated me, and finally gave me references to come and do this PhD at EPFL. Omar is and will remain a strong inspiration for me in my professional life.

I would like to express my deepest gratitude and friendship to Roger Rochat, Hans-Jörg

## Acknowledgements

---

Bühlmann, Nicolas Leiser and also Damien and Yoan Trollet for their invaluable help and friendliness. There exist no experimental problem that can resist to this set of incredible people. On the administrative side I would like to thank Laurence and Claire-Lyse at LOEQ and Pierrette Paulou, formerly at the EDPO office, for their constant kindness and helpfulness.

I cannot help to mention the set of extraordinary people that I have been given to meet during my stay at EPFL, and who contributed all, in one way or the other, to make of these four years such an unforgettable time of my life: Raphaël Butté, Yohan Léger, Lise Lahourcade, Jana, Kaja, Roland, Verena, Jens and also the Lab. of Polymer and Composite Technology crew: Mathieu, Sam, Basile, Erica, Alessandra and Fabio, Marina and Raphaël.

My deepest thanks and loving thoughts go to my parents and my sister, for their unconditional love, guidance, encouragements and support throughout my life and my studies. There are no words to say how much they mean to me. Finally I have a set of special thanks for a set of very special people to me: Alexandre and Florence, Romain (Tiche) and Quynh-Nhu, Paul and Bénédicte, Farid and Rionach, and Romain (Chico).

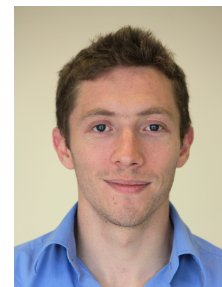
*Lausanne, 18 Juillet 2013*

N. D.



# Nicolas DESCHARMES

Date of birth: April 2<sup>nd</sup>, 1982 (31 years old)  
Nationality: French  
Other: Single, Swiss working permit B and driving license holder.  
Address: Chemin de Rionza 9, 1020 RENENS (VD), Switzerland  
Phone: 0(0 41) 76 766 63 83  
Email: [ndescharmes@gmail.com](mailto:ndescharmes@gmail.com)



## STRENGTHS

---

- **Engineer** specialized in **Optics, Photonics and Optoelectronics**.
- **Four years of professional experience** in a research and development **start-up company**.
- Self-motivated, dynamic and adaptable individual. Willing to travel.

## WORK EXPERIENCE

---

Aug 09 – this day:	<b>Doctoral assistant - EPFL</b> (Switzerland) Development and investigation of silicon photonic nanostructures for the optical sensing and trapping of nanoparticles. Microfluidic circuits design, fabrication and operation. Design and assembly of an optical test bench combining a fluorescent imaging microscope, a near-infrared microscope, an optical tweezers beam and a confocal sensor. Scientific reporting and international conferences.
	<b>Optical engineer - Dyoptika</b> (Ireland) Development of anti-speckle systems for laser video projection. Development of an anti-aliasing system based on adaptive optics for high-definition imaging. Worldwide customer support. Pre-sales application testing and customization. Patent writing and reporting.
Oct 05 – July 09:	<b>Optical engineer</b> (intern) – <b>Institute of Astrophysics of Canary Islands</b> (Spain) Development of an adaptive optics bench for the testing of a prototype on FPGA-based control system for very large telescopes. Interferometric testing and characterization of Silicon Nitride membrane mirrors.
Feb 05 - Aug 05:	

## ACADEMIC RECORD

---

2013	<b>PhD degree candidate</b> - to be defended Summer 2013, major: <b>Photonics</b> Ecole Polytechnique Fédérale de Lausanne, Switzerland.
2005	<b>Engineering degree</b> , major: <b>Optoelectronics</b> ENSSAT, Rennes I University, France.
2002	Preparatory degree, major Mathematics, Physics and Chemistry, Carnot institute, Dijon, France.

## TECHNICAL SOFTWARES

---

**Ray tracing:** Zemax, Oslo, Solstis      **Numerical simulation:** Matlab      **Automation:** Labview

## LANGUAGES

---

**French:** native      **English:** fluent      **Spanish:** fluent      **German:** basic

## EXTRA CURRICULAR ACTIVITIES

---

Running, Rugby sevens, Photography.